MARTIN MARIETTA ENERGY SYSTEMS LIBRARIES
3 4456 0361404 2

139

CENTRAL RESEARCH LIBRARY
DOCUMENT COLLECTION

ORNL-2767
Reactors-Power

# GAS-COOLED REACTOR PROJECT

# SEMIANNUAL PROGRESS REPORT

# FOR PERIOD ENDING JUNE 30, 1959

CENTRAL RESEARCH LIBRARY
DOCUMENT COLLECTION
LIBRARY LOAN COPY
DO NOT TRANSFER TO ANOTHER PERSON
If you wish someone else to see this document, send in name with document and the library will arrange a loan.

OAK RIDGE NATIONAL LABORATORY
operated by
UNION CARBIDE CORPORATION
for the
U.S. ATOMIC ENERGY COMMISSION

Printed in USA. Price $3.50. Available from the

Office of Technical Services
Department of Commerce
Washington 25, D.C.

LEGAL NOTICE

This report was prepared as an account of Government sponsored work. Neither the United States, nor the Commission, nor any person acting on behalf of the Commission:

A. Makes any warranty or representation, expressed or implied, with respect to the accuracy, completeness, or usefulness of the information contained in this report, or that the use of any information, apparatus, method, or process disclosed in this report may not infringe privately owned rights; or

B. Assumes any liabilities with respect to the use of, or for damages resulting from the use of any information, apparatus, method, or process disclosed in this report.

As used in the above, "person acting on behalf of the Commission" includes any employee or contractor of the Commission, or employee of such contractor, to the extent that such employee or contractor of the Commission, or employee of such contractor prepares, disseminates, or provides access to, any information pursuant to his employment or contract with the Commission, or his employment with such contractor.

ORNL-2767

Reactors — Power
TID-4500 (14th ed.)

Contract No. W-7405-eng-26

# GAS-COOLED REACTOR PROJECT

# SEMIANNUAL PROGRESS REPORT

for Period Ending June 30, 1959

Staff

Oak Ridge National Laboratory

DATE ISSUED

AUG 14 1959

OAK RIDGE NATIONAL LABORATORY
Oak Ridge, Tennessee
operated by
UNION CARBIDE CORPORATION
for the
U.S. ATOMIC ENERGY COMMISSION

3 4456 0361404 2

CONTENTS

SUMMARY ..... vii

PART 1. DESIGN INVESTIGATIONS

1. ADVANCED REACTOR CONCEPTS ..... 3

Direct-Cycle Steam-Cooled Reactor ..... 3

Preliminary Designs for Two Integrated Gas-Cooled Reactor Core and Steam Generator Units ..... 6

2. REACTOR DESIGN ..... 15

Thermal Performance of Fuel Elements ..... 15
Effect of Power Distribution on Fuel Element Surface Temperatures ..... 15
Thermal Analysis of Fuel Elements ..... 16
Analysis of Flow in a Scalloped Channel ..... 17
Comparison of Pebble Fuel Beds and Clustered Fuel Rods ..... 23
Dynamic Analysis of Thermal Radiation from Fuel Capsule to Graphite ..... 24

Structural Investigations ..... 25
Stress Analysis of Grid Structure ..... 25
Study of Fuel Element Cladding Behavior ..... 26
Tube-Buckling Experiments ..... 27
Experimental Analysis of Perforated Plates ..... 28

Study of Helium Ionization ..... 30

Containment Vessel Study ..... 34

Reactor Physics ..... 39
Fast-Neutron Flux in the PEGCPR Pressure Vessel .... 39
Control Rod Worth in the EGCR ..... 40
Effect of Control Rods on Power Distribution ..... 45
EGCR Experimental Loops ..... 50
Power-Density Distribution in Fuel Clusters ..... 54

3. EXPERIMENTAL INVESTIGATIONS OF HEAT TRANSFER AND FLUID FLOW ..... 58

Fluid Friction Characteristics ..... 58

Flow Modification Studies ..... 63

Resistance-Heated-Tube Heat-Transfer Experiment ..... 71

Static Rod Bowing Experiment ..... 77

Heat Transfer by Mass Transfer Measurements ..... 80

4. ADVISORY SERVICE TO THE AEC ..... 92
Review of PEGCPR Design ..... 92
EGCR Experimental Facilities Evaluation ..... 92
EGCR Hazards Evaluation ..... 94

PART 2. MATERIALS RESEARCH AND TESTING

5. METALLURGICAL DEVELOPMENTS ..... 99
Bulk $UO_2$ Fuel Material ..... 99
$UO_2$ Processing and Fabrication ..... 99
Thermal Conductivity of $UO_2$ ..... 101
High-Temperature Compression Testing of $UO_2$ ..... 102
$UO_2$-Graphite Compatibility ..... 102
Mechanical Properties of Fuel Capsule Material ..... 103
Tube-Burst Tests ..... 103
Strain-Cycling and Relaxation Studies ..... 104
Bowing Studies ..... 106
Effect of Gaseous Environments on Properties of Type 304 Stainless Steel ..... 106
Effect of Environment on Creep-Rupture Properties .. 107
Examination of Creep Specimens After Test ..... 107
Environmental Effects on Fatigue ..... 110
Reactions of Type 304 Stainless Steel with Gases ... 114
Manufacturing Developments ..... 115
Manufacturing Variables in End-Closure Fabrication ..... 115
End-Closure Testing ..... 120
End-Closure Inspection ..... 121
Selection of Reference End Closure ..... 122
Inspection of Fuel Capsule Tubing ..... 124
Evaluations of In-Plant Inspections of Capsule Tubing ..... 124
Evaluation of Welded Tubing ..... 125
Evaluation of Thin-Walled Tubing ..... 125
Inspection of Engineering Materials ..... 126
Beryllium Investigations ..... 128
Evaluation of Extruded Tubing ..... 128
Welding and Brazing ..... 128
6. IN-PILE TESTING OF COMPONENTS AND MATERIALS ..... 131
Fuel Capsule Irradiation Program ..... 131
Full-Diameter Prototype Fuel Capsules ..... 131
Reduced-Size Prototype Fuel Capsules ..... 134
Miniature Capsule Fission-Gas-Release Experiments .. 146

Examinations of Irradiated Capsules ..... 148
Analysis of Fission-Gas-Release Data ..... 148
Method of Calculation of Fission-Product Evolution ..... 155
Post-Irradiation Pellet and Capsule Examinations ... 157

Instantaneous Fission-Gas-Release Experiment ..... 164

Closed-Cycle-Loop Irradiation Facility in ORR ..... 169

SiC-Si Coating for High-Density Graphite ..... 172

Neutron Damage to Chromel-Alumel Thermocouples ..... 173

Radiation Effects on Structural Steels ..... 176

Status of Hot Cell Modifications and Hot Cell Equipment ..... 179

7. OUT-OF-PILE TESTING OF MATERIALS AND COMPONENTS ..... 180

Materials Compatibility Tests ..... 180
Static Tests ..... 181
Low-Pressure Thermal-Convection Loop Tests ..... 184
High-Pressure Thermal-Convection Loops ..... 188
Forced-Circulation Loop Test ..... 188

Evolution of Gases from Graphite ..... 190

Analyses of Gases Evolved by Graphite ..... 203

8. DEVELOPMENT OF TEST LOOPS AND COMPONENTS ..... 205

ORR Gas-Cooled In-Pile Loop ..... 205

Special Gas Compressors and Electric Motors ..... 205
Grease-Lubricated Centrifugal Compressors ..... 206
Regenerative Compressors ..... 206
Gas-Bearing Compressors ..... 208
Electric Motors for High-Temperature Service ..... 211
Compressors for Forced-Circulation Loop Operating with Argon ..... 211

GAS-COOLED REACTOR PROJECT SEMIANNUAL PROGRESS REPORT

## SUMMARY


### Part 1. Design Investigations

#### 1. Advanced Reactor Concepts

A steam-cooled water-moderated reactor for a 20,000-shp plant for merchant ship propulsion was studied. It was concluded on the basis of the hazards involved that the system would be much better suited to a central-station application. Further, the steam conditions that conform to present-day marine practice are considerably below those which would fully utilize steam as a coolant and the Loeffler steam cycle proposed for this application. Higher steam conditions would lead to a much higher reactor output, and the central-station plant could cope with the hazards involved in the rupture of a fuel element and the consequent contamination of the steam cycle.

Two integrated gas-cooled reactor core and steam generator units that would utilize ceramic fuels were investigated. One design consists of a small-diameter GCR-2 type of core and a steam generator heat transfer matrix incorporated into a single pressure vessel. The second design consists of a small BeO-moderated core cooled with $CO_2$ at 1000 psi. Both plants were designed on the basis that they would operate with less than 0.1% of the fission products leaking from the fuel elements into the cooling gas. The performance characteristics of these two systems were compared with the characteristics of other gas-cooled systems, and the areas that would require development work were delineated.

#### 2. Reactor Design

The fuel element surface and coolant gas temperatures were determined for various power density distributions in the PEGCPR. This reactor is designed with fixed orifices to match the coolant flow to the heat generated. It was established that if bank operation of the control rods and a mixed-mean exit gas temperature of 1050°F were specified, the fuel element surface temperature would be 1370°F.

A new model for determining the temperature gradients and the thermal stability of a rod cluster in a circular channel is being developed. It was found that the method used previously gave results that were too large. The parameters considered are the length, diameter, and coefficient of thermal expansion of the rods; the geometry of the cluster and channel; the heat flux in the rods; the gas flow rate in the channel; and the gas properties.

A septafoil fuel-element cluster in a coolant channel with a scalloped cross section was analyzed to determine whether the coolant flow with this geometry would improve the temperature distribution on the surface of the fuel elements. The conditions for minimum peripheral rod bowing were established, and relationships between rod cluster length and operating parameters were defined.

Calculations were made of the ideal core pumping power required for the pebble-bed and clustered-fuel-rod reactor core concepts in order to compare the performance of these reactors. The solution for 19-rod clusters of 1/2-in.-dia fuel rods gave a core pumping power of only 5% of that required for the pebble-bed core. The helium-film temperature gradient was found to be greater for the clustered rods than for the bed of 1 1/2-in.-dia balls. If equal gas-film temperature gradients were assumed, the power required by the clustered rods would increase somewhat.

An analysis of the effect of thermal radiation in limiting the maximum fuel capsule temperatures during a loss of coolant accident in a GCR-2 type of reactor was performed on the Reactor Controls Analog Facility. Calculations were made for three values of the thermal conductivity of $UO_2$. The maximum value of the capsule surface temperature was within or above the range of recommended annealing temperature (1800 – 1950°F) of type 304 stainless steel in every case examined.

A method has been developed by which an accurate analysis may be obtained of the deflection and stresses in a beam of a grid structure if the interaction forces at the intersections of the cross beams are known. Studies were initiated of the stresses and displacements of cylinders

with various temperature distributions in order to establish design requirements for intermediate spacers to counteract rod movement in a GCR-2 type of fuel element.

Tube buckling experiments are under way, and a curve of critical pressure as a function of unsupported length has been obtained. The results obtained in this study will be compared with the results of similar tests on commercial aircraft tubing in order to evaluate the effects of different tolerances on fabrication.

The stresses and deflections in perforated plates are being investigated experimentally. The effect of hole size will be studied using both a square- and a triangular-pitch hole pattern.

A study was made of the available information on helium ionization and electrical breakdown at high pressures and temperatures. Estimates were made for design purposes of the effects of temperature and pressure on the breakdown voltage, but it was concluded that specific experimental data should be obtained.

A parametric study was made of the factors affecting containment vessel costs and size limitations. Curves were plotted that will be useful in the economic evaluation of reactor conceptual designs.

The fast-neutron dose to the PEGCPR pressure vessel was calculated. The flux was found to depend significantly on the thickness of the reflector, and thus the thickness of the reflector may be determined as much by the need to protect the pressure vessel as by reactivity considerations. Available information indicates that an integrated neutron flux of $10^{18}$ neutrons/cm$^2$ will probably not have a deleterious effect on the room-temperature ductility of low-carbon steels, but a total dose of $5 \times 10^{18}$ neutrons/cm$^2$ almost certainly would. The calculations indicate that with an active core 11.08 ft in diameter and a 71-cm-thick reflector, the total exposure to the inner portion of the pressure vessel in 20 years would be $1.6 \times 10^{18}$ neutrons/cm$^2$.

A detailed study is being made of the worth of the $B_4C$ control rods of the EGCR. The effects of leakage, the presence of the through tubes for experimental loops, rod interaction effects, and the effect

of the nonuniform array resulting if only 21 control rods are inserted are included in this study.

Two-dimensional four-group diffusion theory calculations have been made on a number of configurations of control rods in order to determine the effect of the control rods on power-density distribution. Power-density maps have been prepared for several configurations.

Calculations have also been made to determine the effect the EGCR experimental loops will have on the neutron flux and thermal performance of the reactor core. The results indicate that the loop tubes will have a somewhat beneficial effect on the radial power distribution. The effects of the presence of experimental fuel elements in the through tubes on the flux distributions near the tubes and on the reactivity of the reactor have been studied. The gamma-ray heating in the 5-in.-dia loop due to reactor core gamma rays and to gamma rays produced in loop experiments has been calculated.

Calculations have been made to determine the validity of various models used to predict the power-density distribution within a cluster of steel-jacketed $UO_2$ fuel rods. It was found that it is possible to construct the power distribution in the cluster of rods from flux distributions obtained with the annular P-3 model.

3. Experimental Investigations of Heat Transfer and Fluid Flow

The study of the contribution of spacers and hangers to the overall pressure drop in a full-scale model of a fuel channel was continued. The pressure loss coefficient associated with a hanger-spacer combination was determined to be 0.5. Because of the effect of the hangers and spacers on the turbulent structure of the flow, the skin friction factor for the full-scale channel was found to differ significantly from the result obtained previously with long, bare tubes.

The effect of swirl-flow on surface velocity patterns in the septafoil geometry was investigated. Four different swirl generators were studied using cotton fibers cemented to the tube surface to visualize the flow. Observations showed rapid decay of the helical flow, except where the swirl was restricted to the peripheral region. In all cases

high pressure losses existed, and regions of flow stagnation and separation were seen.

An unexpected skewness in the circumferential temperature patterns observed in the heated-tube experiment led to the introduction of a weir in the entrance region. The resulting decrease in air flow generated excessive bowing, and caused eventual burnout of the tubes. It has been postulated that in certain ranges of flow, the interaction between tube displacement and diametrical temperature difference is unstable. Therefore, the experimental apparatus has been modified to study the criteria for tube stability. An independent study was initiated to evaluate the bowing of a single tube under varying diametrical temperature differences. Experimental results show the bowing to be about 12% less than that predicted by linear theory.

Naphthalene-to-air mass-transfer experiments have been used to measure the heat transfer in septafoil geometries and to establish the effects of rod spacing ratios on the heat transfer. An optimum condition was approached for a spacing in which the distance between the surfaces of the central and peripheral tubes was equal to that between the outer surface of the peripheral tube and the channel wall. The existence of flow separation and stagnation was verified by mass-transfer studies with a swirl generator located at the entrance to the test unit.

4. Advisory Service to the AEC

A thorough review was carried out of all design studies, specifications, and drawings for the Title I design of the prototype enriched-uranium gas-cooled power reactor (PEGCPR). The uncertainties in the design were identified. A study was then made of the Title I design to define and evaluate the modifications that would be required to adapt the reactor to use as an experimental facility.

The experimental reactor is to be built at an Oak Ridge site, and it is to be called the Experimental Gas-Cooled Reactor (EGCR). It will have four large (9-in.-dia) and four small (5-in.-dia) tubes through the core that will be fitted for coupling to piping to complete closed loop experimental facilities. Completely self-contained equipment cells

will be provided for the experimental loops.

Assistance was provided in the preparation of a report giving details of a hazards evaluation of the EGCR. A containment vessel was specified for the reactor and steam-generating portions of the plant because of the experimental facilities to be included. Criteria have been established for radiation levels for the various operations and for the instrumentation required to monitor the activity, and a site for the reactor has been selected.

## Part 2. Materials Research and Testing

### 5. Metallurgical Developments

A continuous double-calcination process has been developed and is being used for the production of $UO_2$ powder of various enrichments for the irradiation program and other component testing work. The individual batches of oxide being produced are large enough for a good check on the reproducibility obtained with this process. The density of the sintered pellets prepared from the powder by the standard fabrication technique has varied from 93 to 95% of theoretical.

A process was also developed for the fabrication of solid pellets with a density of 75% of theoretical for the irradiation program. These pellets are prepared from a special, high-calcined oxide powder by the standard fabrication technique.

An intensive study of previous work on the thermal conductivity of $UO_2$ is being conducted. The spread in the available values is large, and there are many uncertainties in the variables which must be evaluated.

Information is being obtained on the high-temperature deformation properties of $UO_2$, and the thermal stability of $UO_2$ dispersed in graphite is being studied to determine the maximum temperature at which these materials are compatible.

The conditions that produce failure of type 304 stainless steel capsules from internal pressure have been determined. The strain at which failure occurs may be as low as 2 to 3% at temperatures of 1300°F. Strain-cycling tests on capsule tubing have shown its behavior to be

similar to that of Inconel. Temperature appears to have little influence on the number of cycles to failure in the range 1300 to 1500°F. Preliminary results of studies of environmental effects on fatigue failure in strain-cycling tests indicate that for type 304 stainless steel the time to rupture may be reduced drastically in air.

An extensive program of creep testing of type 304 stainless steel in various gaseous environments has been initiated. Preliminary results indicate that creep is sharply accelerated in CO and is slightly greater in $CO_2$ than in most other environments. Examinations of unstressed specimens and creep specimens after exposure in the same environment have given an indication of the reactions involved. Magnetic surface films were produced on all specimens except those exposed to argon and hydrogen. The reactions of type 304 stainless steel with CO and with flowing and static $CO_2$ were studied.

The manufacturing variables involved in fabricating end closures for fuel capsules have been studied in preparing capsules for the ETR and ORR capsule irradiation program, for component tests in loops, and for various mechanical tests. Automatic equipment has been used to assure optimum control of the welding variables. The results obtained thus far show that each of the three types of end closures is stronger than the capsule wall.

A specification for the helium leak testing of capsules has been completed and is being evaluated. Radiographic and ultrasonic techniques for inspection of all three end closures are being developed.

The edge-fusion type of end closure has been selected as the reference design, primarily because of ease of assembly and weldability. This joint cannot be fully inspected, but proper control of the welding procedure will produce reliable joints.

In-plant inspection of capsule tubing was evaluated by complete inspection of 1300 ft of tubing which was inspected by penetrant and eddy-current techniques during manufacture. The only serious deficiency in this lot of tubing was a considerable variation in wall thickness. A second lot of 1500 ft was procured without any specified inspection and

is now being evaluated.

Two lots of type 304 stainless steel tubing having 0.003- and 0.004-in. wall thicknesses were evaluated by complete inspection. The wall thickness of this tubing varied as much as 25%. Other serious deficiencies were relatively deep draw marks and pitting on the inner surface.

A batch of 50 ft of as-extruded beryllium tubing 0.80-in. in diameter by 0.040-in. nominal wall thickness was also evaluated. The wall thickness varied from 0.036 in. to 0.053 in. Other defects noted were deep scratches on the inner surface and high-density inclusions. Attempts to produce capsule end closures on this tubing failed because of porosity in the weld zone. Contaminants which might cause this porosity were noted but have not been identified. Brazing techniques and brazing alloys for use with beryllium are being developed.

6. In-Pile Testing of Components and Materials

The experimental facility for irradiation of full-diameter prototype fuel capsules in the ORR was completed and irradiation of eight experimental capsules was initiated. Equipment was completed for similar irradiations in the ETR, but installation of the 14-unit facility in the reactor has been delayed by interference from several large loops.

The helium-cooled loop for operation in the General Electric test reactor was also completed. This loop consists of five irradiation facility tubes. Considerable difficulty has been encountered, however, with the compressors and their shaft seals. Repeated failures have resulted in the loss of helium and delays in calibrating thermocouples. Thermal flux measurements have been made. Because of the difficulties encountered the assemblies installed in the facility tubes have accumulated little irradiation time.

Six miniature capsules are installed in LITR facilities for experimental determinations of fission-gas release as a function of temperature, and six have been removed for examination.

The temperatures of irradiation have been limited thus far by the lack of satisfactory thermocouples for temperatures above 2000°F.

The data accumulated thus far on fission-gas release show that below central operating temperatures of approximately 2250°F the ratio of radioactive gas existing outside the $UO_2$ pellet to the total existing at the time of sampling is small. One capsule with a central operating temperature of 2550°F released 9% of the existing $Xe^{133}$, that is, more than 200 times that found for any of the lower temperature experiments. Post-irradiation heat treatments at 2100°F and at 2500°F caused the evolution of considerable amounts of solid fission products.

Examinations of the $UO_2$ pellets used in the fission-gas release experiments have revealed extensive cracks, but practically no dimensional changes. Orange-colored scales have been found on the surface of the type 304 stainless steel cladding, but there has been insufficient material for analysis. Density changes in the pellets have been within expected error in the measurements. The fission products were leached from the capsule walls, and data were obtained for comparison with the total existing at time of shutdown.

An instantaneous fission-gas-release experiment has been under way for about three months. The activity of the fission products in the gas stream was unexpectedly higher than was predicted by the capsule tests described above in which only long-lived isotopes were measured. At a fuel temperature of 1820°F, the activity in the gas stream reached an apparent equilibrium in 1 hr of irradiation. The following isotopes were identified in a trapped gas sample: $Kr^{87}$, $Kr^{88}$, $Kr^{85m}$, $Xe^{133}$, $Xe^{135}$, $Xe^{138}$, $Cs^{138}$, $Rb^{88}$, $I^{131}$, $La^{140}$. The irradiation flux was $1 \times 10^{14}$ neutrons/cm$^2$.sec. Improved instrumentation is being installed to identify the short-lived products.

Construction of the closed-cycle-loop facility for irradiations in the ORR was completed. The first capsule to be irradiated will consist of $UO_2$ canned in coated graphite. The coating on the graphite is siliconized silicon carbide. Coatings of this type are being examined for oxidation resistance after irradiation. Samples tested for 186 hr at 2000°F in air have shown no weight changes.

Experiments conducted in the ORR have shown that irradiation has no significant effect on the thermal response of Chromel-Alumel

thermocouples. Slight errors can be reduced by annealing, and there appears to be a decrease in error with increasing neutron dosage.

The effects of fast-neutron irradiation on steels and welds used in pressure vessel construction are being studied. Experimental equipment has been assembled, and irradiations were initiated in the ORR. Data were analyzed which indicate that irradiation at temperatures between 200 and 500°F may lead to greater increases in ductile-brittle transition temperatures than does irradiation at lower temperatures. The beneficial effects of elevated irradiation temperatures become significant in a narrow temperature range between about 550 and 600°F, which varies for different heats of the same class of steels.

7. Out-of-Pile Testing of Materials and Components

Engineering-scale out-of-pile tests of reactor materials compatibility and fuel element structural integrity were continued. Three 1000-hr, pot-type, static helium tests were completed in which various specimens were exposed to the impurities evolved from type AGOT graphite. The system was modified for the latter two of these tests so that the metal specimens were held at a temperature 400°F or more above the graphite and gas temperatures. The test section temperatures during these tests were 1500°F near the top and 1300°F near the bottom. A test is under way in which the maximum test section temperature is 1600°F, and a specimen is being prepared for testing at 1800°F.

With one exception the samples of austenitic stainless steels exposed in these tests showed no surface changes other than a thin, tightly adherent, black oxide tarnish. The exception was a type 304 stainless steel specimen which was held at 1500°F and which formed a silver-colored, nonmagnetic, poorly adherent layer that spalled and revealed a thin gray under layer. Analyses of the reaction layers are under way. Anomalies observed in the gas evolution of the graphite during these tests are being studied.

Three low-pressure thermal-convection loop tests, in which low-velocity helium circulation was induced by a temperature differential imposed on the loop, were also completed. The austenitic stainless

steels exposed in these tests have gained weight slightly and have formed thin, gray-to-black reaction layers. The low-alloy steels showed higher weight gains and heavier reaction layers. The reaction layers on T-1, Croloy 2-1/4, and Croloy 3M specimens were silvery, and exfoliation of the layers occurred upon handling.

Two high-pressure thermal-convection loops are now operating with helium at a pressure of approximately 300 psig. The test sections of these each contain type AGOT graphite and simulated full-scale EGCR fuel element assemblies. The maximum gas temperature in the loop is 1400°F.

A 1000-hr test was completed in a forced-circulation loop in which the test section contained type TSF graphite and a simulated full-scale EGCR fuel element assembly. Argon was circulated in the loop at 1400°F, 30 psig, and a velocity of 300 ft/sec. Examinations of the loop components have not been completed.

In the study of the volumes and compositions of gases evolved from graphite the previously used temperature interval of 200 to 1000°C has been extended to 2000°C, and larger samples have been examined. Also, rates of gas evolution have been measured at 300, 600, and 1000°C. The application of gas chromatography has permitted separate determinations of $N_2$ and CO, which were not possible by mass spectrometry. It appears that CO is a major fraction of the mass 28 material obtained upon heating to 1000°C, but below 400°C $N_2$ is the major fraction. The total volume of gas evolved per unit volume of graphite appears to be independent of sample size. Preliminary data on rate of evolution of gases indicate a marked effect of temperature. The evolution rate is very high during the initial heating period.

8. Development of Test Loops and Components

The design study of a gas-cooled loop for experimental studies in the ORR of advanced fuel elements was completed. Tests of component mockups are under way.

Investigations are under way of gas compressors for producing the high fluid heads at low volumetric flows that are required for service applications such as the ORR gas-cooled loop. Tests are being made of

grease-lubricated centrifugal compressors and of regenerative compressors, and a gas-bearing compressor is being purchased.

Electric motors designed to produce 12 hp at 24,000 rpm and to operate at an ambient temperature of 600°F were obtained for testing.

# PART 1. DESIGN INVESTIGATIONS

# 1. ADVANCED REACTOR CONCEPTS

## Direct-Cycle Steam-Cooled Reactor

A preliminary study was made of a steam-cooled water-moderated reactor for a 20,000-shp plant for merchant ship propulsion.[1] The purpose of this study was to investigate the advantages of a direct-cycle system that coupled conventional propulsion equipment with a reactor operating at temperatures and pressures commensurate with modern power plant practices.

A flow diagram of the system is shown in Fig. 1.1. Steam from the reactor is piped directly to the main propulsion turbines, to the ship's service electrical generator sets, to the turbine-driven steam blowers used to recirculate steam through the reactor, and to the Loeffler drums. Since the possibility exists of varying degrees of contamination in the main steam system, a double heat exchanger with an intermediate heat transport loop was used to provide nonradioactive steam for distribution throughout the ship.

The reactor is water moderated and beryllium oxide and water reflected, and it has a total thermal output of 73 Mw. The fuel elements are seven-rod clusters of stainless-steel-clad enriched $UO_2$ pellets. Moderator cooling is achieved by using the moderator zone of the reactor as the final stage of feedwater heating. The steam conditions were chosen to conform to present-day marine practice, where 850-psia, 850°F steam at the turbine inlet are found on vessels with power plants in the range of 20,000 shp. These conditions are considerably below those which fully utilize two attractive features of the system, that is, the use of steam as a coolant and the use of the Loeffler steam cycle.

Steam has several special advantages as a coolant for a marine application. It is readily available and inexpensive, it has a

---

[1] H. L. Falkenberry, R. S. Holcomb, and G. Samuels, A Preliminary Study of a Direct-Cycle Steam-Cooled Reactor for Merchant Ship Propulsion, ORNL-2759 (to be issued).

UNCLASSIFIED
ORNL-LR-DWG 39189

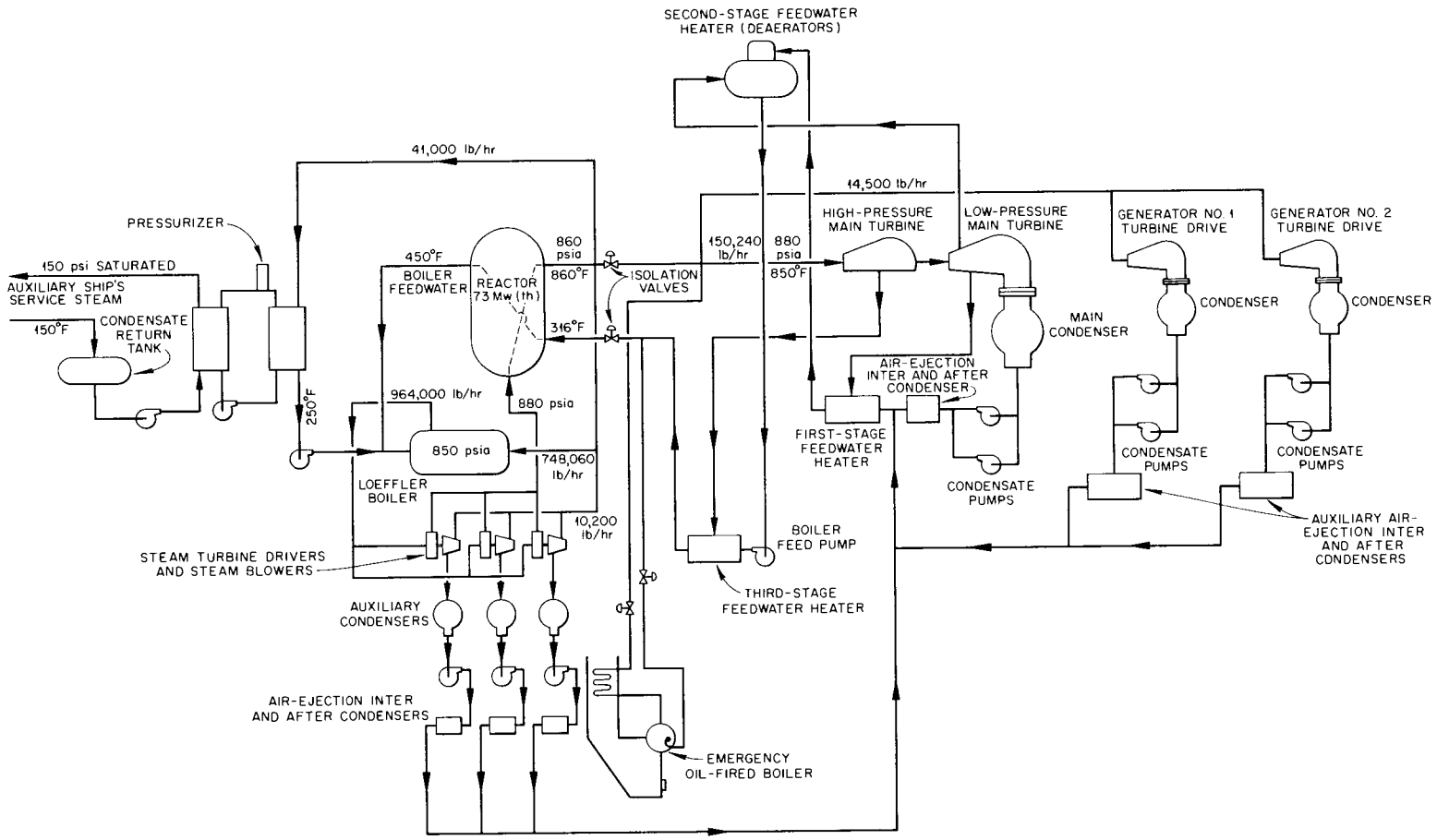


**Fig. 1.1. Flow Diagram of Direct-Cycle Steam-Cooled Reactor.**

sufficiently low activation cross section for the coolant piping to require little shielding, and its short-lived activity allows quick access to the coolant system. Its merit as a heat transfer medium depends on the system pressure. At lower pressures, steam suffers in comparison with helium and $CO_2$, but, as the pressure is increased, its properties improve so that at about 1000 psi it is comparable to helium and $CO_2$. At still higher pressures, it is superior to both gases because both the specific heat and thermal conductivity of steam increase with pressure, while these properties are practically constant for most gases.

In the Loeffler steam cycle, part of the superheated steam leaving the reactor is mixed with feedwater to generate saturated steam which then passes through the reactor. The remaining fraction of the superheated steam is delivered to the main turbine and auxiliaries. The Loeffler drums are direct-contact heat exchangers which serve as a desuperheater and boiler. The drums are horizontal, cylindrical vessels with superheated steam inlet headers and diffusers, a condensate inlet, and a saturated steam outlet. Thus the cost and maintenance of the intermediate heat exchanger of the nominal gas-cooled reactor cycle is greatly reduced by eliminating the more expensive shell-and-tube type construction. An alternate method of supplying saturated steam to the reactor is the use of a spray chamber or series of chambers and separators in place of the drums. Although this system was not investigated in detail, it appears to be attractive from both space and cost considerations.

The conclusions of the study are that the system investigated is much better suited for central-station application than for marine propulsion service. The conclusions are based primarily on the hazards involved in the use of a direct-cycle where failure of a fuel element would lead to fission-product contamination of the entire machinery system. Since many essential activities require access to the machinery space, gross contamination of the system could not be tolerated.

For central-station application, higher steam conditions would lead to much higher reactor output than that obtained under the more or less "standard" marine conditions of 850 psi and 850°F. Also, in the event of a reactor accident, the removal of decay heat from the fuel element would be much more simpler, since more space would be available to design for natural convection and auxiliary power sources would be available.

## Preliminary Designs for Two Integrated Gas-Cooled Reactor Core and Steam Generator Units

Studies of reactors designed for operation with ceramic fuel elements have continued. Previous work[2] indicated that, if the fission-product release to the cooling gas can be kept to something of the order of 1 part in 10,000, the maintenance problems for the contaminated heat exchangers and blowers will be quite manageable. While few data are available, there are indications that through the use of coatings it may be possible to hold the fission-product release from ceramic fuel elements to this or lower levels. Therefore a study of the potentialities of such reactors was made to disclose both the incentives to achieve them and the development problems.

The previous studies had indicated that it would be well to depart from the Calder Hall reactor core and steam generator configuration to reduce the size and cost of both the shielding and the containment vessel that would be required with a contaminated-gas system. Thus the first step in the study was to evolve a new power plant configuration based on the GCR-2 core and steam generator heat transfer matrix to see what could be accomplished by incorporating a reactor core and steam generator in a single pressure vessel in order to exploit the high-temperature capabilities of ceramic fuel elements. The results looked quite promising and indicated that further improvements might be effected through the use of a smaller diameter core. In view of the possibility of using

---

[2] W. B. Cottrell et al., The HGCR-1, a Design Study of a Nuclear Power Station Employing a High-Temperature Gas-Cooled Reactor with Graphite-$UO_2$ Fuel Elements, ORNL-2653 (to be published).

beryllium oxide as the moderator in a gas-cooled reactor to take advantage of the (n,2n) reaction and thus improve the conversion ratio or possibly even achieve breeding, a design was also prepared for a small, BeO-moderated core cooled with $CO_2$ at 1000 psi. Both plants were designed on the basis that they would operate with less than 0.1% of the fission products leaking from the fuel elements into the cooling gas, and the shielding and the design provisions for maintenance were made accordingly.

Vertical sections through the two proposed designs are shown in Figs. 1.2 and 1.3, and some pertinent data on these two design proposals are presented in Table 1.1, along with similar data for the GCR-2, the HGCR-1, and a typical coal-fired steam plant of recent design. The data in the lower portion of the table give an indication of the relative capital costs of the various plants. Of course, the special problems peculiar to reactors and the relatively high cost per pound of large reactor pressure vessels render out of the question a direct comparison between the reactor plants and a conventional coal-fired plant, but the data do have some interesting implications.

A review of the two design proposals indicates that combining the reactor core and steam generator in a common pressure vessel to give a single functional unit has the following advantages:

1. Major reductions in the cost of the pressure envelope, the ducts, the shield, and the nuclear plant containment vessel can be obtained.

2. The hot gas ducts and their expansion bellows can be eliminated.

3. A single vertical pressure vessel gives low pumping losses and excellent thermal convection. About 8% of the design power output can be removed at design temperature levels with all blowers stopped.

The study indicates that ceramic fuel elements offer the following advantages:

1. The higher temperature differences available both in the core and the steam generator make possible major reductions in the capital costs of these two components.

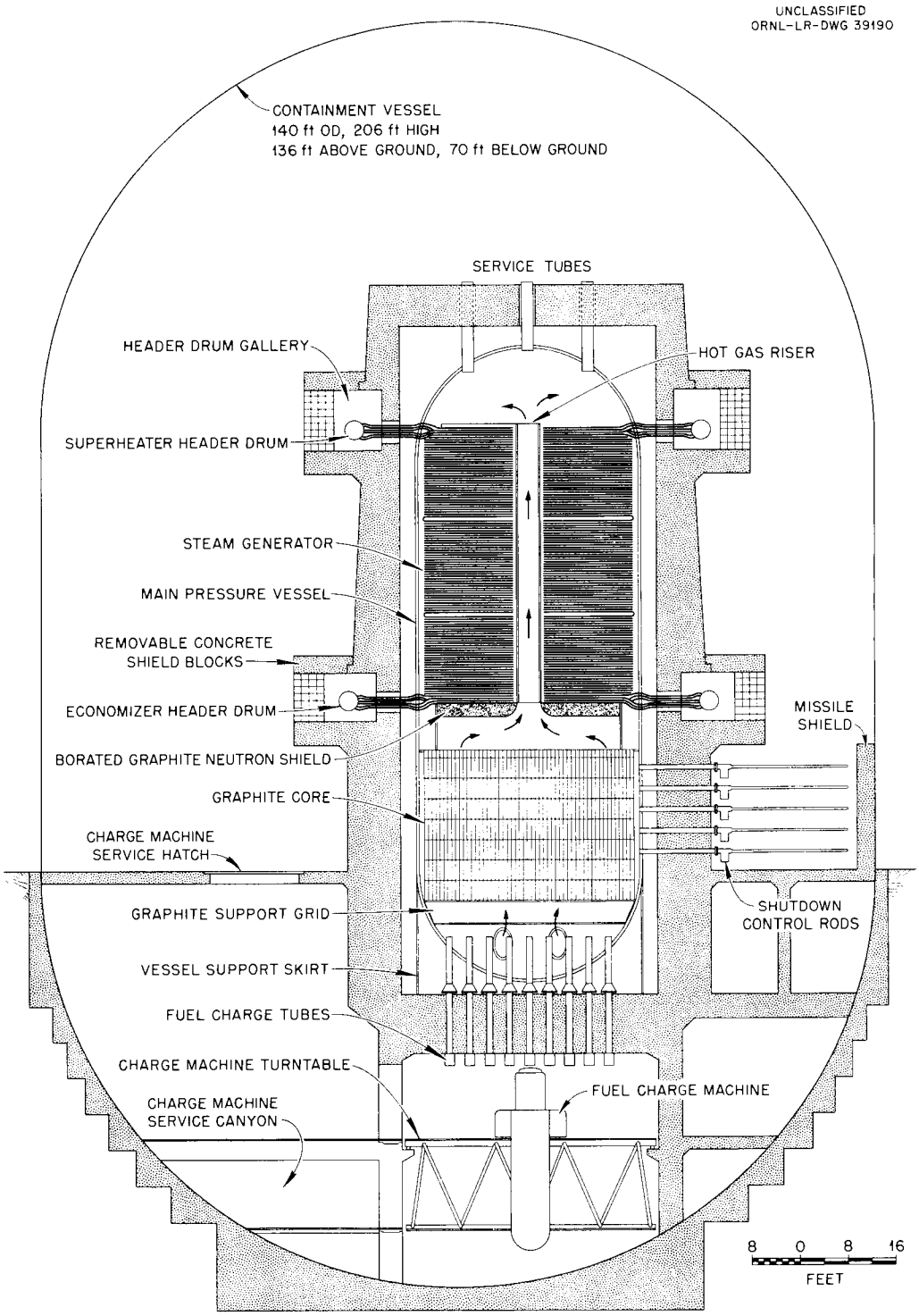


**Fig. 1.2. Ceramic-Fueled GCR-2 Type Reactor Core and Steam Generator in a Single Pressure Vessel.**

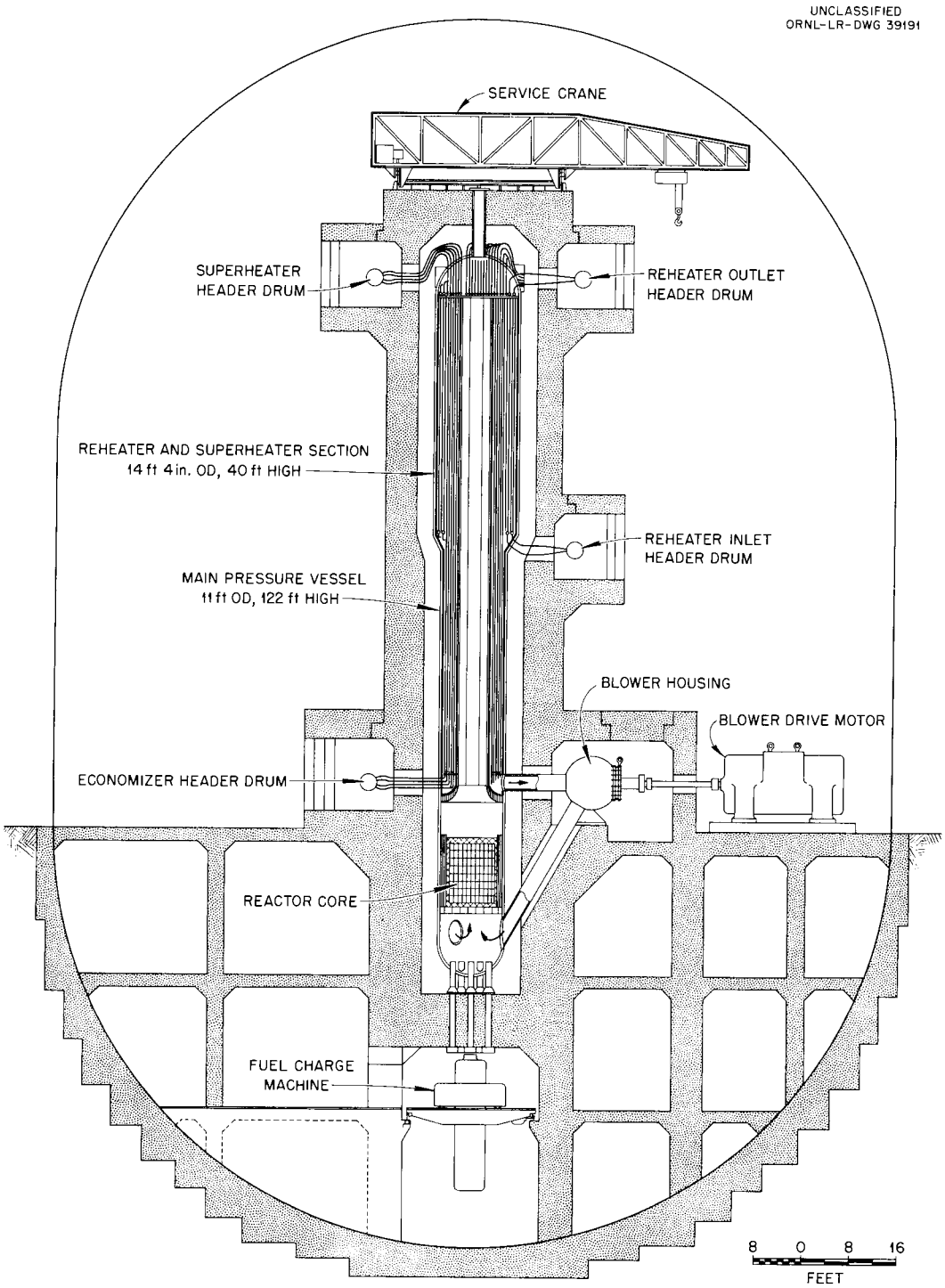


**Fig. 1.3. Ceramic-Fueled BeO-Moderated Reactor Cooled with $CO_2$.**

Table 1.1. Summary of Design Features and Factors Affecting Capital Costs

| | GCR-2 | HGCR-1 | HGCR-2 | HGCR-3 | Comparative Plant |
|---|---|---|---|---|---|
| Description | Reference design | GCR-2 with shielding for steam generator | Unified GCR-2 core and steam generator | Unified BeO core and steam generator | Coal-fired steam plant |
| Activity in gas system, curies | $10^2$ | $10^7$ | $10^6$ | $10^6$ | |
| Net electrical power output, Mw | 225 | 1130 | 468 | 464 | 465 |
| Steam temperature to turbine, °F | 950 | 1050 | 950 | 1050 | 1050 |
| Steam pressure to turbine, psia | 950 | 1450 | 950 | 2400 | 2400 |
| Specific power in fuel, kw/kg of $U^{235}$ | 228 | 1810 | 456 | 2000* | |
| Power density in core, kw/liter | 1.716 | 7.72 | 3.43 | 97.8 | |
| Power density in steam generator, kw/liter | 0.725 | 2.05 | 1.45 | 2.58 | 0.161 |
| Weight of steel in reactor coolant system, pressure envelope, and support structure lb/kw(e) | 19.4 | 6.5 | 6.0 | 1.9 | |
| Weight of steel in steam generator tubes, lb/kw(e) | 8.0 | 3.2 | 3.85 | 1.93 | 9.1 |
| Weight of steel in containment vessel, lb/kw(e) | 0 | 5.6 | 6.4 | 6.4 | |
| Total weight of steel required for steam generation, lb/kw(e) | 27.8 | 15.5 | 16.4 | 10.4 | 30 |
| Volume of concrete in shield, $yd^3$/kw(e) | 0.053 | 0.0228 | 0.015 | 0.011 | |
| Building height above ground, ft | 90 | 155 | 142 | 142 | 126 |
| Building depth below ground, ft | 35 | 65 | 70 | 70 | 34 |
| Building cross-sectional area, $ft^2$ | 14,400 | 39,000 | 15,400 | 15,400 | 33,000 |

*Preliminary rough estimate; value depends on uranium-thorium ratio and can be reduced to give an increase in conversion ratio at the penalty of an increase in fuel investiment.

2. The available test data indicate that, except for the inert gases, the bulk of the fission-product activity escaping from the fuel element will plate out in the heat exchanger.

3. Elimination of the burst-slug detection equipment will reduce both the capital cost and the costs of operation and maintenance.

The proposed design for a BeO-moderated core fitted with a BeO-$UO_2$-$ThO_2$ fuel element appears to have the following characteristics. The use of BeO in place of graphite as the moderator makes possible a much smaller core for a given power output. This permits a much higher cooling gas system pressure and hence a lower capital cost for the core, heat exchanger, shield, and containment vessel. The BeO moderator will permit the use of $CO_2$ in place of helium for operation at temperatures up to 2500°F. For small reactor cores in which the void fraction is important, the higher volumetric specific heat of $CO_2$ permits a substantial increase in power output from a given size of core over that obtainable with helium. The (n,2n) reaction in BeO holds promise of increasing the conversion ratio (and possibly breeding) in a BeO-moderated gas-cooled reactor. The type of core proposed is particularly advantageous from this standpoint because its high operating temperature in a $CO_2$ atmosphere should drive off the $Li^6$ formed from the $(n,\alpha)$ reaction because the vapor pressure of lithium carbonate at operating temperatures would run from 1 to 10 mm Hg, and the BeO of the moderator could be a relatively inexpensive, porous type.

The fission-product retention of dense BeO-$UO_2$ fuel elements should be inherently better than that of graphite-$UO_2$ fuel elements. Aside from the lower activity release with BeO fuel elements, the smaller size of the heat exchanger and blowers should lead to a system presenting less difficult maintenance problems than for a similar system designed for a graphite reactor. The coefficient of thermal expansion of BeO is about the same as that of structural steel, and the data available indicate that it is dimensionally stable under irradiation. These characteristics make the design of the core much easier than is the case with graphite. Since BeO is chemically inert relative to air,

the hazard potential present in graphite reactors designed for operation above 1400°F is eliminated. The cost of the BeO for the moderator appears to be less than the cost of the graphite for the GCR-2 because of the much smaller core size for a given power output.

If a $U^{235}$- or $U^{233}$-thorium combination is used to achieve a high conversion ratio (or possibly breeding), changes in reactor core size have little effect on total neutron losses to leakage, and hence very good neutron economy can be obtained with small reactor cores. In effect, the reactor designer has the option of changing the ratio of the mass of thorium closely associated with the fuel in the core proper to the mass of thorium in the blanket surrounding the reflector as he changes the core diameter. The thermal conductivity and resistance to thermal stress of $UO_2$-BeO matrices are much superior to the corresponding values for pure $UO_2$ or $ThO_2$ materials. Matrices of $UO_2$ and graphite have even better thermal conductivity and resistance to thermal shock than BeO.

Steam turbine drives for the blowers would be better than electric motors for the proposed reactors because they would permit a major reduction in containment vessel size and cost.

These two design studies were undertaken in part to bring out the development problems which would characterize power plants of this type. It is apparent from these studies that a number of the problems are particularly vital.

The fission-product escape from the ceramic fuel elements must be limited to 0.01% or less in order to give a blower installation which can be maintained fairly readily and to keep the problems of servicing the fuel-charging machinery within reasonable bounds. No test data appear to be available for BeO-$UO_2$ fuel elements operating in $CO_2$ at high temperatures. It seems likely that the results of such tests would be more favorable than for tests run in air if the water vapor content of the $CO_2$ is kept to a few parts per million.

A set of multigroup calculations should be carried out for the type of beryllia-thoria-urania core proposed. These should include the

effects of various distributions of thoria between the core and the blanket and the effects of core diameter on conversion ratio, allowable burnup in the fuel per loading, control, etc. This work may indicate that multiregion or convoluted cores should also be considered as means of increasing the core-blanket interfacial area.

The rate at which the lithium formed from the $(n,\alpha)$ reaction will escape from the BeO moderator blocks when surrounded by a $CO_2$ atmosphere in the temperature range from 650 to 1500°F should be determined experimentally. Some work on this might be done by using available BeO specimens which have already been irradiated in the MTR. The BeO porosity, fabrication procedure, and operating temperature will all influence the rate of evolution of $Li_2CO_3$.

The allowable thermal stresses in $BeO-UO_2-ThO_2$ fuel elements should be investigated. Rough sorting tests could be run first by imposing radial temperature differences on tubular specimens over a series of temperatures from 800 to 2000°F. The effect of cycling the radial temperature difference in the BeO tube should also be investigated. In-pile tests should then be run to give a better simulation of full-scale reactor conditions. Since most of these tests would require in-pile times of only 0.5 to 10 hr, the problems of fission-product accumulation and escape would be much reduced.

A study should be made of the problems associated with the charging machine for a system making use of ceramic fuel elements which would disperse contamination in the charge machine.

The cost of fabricating the $BeO-UO_2-ThO_2$ fuel elements should be investigated, along with the cost of fabricating the BeO moderator blocks. The problems associated with erecting the large reactor-steam generator pressure vessel should be studied.

The relative costs of the five plants described in Table 1.1 should be investigated to determine whether the over-all capital costs for these plants are consistent with the cost indications given by such parameters as pounds of steel or cubic yards of concrete per kilowatt-hours of net electrical output.

The effects on over-all power plant costs of both lower reactor core power densities and lower design power outputs should be determined for the BeO reactor. It seems likely that the power density in the core might be halved without increasing the capital costs seriously. The effects of using a steam turbine blower drive as compared with an electric motor for the BeO reactor should be determined, particularly from the standpoint of containment vessel costs.

## 2. REACTOR DESIGN

### Thermal Performance of Fuel Elements

#### Effect of Power Distribution on Fuel Element Surface Temperatures

The fuel element surface and coolant gas temperatures were determined for various power density distributions in the prototype experimental gas-cooled reactor (PEGCPR) being designed by personnel of Kaiser Engineers and the Nuclear Products-Erco, Division of ACF Industries (now Atomic Energy Division, Nuclear Power Department, Allis-Chalmers Mfg. Co.) In this type of reactor the performance of the plant is limited by the maximum fuel element surface temperature. In order to obtain a high mixed-mean exit gas temperature and consequently a high thermal efficiency, it is essential that the channels in a lower power region of the reactor be orificed to match the flow to the heat generated. Since the orifices for the PEGCPR are fixed in size, any large variation in radial power distribution would necessitate replacement of the orifices and would seriously affect operation of the reactor. Therefore bank operation of the control rods is specified. For bank operation of the rods and a mixed-mean exit gas temperature of 1050°F, the fuel element surface temperature was found to be 1370°F.

Performance calculations were completed for four additional control rod positions. In all cases the orifices for metering the gas flow to the individual channels were assumed to be sized for the case with the central control rod one-half inserted and the others withdrawn. The cases considered and the maximum cladding temperature for a mixed-mean exit gas temperature of 1050°F are given on the following page.

Although no additional calculations were made to determine the optimum orifice sizes, it is obvious that, if the sizes were fixed for some intermediate rod insertion, the maximum surface temperature for the one-half inserted to fully inserted range would be about 1300 to 1320°F.

| Control Rod Position | Maximum Cladding Temperature (°F) |
|---|---|
| Central control rod one-half inserted, others withdrawn | 1260 |
| Central control rod three-fourths inserted, others withdrawn | 1300 |
| Central control rod fully inserted, others withdrawn | 1370 |
| Central control rod fully inserted, others at edge of active core | 1380 |

Thermal Analysis of Fuel Elements

The method described previously[1] for determining the temperature gradients through rod clusters in circular channels was applied to the case of a seven-rod cluster in a scalloped channel.[2] Analyses of the results of both the circular- and scalloped-channel calculations indicate that the assumption of fully developed momentum and heat transfer leads to thermal gradients which are too large.

A new model for determining the temperature gradients and also the thermal stability of a rod cluster in a circular channel is therefore being developed. The criterion for stability is that the deflection of the rods caused by some initial temperature difference must result in an increase in the temperature difference which is less than the initial difference; that is, the system must be convergent. Another obvious condition is that the equilibrium locations of the rods must be such that they are not in contact with adjacent rods or the channel wall. It is therefore necessary that the equations establish not only the convergence or divergence of the system but also the final positions of the rods. An iterative procedure must be used in which the equations for determining temperature and position of the rods are repeatedly solved until the

[1] GCR Semiann. Prog. Rep. Dec. 31, 1958, ORNL-2676, p 10.

[2] L. G. Epel, Temperature Structure in the Gas-Cooled Reactor Fuel Elements Using a Scalloped Coolant Channel, ORNL CF 59-3-39 (March 16, 1959).

final rod position is found or until the system is shown to be divergent. The numerical calculations are being made with an IBM 704 digital computer.

Several basic assumptions must be made in order to derive the equations for predicting system performance. The principal assumption is that there is no transverse mixing between adjacent flow passages through the rods. The assumption is also made that the conduction of heat through the gas or through the fuel element is negligible. This assumption is justified because of the poor thermal conductivity of both the gas and the $UO_2$ and also the rather thin wall and relatively poor conductivity of the stainless steel. As the temperature differences between adjacent flow passages required to produce an unstable system are small, the potential for heat flow through the gas or element is small compared with the heat flux from the elements.

The parameters considered in the model are the length, diameter, and coefficient of thermal expansion of the rods; the geometry of the cluster and channel; the heat flux in the rods; the gas flow rate; and the gas properties. Preliminary comparisons of calculated results with results from the resistance-heated-tube experiments[3] indicate fair agreement.

Analysis of Flow in a Scalloped Channel

The nonuniform, circumferential, surface-temperature structure existing with the septafoil arrangement of the GCR-2 (evidenced in both analytical calculations and experimental studies) leads to axial bowing of the fuel rods. Two major possibilities for alleviating this bowing are (1) switching from the septafoil geometry to some other configuration and (2) modifying the septafoil (including the channel wall) in such a way as to eliminate, or at least to decrease, the surface temperature maldistribution. Since the septafoil cluster is easily fabricated and has the high surface-to-volume ratio necessary for efficient heat

---

[3] GCR Semiann. Prog. Rep. Dec. 31, 1958, ORNL-2676, p 36.

transfer, it was decided that the initial effort should be in the direction of developing a suitable modification of this system.

Epel and Furgerson[4] suggested that the surface temperature distribution of a septafoil fuel-element cluster might be improved if the flow channel had a scalloped cross section. This configuration was conceived by envisioning the seven elements, each surrounded by an annular flow channel, arrayed in an equilateral triangular lattice which was collapsed sufficiently to cause overlap of the individual channels at the points of closest approach of the tubes. This configuration is shown in Fig. 2.1.

The coolant channel was divided into an outer flow region, $A_o$, and an inner flow region, $A_i$, as indicated on Fig. 2.1, and an analytical study was made[5] to determine the conditions under which the average fuel element surface temperatures in these two flow regions would have equal values. In this analysis, the following assumptions were made. (1) The inner and outer flow regions are hydrodynamically and thermally isolated. (2) The inner and outer flow regions have the same length. (3) The pressure drop through each region is the same. (4) The fluid physical properties in each region are the same. (5) Uniform heat transfer exists around the fuel-element surface. (6) Fully turbulent flow exists along the entire length of the flow channel. (7) The fluid friction in both flow regions follows the same relationship, $f \sim N_{Re}^{-0.2}$, where f is the friction factor and $N_{Re}$ is the Reynolds modulus. (8) The heat transfer in each of the flow regions is described by the same law, $h \sim N_{Re}^{0.8}$, where h is the heat transfer coefficient. (9) The inlet fluid temperature is the same for both the inner and outer flow regions.

---

[4] L. G. Epel and W. T. Furgerson, Temperature Structure in Gas-Cooled Reactor Fuel Elements and Coolant Channel, ORNL CF 58-5-97 (May 27, 1958).

[5] J. L. Wantland and G. J. Kidd, Jr., A Method for Determining the Optimum Dimensional Parameters of a Scalloped Channel so as to Minimize Fuel-Element Bowing in a Septafoil Arrangement, ORNL CF 59-6-8 (to be published).

The analysis showed that under the assumptions made the condition of equal average fuel-element surface temperature for the two flow regions could exist at only one axial position in the cluster. For a given flow condition and fuel rod diameter, d, however, the rod spacing, S, and the scallop radius, R, can be chosen so that this condition exists at the geometrical midplane of the fuel-element cluster. For this condition the outer flow region has a higher surface temperature than that of the inner flow region for the inlet half of the cluster; this situation is reversed in the outlet half. Thus, the direction of peripheral rod bowing and the average surface temperature gradients are illustrated in Fig. 2.2.

Since location of the position of equal average surface temperatures at the midplane of the cluster produces the condition of minimum peripheral rod bowing, a parameter $N^*$ of the flow system is defined as the value of the dimensionless ratio $h_t a_t / w_t c_p$ that satisfies this condition, where $h_t$ is the mean cluster heat transfer coefficient, $a_t$ is the total heat transfer area of the cluster, $w_t$ is the total coolant mass flow rate through the channel, and $c_p$ is the mean specific heat at constant pressure of the coolant. In Fig. 2.3, $N^*$ is plotted versus $R^{++}$ for $S^{++} = 1.2$, 1.4, and 1.6, where $R^{++} = R/d$ and $S^{++} = S/d$. The ranges of positive $N^*$ are shown in Fig. 2.3 (negative $N^*$ has no physical meaning in this analysis). For the same values of $R^{++}$ and $S^{++}$, the dimensionless parameters $A^*$, $P^*$, and $D_e^*$ are plotted in Fig. 2.4, where $A^*$ is the total cross-sectional flow area divided by the total cross-sectional area of the fuel elements, $P^*$ is the total flow "wetted" perimeter divided by the total heated (fuel-element) perimeter, and $D_e^*$ is the total equivalent hydraulic diameter of the channel divided by the fuel element diameter ($D_e^* = A^*/P^*$).

The usefulness of this analysis is probably best illustrated by a numerical example. Consider a reactor having 1-in.-dia fuel rods spaced on 1.4-in. centers ($S^{++} = 1.4$) in a channel through which gas is flowing at the rate of $w_t = 3000$ $lb_m/hr$. The gas is assumed to have the following properties: dynamic viscosity, $\mu = 0.09$ $lb_m/hr \cdot ft$;

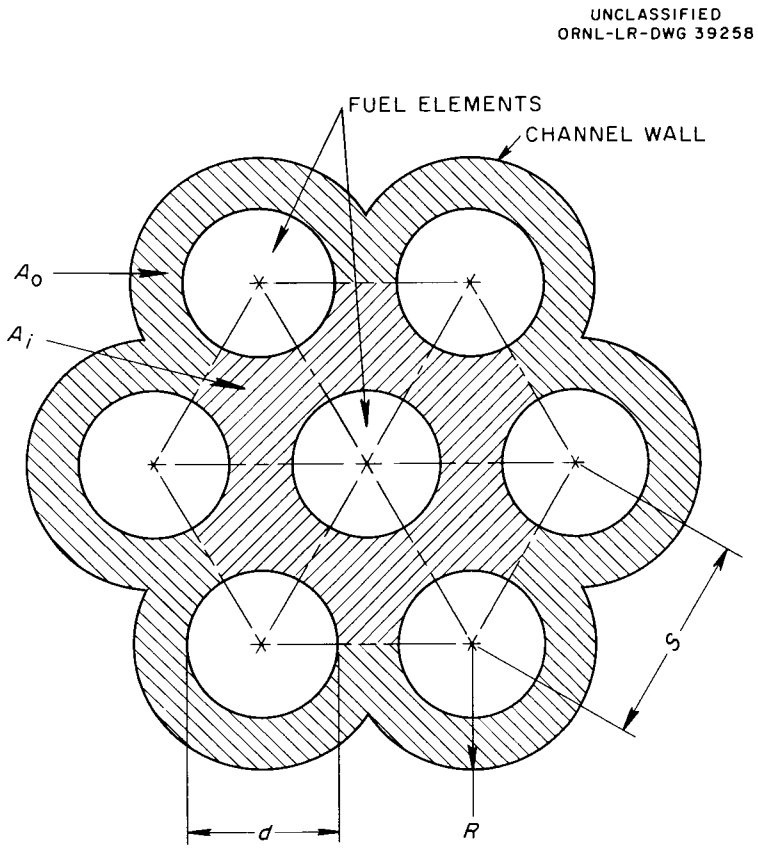


Fig. 2.1. A Scalloped Cross-Sectional Coolant Channel Containing Septafoil Fuel Elements.

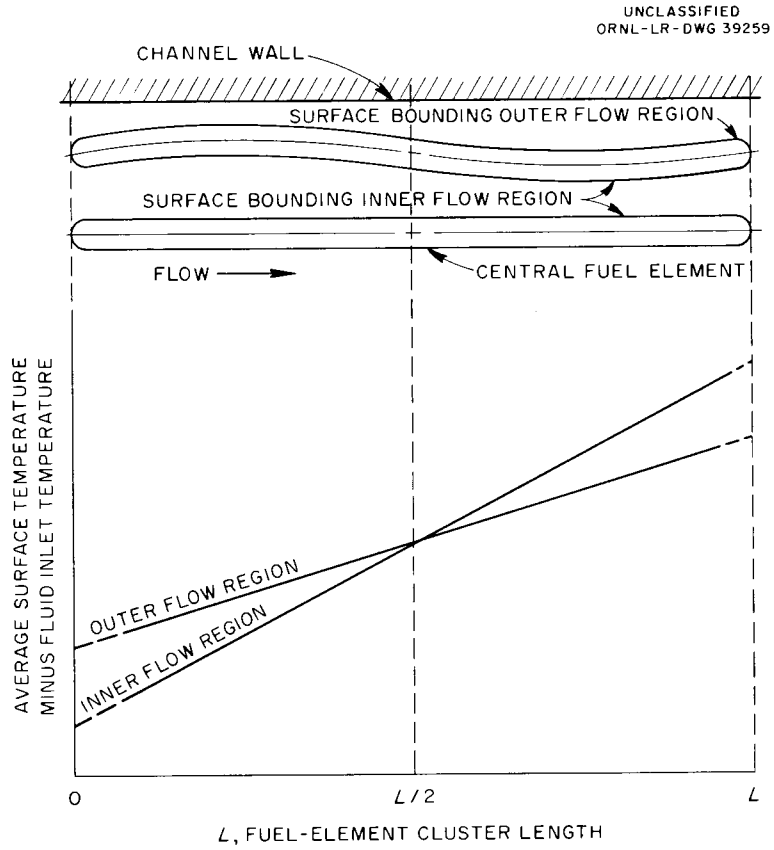


Fig. 2.2. Fuel Element Surface Temperature and Deflection for Minimum Bowing.

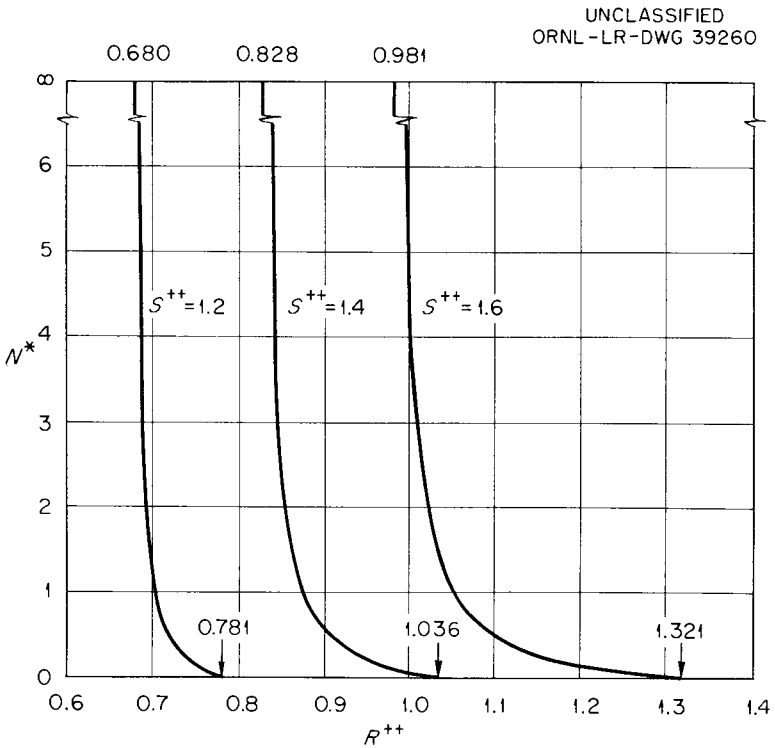


**Fig. 2.3. N* as a Function of $R^{++}$ for $S^{++}$ = 1.2, 1.4, and 1.6.**

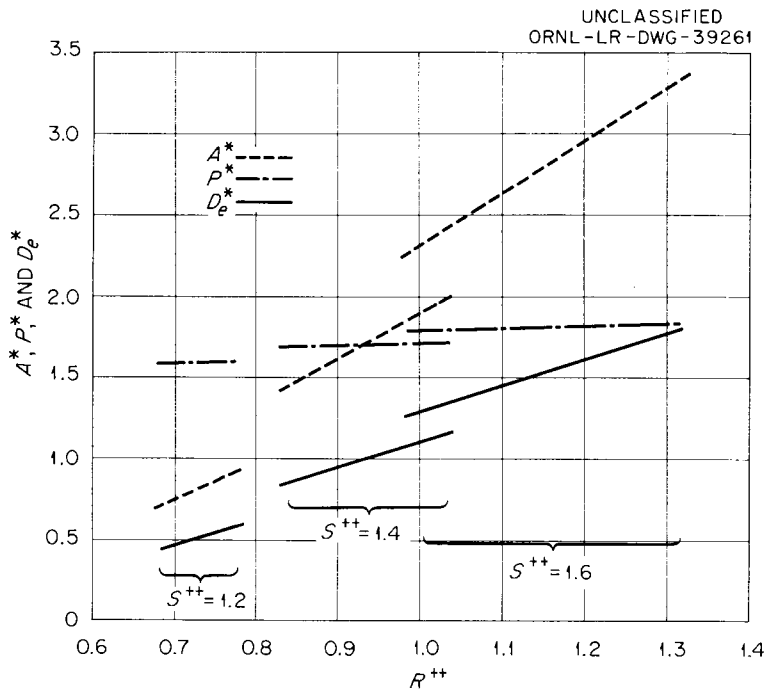


**Fig. 2.4. $A^*$, $P^*$, and $D_e^*$ as a Function of $R^{++}$ for $S^{++}$ = 1.2, 1.4, and 1.6.**

thermal conductivity, k = 0.16 Btu/hr·ft·°F; and Prandtl modulus, $N_{Pr} = 0.7$. Using the correlation

$$N_{Nu} = 0.023\ N_{Re}^{0.8}\ N_{Pr}^{0.4} \quad , \tag{1}$$

where the Nusselt modulus, $N_{Nu} = h_t D_{e_t}/k$, and $D_{e_t}$ is the total equivalent hydraulic diameter, the optimum rod cluster length can be determined for values of $R^{++}$ of 0.9 and 1.0. Thus, for $R^{++} = 0.9$ (and $S^{++} = 1.4$), Fig. 2.3 yields $N^* = 0.55$ and Fig. 2.4 gives $A^* = 1.61$, $P^* = 1.70$, and $D_e^* = 0.95$. The total wetted perimeter $P_t = P^*\pi d = 3.12$ ft, and $D_{e_t} = D_e^* d = 0.079$ ft. The Reynolds modulus is then calculated to be

$$N_{Re} = \frac{4w_t}{P_t \mu} = 42,700 \quad ,$$

and from Eq. 1 $h_t = 204$ Btu/hr·ft$^2$·°F. Since the cluster length is given by, $L = N^* w_t c_p / h_t 7\pi d$, the optimum cluster length is found to be 5.3 ft. Similarly, for $R^{++} = 1.0$ (and $S^{++} = 1.4$), $N^* = 0.19$, $A^* = 1.90$, $P^* = 1.71$, and $D_e^* = 1.11$. By the same procedure, the optimum cluster length is determined to be 2.1 ft. Thus relatively small changes in channel parameters (18% for $A^*$, < 1% for $P^*$, and 17% for $D_e^*$) result in reduction of the optimum cluster length by a factor of 2.5. If other criteria establish the desired rod cluster length, an iterative technique can be used to determine the optimum channel parameters for the chosen cluster length.

In this analysis, a number of simplifications have been made to facilitate the solution. The analysis could be made more exact by eliminating some of these assumptions (such as constant heat generation, complete gas mixing between clusters, and uniform physical properties and heat transfer coefficients) and by dividing the flow channel into a greater number of flow regions. However, it is felt that this analysis provides much insight into the surface temperature structure of this type of reactor core geometry. It is planned to check the results of this analysis experimentally.

Comparison of Pebble Fuel Beds and Clustered Fuel Rods

The ideal core pumping power, expressed as a fraction of the heat transferred in the core, for the pebble-bed and the clustered-fuel-rod reactor core concepts was calculated to provide a quantitative basis for comparison of the performance of these two types of reactor core. The pebble-bed design proposed by Sanderson & Porter[6] was taken as the reference design, and the coolant flow rate was varied while the reactor core power was held constant. The pumping power was plotted against helium mass flow per square foot of core face area.

In order to compute comparable data for the clustered-fuel-rod system, it was necessary to define a comparable reactor system. To do this, the same core height, core diameter, and core void volume were used. The void fraction assumed was 0.29, which is the average for the pebble-bed reference design; it was determined from the relative volumes of the randomly packed 1 1/2-in.-dia fuel spheres (void fraction, 0.39) and the solid graphite blocks. A system of equations was set up describing a reactor with a 0.29 void fraction and with M fuel rods per cluster in N fuel channels. The solution for 19-rod clusters of 1/2-in.-dia fuel rods indicates a core pumping power only 5% of that required for the pebble-bed core at the rated design point for the Sanderson & Porter system.

These results, which are dependent upon the temperature gradient allowed in the fuel material, are reported for a 270°F radial gradient through the 1/2-in.-dia fuel rods and are comparable with the results reported by Sanderson & Porter. For the cases solved to date, the helium-film temperature gradient is greater for the clustered rods than for the bed of 1 1/2-in.-dia balls. Increasing the fuel rod diameters brings the helium-film temperature gradient values closer together for a given case (19 rods/cluster), but the geometric limitations of the clustered-rod system are reached before the film drops become equal.

---

[6]Staffs of Sanderson & Porter and Alco Products, Inc., Design and Feasibility Study of a Pebble Bed Reactor-Steam Power Plant, S&P 1963, May 1, 1958.

It appears that a solution for equal gas-film temperature gradients for both concepts could be obtained by relieving the rod cluster case of the stipulation of the 29% core void volume which was selected by Sanderson & Porter as best for the pebble-bed design. It is expected that the pumping power required by the clustered rods would increase somewhat.

Dynamic Analysis of Thermal Radiation from Fuel Capsule to Graphite

Calculations of the effect of thermal radiation in limiting the maximum fuel capsule temperatures during a loss of coolant accident[7] indicated a need for a dynamic analysis of the condition. An examination of the problem was therefore carried out as part of the analog computer investigations of the behavior of a gas-cooled reactor with respect to safety and control.[8] For this analysis, which was performed on the Reactor Controls Analog Facility, a unit cell rather than the complete reactor core was used as the model.

The unit-cell model was composed of $UO_2$ fuel sealed in a stainless steel capsule which was enclosed in a graphite channel. The effect of radiation from the stainless steel to the graphite was determined following the simultaneous loss of heat removal by coolant flow and cessation of nuclear power generation in the $UO_2$. Heat contribution due to the decay of fission products was neglected. Temperature variations of the capsule were determined as parameters of $UO_2$ thermal conductivity for the absolute maximum possible variations in the capsule emissivity and surface area available for radiant heat transfer to the graphite. Thermal radiation from the fuel capsule to the graphite provided the only mechanism of heat removal from the stainless steel.

In order to account for heat conduction as well as for heat storage, the $UO_2$ was divided into three cylindrical sections of equal volume, and the entire volume of each section was assumed to be at the mean

---

[7] The ORNL Gas-Cooled Reactor. Materials and Hazards, ORNL-2505, (May 22, 1958).

[8] R. M. Pierce and C. S. Walker, An Analog Computer Technique for Examining the Effect of Thermal Radiation from the EGCR Fuel Element, ORNL CF 59-6-33 (in preparation).

temperature of that particular section. The 8-in. by 8-in. moderator module was resolved into an equivalent cylinder with an inside diameter of 2.93 in. This cylinder was divided into three cylindrical sections, the inside section containing 10% of the total volume, and the remaining two sections each containing 45% of the total volume. Data from KE-ACF reports[9] were used in computing the initial steady-state temperature profiles in the graphite and fuel element. The unit cell was assumed to be located at the point of maximum power generation within the reactor, which produced a steady-state fuel capsule surface temperature of 1450°F. The graphite surface temperature was taken as 820°F, with an average graphite power density from gamma heating of 9.1 $Btu/ft^3 \cdot sec$ and a factor of 2 decrease in power density from inside to outside of the equivalent graphite cylinder.[10] The initial steady-state temperature profile of the fuel element was computed for three values of the thermal conductivity of $UO_2$: 1.0, 0.55, and 1.5 Btu/hr·ft·°F.

The independent variable for each simulator run was the factor f defined in Fig. 2.5. The temperature in Fig. 2.5 is the maximum reached by the stainless steel capsule for a given value of f following the complete loss of both coolant flow and nuclear power generation. The maximum value of the capsule surface temperature was within or above the range of the recommended annealing temperature (1800-1950°F) of type 304 stainless steel[11] in every case examined.

## Structural Investigations

### Stress Analysis of Grid Structure

An accurate analysis of the deflection and stresses in a beam of a grid structure may be obtained provided the interaction forces at the

---

[9] ACF Job Rep. No. 3-225, Feb. 3, 1959; ACF Job Rep. No. 3-225-1.0, Feb. 2, 1959; ACF Job Rep. No. 3-225-4.0, Feb. 6, 1959; ACF Job Rep. No. 3-225-5.0, Feb. 2, 1959.

[10] W. T. Furgerson, ORNL, personal communication.

[11] Stainless Steel Handbook, Allegheny Ludlum Steel Corporation, Pittsburgh, 1951.

intersections of the cross beam are known. The values of the interaction forces are obtained by solving a set of simultaneous equations derived from the requirement that two beams have equal deflections at their common intersection. In the analysis, elementary beam theory is employed, and the tedious notation and bookkeeping problem associated with the derivation of the set of simultaneous equations is systematized in a straight-forward manner with the aid of matrix theory.

Several examples have been worked out to illustrate the application of the method. Most of the calculations can be carried out on an ordinary desk calculator, depending on the number of simultaneous equations to be solved. A minimum number of equations is involved if the grid structure has symmetry about the two diagonals as well as the two center lines.

Study of Fuel Element Cladding Behavior

In order to establish the design requirements for intermediate spacers to counteract rod movement in a GCR-2 type of fuel element, a means for predicting the warping or bowing characteristics of a rod is required. Since the behavior of a given rod depends upon the temperature distribution in the cladding, analytical studies are being made of cylinders with various temperature distributions.

Preliminary studies for the stress and displacement analysis of a thin cylindrical shell with a nonsymmetrical temperature distribution have been completed. The three basic simultaneous partial-differential equations for such an analysis can be satisfied by taking each of the three displacements (the three independent variables) in the form of a double trigonometric series, provided the temperature function is expressed by a similar series.[12] The temperature function, in this case, is taken to be of the following form:

$$\sum_m \sum_n D_{mn} \cos n\theta \sin \frac{m\pi x}{L} , \qquad (m,n = 1,2, \ldots)$$

[12] S. Timoshenko, Theory of Plates Shells, p 433, McGraw-Hill, 1940.

where L is the length of the shell, $\theta$ and x are the angular and axial coordinates, respectively, and the coefficient, $D_{mn}$, is a predetermined function of the summation indices m and n. A function of this type allows for temperature variations in both the axial and circumferential directions and provides that the axial bending moments and radial displacements are zero at the ends.

The equations are being programmed for the IBM-704, and several variations of the temperature function will be used in the shell studies. For the initial calculations, a function of the general form

$$t = t_o \left(1 + \frac{Ax}{L}\right) \left[B - \cos\left(\theta + \frac{2\pi xC}{L}\right)\right]$$

has been selected. Each of the constants, A, B, and C, can be either zero or 1, depending upon the precise function desired.

The analysis is also applicable to a shell which is subjected to a pressure loading that can be described by the function given above. Therefore, the elastic analysis of a cylinder with a uniform pressure loading over a small surface area (simulating the load imposed by a concentrated force) can also be examined.

The accuracy required in representing the actual pressure loading or temperature distribution by the series function will establish the number of terms which must be used. However, the stresses and displacements can be considered to be accurate for the function that is represented by the resulting finite series.

The preliminary study has revealed that the stresses and displacements of a shell are dependent only upon the radius-to-thickness and the radius-to-length ratios. The influence of these parameters will be investigated further.

Tube-Buckling Experiments

As a part of the tube-buckling study being carried out at the University of Tennessee,[13] tests have been completed for determining the

[13] GCR Semiann. Prog. Rep. Dec. 31, 1958, ORNL-2676, p 17.

"infinite" length for a 0.70-in.-ID, 0.020-in.-wall tube. The inside surface of each test specimen was honed, and the outside surface was ground; thus the inside diameter and wall thickness were held to a tolerance of ±0.001 in.

A curve of critical pressure as a function of unsupported length and a diagram of the method of tube support used during testing are presented in Fig. 2.6. The critical pressure is independent of length for tubes greater than ~9 in. long (length-to-diameter ratio = 12.5); therefore tubes in this category can be considered "infinite" in length from the collapse standpoint.

The range of critical pressure for repeated tests on specimens of the same dimensions was less than 9% of the mean value in all cases. In later tests, with specimens having higher thickness-to-diameter ratios, the range was less than 2% of the mean value. Collapse tests were conducted[14] on commercial aircraft tubing for which much broader dimensional tolerances were used, and hence the effects of the close tolerances being used in this study will be determined by comparisons of the data.

Experimental Analysis of Perforated Plates

An experimental investigation of the stresses and deflections in perforated plates has been initiated. The purpose of this investigation is to obtain design data and to provide basic information for the theoretical analysis of these structures. For a plate with a given outside diameter and thickness, the effect of hole size will be studied using both a square- and a triangular-pitch hole pattern.

Tests have been completed on a 15 1/16-in.-dia circular tube sheet with an equilateral triangular hole configuration and clamped edges. The tube sheet was made of 1/4-in.-thick aluminum. Strain gages were mounted along the diameters of the sheet at predetermined locations relative to the holes, and stresses were calculated from the strain

[14] The Strength of Tubes Under Uniform External Pressure, Wing Commander P. C. Cleaver, C.P. No. 253, Aircraft Research Council, London.

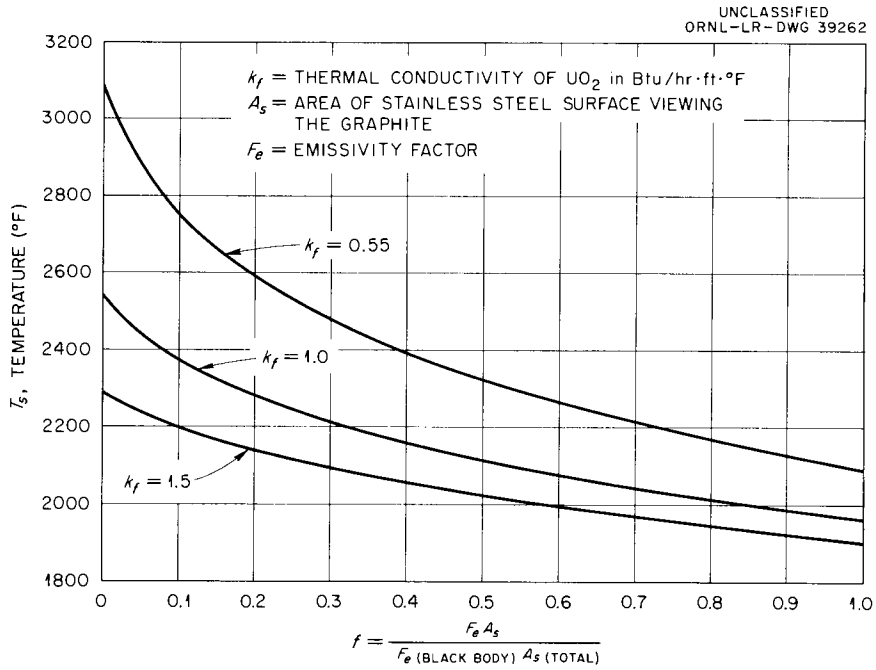


**Fig. 2.5. Maximum Surface Temperature of Fuel Capsule Following Complete Loss of Coolant Flow and Nuclear Power Generation.**

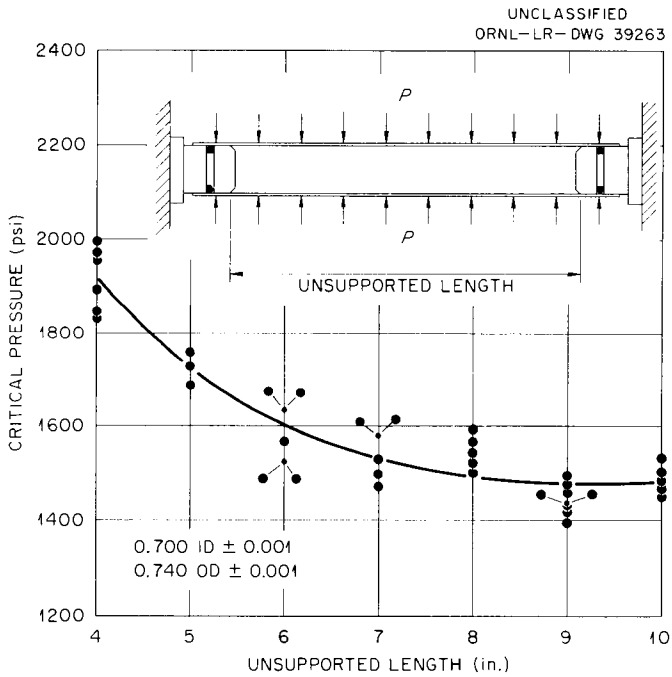


**Fig. 2.6. Critical Pressure of Cylindrical Tube vs Length.**

measurements. The deflections along a diametral line were also determined. The sheet was loaded by hydrostatic pressure and a portion of the load, corresponding to the area of the holes, was carried by means of a thin plastic film stretched over the entire plate. The diameters of all the 121 holes were the same for a given run, and, for each subsequent run, the hole size was increased. The deflections and stresses were determined first for the solid plate and then for the perforated plate in which the hole size was varied from 1/16 to 1 in. in diameter.

The tube sheet with strain gages attached is shown in Fig. 2.7, and the measured deflection along a radius is shown in Fig. 2.8, with hole size as a parameter. The theoretical deflection curve for a solid plate with a fixed edge is also shown in Fig. 2.8. The difference in the theoretical and experimental curves for the solid sheet can be attributed to a lack of rigidity at the clamped edge. The maximum stresses in the radial and tangential directions, as a function of hole diameter, are shown in Fig. 2.9. In the cases of the solid plate and the perforated plate with small holes, the maximum stress occurs at the edge of the sheet. For the larger holes, the maximum occurs at the edge of the central hole. Thus, in the latter case, the maximum stress location is the same as for a plate with a simply supported edge. The maximum stress at the outside edge of the plate is approximately equal to that at the edge of the central hole for a hole diameter of 5/8 in. The maximum stress, maximum deflection, and area ratios were calculated using the solid plate as a basis, and the results are given in Fig. 2.10. For the larger hole diameters, the stress and deflection ratios increase much more rapidly than the area ratio. The deflection increases by a factor of 3.1 when 53.3% of the metal is removed, and the stresses increase by a factor of 3.3.

## Study of Helium Ionization

A study was completed of helium ionization and electrical breakdown at high pressures and temperatures, and the data were compared with

**Fig. 2.7. Perforated Plate with Strain Gages.**

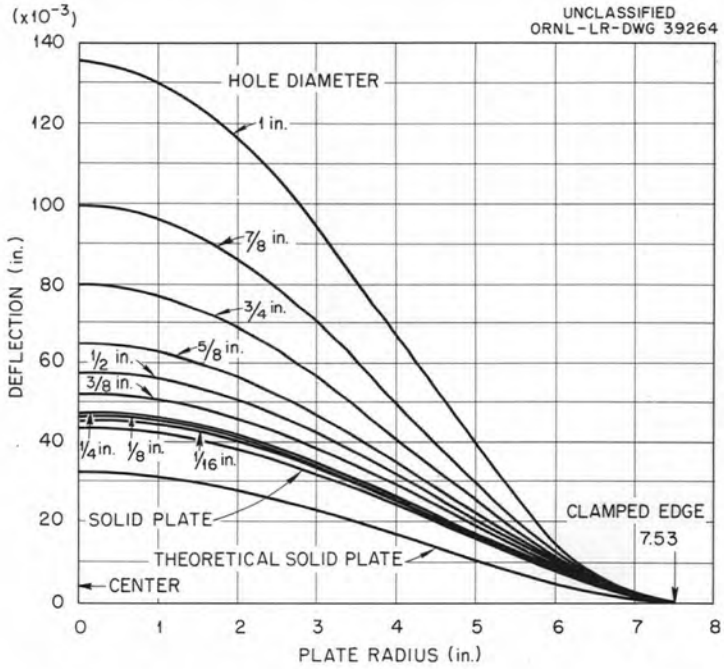


**Fig. 2.8. Deflection of a Perforated Circular Clamped Aluminum Plate Under a Test Pressure of 20 in. Hg.**

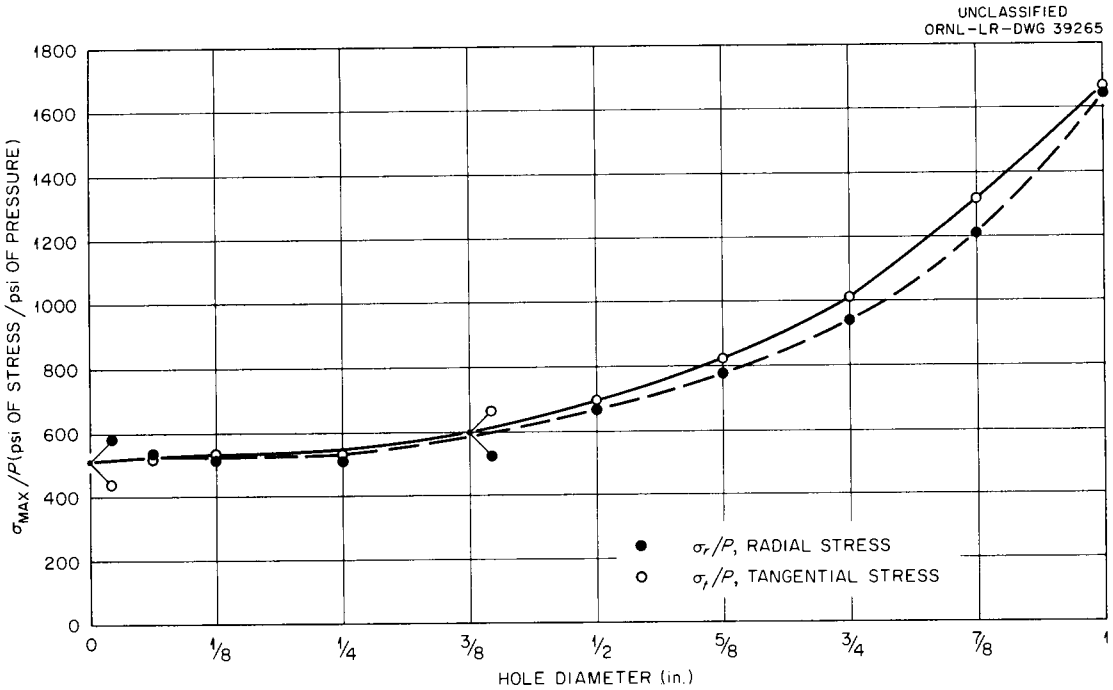


**Fig. 2.9. Maximum Radial and Tangential Stresses of a Perforated, Circular, Clamped Aluminum Plate Under a Test Pressure of 20 in. Hg.**

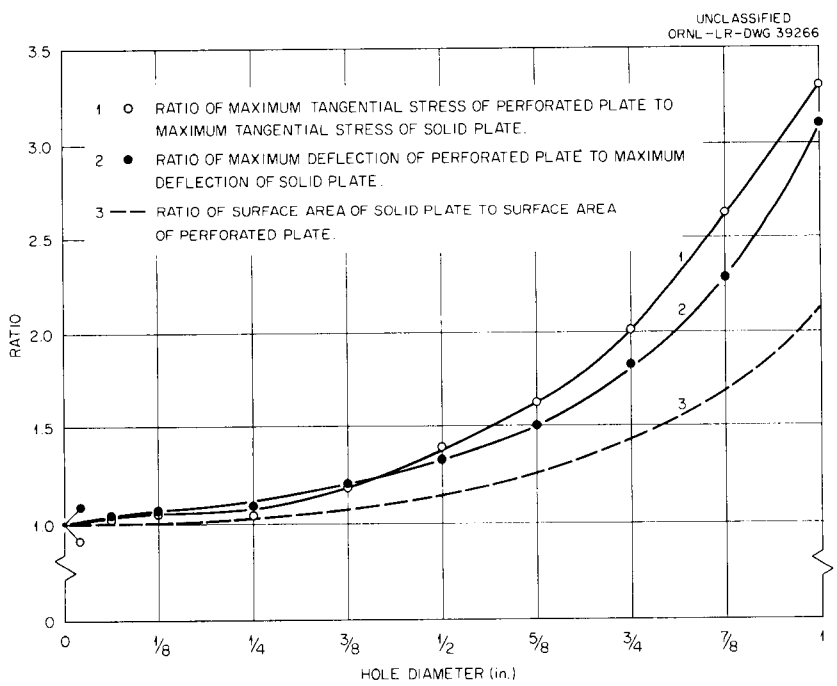


**Fig. 2.10. Stress, Deflection, and Area Ratios of a Perforated Plate vs a Solid Plate Under the Same Total Load (A maximum Test Pressure of 20 in. Hg).**

data for air and hydrogen.[15] Adequate theoretical information and experimental data with regard to the insulating characteristics of specific electrode configurations in air, hydrogen, and helium at standard atmospheric temperatures and pressures were found, but only a limited amount of information was found for helium, hydrogen, and air at pressures above atmospheric. Insufficient information is available with respect to the effects of temperature on the breakdown voltages for gases.

A rough evaluation indicates that the breakdown of helium occurs at a voltage approximately one-tenth the breakdown voltage of air and approximately one-fourth the breakdown voltage of hydrogen. Increasing the temperature of helium from 80 to 1000°F is estimated to reduce the breakdown voltage by at least a factor of 2.7 as a result of the reduced gas density. It appears to be quite likely that the breakdown voltage would be reduced even more because of the behavior of the gas molecules and the electrodes at the higher temperatures. The breakdown voltage for an air gap at 80°F would be expected to be approximately 27 times greater than the breakdown voltage for the same gap in helium at 1000°F. The uniformity of the field, which is a function of the configuration of the electrodes, may also affect the gas breakdown voltage by a factor of 2 or 3. An increase in pressure will result in an increase in the breakdown voltage, within limits, depending upon the gas and the uniformity of the electric field.

Contaminants in a gas have also been found to greatly affect the breakdown voltage. A classic example of this is the addition of 0.1% argon to neon to obtain breakdown at one-fourth the breakdown voltage of pure neon and at one-tenth the breakdown voltage of pure argon.

The information obtained in this study suggests that the following three assumptions might be used in estimating design information:
(1) The breakdown voltage will increase with increasing spacing and

---

[15] R. D. Stulting, Electrical Insulation Characteristics of Helium Gas at High Pressures and Temperatures, ORNL CF 59-2-22 (Feb. 2, 1959).

increasing pressures to 5 to 10 atm. Very little increase in breakdown voltage results from higher pressures. (2) The breakdown voltage will vary inversely with the absolute temperature. Experimental verification of this effect is not available. (3) In addition to the allowance for factory test voltages, a factor of safety of 25% should be applied to the voltage.

As a result of the many variables and the relatively large effect of these variables, it is necessary to obtain specific experimental data when accurate breakdown voltage values are required. The general effects of increased temperature should be verified by experimental data. The combined effects of increased temperature and increased pressure should be investigated. The importance of obtaining additional information for helium is accented by its relatively poor insulating characteristic.

## Containment Vessel Study

A parametric study of factors affecting containment vessel costs and size limitations was conducted in order to provide data which can materially speed the economic evaluation of reactor conceptual designs. The data obtained on the unit cost of spherical containment vessels as a function of vessel diameter and vessel wall thickness are presented in Fig. 2.11. The installed cost of a spherical containment vessel as a function of vessel diameter and wall thickness may be obtained from Fig. 2.12. The costs of cylindrical containment vessels with hemispherical heads as a function of vessel diameter, vessel wall thickness, and cylindrical shell height are presented in Figs. 2.13 through 2.18.

Cylindrical containment vessels would be subjected to loads such as snow, wind, and vessel head weight which would necessitate a limit to the cylinder height for any particular wall thickness to prevent buckling failure. The height limits imposed by such buckling loads are plotted in Figs. 2.19 through 2.24 as a function of vessel diameter, vessel wall thickness, and a safety factor. Since rigorous analysis

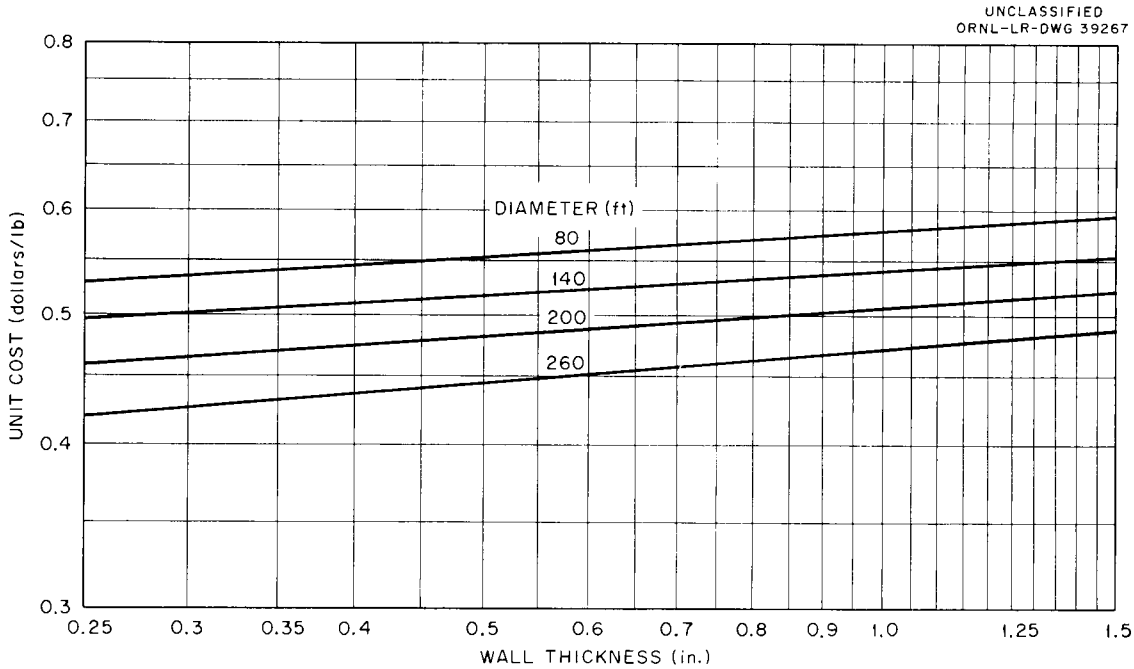


**Fig. 2.11. Spherical Containment Vessel Unit Cost as a Function of Diameter and Wall Thickness.**

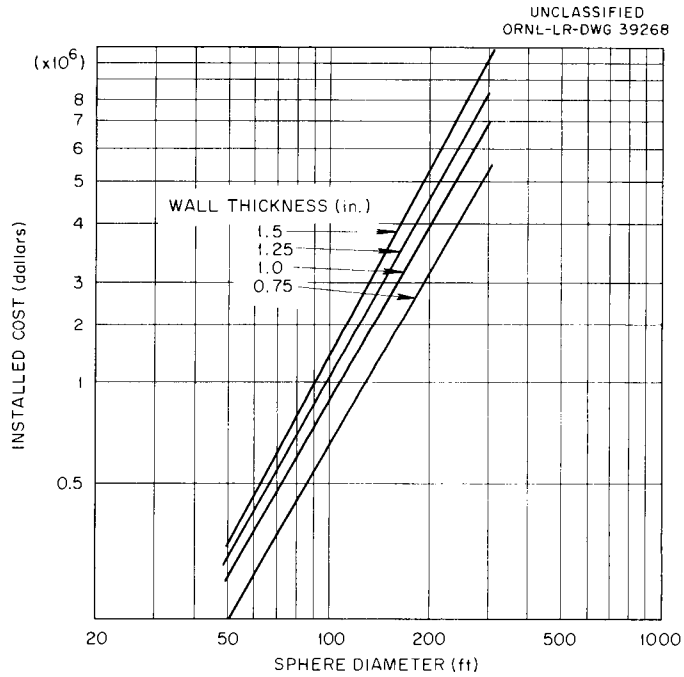


**Fig. 2.12. Approximate Installed Cost of a Spherical Containment Vessel as a Function of Diameter and Wall Thickness.**

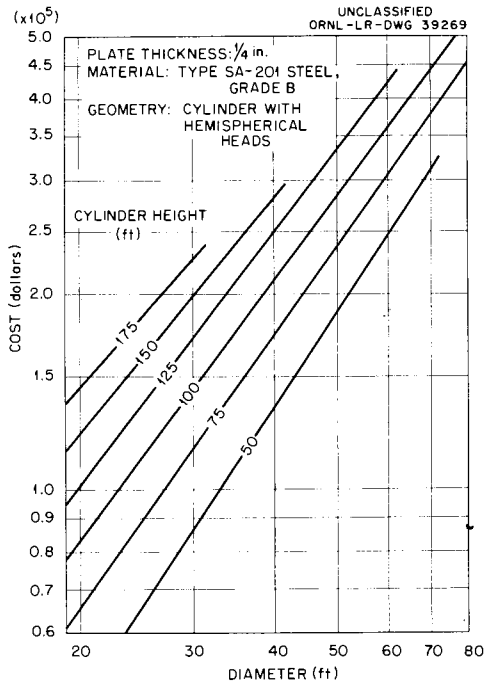


**Fig. 2.13. Approximate Cost of Cylindrical Containment Vessels Fabricated from $\frac{1}{4}$-in.-Thick Plate.**

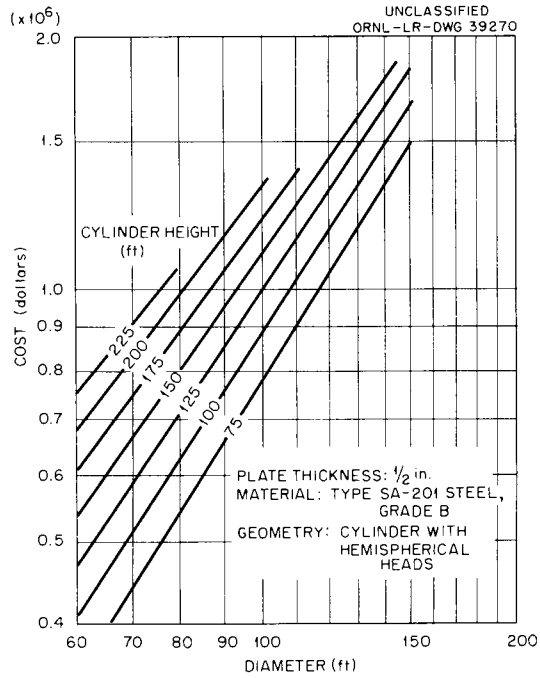


**Fig. 2.14. Approximate Cost of Cylindrical Containment Vessels Fabricated from $\frac{1}{2}$-in.-Thick Plate.**

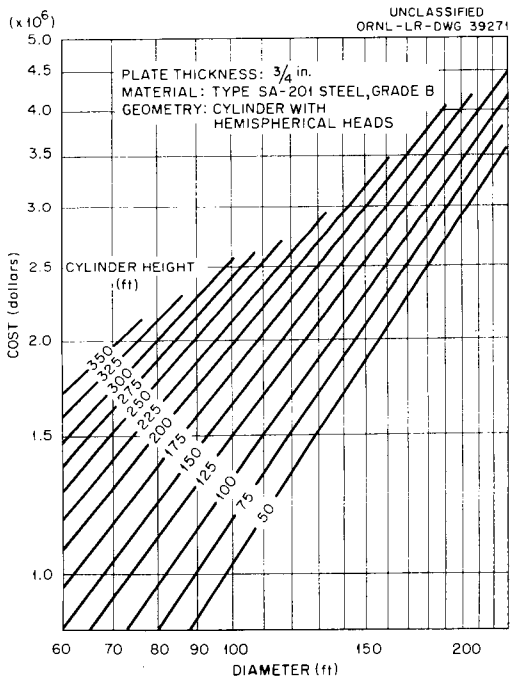


**Fig. 2.15. Approximate Cost of Cylindrical Containment Vessels Fabricated from $\frac{3}{4}$-in.-Thick Plate.**

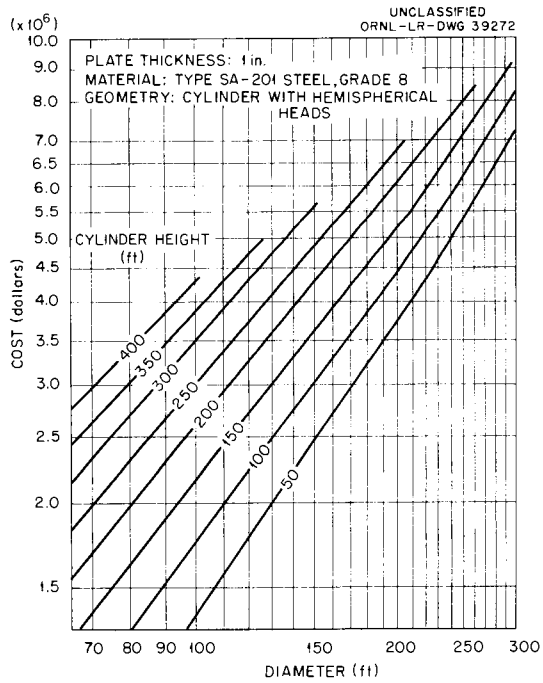


**Fig. 2.16. Approximate Cost of Cylindrical Containment Vessels Fabricated from 1-in.-Thick Plate.**

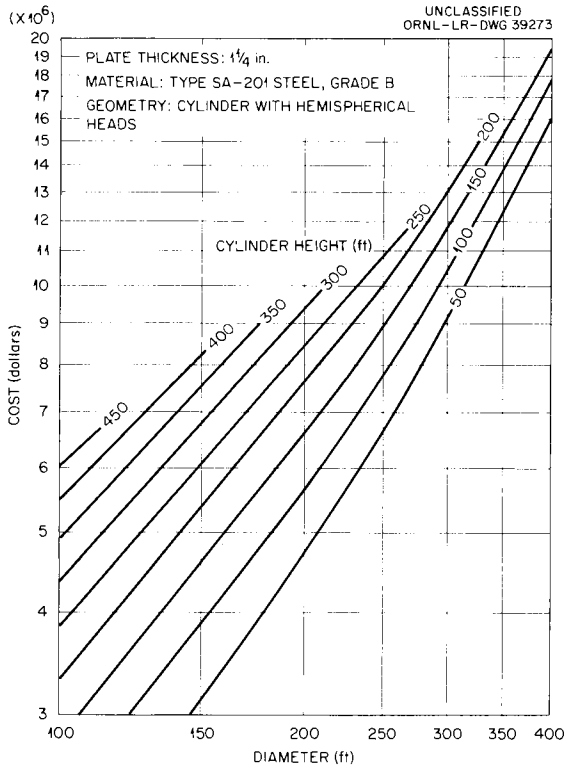


**Fig. 2.17. Approximate Cost of Cylindrical Containment Vessels Fabricated from $1\frac{1}{4}$-in.-Thick Plate.**

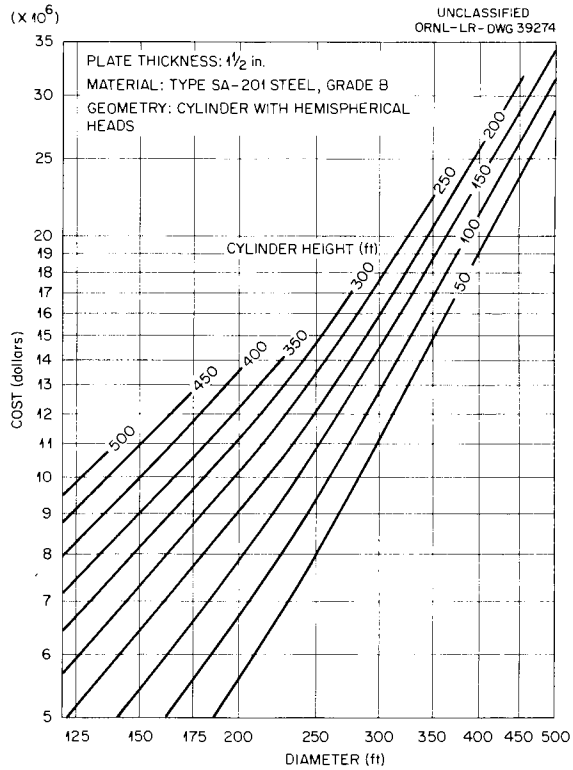


**Fig. 2.18. Approximate Cost of Cylindrical Containment Vessels Fabricated from $1\frac{1}{2}$-in.-Thick Plate.**

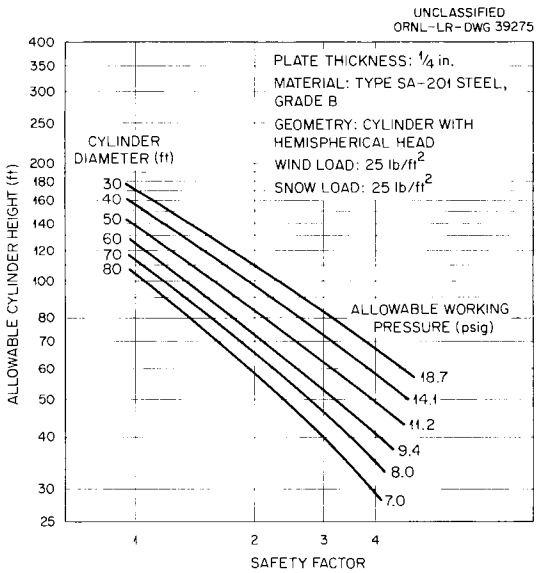


**Fig. 2.19. Allowable Height of $\frac{1}{4}$-in.-Thick Cylindrical Vessel with Buckling Loads.**

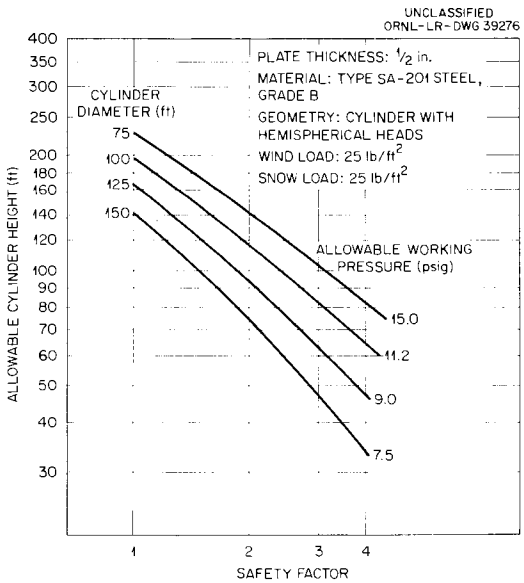


**Fig. 2.20. Allowable Height of $\frac{1}{2}$-in.-Thick Cylindrical Shell with Buckling Loads.**

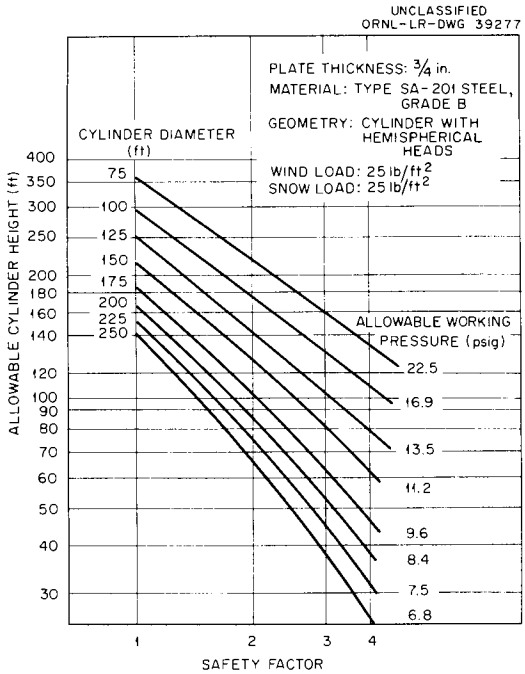


**Fig. 2.21. Allowable Height of $\frac{3}{4}$-in.-Thick Cylindrical Vessel with Buckling Loads.**

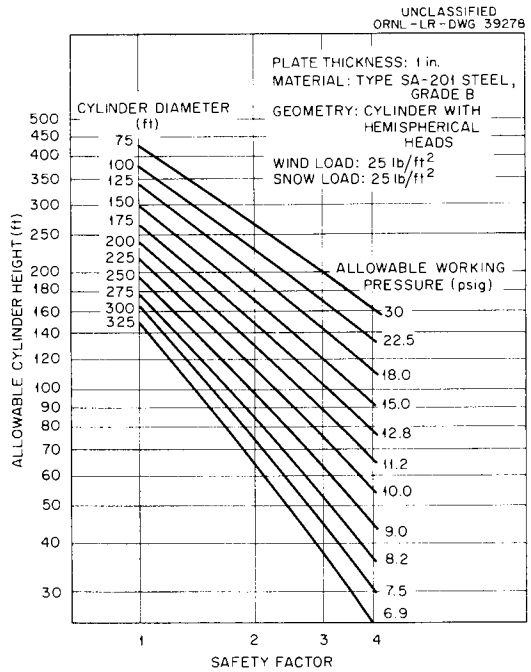


**Fig. 2.22. Allowable Height of 1-in.-Thick Cylindrical Vessel with Buckling Loads.**

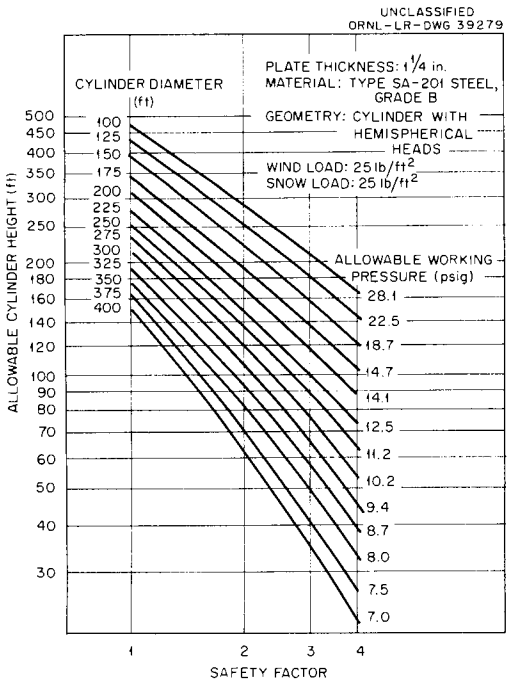


**Fig. 2.23. Allowable Height of $1\frac{1}{4}$-in.-Thick Cylindrical Vessel with Buckling Loads.**

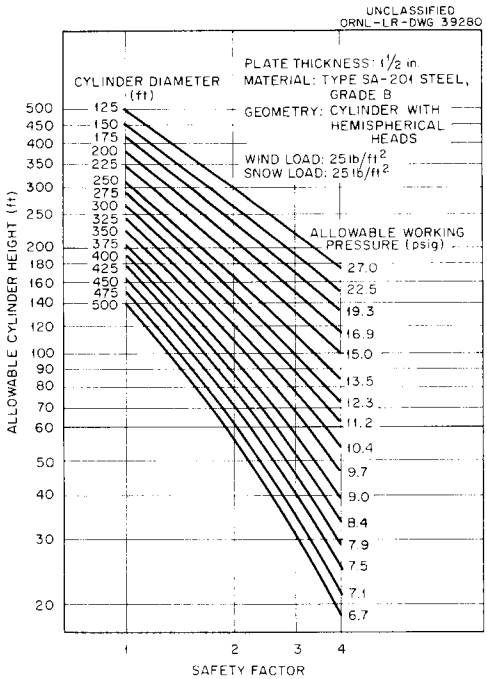


**Fig. 2.24. Allowable Height of $1\frac{1}{2}$-in.-Thick Cylindrical Vessel with Buckling Loads.**

was not required in the determination of the critical buckling loads of the cylindrical shells, use was made of the method outlined by the Army-Navy-Civil Committee on Aircraft Requirements.[16]

## Reactor Physics

### Fast-Neutron Flux in the PEGCPR Pressure Vessel

The effect of fast-neutron irradiation on the strength and ductility of pressure vessel steels is not yet completely established (see Chap. 6, this report), but the available information indicates that an integrated fast-neutron flux of $10^{18}$ neutrons/cm$^2$ will probably not have a deleterious effect on the room-temperature ductility of low-carbon steels, while an integrated flux of $5 \times 10^{18}$ neutrons/cm$^2$ almost certainly would.[17]

The fast-neutron dose (neutrons with energy above 1 Mev) has been calculated for the PEGCPR pressure vessel by multigroup methods and by application of results of moments-method calculations performed at NDA.[18] The NDA calculations showed that in graphite the fast-neutron spectrum becomes nearly independent of depth of penetration into the graphite for depths greater than 30 to 40 g/cm$^2$. This finding made possible a simplified calculation of the neutron-flux spectrum and the intensity at the surface of the reflector. The calculation was done by dividing the core into a series of equivalent, point, neutron sources whose strength was obtained from the radial power distribution in the midplane of the reactor (a peak-to-average axial power ratio of 1.5 was assumed). The contributions of these point sources to the neutron flux at the reflector surface were then summed numerically to obtain the total flux.

---

[16] Strength of Aircraft Elements, ANC-5, Army-Navy-Civil Committee on Aircraft Requirements (Oct. 1940, Rev.).

[17] J. C. Wilson et al., Solid State Div. Ann. Prog. Rep. Aug. 31, 1958, ORNL-2614, p 98.

[18] J. Certaine et al., Penetration of Neutrons from a Point Fission Source Through Carbon and Hydrocarbons, NDA 12-18 (June 30, 1956).

The spectral distributions at the inner surface of the pressure-vessel thermal barrier are shown in Fig. 2.25 for various reflector thicknesses, and the integrated fluxes are shown in Table 2.1.

Table 2.1. Pressure Vessel Exposure to Fast Neutrons (1 to 12.1 Mev) from an Active Core 11.08 ft in Diameter

| Reflector Thickness (cm) | Total Neutron Flux Above 0.1 Mev ($n/cm^2 \cdot sec$) | Total Exposure in 20 Years ($neutrons/cm^2$) |
|---|---|---|
| 61 | $6.4 \times 10^9$ | $4.0 \times 10^{18}$ |
| 67.3 | $3.42 \times 10^9$ | $2.2 \times 10^{18}$ |
| 71 | $2.48 \times 10^9$ | $1.6 \times 10^{18}$ |

It may be seen from Fig. 2.25 that the fast-neutron flux, as determined by the moments method, exceeds that obtained from the multigroup calculation by a factor of 6 to 8 below 1 Mev and by a factor of about 4 above 2 Mev. From the table it may be seen that the flux depends very much on the reflector thickness; it decreases an order of magnitude in about 10 in. of graphite. Thus, the proper thickness of the reflector may be determined as much by the need to protect the pressure vessel as by reactivity considerations. The figures given in Table 2.1 apply at the inner surface of the thermal barrier, a 1-in.-thick steel layer just inside the pressure vessel. The attenuation through the thermal barrier is 20%, and, through the pressure vessel, an additional factor of 2.5. The fluxes given are therefore essentially those that determine the radiation damage effects to the inner portion of the pressure vessel.

Control Rod Worth in the EGCR

A detailed study is being made for the purpose of determining the shutdown worth of the $B_4C$ control rods of the EGCR. Both multigroup and few-group methods have been employed and the most up-to-date results explicitly include the effects of leakage, the presence of the through tubes for experimental loops, rod interaction effects, and the nonuniform array resulting if only 21 control rods are inserted. The latter

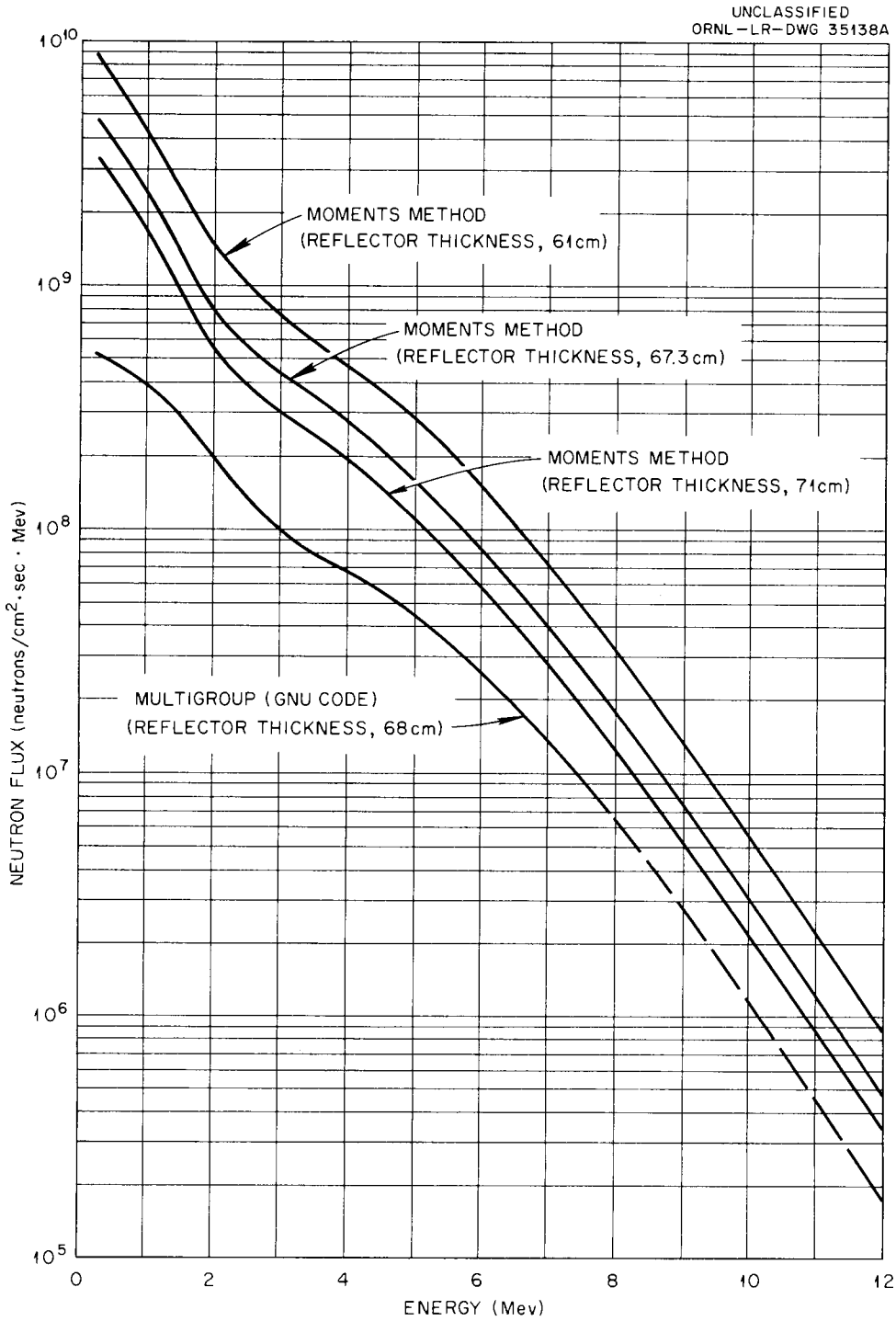


**Fig. 2.25. Comparison of Midplane Neutron Flux Spectrum at Interface of Reflector and Thermal Barrier (PEGCPR).**

consideration results from the probable elimination from the design of four control rods because of conflicts with the mechanical design of the core graphite structure.

The multigroup calculations were all performed for the control rod supercell formed by the rod and its associated nine core-lattice cells. Since diffusion theory was used in the control material analyses, the rod worth was known to be overestimated, but considerable information was obtained on the amount of epithermal absorption in the boron. Typical results are illustrated in Fig. 2.26. It may be seen that the $B_4C$ control rod has considerable epithermal absorption, with about 60% of all absorptions occurring above 1 ev. The boronated (1.5% B) stainless steel rod, on the hand, has slightly more than 30% of all absorptions above this energy. In this comparison the difference in epithermal absorption resulted in a worth of the $B_4C$ rod which was 1.43 times that for the stainless steel rod. In both cases the epithermal absorptions are quite important.

In order to remove the condition that diffusion theory be applied in the case of the strongly absorbing control material, four-group calculations were performed in which an extrapolation length into the rod was specified for the thermal group and the lowest epithermal group, and diffusion theory was applied to the rod calculations for the two highest energy groups. The group structure used in these calculations is given below:

| Group Number | Energy Limits (ev) |
|---|---|
| 1 | $10^7$ to $1.832 \times 10^5$ |
| 2 | $1.832 \times 10^5$ to 4.564 |
| 3 | 4.564 to 0.03075 |
| 4 | 0.03075 |

The multigroup calculations were performed first, and the resulting energy dependence of the flux was used to compute average cross sections for each material in the two highest energy groups. In order to obtain a reasonable representation of the energy dependence of the flux in the

immediate epithermal region, the cross sections for group 3 were specified in such a way that the flux in this group was equivalent to the Campbell-Freemantle form.[19] That is, a linear variation with energy was assumed from E = KT to E = 3.5 KT, followed by a constant portion from E = 3.5 KT to E = 5.0 KT. Above 5.0 KT the variation was assumed to be given by the multigroup calculations.

The application of this model of the flux in calculating the average absorption and fission cross sections is straightforward, since the energy variation is given explicitly. The effective removal cross section, $\Sigma_R$, was calculated by neglecting leakage and using the condition that all neutrons slowed down into group 3 must either be absorbed or slowed down into the thermal group. Since the slowing-down density at the top of group 3 is independent of the form of the flux in group 3, the following expression can be written for this group:

$$\Sigma_R^{CF} \bar{\phi}_{CF} + \int \phi_{CF}(E)\, \Sigma_a(E)\, dE = \Sigma_R^{o} \phi_o + \int \phi_o(E)\, \Sigma_a(E)\, dE \quad ,$$

where CF refers to the Campbell-Freemantle flux, and o refers to the approximately 1/E multigroup flux. This equation is sufficient for determining $\Sigma_R^{CF}$ if it is assumed that

$$\Sigma_R^{o} = \frac{\xi\, \Sigma_s}{\Delta u} \quad ,$$

where $\Delta u$ is the lethargy width of the group.

With the average group cross sections for each element computed in the manner described above, a P-3 cell calculation was done for each of the four groups to determine the flux disadvantage factors required to form an equivalent homogeneous core material. In these P-3 calculations the removal cross section was added to the absorption cross section.

The extrapolation lengths in groups 3 and 4 were calculated from the core transport cross section and the rod radius by assuming that the

---

[19] C. G. Campbell and R. G. Freemantle, Effective Cross Section Data for Thermal Reactor Calculations, AERE RP/R 2031 (Aug. 1956).

rod is black to all neutrons in these groups.[20] The macroscopic absorption cross sections of $B_4C$ in the four-group scheme are given below:

| Group | $\Sigma_a$ for $B_4C$ ($cm^{-1}$) |
|---|---|
| 1 | 0.0135 |
| 2 | 0.807 |
| 3 | 16.98 |
| 4 | 55.41 |

The reasonable nature of the assumption of blackness in groups 3 and 4 is clear from the magnitude of the absorption cross sections in these groups.

The results of the supercell calculations made with the methods described above for a 2.0% core enrichment are given in Table 2.2. In

Table 2.2. Control Rod Worth in the Cold-Clean EGCR with 2.0% Enrichment

| Calculational Method | Fuel Channels Per Control Rod | $\delta k_\infty$ |
|---|---|---|
| 4 group | 16 | 0.152 |
| 4 group | 9 | 0.277 |
| 31 group | 9 | 0.324 |

each case the number of fuel channels per control rod is specified. It should be remembered that diffusion theory was applied to the control-rod region in the 31-group calculation.

In addition to the calculations described above, which predict the rod worth in an infinite reactor containing a uniform lattice of control rods, the rod worth has also been determined in the finite, reflected

[20] B. Davison and S. Kushneriuk, Linear Extrapolation Length for a Black Sphere and a Black Cylinder, MT-214 (March 30, 1956) (or Reactor Handbook, Vol. 1, p 395).

core containing the nonuniform array of 21 rods and the eight experimental through tubes incorporated in the present EGCR design. The geometry of this calculation is shown in Fig. 2.27.

The two-dimensional character of this configuration was retained explicitly through the use of the PDQ code for the IBM 704. The same four-group arrangement was used; the previous one-dimensional calculations were used to specify extrapolation lengths for the first two groups. In order to remain within the maximum allowable number of mesh points for the PDQ code, a square approximation to the rods was made by using the work of Hurwitz and Roe[21] to determine the dimensions of a square whose effective radius equals that of the rod.

In order to eliminate the error introduced by this approximation, a correction factor was determined by comparing the $\delta k_\infty$ of the square rod in a cylindrical supercell to that of the cylindrical rod in a cylindrical supercell. This correction was a reduction of approximately 7% in the computed $\delta k$. With this correction, the worth of the array of rods shown in Fig. 2.27 was calculated to be $\delta k_{eff} = 0.182$ in the cold-clean core with 2.0% enrichment.

Effect of Control Rods on Power Distribution

It is generally believed that it will be advantageous, in a large graphite-moderated power reactor, to stagger the replacement of spent fuel elements in such a way as to keep the excess reactivity of the reactor as low as possible, and to approximate the continuous loading scheme that is known to maximize the fuel reactivity lifetime for a given fuel enrichment. Nonetheless, some excess reactivity will be required for operational purposes, such as to override the xenon transient following a power reduction. In the design of the PEGCPR, an allowance of 1% excess reactivity was made for operating purposes. This reactivity must be compensated by the control rods, which can be inserted in any of a number of possible patterns. Since the axial buckling of the reactor is quite small (about $2.8 \times 10^{-5}$), it takes a rather deep insertion of

[21] H. Hurwitz, Jr. and G. M. Roe, J. Nuc. Energy 2, 85 (1955).

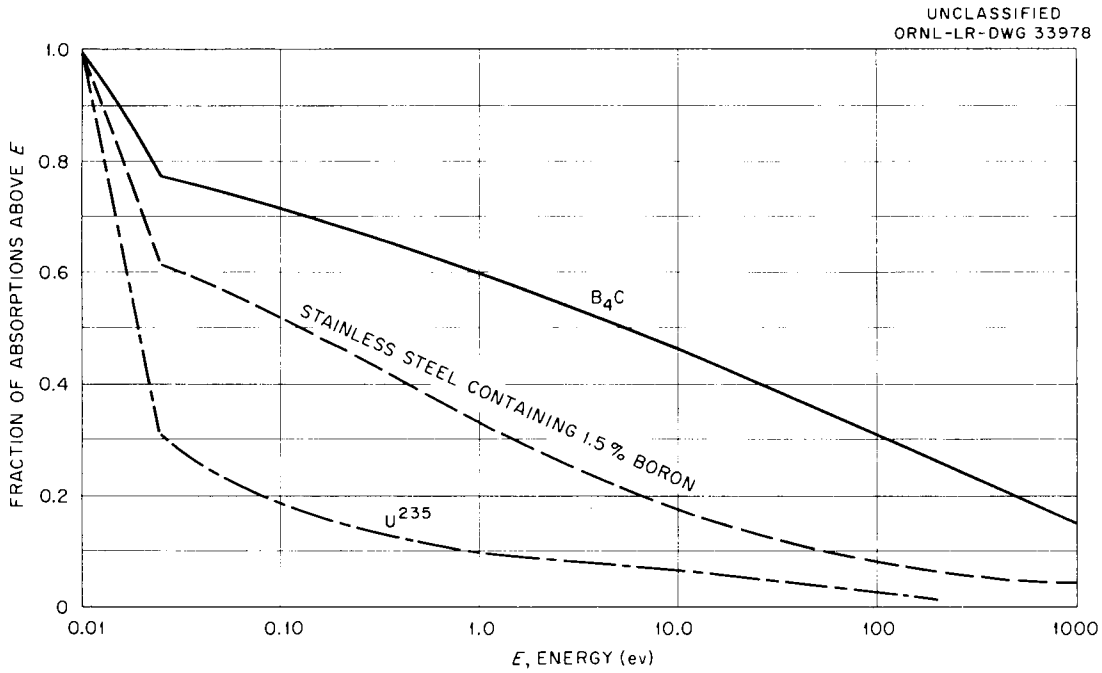


**Fig. 2.26. Neutron Absorptions in Fuel and Control Rods of the EGCR Obtained by Using Diffusion Theory in the Control Rod Calculations.**

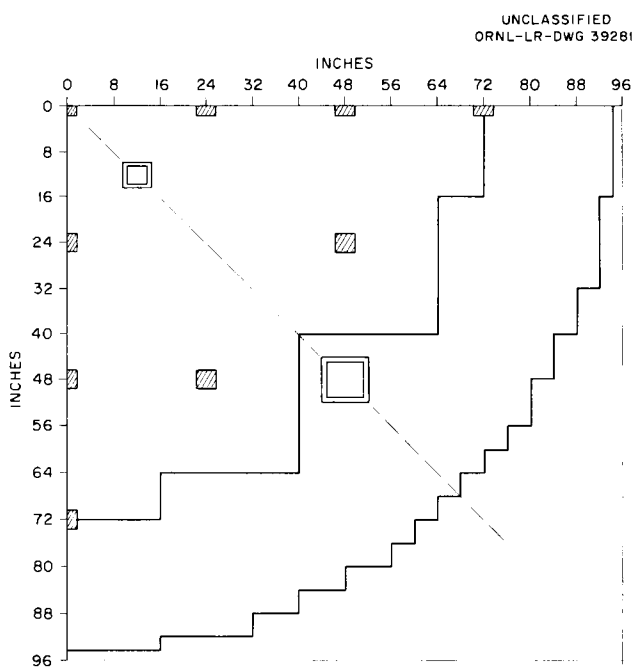


**Fig. 2.27. Geometry of EGCR with 21 Control Rods and 8 Experimental Tubes.** One quadrant of the core and reflector is shown.

all control rods in a bank to produce a significant reactivity change. Values of reactivity vs depth of insertion of the bank of control rods have been calculated,[22] and are listed below:

| Depth of Insertion (ft) | $\delta k_{eff}$ |
|---|---|
| 2 | 0.005 |
| 4 | 0.013 |
| 6 | 0.024 |
| 8 | 0.042 |

The active height of the core is 14.5 ft.

While insertion of the control rods from the high-temperature end of the reactor will have the effect of depressing the heat generation rate near that end, it will also have the effect of peaking the axial power distribution at or below the midplane of the core, and it will result in an increase in the maximum fuel surface temperature.

In order to explore the possibility that other control rod configurations might have a less serious, and, possibly, even a beneficial effect on the fuel temperature, two-dimensional four-group diffusion theory calculations have been made of a number of configurations of control rods, partially or fully inserted. In the cases considered, the rods were concentrated near the center of the reactor to achieve some flattening of the over-all power distribution. All the calculations were done for a uniform, fresh, core loading of 2.0% fuel enrichment. The cases considered included, among others, the central control rod inserted to the midplane of the core, three-quarters inserted, and fully inserted; the central rod plus the four adjacent rods; and the four adjacent rods only. A vertical power-density map for the central rod, half-inserted, and horizontal power-density maps for the other cases are presented in Figs. 2.28 through 2.31. The peak-to-average power-density ratios in the radial direction, the over-all power-density

[22] E. R. Wagner, Effect of Control Rods on the Power Distribution of the PEGCPR, Job Report No. 3-135-4.0 (Feb. 25, 1959).

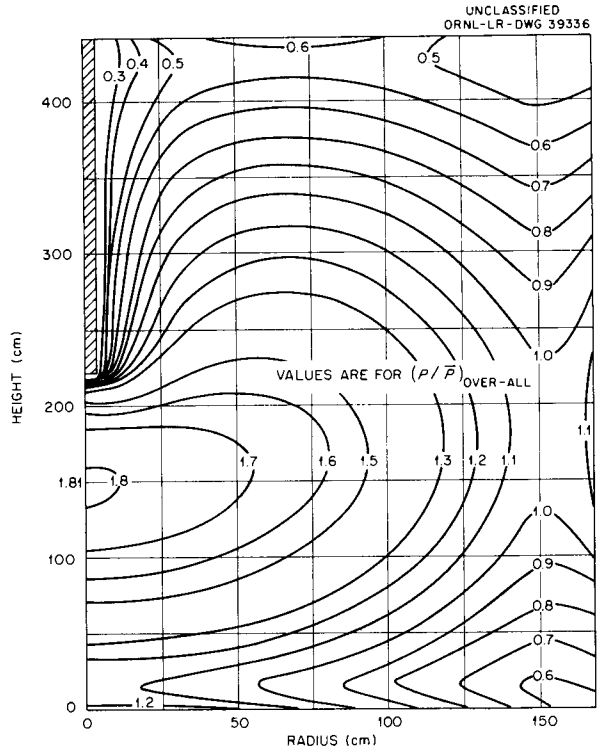


**Fig. 2.28. Power-Density Distribution in EGCR Without Loop Tubes and with Central Control Rod Inserted to Core Midplane. A vertical section of the core is shown.**

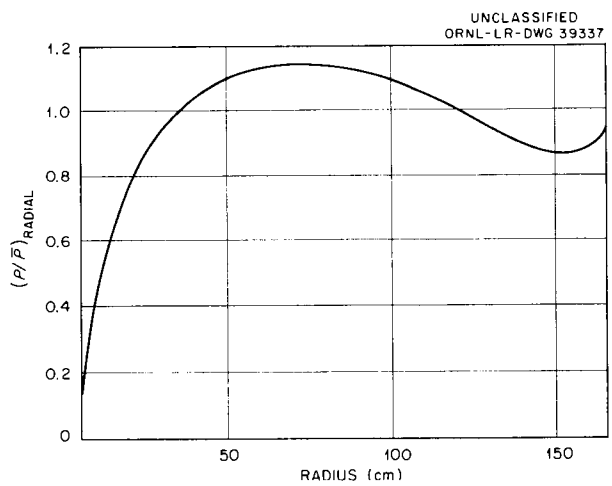


**Fig. 2.29. Radial-Power Distribution in EGCR Without Loop Tubes and with Central Control Rod Fully Inserted.**

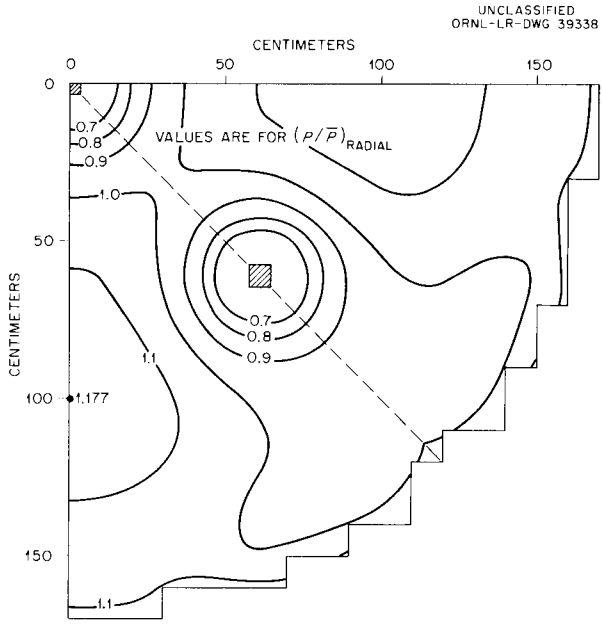


**Fig. 2.30. Radial Power-Density Distribution in EGCR Without Loop Tubes and with Five Central Control Rods Fully Inserted.**

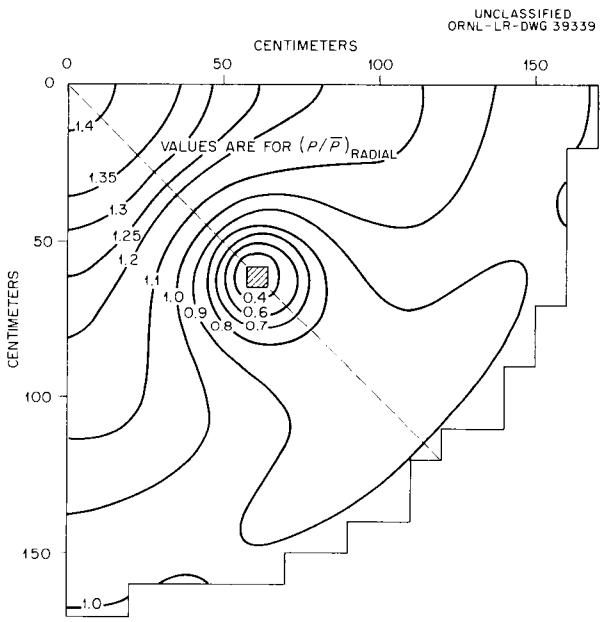


**Fig. 2.31. Radial Power-Density Distribution in EGCR Without Loop Tubes and with Four Central Control Rods Fully Inserted.**

ratios, and the change in effective multiplication factor produced by each configuration are listed in Table 2.3. The control rods are located at the corners of 24-in. squares, and the array can be inferred from the illustrations.

Table 2.3. Effect of Various Control Rod Configurations

| Configuration | Power-Density Ratios | | $\delta k_{eff}$ |
|---|---|---|---|
| | $(P_{max}/\overline{P})_{radial}$ | $(P_{max}/\overline{P})_{over\text{-}all}$ | |
| No rods | 1.37 | 1.70 | |
| Central rod (half inserted) | | 1.81 | 0.0076 |
| Central rod (three quarters inserted) | | 1.54 | 0.0186 |
| Central rod (fully inserted) | 1.14 | 1.41 | 0.0234 |
| Central rod plus four adjacent rods | 1.18 | 1.46 | 0.0795 |
| Four adjacent rods only | 1.42 | 1.77 | 0.0615 |

It may be seen from these results that a significant flattening of the flux can be achieved with the central rod alone. The problem of orificing the coolant flow through the reactor to take advantage of these power distributions, and the resulting fuel surface temperatures, are discussed in a preceding section of this chapter.

EGCR Experimental Loops

In designing experimental loop facilities for the EGCR, it is necessary to take into account the effect that the reactor through tubes and the possible experimental assemblies in the loops may have on the neutron flux and on the thermal performance of the reactor core. It is recognized that steel pipes penetrating the reflector near the core edge will have the effect of increasing the radial peak-to-average power-density ratio, while tubes placed judiciously in the core might decrease the peak-to-average power-density ratio. Calculations have been made

with the use of two-dimensional four-group diffusion theory to determine the power distribution for a number of different loop configurations. The loop configurations considered included 5-in.-OD, 0.168-in.-wall, stainless steel pipes located at the corners of a 24-in. square centered on the reactor axis, and 9-in.-OD, 0.31-in.-wall, stainless steel tubes located just outside the core at the corners of a 96-in. square. The power-density ratios for several configurations of empty loop tubes are given in Table 2.4. These data indicate that the loop tubes will

Table 2.4. Effect of Loop Tubes on Power Distribution in EGCR

| Case | Configuration | Power-Density Ratio $(P_{max}/\overline{P})_{radial}$ |
|---|---|---|
| 1 | No loops | 1.37 |
| 2 | Four 9-in.-dia tubes | 1.60 |
| 3 | Four 9-in.-dia tubes plus central control rod | 1.28 |
| 4 | Four 9-in.-dia tubes plus four 5-in.-dia tubes | 1.26 |

have a somewhat beneficial effect on the radial power distribution. The horizontal power density maps for cases 3 and 4 are shown in Figs. 2.32 and 2.33.

The presence in the loops of various experimental fuel elements may be expected to alter the flux distribution near the loops and to influence the reactivity of the reactor. Multigroup supercell calculations were performed for various representative experiments installed in 5-in.-dia EGCR loops. Although the loops are not concentric with the reactor, the reactor power-density distribution in four directions from the loop axis (in both directions along a reactor diagonal and in both directions along a line passing through the next 5-in.-dia loop) were

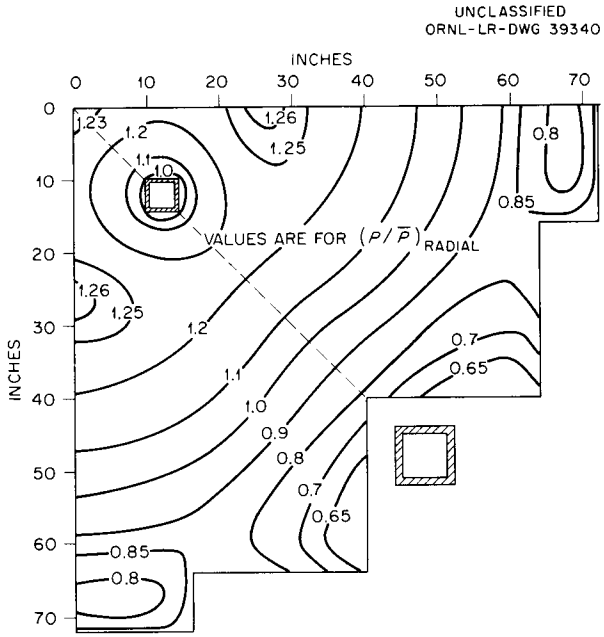


**Fig. 2.32. Radial Power-Density Distribution in EGCR with Four 9-in.-dia Loop Tubes and Four 5-in.-dia Loop Tubes.**

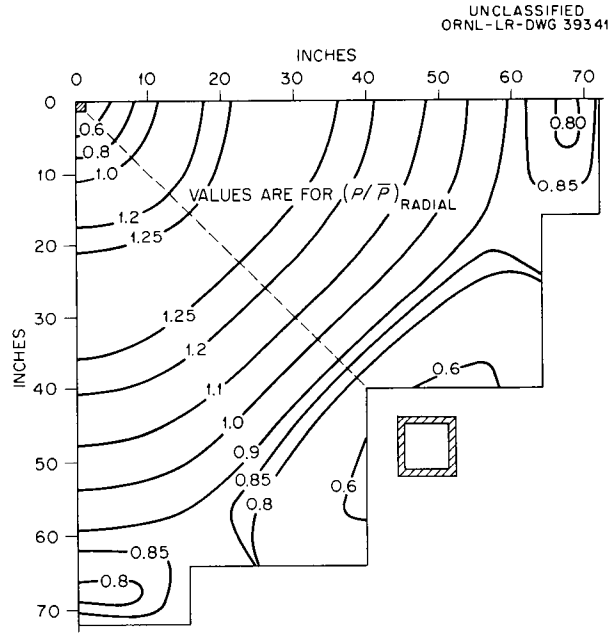


**Fig. 2.33. Radial Power Density Distribution in EGCR with Four 9-in.-dia Loop Tubes and the Central Control Rod Inserted.**

practically symmetrical about the loop axis, as determined by two-dimensional diffusion-theory calculations of the reactor with the four 5-in.-dia loops. It was therefore thought reasonable to calculate the effect of various loop contents by using a cell calculation with a flat-flux boundary condition about 15 in. from the loop axis. The loop itself, and contents, are represented exactly, while the surrounding core material is treated as being homogeneous. Cases calculated were: (1) empty loop tube; (2) tube filled with graphite, of density 1.15 g/cm$^3$; (3) graphite plus uranium; (4) graphite plus boron; (5) an EGCR fuel element, including sleeve, enriched to 10% $U^{235}$. Results of the calculations are presented in Table 2.5. It may be seen that for a carbon-

Table 2.5. Effect of Loop Contents on EGCR

| Case | Ratio of Carbon to Uranium Atoms | Ratio of Carbon to Boron Atoms | Loop Power (kw) | $\delta k$ for One 5-in.-dia Loop | Power-Density Ratio $(P/P_o)$[a] |
|---|---|---|---|---|---|
| 1 | | | 0 | 0 | 1.000 |
| 2 | $\infty$ | | 0 | 0.0003 | 1.006 |
| 3A | 200 | | 1040 | 0.0078 | 0.978 |
| 3B | 500 | | 650 | 0.0053 | 0.989 |
| 3C | 1000 | | 450 | 0.0038 | 0.996 |
| 3D | 2000 | | 240 | 0.0024 | 1.000 |
| 3E | 5000 | | 100 | 0.0013 | 1.004 |
| 4A | | 1000 | | -0.0033 | 0.992 |
| 4B | | 2000 | | -0.0018 | 0.998 |
| 5 | | | 870 | 0.0034 | 0.974 |

[a]Power density in neighboring fuel channels relative to empty loop case.

to-$U^{235}$ ratio of 200 (case 3A) in all four loops, the positive reactivity contribution would be about 0.03, if a power of 1040 kw in each loop were allowable. However, if the experimental assemblies were reduced in

length to limit the power in each loop to 500 kw, the combined reactivity of the four loops would be 0.02.

The gamma-ray heating in the 5-in.-dia loop due to reactor core gamma rays and to gamma rays produced in loop experiments, was calculated. The average heat generation in the tube wall due to neighboring fuel channels is 0.23 $w/cm^3$, while that due to an experimental cluster of seven 3/4-in.-dia $UO_2$ rods, with a fission power density of 20 Mw/MT, would be about 0.78 $w/cm^3$.

Power-Density Distribution in Fuel Clusters

The power-density distribution within a cluster of steel-jacketed $UO_2$ fuel rods will have an important influence on the heat-transfer and thermal-stability characteristics (see previous section of this chapter) of the fuel element. In order to ascertain the validity of various models used to predict this distribution, calculations have been made for several fuel clusters for which detailed flux plots have been obtained experimentally at Atomics International. The cases studied were: (1) a cluster of seven 3/4-in.-dia uranium-metal rods in a graphite moderator, with a 9 1/2-in.-square lattice, and a fuel enrichment of 2.78%;[23] (2) six of the above rods with one graphite rod in the center;[24] (3) seven 3/4-in.-dia natural-uranium-metal rods, graphite moderator, 9 1/2-in. pitch;[25] (4) cluster of four 0.9% enriched, 1.0-in.-dia, uranium-metal rods, graphite moderator, 9 1/2-in. pitch.[26]

---

[23] W. W. Brown et al., Exponential Experiments with Graphite Lattices Containing Multirod Slightly Enriched Uranium Fuel Clusters, NAA-SR-3096 (Jan. 15, 1959); R. A. Laubenstein, Exponential Experiments on Graphite Lattices Which Contain Multirod Fuel Elements, A/Conf.15/P/594 (June 1958).

[24] Ibid.

[25] R. A. Laubenstein et al., Sodium Graphite Reactor Quar. Prog. Rep. Jan.-Mar. 1955, NAA-SR-1347, p 18 (Oct. 1, 1955) (classified).

[26] R. A. Laubenstein et al., Sodium Graphite Reactor Quar. Prog. Rep. Oct.-Dec. 1954, NAA-SR-1292, p 19 (May 15, 1955).

The calculations were made with a one-velocity, one-dimensional, P-3 approximation to the neutron-transport equation. Effective neutron cross sections were computed at several different neutron temperatures. While the central rod was represented exactly, the outer ring of rods was represented by a concentric annulus. Several different combinations of the diameter, thickness, and density of the annulus were tried, all having the same total amount of uranium. The model that appears most satisfactory is an annulus having a diameter equal to the maximum diameter of the fuel cluster, a thickness equal to one fuel rod diameter, and an appropriately reduced uranium density. The best neutron temperature appears to be approximately that computed from the formula of Coveyou, Bate, and Osborn,[27] with an average absorption cross section computed by taking the flux disadvantage factor into account (an iterative procedure may be necessary).

Results for cases 1 and 3 are shown in Figs. 2.34 and 2.35. The principal feature of the distribution that is not given very well is the slight upswing of the flux between the inner edge of the outer rod and the surface of the inner rod. The power-density gradient across the outer rods is given sufficiently well for heat transfer calculations.

It may be shown from the curves of ref. 23 that the flux traverse in the outer rod perpendicular to a diameter of the cluster is given quite well by averaging the outer and inner portions of the flux trace taken parallel to the cluster diameter. The 45-deg trace is quite close to the 0-deg trace. It is thus possible to construct the power distribution in the cluster of rods from flux distributions obtained with the annular P-3 model. The ratio of average moderator flux to average fuel flux in each case is given in Table 2.6.

---

[27] R. R. Coveyou, R. R. Bate, and R. S. Osborn, J. Nuc. Energy 2, 153 (1956).

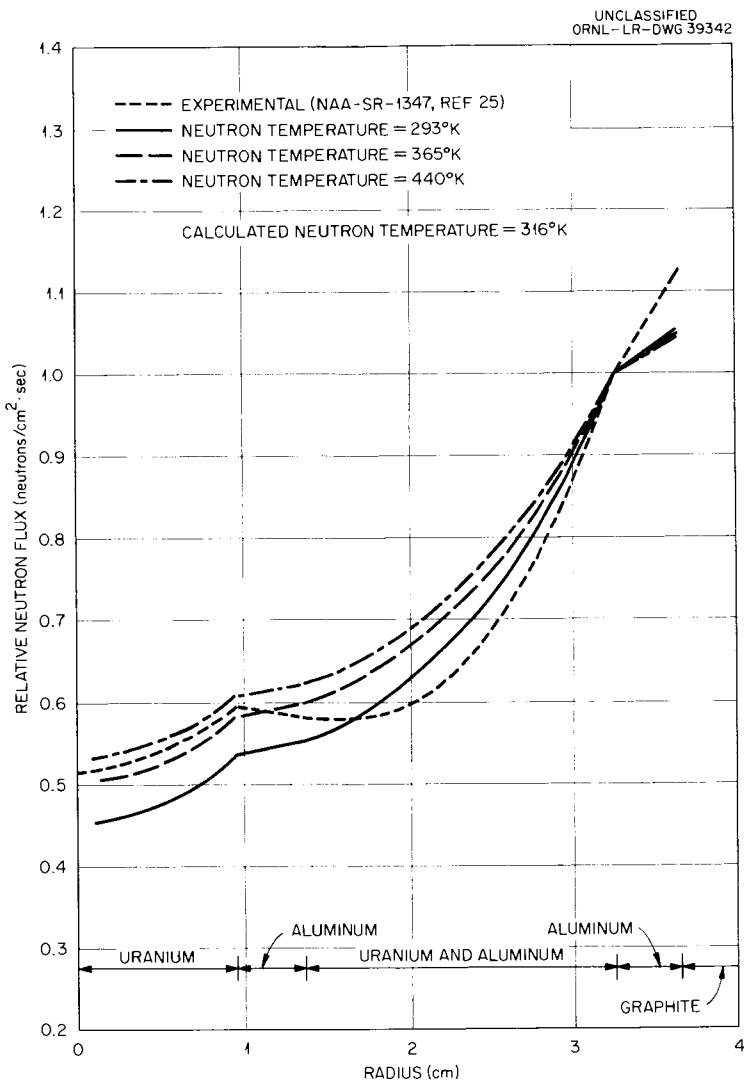


**Fig. 2.34. Flux Distribution in $\frac{3}{4}$-in.-dia Natural Uranium Fuel Rods in Seven-Rod Clusters on a 12-in. Lattice Pitch.**

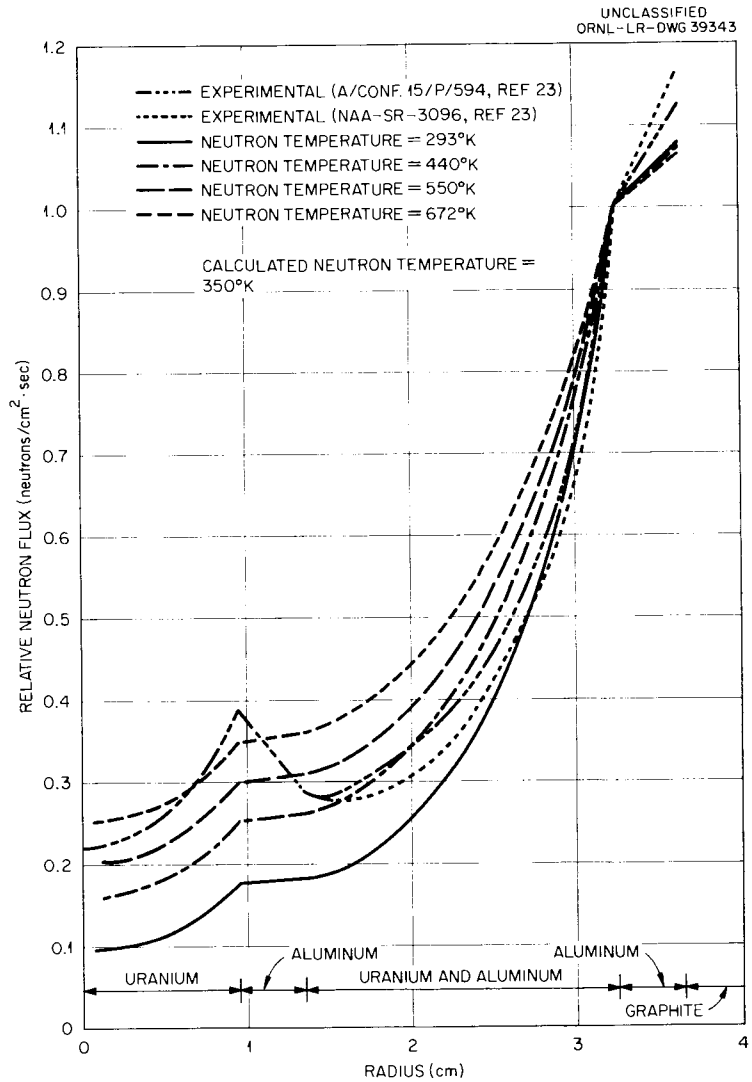


**Fig. 2.35. Flux Distribution in $\frac{3}{4}$-in.-dia 2.78% Enriched Fuel Rods in Seven-Rod Clusters on a $9\frac{1}{2}$-in. Lattice Pitch.**

Table 2.6. Flux Disadvantage Factors, $\bar{\phi}_{mod}/\bar{\phi}_{fuel}$

| Case | Calculated | Experimental |
|---|---|---|
| 1 | 4.72 | 4.78 |
| 2 | 4.09 | 4.22 |
| 3 | 2.42 | 2.53 |
| 4 | 3.08 | 2.82 |

## 3. EXPERIMENTAL INVESTIGATIONS OF HEAT TRANSFER AND FLUID FLOW

### Fluid Friction Characteristics

Flow studies were continued with the previously described[1] full-scale Plexiglas model of a single fuel channel. The 3.25-in.-dia channel contained six complete fuel-rod clusters, each cluster being 40 in. long and consisting of seven 0.842-in.-dia rods arranged on 1.094-in. centers. Static pressures were obtained at 14 stations along the channel, as shown in Fig. 3.1. At each position six pressure taps were connected to the piezometric ring in order to obtain valid average pressures.

Initial channel over-all pressure drop measurements (station 1 to station 14) with this apparatus were used to calculate the value of $K_S$, the hanger-spacer pressure loss coefficient. The skin friction contribution to the total pressure loss had been evaluated in a separate bare-tube (no hangers or spacers) experiment. Since by use of this procedure, the resulting value of $K_S$ was the small difference between two sets of experimental data of similar magnitude, question existed as to the accuracy of the value obtained. The current investigation was therefore intended as a direct measurement of this pressure-loss coefficient. At the same time the skin friction factor, f, was determined for the straight portion of the clusters, and additional data were obtained on the total equivalent friction factor, $f_T$.

The pressure loss for each bare-tube section of the channel (for example, the general regions h-i or j-k in Fig. 3.1) was used to evaluate the skin friction factors. Thus

$$\Delta p_{j-k} = f_{j-k} \frac{\Lambda_{j-k}}{d_e} \frac{\rho \bar{u}^2}{2g_c} , \qquad (1)$$

where $\Lambda_{j-k}$ is the length of the bare section between pressure rings j and k. The over-all skin friction factor for the channel is

[1] GCR Semiann. Prog. Rep. Dec. 31, 1958, ORNL-2676, p 28.

UNCLASSIFIED
ORNL-LR-DWG 39192

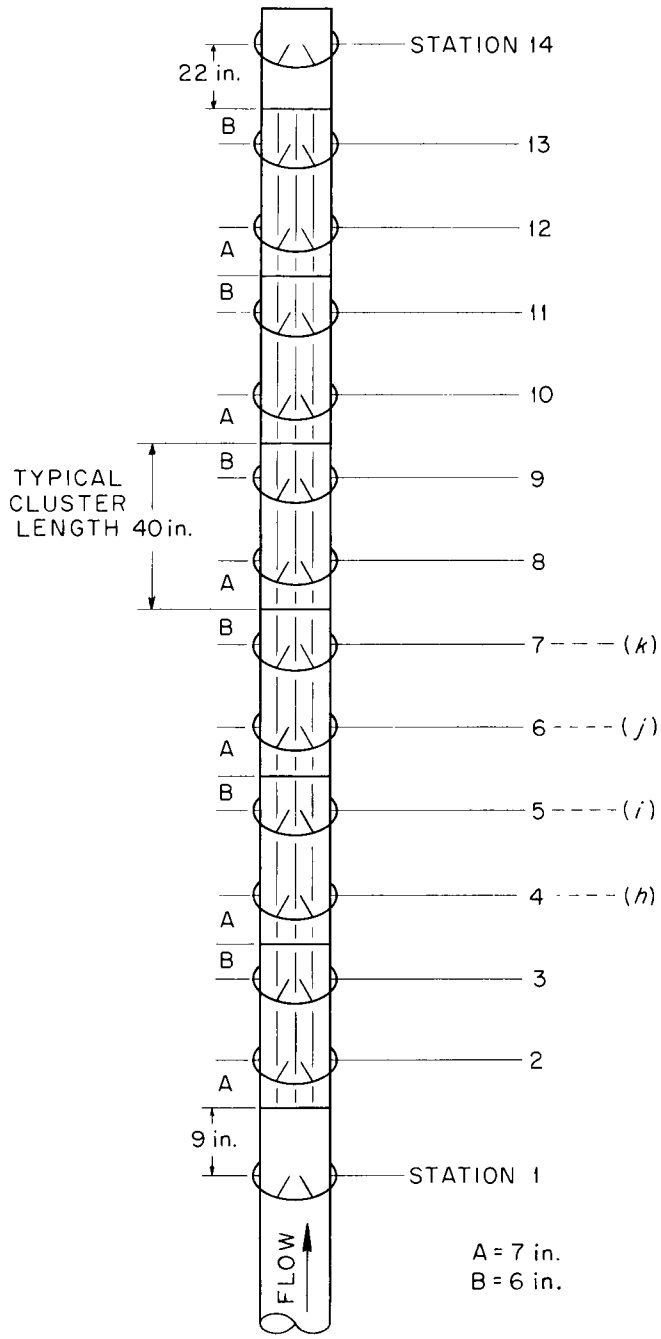


**Fig. 3.1. Schematic Diagram of the Plexiglas Model of a Full-Scale Fuel Channel Showing Static-Pressure Measuring Stations.**

then obtained as the mean of the individual factors:

$$f = \frac{\sum_{j-k} f_{j-k}}{n} , \qquad (2)$$

where j-k assumes the successive values 2-3, 4-5, ..., 12-13, and n is the number of bare-tube sections (here, n = 6). The results of these measurements of the factor f are given in Fig. 3.2. Analysis of the data yielded the correlating equation

$$f = 0.082\ N_{Re}^{-0.11} \qquad (3)$$

Also shown for comparison is the Blasius equation for flow within circular tubes,

$$f = 0.316\ N_{Re}^{-0.25} . \qquad (4)$$

In contrast with Eq. 3, the earlier experiment[1] with long bare-tubes gave the result

$$f = 0.282\ N_{Re}^{-0.232} . \qquad (5)$$

The difference in slope between Eqs. 3 and 5 measures the influence of the hanger-spacer assemblies on the turbulent structure in the channel. A variation in $f_{j-k}$ along the channel was also observed. This is illustrated for several values of the Reynolds modulus in Fig. 3.3. While the cause of this phenomenon is not certain, it must relate in part to geometrical differences in the individual clusters. An indication is thus obtained of the variation in heat transfer which may be expected between fuel elements arranged along a channel.

The individual hanger-spacer loss coefficients were determined from the pressure loss data for the regions i-j of Fig. 3.1. Since the pressure-measuring stations were located well upstream and downstream of the hanger-spacer units (approximately 6 in.) to minimize turbulence effects at the static taps, the data were corrected for the skin friction loss associated with the rod length, $\lambda_{i-j}$, included

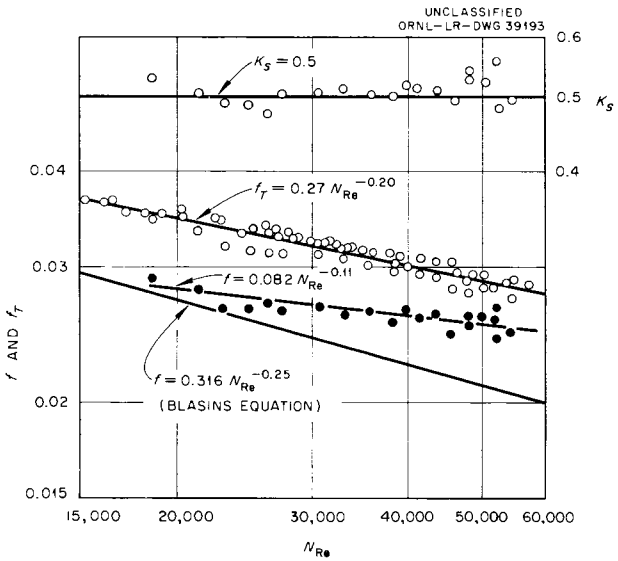


**Fig. 3.2. Fluid-Friction Characteristics of the Full-Scale Plexiglas Model of a Septafoil Fuel Channel.**

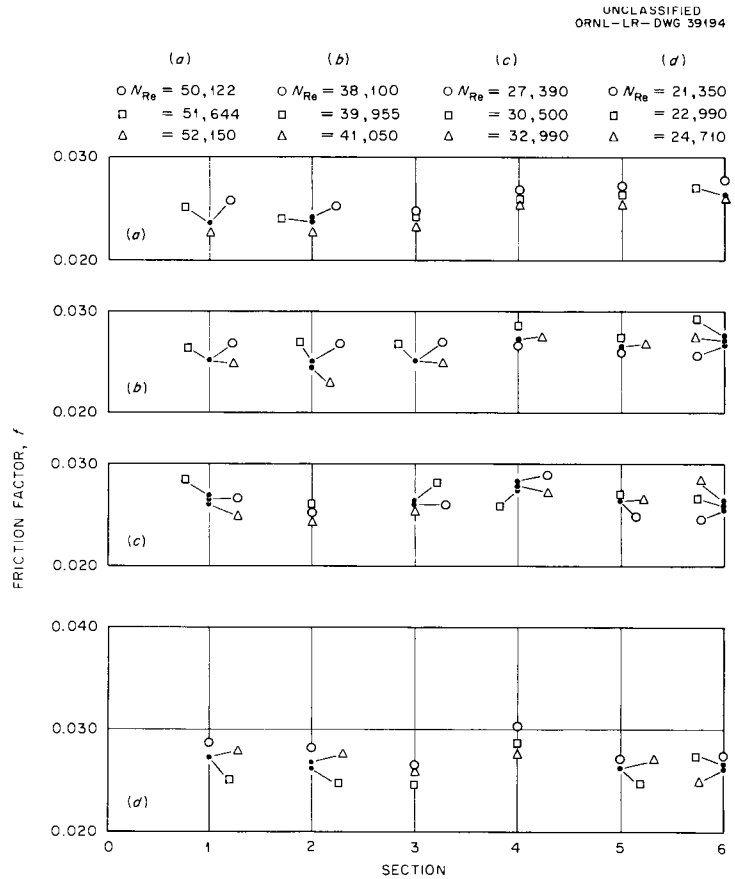


**Fig. 3.3. Local Values of Septafoil Friction Factors as a Function of the Reynolds Modulus and Channel Position.**

between the pressure taps. The pressure loss is then given by the equation

$$\Delta p_{i-j} = \left( K_{i-j} + f_{h-i} \frac{\lambda_i}{d_e} + f_{j-k} \frac{\lambda_j}{d_e} \right) \frac{\rho \bar{u}^2}{2g_c} \quad . \tag{6}$$

The variation in f between the rod clusters necessitates the inclusion of two bare-tube terms in Eq. 6; the quantities $f_{h-i}$ and $f_{j-k}$ are as given by Eq. 1. The average hanger-spacer pressure loss coefficient can be written as

$$K_S = \frac{\sum_{i-j} K_{i-j}}{n - 1} \quad , \tag{7}$$

since there are n - 1 hanger-spacer units associated with the n rod clusters. In Eq. 7, i-j takes on the successive values 3-4, 5-6, ..., 11-12. The results (plotted in Fig. 3.2) show that the pressure loss coefficient is essentially independent of the Reynolds modulus; over the $N_{Re}$ range from 15,000 to 60,000, the average value of the hanger-spacer loss factor was found to be

$$K_S = 0.5 \quad . \tag{8}$$

This value is consistent with the earlier result based on over-all pressure measurements.

On the basis of more complete data, the correlation for the total equivalent friction factor has been revised. Thus,

$$f_T = 0.27 N_{Re}^{-0.20} \quad . \tag{9}$$

As previously expressed, the total pressure drop for a septafoil geometry fuel channel can be written as

$$\Delta p_T = n \left( K_S + f \frac{l}{d_e} \right) \frac{\rho \bar{u}^2}{2g_c} \quad , \tag{10}$$

where n is the number of rod clusters and $l$ is the bare-tube length of a single cluster. The values of $K_S$ and f are determined by Eqs. 8

and 3, respectively. In writing Eq. 10 it was assumed that the effect of the initial spacer (between stations 1 and 2) and the final hanger (between stations 13 and 14) was identical to that of the interior hanger-spacer combinations. It is believed that any error so introduced is within the precision of the present experimental results.

## Flow Modification Studies

It has been suggested that swirling flow could be used to reduce the nonuniformity[2] of the circumferential temperature distributions in the septafoil geometry. Accordingly, an apparatus was constructed in which various swirl generators could be located at the inlet and their effect on the flow observed by the deflection of cotton fibers attached to the outer surfaces of the tubes. The prime variable studied in these initial experiments was the persistence of the swirl along the rod cluster.

The experimental channel was formed from a 4-in.-ID Plexiglas tube, and it contained a 45-in. long rod cluster consisting of six aluminum rods and one thin-walled glass tube (all 1 in. in outside diameter). A general view of the system is shown in Fig. 3.4, and the details of the entrance region are shown in Fig. 3.5. The entire unit was attached to the previously described[1] air-supply manifold.

Rectangular grids were etched on the outer surface of the glass tube at three locations; a typical section is shown in Fig. 3.6. Preliminary studies indicated that single thin cotton threads were most effective as flow indicators. Since flow direction rather than local turbulence was to be studied, the threads were of 3/4 to 1 1/2 in. in length. By rotating and interchanging the glass tube, all regions of the flow could be observed. Thus, in Fig. 3.6 the instrumented area of the tube (grid plus threads) is facing the channel wall, while in Fig. 3.7 the tube has been turned to face the central tube. Straight flow existed in both instances, and, as may be seen, the threads are

---

[2] *Ibid.*, p 36.

UNCLASSIFIED
PHOTO 33227

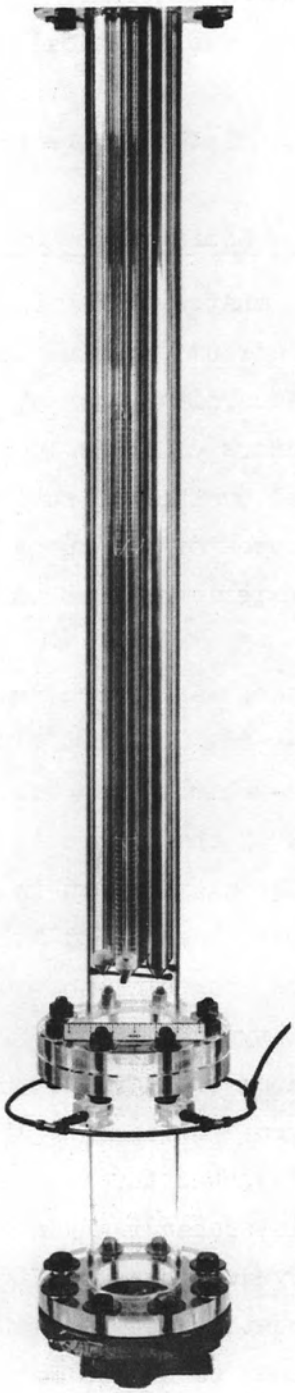

Fig. 3.4. Experimental Test Section for Flow Modification Studies.

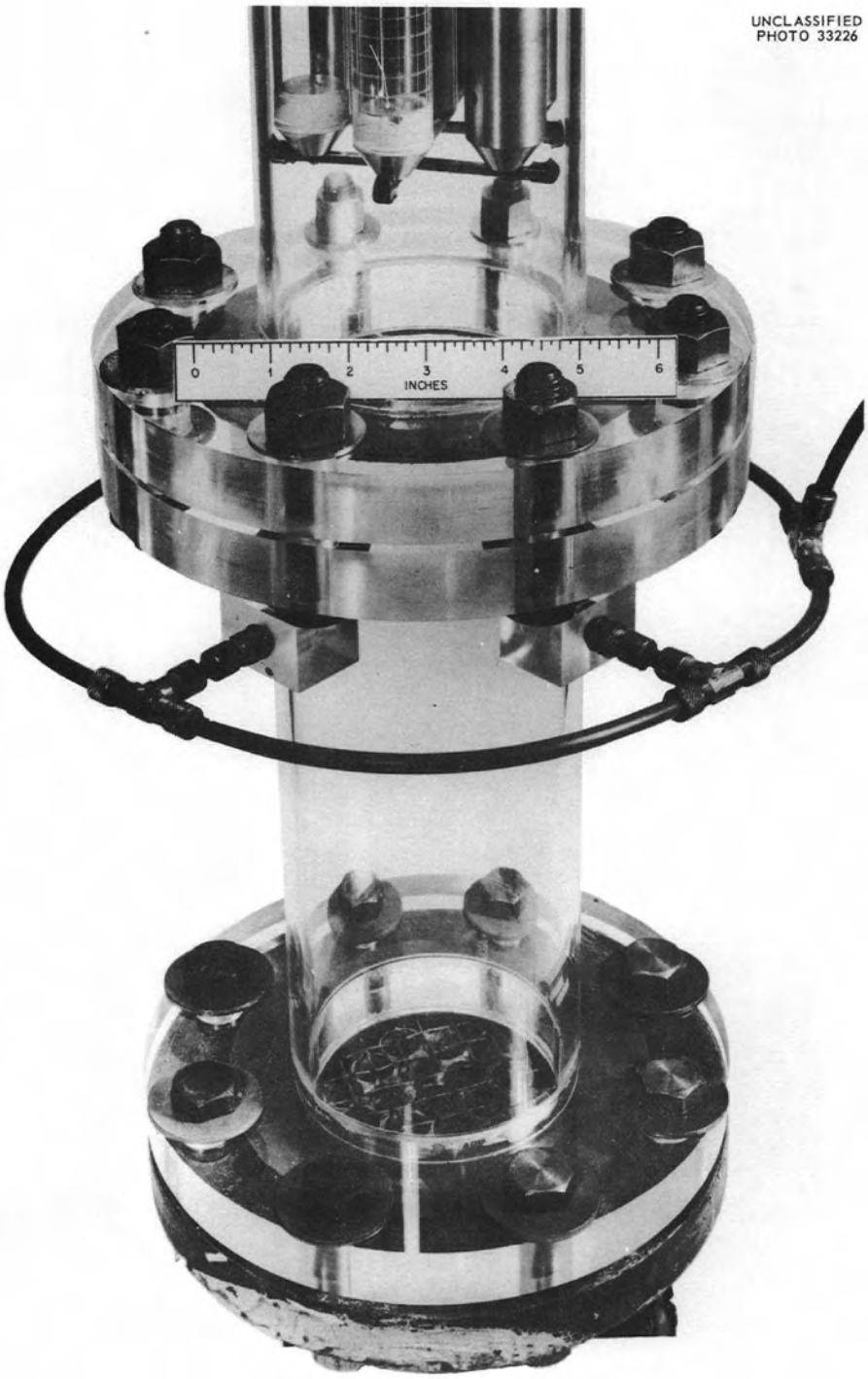


Fig. 3.5. Entrance Region for Experimental Test Section.

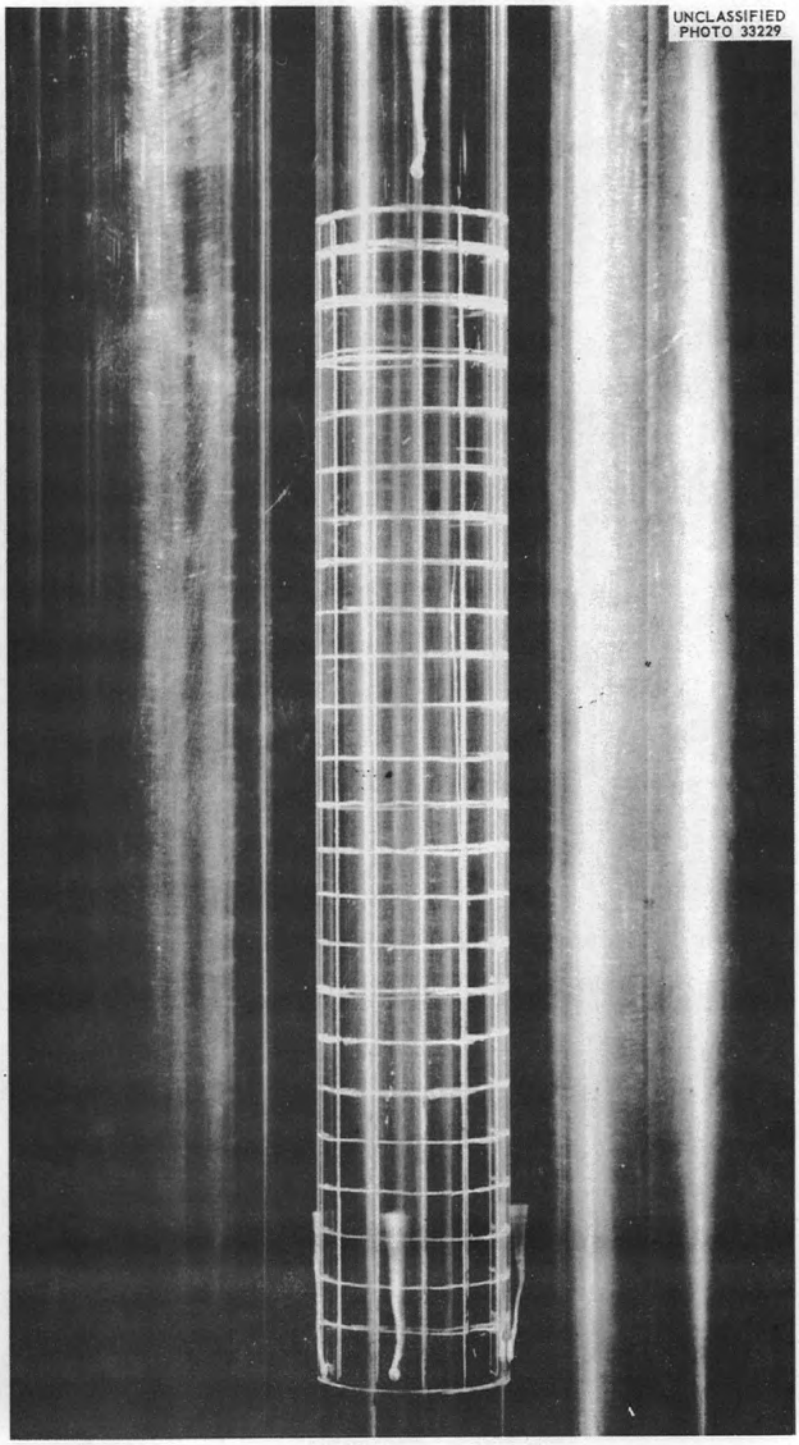


Fig. 3.6. Threads on Outer Surface of Peripheral Rod.

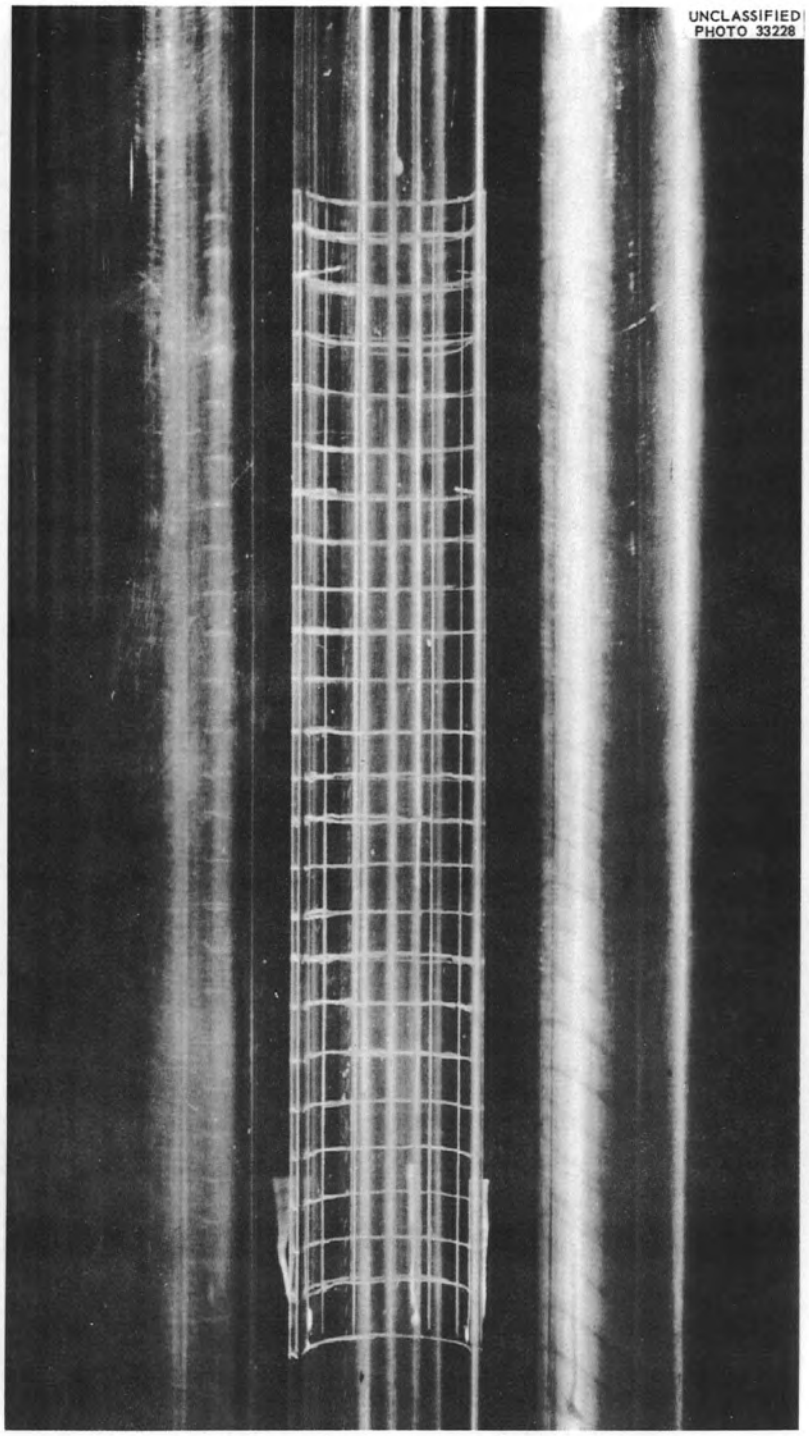


Fig. 3.7. Threads on Inner Surface of Peripheral Rod.

aligned parallel to the vertical grid lines. The flutter of the threads as a result of the turbulence of the flow is also clearly visible.

Details of the various swirl generators examined are shown in Fig. 3.8. In the first series of tests, six individual generators (Fig. 3.8d) were mounted on the upstream ends of the peripheral rods to produce intermeshing spiral flow concentric with the rods. Observations over a range of rod spacings indicated that the swirls thus generated decayed completely within 7 to 9 in. (approximately 10 equivalent diameters) of the cluster entrance. This rapid damping results from the difficulty in maintaining spiral flow over a convex geometry without providing auxiliary turning surfaces. Therefore, in a second test, a single generator was installed to create rotating flow concentric with the centerline of the channel (see Fig. 3.8a). Since this unit failed to produce swirl of any significant magnitude, it was modified to the form shown in Fig. 3.8b by extending the vanes. With this generator, helical flow could be maintained in the flow region adjacent to the channel wall for the entire length of the channel. However, at no tube spacing ratio did spiral flow persist in the inner flow region. It was further observed that the use of this generator doubled the pressure loss in the system in relation to that experienced with straight flow. Regions of flow separation were also noted on the peripheral rods; these have been verified in the mass transfer experiments described in a following section of this chapter.

This last experiment led to the design of a generator to create spiral flow in the peripheral flow region only. This generator is shown in Fig. 3.8c. Coupled with this, helical grooves were cut into the channel wall to assist in maintaining the flow along the cluster length. This channel is pictured in Fig. 3.9. Four grooves, 1/2 in. wide and 1/8 in. deep, were machined in the inner wall at a helical angle of 45 deg. Initial studies without the entrance vane showed that some rotating flow was maintained (thread deflections of 5 to 10 deg) throughout the length of the channel with pressure losses essentially the same as those which occurred in straight flow. Introduction of the

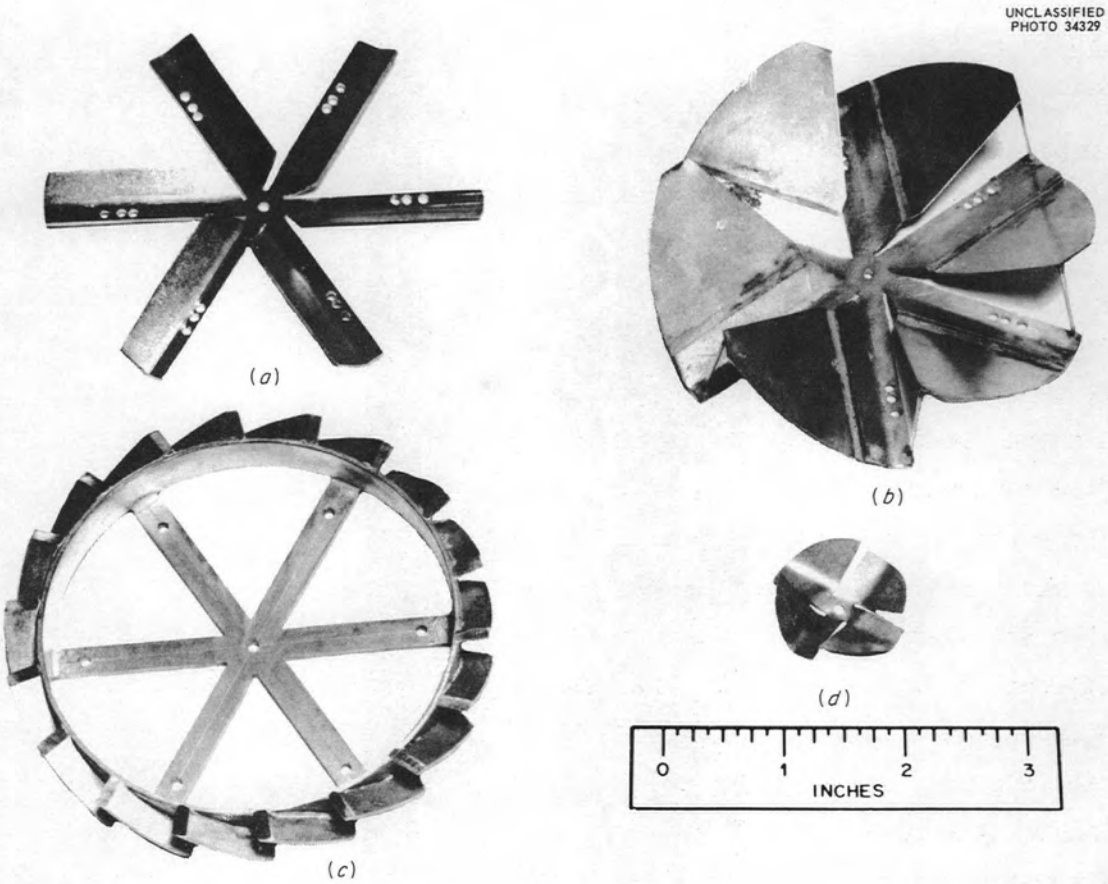


**Fig. 3.8. Swirl-Flow Generators for Flow Modification Studies.**

UNCLASSIFIED
PHOTO 45886

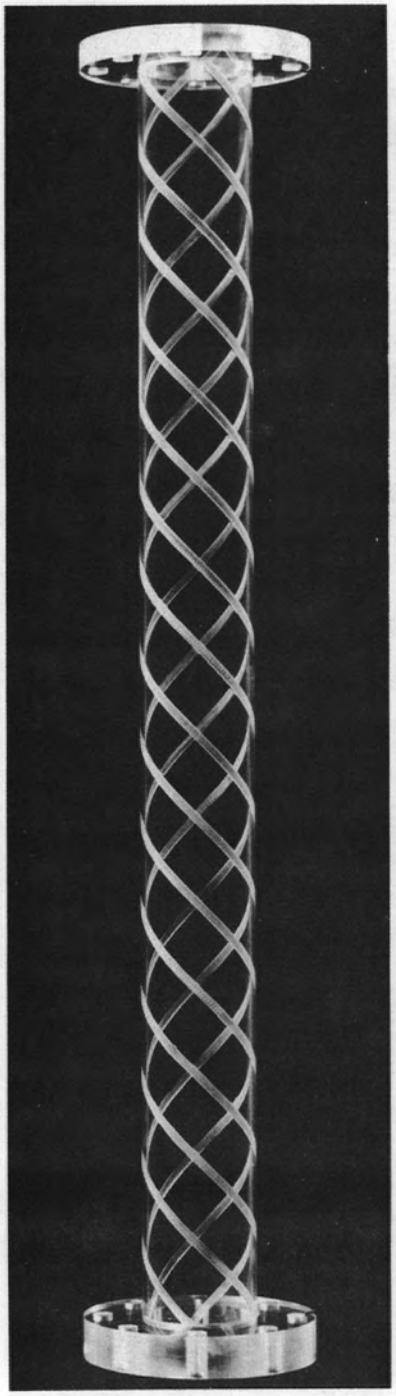

**Fig. 3.9. Helically Grooved Flow Channel.**

generator did not greatly increase the strength of the swirl flow but did add appreciably to the pressure drop. Investigations with the helically grooved channel are continuing.

## Resistance-Heated-Tube Heat-Transfer Experiment

The initial heat-transfer measurements[2] with an electrical-resistance-heated model of a single seven-rod tube cluster raised a question as to whether the observed asymmetries in the circumferential temperature profiles were representative of those to be expected in a reactor or were the result of the specific entrance conditions of this apparatus. To resolve this issue, the test unit entrance was modified by removing the V-shaped baffle. Circumferential temperature profile data for the new condition showed essentially no change in the shape or skewness of the profile; the results of run B-268 without the baffle are compared in Fig. 3.10 with the results of run A-232 with the baffle in place. A significant change was found in the maximum-to-minimum temperature difference. Since the flow and power generation in the two runs were nearly identical, it is difficult to explain the decreased temperature difference.

In view of these results, the entrance was further altered by covering completely the lower 92% of the cylindrical distribution screen. The restrictive weir thus formed forced the flow to "spill" uniformly around the periphery of the inlet region. The results of run C-51 with this weir in place are also plotted in Fig. 3.10. Again, there appears to be no change in the appearance of the temperature profile. Since the total head available was limited by the characteristics of the air blower, the additional pressure drop caused by the weir resulted in a decrease in the flow of approximately 19%. This in part explains the increased temperature differences for run C-51 in comparison with those for run A-232 at the same power generation.

Following several preliminary runs with the weir entrance, an inconsistency noted in the data led to shutdown of the apparatus and eventual disassembly of the test section. The tubes that were removed

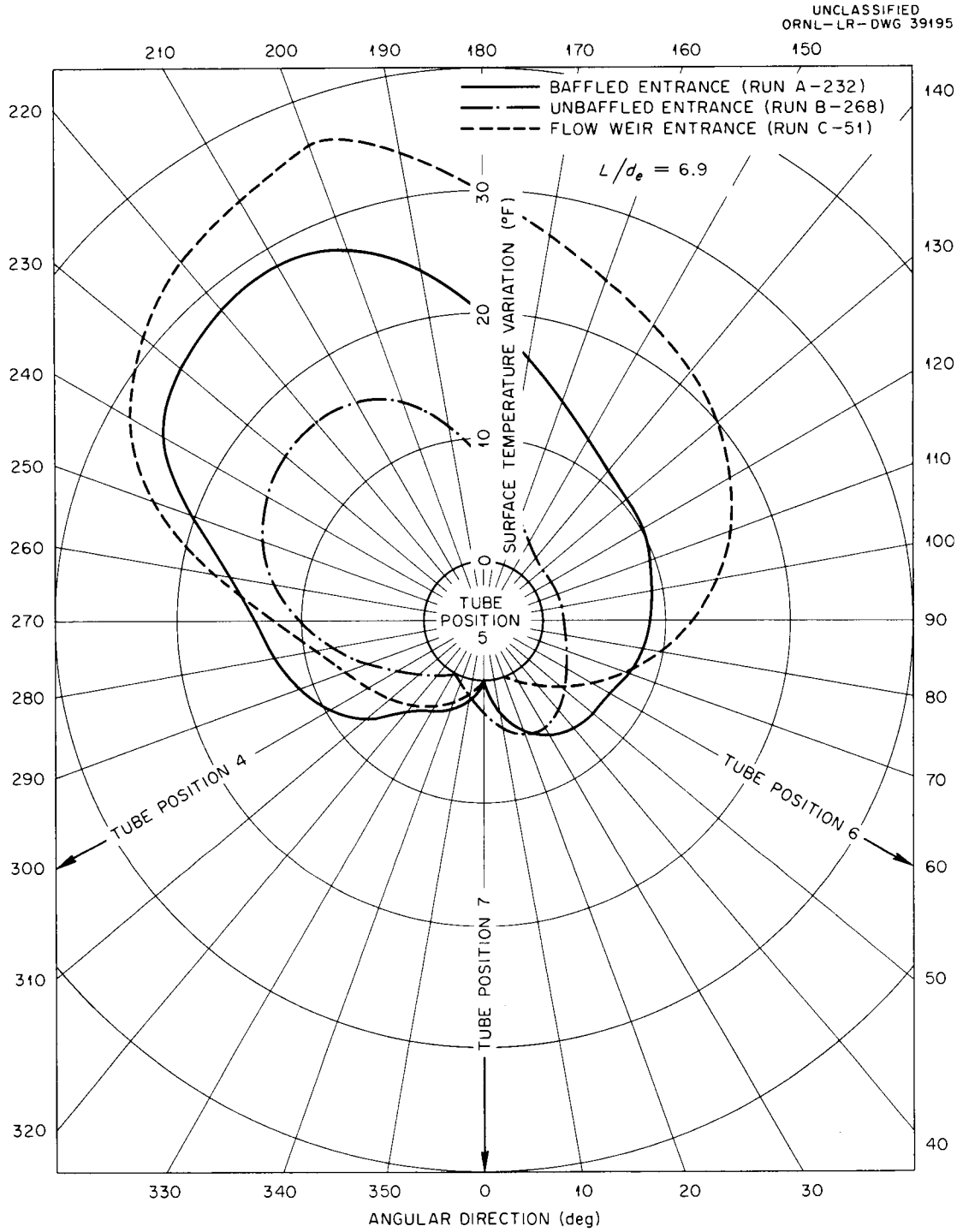


**Fig. 3.10. Comparison of Circumferential Temperature Profiles Obtained in Resistance-Heated-Tube Experiments for Several Entrance Geometries.**

are shown in their original orientation in Figs. 3.11 and 3.12. The extensive damage to the test unit is apparent in these photographs. Considerable evidence of tube-to-tube and tube-to-channel wall contact was found. Tubes 1 and 6 (power terminal tubes) were most severely affected, with the major amount of the damage occurring in the central region of the tubes. In several areas on these two tubes, portions of the tube wall adjacent to other tubes or to the graphite channel wall had melted completely and left holes as large as 3/8 in. wide and 3 in. long. Several such regions are visible in Fig. 3.11. All seven tubes showed arcing damage (surface craters and small perforations) from contact with all possible adjacent surfaces. In addition, the tubes retained permanent warpage (see Fig. 3.12), with displacements of as much as 1/4 in. from the original tube centerline.

The white rings marked on tubes 3 and 5 in Figs. 3.11 and 3.12 indicate the positions at which circumferential temperature traverses had been made. Strangely, only minor damage exists at these locations, so it is difficult to establish whether the arcing had been restricted to the final tests (series C) or had occurred progressively through the earlier studies (series A and B).

In attempting to ascertain the cause of the apparatus failure, the following possibilities were considered in detail: (1) initial deformation of the tubes during installation of the electrical connectors after insertion of the tubes into the graphite channel, (2) lack of longitudinal thermal expansion relief because of undue rigidity imparted to the cluster by the electrical connectors, (3) excessive stressing of the tubes as the result of the on-off cycles of normal operation, (4) thermal relief of original stresses in the tubing, (5) deflection of the tubing under the fields associated with the flow of a current through a conductor, (6) uneven $I^2R$ heating because of dimensional variations in the tube wall thickness, (7) maldistributions in the flow caused by the inlet header configuration, and (8) resonance with the 120-cps electrical power used in heating the tubes. It was concluded that, in themselves, each of these effects was too small to cause the damage

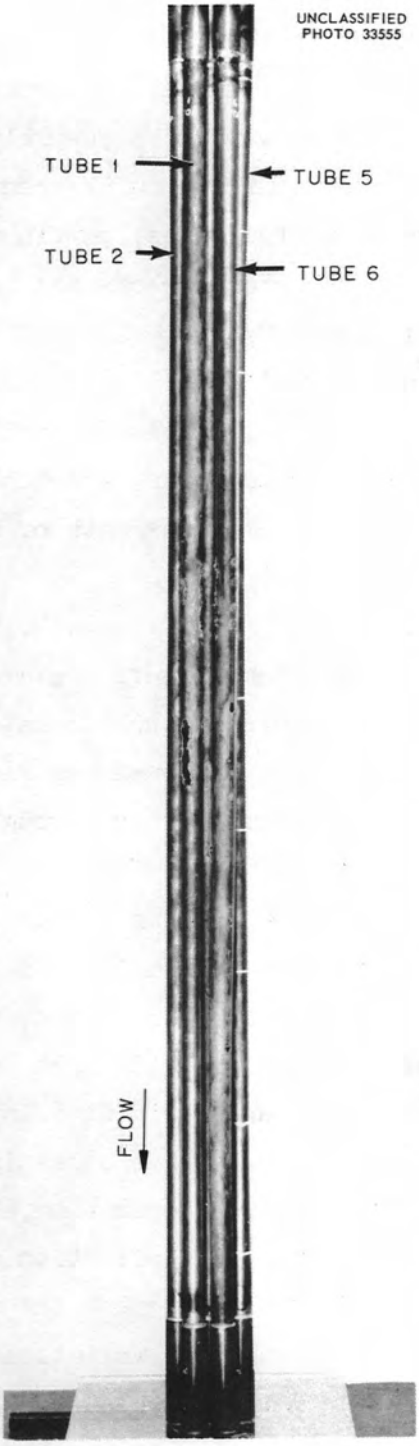


Fig. 3.11. Reassembled Tube Cluster Showing Areas of Maximum Damage.

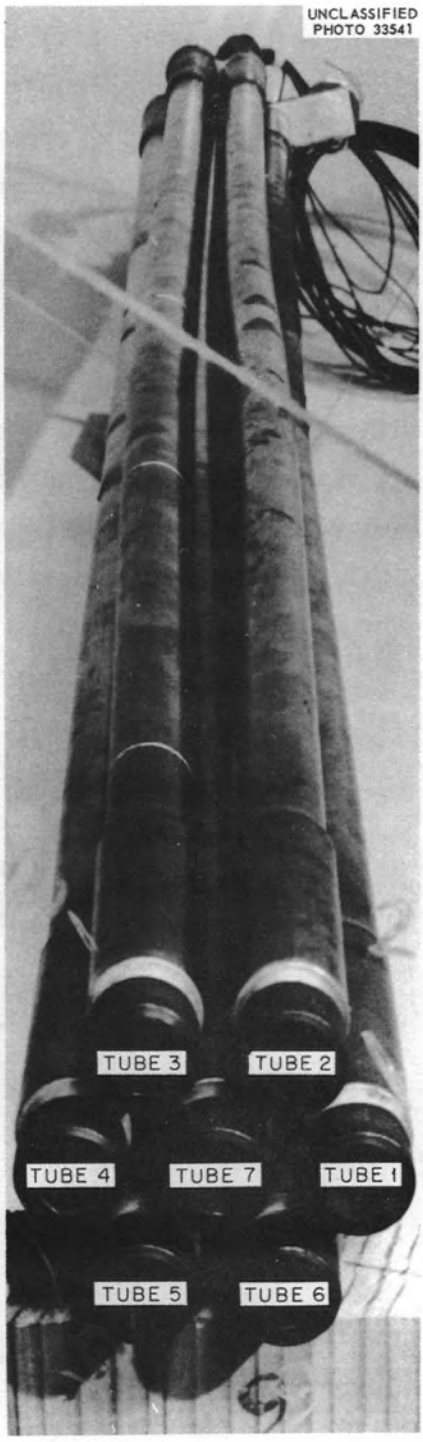


Fig. 3.12. Reassembled Tube Cluster Showing Typical Tube Warpage.

observed. In combination, however, they could result in system failure in the mode obtained. It should be noted that the eight factors listed above relate specifically to the experimental heat-transfer apparatus and are not to be expected in a reactor.

Prior to shutdown, the heat flux (approximately 7600 Btu/hr·ft$^2$) was the same as in the earlier studies. The Reynolds modulus, however, was somewhat lower (56,000 as compared to 69,000). It has been postulated that at the reduced flow the system was operating in a region of instability such that incremental increases in diametrical temperature differences gave rise to excessive bowing. The interaction between the bowing and the temperature difference across the tube diameter then amplified until contact and failure occurred. Conversely, it is supposed that a range of flow conditions exists such that the bowing vs temperature difference interaction is damped and the tube assumes a stable position (albeit displaced from its original position).

The experimental apparatus has therefore been modified in order to study the criteria for tube stability. (The modified apparatus will be referred to as the model-3 heat-transfer assembly.) Also, an effort has been made to eliminate or minimize the eight possible causes of failure discussed above. The 3.25-in.-ID graphite channel was replaced with a 3.83-in.-ID Pyrex tube so that the cluster could be observed during experimental operation. All tubing used was inspected for flaws by radiographic and ultrasonic techniques; the circumferential variation in the wall thickness was determined at 2-in. intervals along the length of the tube. The tubes were relocated on 1.372-in. centers to correspond to the $\gamma = 4$ ratio[3] existing in the Title I design of the EGCR. An adjustable spacer (see Fig. 3.13) was introduced at the

---

[3]The quantity $\gamma$ is a convenient parameter for comparing cluster geometries. It is defined as the ratio of the length of the inner ligament (distance between surfaces of the central and peripheral rods) to the length of the outer ligament (distance between the surfaces of the peripheral rods and the channel wall).

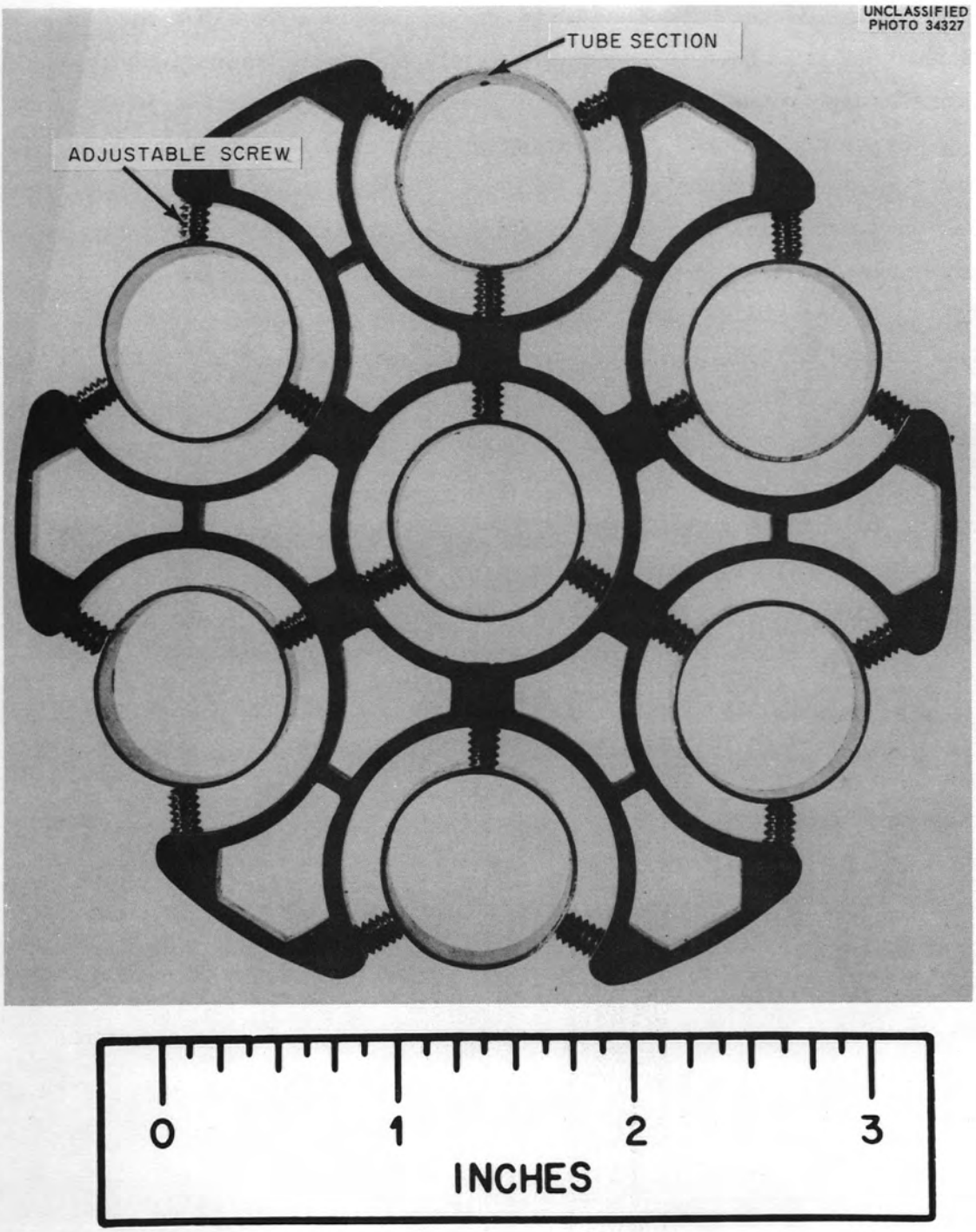


Fig. 3.13. Adjustable Tube Spacer for Use with Model-3 Heat-Transfer Assembly.

center of the tube bundle to enable prebowing of constant and known magnitude. The spacer was fabricated from a 1/4-in. stainless steel plate machined to provide maximum free-flow area (approximately 70% of that existing without the spacer) consistent with the necessary mechanical strength. Positioning of the tubes within the spacer is accomplished by a set of three screws for each of the seven tubes. The electrical connections were modified to provide a parallel, rather than series, circuit. At the spacer, all the tubes will be at the same voltage. Independent power supplies were used for each of the tubes so that the power generation can be adjusted to give any desired flux distribution. With this electrical arrangement, the voltage differences between tubes at any axial position will be small. Thus, if contact should take place, negligible arcing damage will occur. Diametrical temperature differences will be obtained using a probe containing two thermocouple junctions located 180° apart. Provision has been made for temperature probing of all seven tubes; two tubes can be investigated simultaneously if desired. An over-all view of the modified apparatus is presented in Fig. 3.14.

Initial operation of the model-3 heat-transfer assembly is in progress.

## Static Rod Bowing Experiment

The deflection of a single rod under varying diametrical temperature differences was determined to aid in the interpretation of the cluster bowing study described in the preceding section. The experimental system (illustrated in Fig. 3.15) was constructed from a 48-in. length of type 304 stainless steel tubing of 0.75-in. OD and 0.020-in. wall thickness. The unsupported length (between knife edges) was 45 in. A variable heat input was supplied to the top surface of the tube by an electrically insulated Nichrome ribbon cemented to the tube. Diametrically opposite this heater, a split 1/4-in.-OD plastic tube was sealed to the surface. Water flowing through this plastic tube, in direct contact with the metal surface, served as the heat sink. The

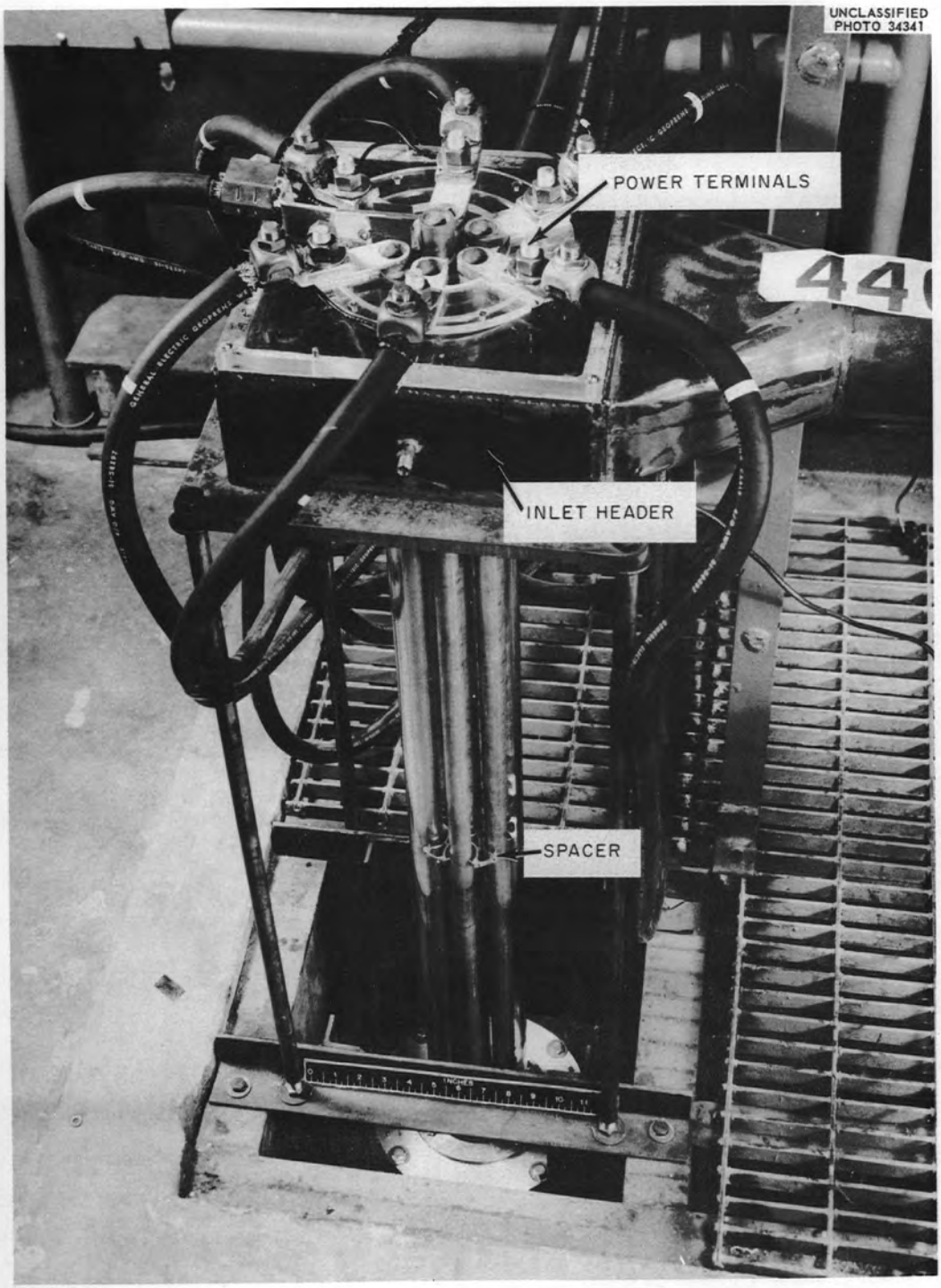


Fig. 3.14. Over-all View of Model-3 Heat-Transfer Assembly.

interior of the stainless steel tube was filled with Vermiculite to ensure heat flow through the tube wall only between the hot and cold strips; the entire apparatus was wrapped loosely with glass wool to minimize external heat losses. Surface temperature differences were measured by nine pairs of thermocouples welded to the tube outer surface adjacent to the heating and cooling strips and uniformly spaced along the unsupported length of the tube. Midsection deflections were established by using a cathetometer to observe the motion of a glass rod attached to the tube (see view A-A in Fig. 3.15).

If a weightless, circular cross-section rod or tube simply supported at each end is subjected to a constant linear temperature difference across a diameter (no internal stress condition), the rod will bow in the form of an arc of a circle. The displacement of the midsection of this rod is given by the equation,

$$\epsilon = \frac{d}{\alpha\,\Delta t}\left(1 - \cos\frac{l\alpha\,\Delta t}{2d}\right), \tag{11}$$

where d is the outside diameter; $l$, the unsupported length; $\Delta t$, the linear temperature difference; and $\alpha$, the linear coefficient of thermal expansion (all terms in consistent units). Using the first two terms of the cosine expansion, Eq. 11 can be approximated by

$$\epsilon = \frac{\alpha}{8}\,\frac{l^2}{d}\,\Delta t \quad . \tag{12}$$

Equation 12 has been used to predict the amount of fuel-rod bowing that will occur in the septafoil geometry under given temperature-difference conditions. If the temperature difference across the diameter is not linear, the center deflection will be different from that determined by Eq. 11. Since estimation of this deflection becomes difficult and tedious, the simple apparatus described above was designed to measure the bowing. In this experiment, a linear temperature gradient existed circumferentially that gave rise to an approximately sinusoidal component along the diameter.

The results of these measurements are shown in Fig. 3.16. For the conditions of the experiment ($\alpha = 9.6 \times 10^{-6}/°F$ for type 304 stainless steel[4] between 32 and 212°F), Eq. 12 can be written

$$\epsilon = 3.24 \times 10^{-3} \Delta t \quad , \tag{13}$$

where $\epsilon$ is given in inches and $\Delta t$ in °F. The experimental data were correlated by the equation

$$\epsilon = 2.84 \times 10^{-3} \Delta t \quad . \tag{14}$$

Midplane deflections are thus some 12% below those predicted by linear theory. For preliminary design evaluation, however, it appears satisfactory to use Eq. 12 for the thin-walled stainless steel cladding.

## Heat Transfer by Mass Transfer Measurements

The study of naphtahlene mass transfer in septafoil geometries for the estimation of heat transfer was continued.[5,6] The apparatus previously described was modified to attain increased experimental precision. An over-all view of the test section is presented in Fig. 3.17, and a closeup view is presented in Fig. 3.18. The unit was mounted vertically above the air-supply manifold, with the air flow upward through the section. The test cluster consisted of seven 24-in.-long, 1.0-in.-dia aluminum rods suspended within a 4.0-in.-ID Plexiglas channel. A naphthalene coating was applied to one of the rods (to be referred to as the "active" rod) over a 10 1/2-in. region beginning 11 in. from the upstream end of the cluster. The active rod was formed by chill-casting the naphthalene on a reduced-diameter section of the rod (59/64 in., lightly knurled). A fine-grained crystalline structure resulted. The coating was then machined

---

[4] Metals Handbook, 1948 ed., American Society for Metals, Cleveland, 1948, p 566.

[5] GCR Semiann. Prog. Rep. Dec. 31, 1958, ORNL-2676, p 47.

[6] J. L. Wantland and R. L. Miller, Heat Transfer in Septafoil Geometries by Mass Transfer Measurements, ORNL CF 59-6-9 (to be issued).

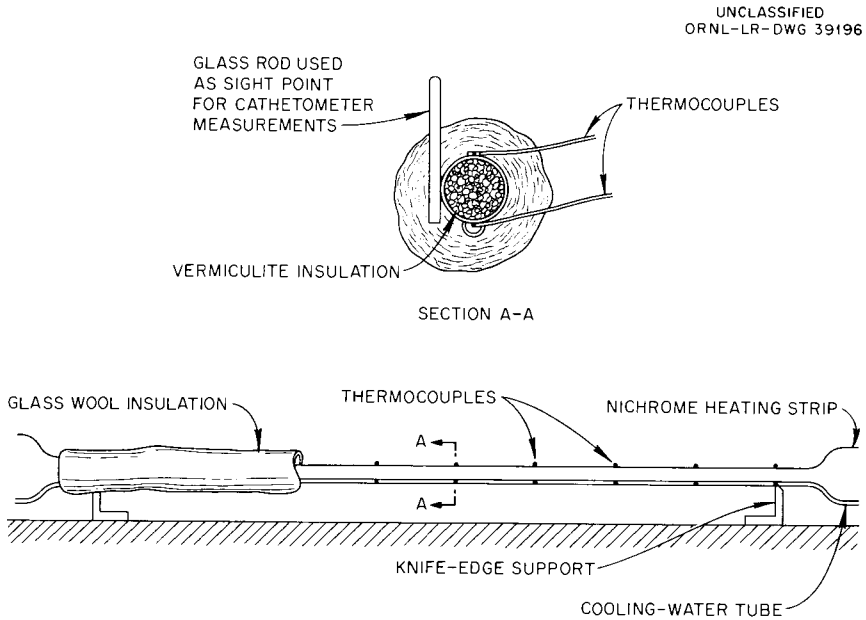


**Fig. 3.15. Diagram of Apparatus for Static Rod Bowing Experiment Shown with Insulation Partially Removed.**

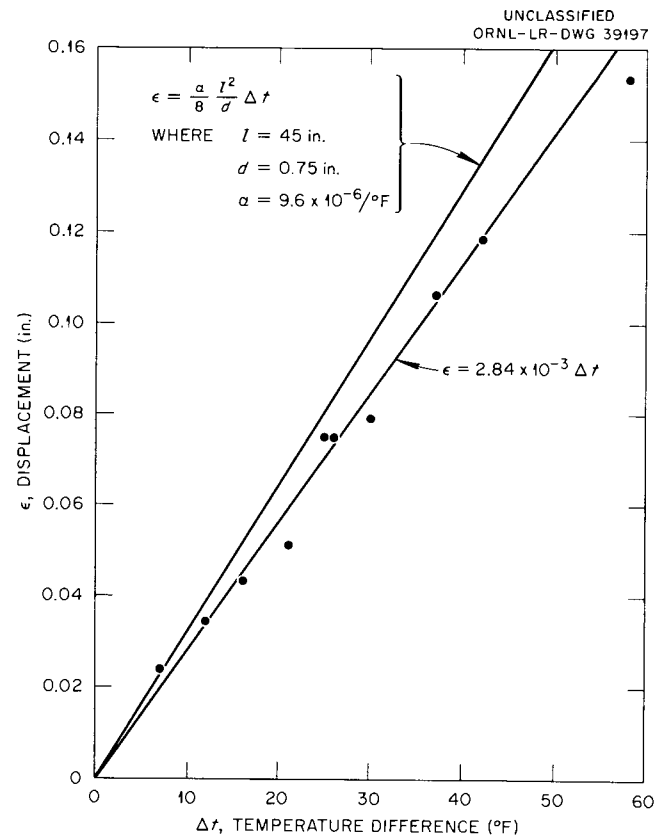


**Fig. 3.16. Experimental Results for the Central Deflection of a Tube with a Sinusoidal Diametrical Temperature Gradient.**

UNCLASSIFIED
PHOTO 33285

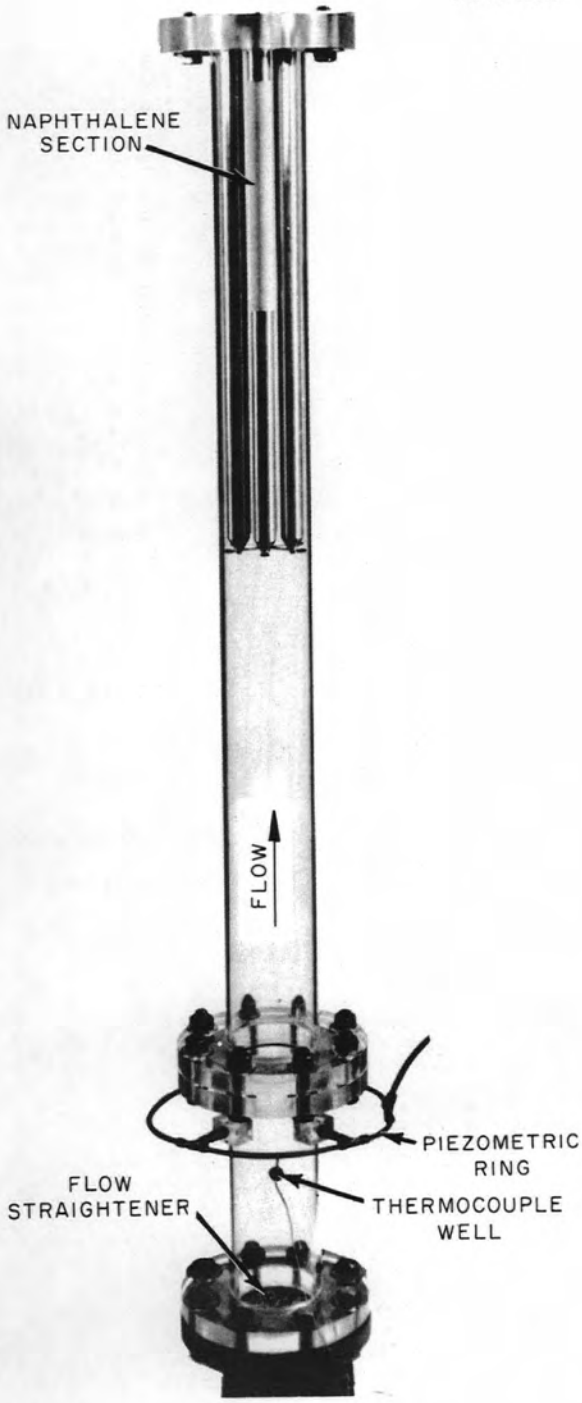


**Fig. 3.17. Mass-Transfer Test Section Shown Mounted in Flow Channel.**

UNCLASSIFIED
PHOTO 33286

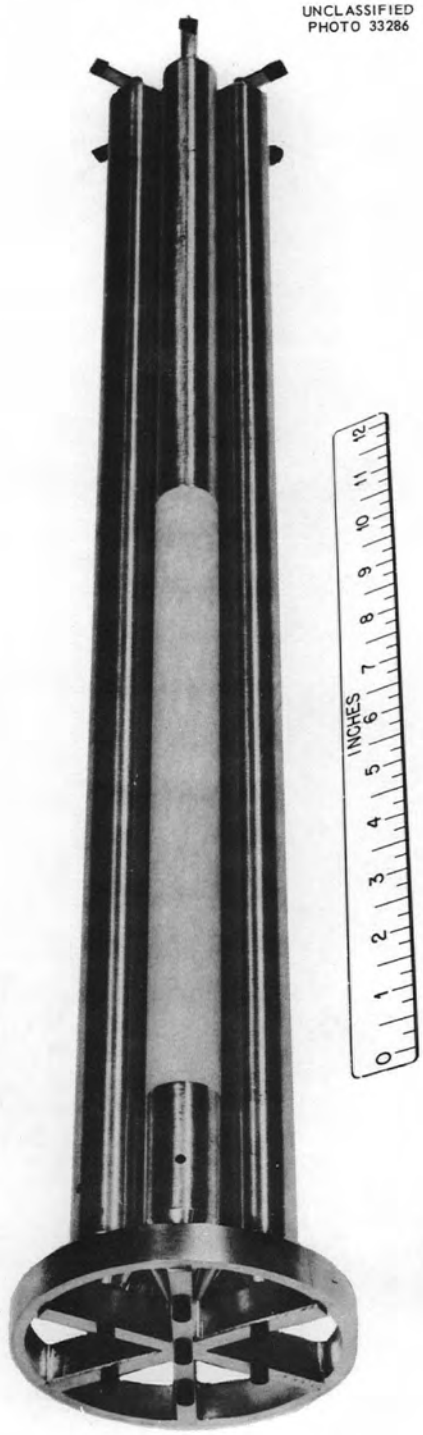


**Fig. 3.18. Rod Cluster with 1.10-in. Center-to-Center Spacing ($\gamma = \frac{1}{4}$).**

to the 1.0-in. diameter of the rest of the rod. A typical rod is shown in various stages of fabrication in Fig. 3.19.

The mass removal was determined by measuring changes in the rod radii at 5-deg intervals around the circumference for a position 9 1/2 in. from the start of the naphthalene coat. The measuring location was thus approximately 25 hydraulic diameters downstream of the hydrodynamic entrance and approximately 12 hydraulic diameters from the beginning of the mass transfer section. The profilometer is shown in Fig. 3.20.

Mass transfer data were obtained for three values of the $\gamma$ ratio:[3] 1/4, 1, and 4. These values correspond, respectively, to rod center-to-center spacings of 1.10, 1.25, and 1.40 in. At each spacing, duplicate runs were made with the active rod first in a peripheral position and then in the central position. In addition, the effect of a right-hand swirl on a peripheral rod at the $\gamma = 4$ location was studied. The maximum difference observed in repeat runs was 9%. In all the runs the Reynolds modulus was 60,000 ±4%.

A summary of the results, which were corrected to $N_{Re} = 60{,}000$ by using the relation $\bar{j}_r \sim N_{Re}^{-0.2}$ and were averaged for the duplicate runs, is presented in Table 3.1. In this table, $\bar{j}_r$ is the mean mass transfer factor for a rod, $j_l$ is the local mass transfer factor, and $\bar{j}_c$ is the mean factor for the entire channel as calculated from

$$\bar{j}_c = \left[6\ \bar{j}_r\ (\text{outer rod}) + \bar{j}_r\ (\text{central rod})\right]/7 \quad . \qquad (15)$$

The deviation of $\bar{j}_r$ and $\bar{j}_c$ from the value $\bar{j} = 0.00255$, calculated from the equation

$$\bar{j} = 0.023\ N_{Re}^{-0.2} \qquad (16)$$

at a Reynolds modulus of 60,000, is also tabulated. Finally, the results are given in graphical form (as the ratios $j_l/\bar{j}_r$ and $j_l/\bar{j}_c$) in Figs. 3.21 through 3.24. Since, by analogy, the mass transfer j-factor is equated to the heat transfer j-factor, these figures can be interpreted as describing the variation in heat transfer around the circumference of any rod.

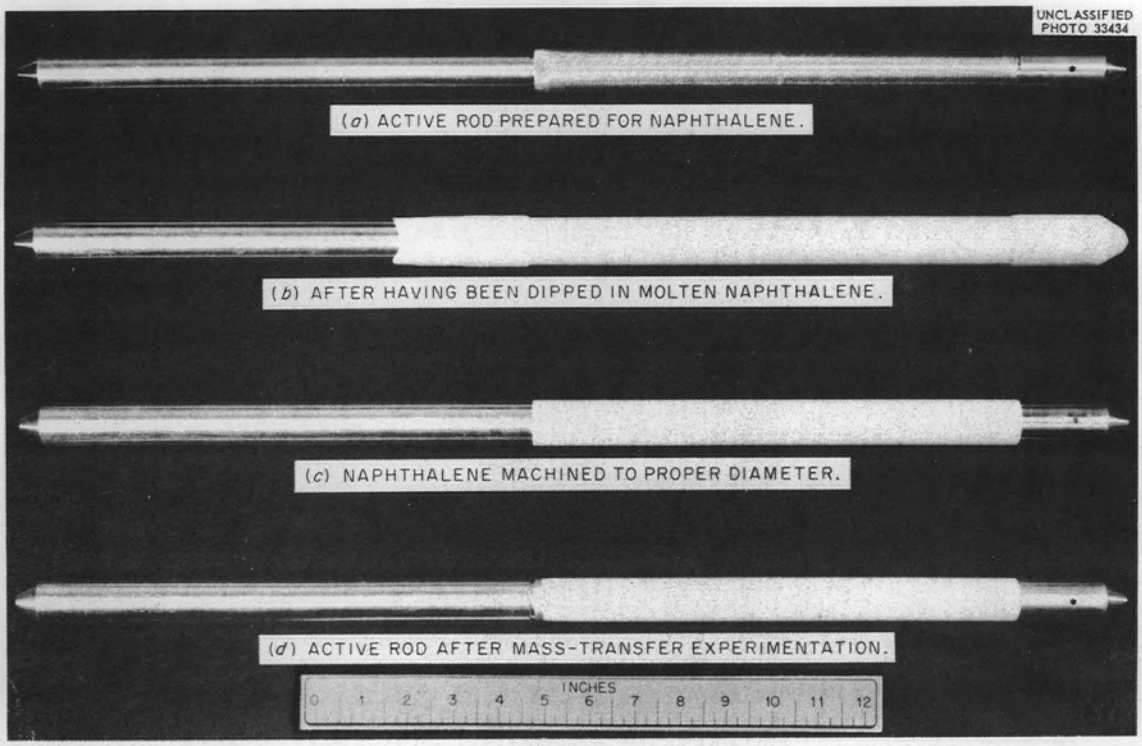


**Fig. 3.19. Active Rod in Various Stages of Fabrication and Exposure.**

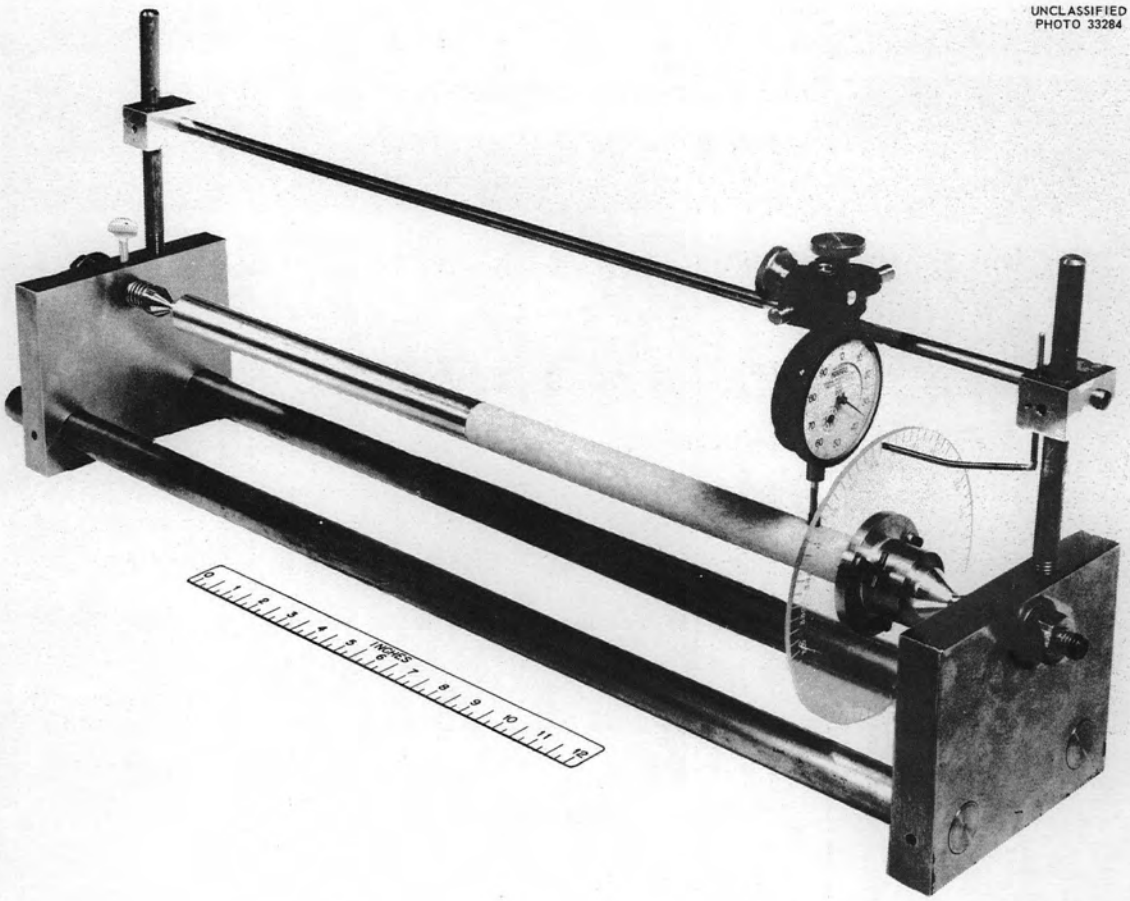


**Fig. 3.20. Active Rod Being Traversed in the Profilometer.**

Table 3.1. Average Mass-Transfer Factors Corrected to $N_{Re} = 60{,}000$

| Run No. | $\gamma$ | Active Rod | $\bar{j}_r$ | Deviation from $\bar{j}_r = 0.00255$ (%) | $\bar{j}_c$ | Deviation from $\bar{j}_c = 0.00255$ (%) | $\bar{j}_r/\bar{j}_c$ | $j_l/j_r$ (max) | $j_l/j_r$ (min) | $j_l/\bar{j}_c$ (max) | $j_l/\bar{j}_c$ (min) |
|---|---|---|---|---|---|---|---|---|---|---|---|
| 1 | 4 | Outer | 0.00313 | +22.7 | 0.00314 | +23.1 | 1.00 | 1.13 | 0.73 | 1.13 | 0.73 |
| 2 | 4 | Central | 0.00323 | +26.7 | | | 1.03 | 1.04 | 0.96 | 1.07 | 0.99 |
| 3 | 1 | Outer | 0.00377 | +47.8 | 0.00368 | +44.3 | 1.02 | 1.10 | 0.93 | 1.12 | 0.95 |
| 4 | 1 | Central | 0.00316 | +23.9 | | | 0.86 | 1.04 | 0.95 | 0.89 | 0.82 |
| 5 | 1/4 | Outer | 0.00300 | +17.6 | 0.00288 | +12.9 | 1.04 | 1.28 | 0.71 | 1.33 | 0.74 |
| 6 | 1/4 | Central | 0.00216 | −15.3 | | | 0.75 | 1.12 | 0.88 | 0.84 | 0.66 |
| 7* | 4 | Outer | 0.00362 | +42.0 | | | | 1.11 | 0.71 | | |

*With swirl generator.

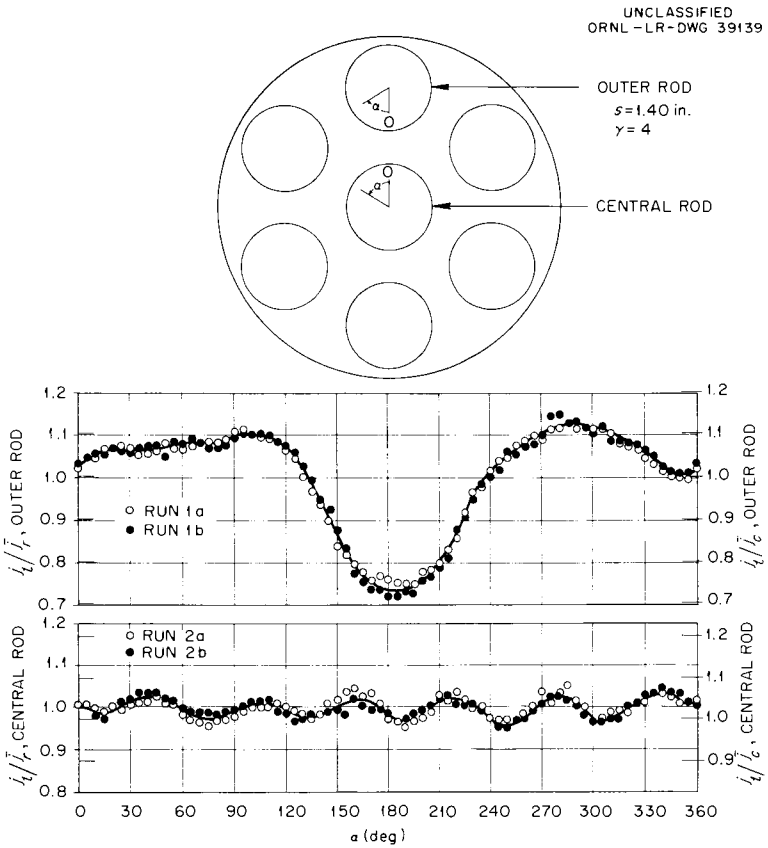


**Fig. 3.21. Local Mass-Transfer Factor Ratios for the 1.40-in. Center-to-Center Rod Spacing ($\gamma = 4$).**

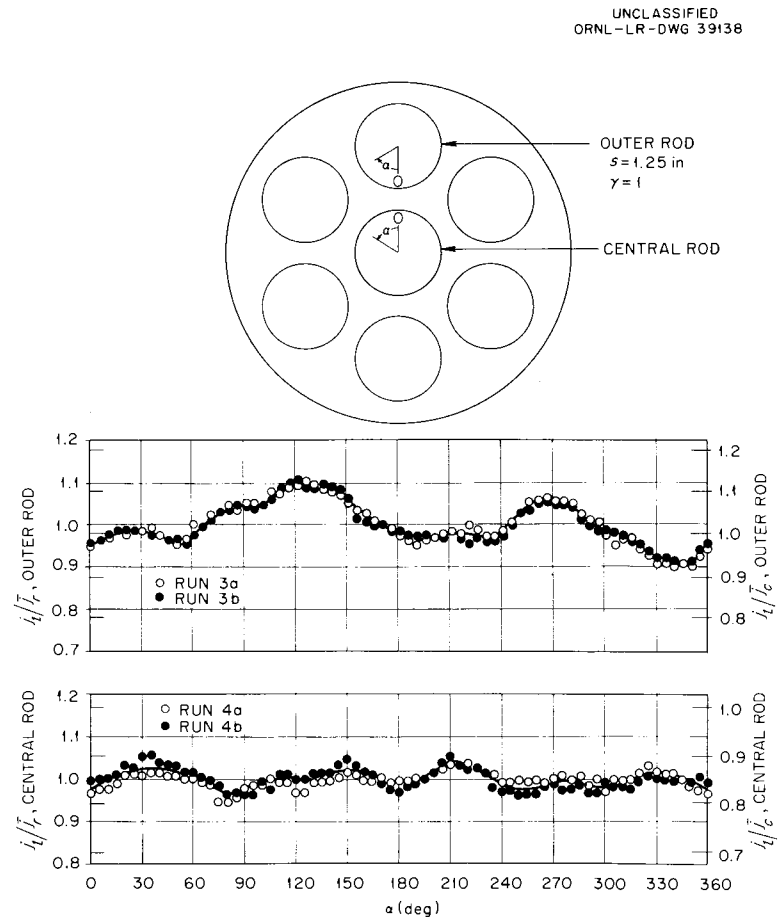


**Fig. 3.22. Local Mass-Transfer Factor Ratios for the 1.25-in. Center-to-Center Rod Spacing ($\gamma = 1$).**

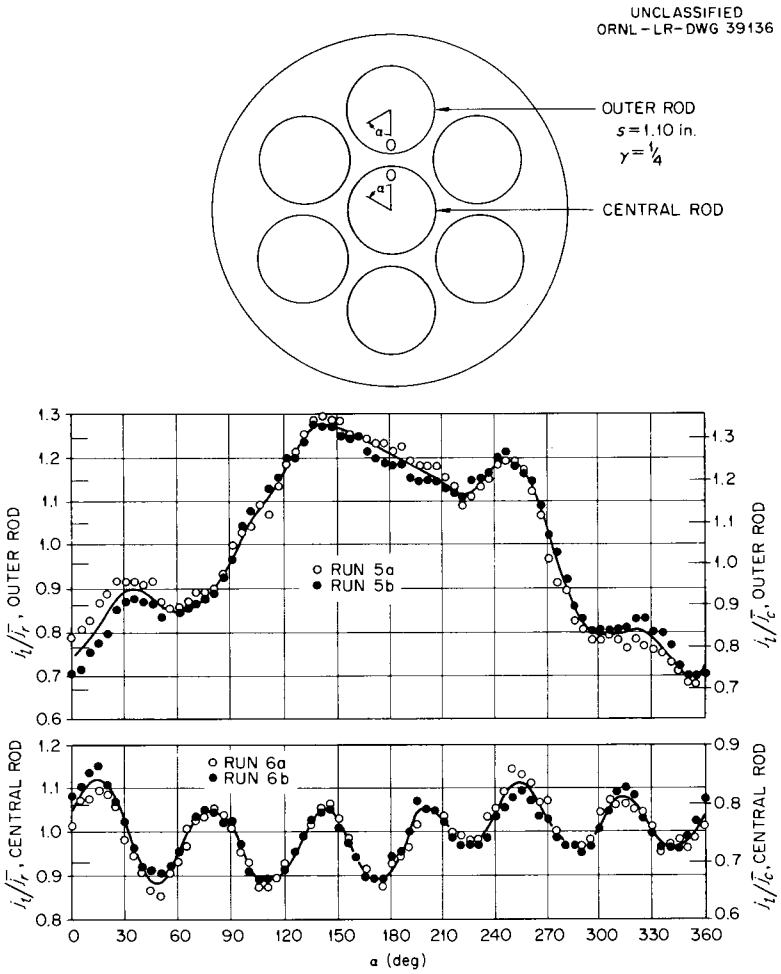


**Fig. 3.23. Local Mass-Transfer Factor Ratios for the 1.10-in. Center-to-Center Rod Spacing ($\gamma = 1/4$).**

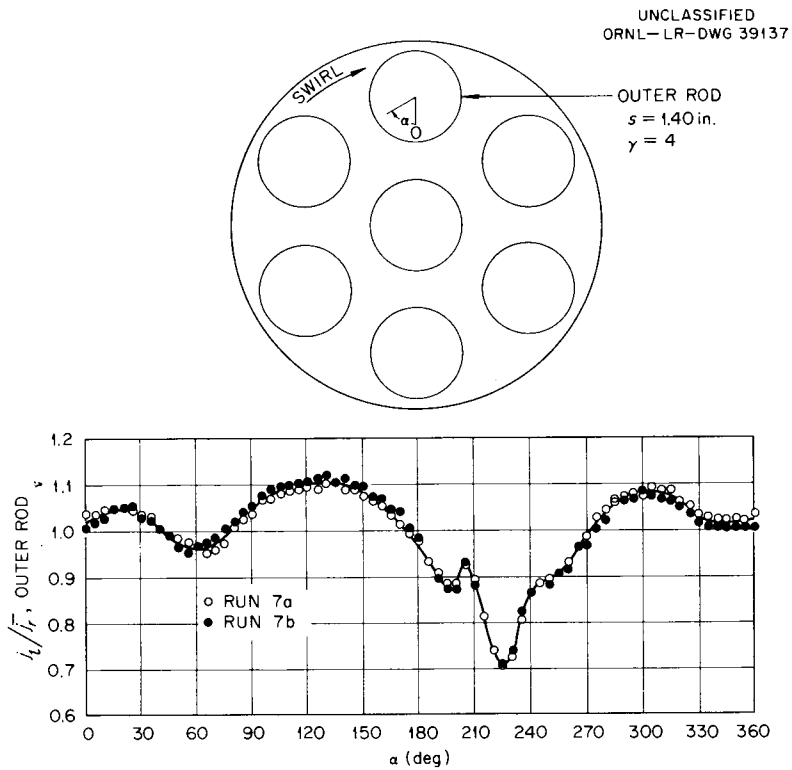


**Fig. 3.24. Outer Rod Local Mass-Transfer Factor Ratios for the 1.40-in. Center-to-Center Spacing ($\gamma = 4$) with Right-Hand Helical-Swirl Generator.**

In general, the results agreed with preliminary qualitative predictions. Thus, for the central rod, $j_l/\bar{j}_r$ showed an approximately sinusoidal variation with an amplitude which increased as the peripheral rods were moved closer to the central rod. The minimums on these curves (j-ratios less than one), corresponding very closely to the points of closest proximity of adjacent tubes, indicate the reduction in heat transfer (mass transfer) caused by pinching of the air flow. The data for the peripheral rod show similar, though more pronounced, variations. Comparing the results of the peripheral and central rods on a common basis (using the $j_l/\bar{j}_c$ ordinate of Figs. 3.21, 3.22, and 3.23), it is found that equivalent heat transfer occurs in equivalent flow regions. By way of example, both the outer and central rods in Fig. 3.23 show a value of $j_l/\bar{j}_c$ of approximately 0.825 for the peak in the vicinity of 300°. The slight displacement of this maximum from the 300° location is probably due to an asymmetry in the flow induced by the entrance to the unit or by the positioning of the cluster within the channel. Deviations of this nature are to be expected also for a fuel cluster located within a reactor.

The final two columns of Table 3.1 give the total spread observed in $j_l/\bar{j}_c$. Thus, for $\gamma = 4$, the total variation was ±20 around a mean (0.73 to 1.13). Similarly, at $\gamma = 1/4$, the variation was ±33%; and at $\gamma = 1$, ±15%. Since it is desirable to have a minimum variation in the heat transfer (as discussed in a preceding section of this chapter), the optimum spacing appears to be in the vicinity of $\gamma = 1$. It is further to be noted that the over-all heat transfer, as measured by $\bar{j}_c$, has a maximum value for this same spacing ratio. The pressure loss, a third factor of importance in establishing the best spacing ratio, has been shown[1] to be independent of the rod spacing for values of $\gamma \leq 4.1$.

Several other factors should also be considered in establishing the ideal rod spacing, such as the effect of nuclear self-shielding and the effect of nonuniform gas temperature distributions at the inlet to a cluster. Estimates indicate that the power generation in

the central rod will, on the average, be less than in the peripheral rods. Further, there will exist a variation in the generation in the peripheral rods themselves, being lower in the regions closer to the cluster center. Looking again at the data for the spacing ratio $\gamma = 1$, it is seen that the ratio $j_l/\bar{j}_c$ is higher for a peripheral rod ($1.04 \pm 0.08$) than for the central rod ($0.85 \pm 0.03$); thus it appears that there is better heat transfer from the peripheral rods than from the central rod. Further, from Fig. 3.22, it appears that the average heat transfer of a peripheral rod is somewhat higher on the outer surface ($\alpha$ between 60° and 300°) than on the inner surface ($\alpha = \pm 60°$). Since anticipated inlet temperature variations cannot be easily duplicated in the mass transfer system, it is proposed to investigate this aspect of the problem in the future heat-transfer studies.

The data of Fig. 3.24, obtained with a swirl generator at the inlet, show a 16% increase in $\bar{j}_r$ for a peripheral rod at a spacing of $\gamma = 4$ over that found with straight-through flow. At the same time, however, there was an appreciable increase in the pressure loss. It is of interest to note that the over-all variation in the ratio $j_l/\bar{j}_r$ was essentially the same as with the straight-through flow (see Table 3.1). Detailed examination of Fig. 3.24, in comparison with Fig. 3.21, shows an abrupt rise in $j_l/\bar{j}_r$ at $\alpha = 205°$ followed by a sharp minimum at $\alpha = 225°$. This can be explained in terms of the high turbulence occurring in the region immediately downstream of the separation of the swirl-flow from the surface and the stagnation existing in the lee of the rod. This result corroborates the earlier data obtained using cotton threads for flow visualization.

The mean mass-transfer factors obtained experimentally are significantly higher than those predicted by Eq. 16 (as high as 48% in one case). This may result from the measuring technique or from additional sublimation during the time necessary for operations such as introducing and adjusting the rod bundle in the channel, removing the bundle, and setting the bundle up for profilometer traverses.

Subsidiary experiments are in progress to establish the magnitude of the latter effect. New techniques that will allow more rapid determination of the mass removal are also being developed.

## 4. ADVISORY SERVICE TO THE AEC

### Review of PEGCPR Design

The ORNL advisory group established to assist the Idaho Operations Office completed its consulting work in connection with the Title I design[1] of the prototype enriched-uranium gas-cooled power reactor (PEGCPR) prepared by personnel of Kaiser Engineers and Allis-Chalmers. A complete review of all design studies, specifications, and drawings was carried out in connection with this work that was followed by a comprehensive oral discussion of the design at Oakland, California, during the period of February 9 to 13, 1959. The purpose of the review work was to make certain that all major areas of significance to the reactor plant design had been examined, to establish a course of action for the resolution of all unsolved problems, to establish a well-defined and adequate research and development program for the PEGCPR, and to identify and bring to the attention of the AEC those uncertainties in the concept which would affect the ultimate success of the design.

The uncertainties in the design which should be resolved were found to include the possible thermal instability of the fuel elements under certain design conditions, the possibilities of fission-gas release from the $UO_2$ pellets, structural problems in the graphite core, mechanical problems in the fuel-handling mechanism, controls problems which affect reactor safety, and nuclear performance characteristics of the core, particularly with respect to control rod programing.

### EGCR Experimental Facilities Evaluation

Following completion of ORNL participation in the review of the KE-ACF Title I design of the PEGCPR in Oakland, a study was undertaken to define and evaluate possible modifications to that design which would

[1] Kaiser Engineers and Nuclear Products-Erco Division of ACF Industries, 30,000 kw Prototype Partially Enriched Uranium Nuclear Power Plant, IDO-24027 (March 1959).

substantially improve its utility as an experimental facility without grossly changing the basic design. This effort resulted in the recommendation that provisions be made for installation of stainless steel tubes through the reactor core to which external piping could be connected to complete in-pile test loop facilities completely isolated from the reactor coolant system. Experimental facilities of this type were recommended both because they are compatible with the reactor design and because they will be of value in testing the various fuel elements being considered for gas-cooled reactors. The closed loops will be of particular value for studying unclad elements and for testing clad elements to failure.

Following the AEC decision to construct a modified version of the KE-ACF designed plant in Oak Ridge, the designation was changed to EGCR (Experimental Gas-Cooled Reactor) and representatives of KE, AC, ORNL, and AEC-ORO convened in Oak Ridge to discuss the design modifications required to provide the aforementioned test tubes through the reactor core. All concerned agreed that four large and four small tubes could be installed in the core of the EGCR and fitted for future extensions of loop piping from the top and bottom ends of the tube to experimental equipment cells. The large and small tubes will be about 9 in. and 5 in. in diameter, respectively. The uncertainties relative to stainless steel behavior at high integrated radiation exposures prompted the group to specify that the eight tubes be replaceable, and design work is proceeding in conformance with this requirement.

Core physics calculations (see Chap. 2, this report) were made to determine the effects of the eight stainless steel tubes in the core on operation of the reactor, and it was shown that the core design power level of about 85 Mw(th) could still be maintained. The four larger tubes will be placed symmetrically around the perimeter of the core, and they will tend to reduce the effectiveness of the reflector. Consequently the slope of the radial flux gradient will be steeper. The four smaller tubes to be located symmetrically about and close to the core centerline will reduce the flux at the center of the reactor

and tend to flatten the radial flux gradient.

A group of completely self-contained below-grade experimental equipment cells will be arranged in an arc around the perimeter of the cylindrical reactor containment vessel to house coolant blowers, heat exchangers, and other test loop equipment. Building floor space for experimental control rooms will be provided adjacent to the main plant control room, and an instrument tunnel will be provided between the control room floor space and the experimental equipment cells. Inside the containment vessel, covered trenches and shielded pipe chases will be provided for future routing of the experimental coolant lines from the experimental tubes to the experimental equipment cells.

## EGCR Hazards Evaluation

The EGCR Preliminary Hazards Summary Report was prepared by KE and AC personnel with the assistance of AEC-ORO and ORNL personnel during the first two weeks of May. The most outstanding feature of the design from the safety viewpoint is the inclusion of a containment vessel for the reactor and steam generating portions of the plant. The inclusion of the container was not dictated by the known hazards associated with the operation of this type of reactor as a power reactor prototype but, rather, by the desired experimental capabilities of the plant. As mentioned in the preceding section, the plant will contain eight experimental loops, and each loop will be capable of operating with unclad fuel elements with a total heat generation capacity of 10 Mw.

The many uncertainties involved in the calculation of radiation exposure from a postulated accident frequently led to gross conservatism in the design of the system. In order that the dose calculations for the EGCR be reasonable and yet on the conservative side, the following assumptions were recommended as the bases for the exposure calculations: (1) The maximum amount of activity that could be released is that associated with the experimental loops, not the reactor. (2) As a consequence of a loss of coolant accident which would result in the

melting of the experimental fuel elements, 100% of the volatile activity and 10% of the nonvolatile activity would be released. (3) The meteorological parameters, as typified by the diffusion constants and wind speeds, for conditions which exist >>50% of the time are conservative. (4) The total body exposure at the nearest approach of uncontrolled land (or at the point of maximum ground concentration if further away) should be no more than 25 r during the first 8 hr after an accident. The allowable leakage rates for the EGCR and the experimental loop containment structures were based on these assumptions.

Potential hazards, such as the pressure buildup in the fuel capsules, the pressure differential across various components in the system as a consequence of a primary system rupture, and the decrease in flow through the reactor as a consequence of reactor seal failure, have been noted but not yet resolved. In particular, the problem of the calculation of the pressure differential across system components is being set up for analysis on the ORNL analog simulator. Preliminary results indicate that the peak pressure drop across the core following a single-ended pipe failure will be slightly less than the pressure required to lift the core or core components.

In conjunction with AEC-ORO personnel, criteria have been established for radiation levels for the various operations and for the instrumentation required to monitor the activity in question. Normal activity releases to the environment from the plant will be 0.1 mpc. A retention pit will be required for the holdup of liquid wastes which will be capable of discharging activity either to the river, if the activity level is low enough, or to portable tanks for transportation to the ORNL waste disposal facilities.

# Part 2. Materials Research and Testing

# 5. METALLURGICAL DEVELOPMENTS

## Bulk $UO_2$ Fuel Material

### $UO_2$ Processing and Fabrication

The possibility of eliminating machining, and its attendant cost, from the fabrication of $UO_2$ shapes is, as indicated in the previous report,[1] directly related to the reproducibility of the powder. The process for making a reproducible $UO_2$ powder has progressed through a double-precipitation batch process and a double-calcination continuous process to a single-calcination continuous process. The single-calcination process was studied in the interest of making the over-all conversion process as simple and economical as possible. Work on this process was started as soon as it was determined that a high-quality and moderately reproducible powder could be made by the double-calcination process and before attempting to work out complete control of the variables in the double process. After several experimental runs, a powder was obtained that had all the characteristics and qualities of the best powders made by the double-calcination process. Attempts to reproduce this powder ended in failure, however, and, because of the shortage of time and the need to use the equipment to produce usable powder for pellet fabrication, further work on a single-calcination process has been deferred.

Batches of $UO_2$ powder are being produced at present by the continuous double-calcination process, and, although these powders are being produced to fill orders, the lots of different sizes and enrichments are serving very well for the reproducibility study. Batch sizes have ranged from 10 to 53 kg. When fabricated under the standard conditions of prepressing at 15,000 psi, forming at 7500 psi, and sintering at 1750°C for 1 hr, the densities of the pellets made from these powders have ranged from 93 to 95% of theoretical, as indicated in Table 5.1. These were all considered to be good batches,

[1] GCR Semiann. Prog. Rep. Dec. 31, 1958, ORNL-2676, p 67.

Table 5.1. Reproducibility of Sintered Density of Pellets Made from Three Batches of $UO_2$ Powder

| Oxide Powder Batch No. | Sintered Density of Pellet (% of theoretical) | Remarks |
|---|---|---|
| 156 | 94.3 | Pellet made from powder taken from first day's run |
| 156-1 | 94.2 | Second day's run |
| 156-2 | 95.3 | Third day's run |
| 156-3 | 93.0 | Fourth day's run |
| 156-4 | 94.5 | Blend of all runs for oxide batch No. 156 |
| 157 | 93.8 | |
| 161 | 93.8 | First day's run |
| 161-A | 93.3 | Second day's run |
| 161-B | 93.6 | Blend of all runs for oxide batch No. 161 |

but the reproducibility of the density is not as good as is wanted. At present, the powder variations are ascribed to variations in the reoxidation step. The equipment is being modified to control this step of the process more closely. The modified unit should be in operation soon and will be used initially on 25- and 100-kg batches.

More than 1800 pellets of various sizes and enrichments have been fabricated. Most of these, approximately 1400, were prepared for the irradiation experiments; the remainder were made for sintering tests to determine the reproducibility of oxide properties.

Several capsules scheduled for irradiation will contain $UO_2$ pellets with a nominal density of 75% of theoretical. These pellets should be sintered at a high temperature so that additional sintering will not occur rapidly during irradiation and so that individual crystallites will grow to a size large enough to retain much of the fission-product gases. Several techniques have been developed for fabrication of these

pellets and have been evaluated on the basis of pellet quality and economy of fabrication. The technique that produces the strongest pellets has involved using a carefully sized, dead-burned oxide. This technique has been rejected, however, in favor of a technique that utilizes a second high-temperature calcination to reduce the activity of the highly active oxide powder. This calcination step reduces the activity just enough so that a pellet with the required density can be produced without having to grind or size the material and without having to modify the standard fabrication technique.

Thermal Conductivity of $UO_2$

A number of thermal-conductivity measurements of sintered $UO_2$ under various conditions have been made at several different installations and by different methods. The spread in the values of several of the investigators, Ross,[2] Kingery,[3] Englander,[4] Scott,[5] Hedge and Fieldhouse,[6] and Eichenberg,[7] varies from ±66% in the 0 to 200°C temperature range to ±16% at 1000°C. Some of the variables in these measurements are methods of fabrication of material and specimens, stoichiometry of the material, and irradiation effects, as well as fundamental differences in methods of measurement. There are, at present, many uncertainties in the variables which must be evaluated before more correct values for the thermal conductivity of $UO_2$ fuel pellets can be selected.

---

[2] A. M. Ross, A Literature Survey on the Measurement of Thermal Conductivity of Several Solids Including Uranium Dioxide, CRFD-762 (March 1958).

[3] W. D. Kingery, J. Am. Ceramic Soc. 37(2), 108 (Feb. 1954).

[4] M. Englander, Note on Measurement of Thermal Conductivity of Sintered Uranium Dioxide, CEA-79 (June 1951).

[5] R. Scott, Thermal Conductivity of $UO_2$, AERE-M/R-2526 (March 1958).

[6] J. C. Hedge and I. B. Fieldhouse, Measurement of Thermal Conductivity of Uranium Oxide, AECU-3381 (Sept. 20, 1956).

[7] J. D. Eichenberg, An In-Pile Measurement of the Effective Thermal Conductivity of $UO_2$, WAPD-200 (Sept. 1958).

## High-Temperature Compression Testing of $UO_2$

In an effort to obtain cursory data on the high-temperature-deformation properties of $UO_2$, a hot-load test was initiated. In this test, high-density $UO_2$ bushings were compressed in a graphite die while being heated by induction in a self-generated CO atmosphere. Specimens were tested at 1200, 1500, 1800, and 2000°C under a pressure of 1000 psi for 1 hr. The specimen tested at 1200°C showed no measurable change. The inside and outside diameters of the specimen tested at 1500°C increased 0.0007 in. and the height decreased 0.0001 in. The specimen tested at 1800°C became extensively oxidized during cooling, but the $UO_2$ bushing remained intact. At 2000°C the $UO_2$ reacted with the materials it contacted and the bushing was destroyed. As after the 1800°C test, no measurements were taken.

## $UO_2$-Graphite Compatibility

The compatibility of $UO_2$ and graphite was studied by heating compacts containing 50 wt % $UO_2$ and 50 wt % C to temperatures ranging from 1350 to 2200°C and holding at temperature for various times. The pellets were prepared by blending -60 +80 mesh, high-fired $UO_2$, Dixon's No. 200-40 graphite, and Bakelite resin No. 2417. The pellets were cold pressed and then carbonized at 1000°C for 1 hr before being tested.

The data presented in Table 5.2 were obtained for specimens packed in lampblack in graphite boats and heated in a system purged continuously with argon. One specimen was tested at 1360°C in a system containing no carbon other than that in the specimen. Pellets containing no $UO_2$ were also tested to determine the amount of carbon lost by reaction with impurities in the gas stream. The extent of reaction was determined by comparative weight-loss and x-ray diffraction techniques. If conversion of the $UO_2$ to UC was complete and no carbon was lost by oxidation from gaseous impurities, the weight loss would be 10.38%. The data indicate that the reaction begins at about 1400°C and proceeds rapidly at 1800°C. Intermediate temperatures will also be studied.

Table 5.2. Results of $UO_2$-Graphite Composite Reaction Tests

| Sample No. | Temperature (°C) | Time Held at Temperature (hr) | Weight Loss (%) | Weight Loss Due to Oxidation (%) | Compounds Present |
|---|---|---|---|---|---|
| 102 | 2200 | 0 | 11.86 | 0.66 | UC, $UC_2$ |
| 182 | 1835 | 0 | 10.24 | 0.65 | $UO_2$, UC, $UC_2$ |
| 258 | 1425 | 19 | 1.56 | 1.00 | $UO_2$, UC |
| 252 | 1425 | 89 | 5.31 | 1.10 | $UO_2$, UC |
| 253 | 1425 | 89 | 2.88 | 1.10 | $UO_2$, UC |
| 263 | 1350 | 72 | 1.08 | 1.51 | $UO_2$ |
| 277[a] | 1360 | 19 | 3.02 | 0.20 | $UO_2$, UC |

[a]No carbon in system except that in specimen.

## Mechanical Properties of Fuel Capsule Material

Investigations of the properties of type 304 stainless steel as a container material for $UO_2$ fuel pellets have continued. The experimental program has included tube-burst testing, strain-cycling and relaxation studies, and investigations of the bowing problem.

### Tube-Burst Tests

The possibility that a fuel capsule wall might burst because of the buildup of internal pressure necessitated an extensive investigation of the time-to-rupture of 0.020-in.-wall type 304 stainless steel capsules in terms of pressure and temperature. Preliminary results of this study were reported previously,[8] and a summary of the data obtained thus far is presented in Fig. 5.1 as a plot of time-to-rupture versus tangential stress and internal pressure. The tangential strains obtained in these tests are summarized on the following page.

[8]GCR Semiann. Prog. Rep. Dec. 31, 1958, ORNL-2676, p 83.

| Temperature (°F) | Tangential Strain (%) |
|---|---|
| 1300 | 2 – 3 |
| 1500 | 3 – 6 |
| 1600 | 2 – 9 |
| 1700 | 3 – 10 |
| 1800 | 6 – 18 |

Strain-Cycling and Relaxation Studies

A fuel capsule might also fail as a result of strain fatigue caused by thermal cycling or pressure cycling. Since creep and relaxation are dominant in the temperature range of interest, considerable plastic strain will result from relatively short periods of stress change. Therefore, an investigation of the isothermal strain-cycling capacity of type 304 stainless steel was started. Tests have been performed thus far on 0.060-in.-wall specimens at 1300 and 1500°F with a frequency of 0.5 cycles per minute. Results of these tests are presented in Fig. 5.2. The data indicate that the temperature has no major influence on the number of cycles-to-fracture from 1300 to 1500°F. Since the stress-rupture properties of type 304 stainless steel and Inconel are approximately the same at these temperatures, it was predicted that their strain-cycling properties would also be comparable. This prediction seems to be confirmed by the results shown in Fig. 5.2.

Relaxation tests of type 304 stainless steel are in progress to demonstrate the changes in volume caused by transformation. Tests at 1200°F with various initial stress levels have demonstrated that the volume change is independent of the initial stress. The increase in length is small and would hardly be observed in creep or tensile testing; however, it causes an apparent 2550-psi additional decrease in the stress in a relaxation test. The 2550-psi decrease in the stress is equivalent to about 0.19% increase in length due to the transformation of the ferrite constituent. Tests performed on type 304 stainless steel after transformation yield relaxation curves which correlate precisely with creep data.

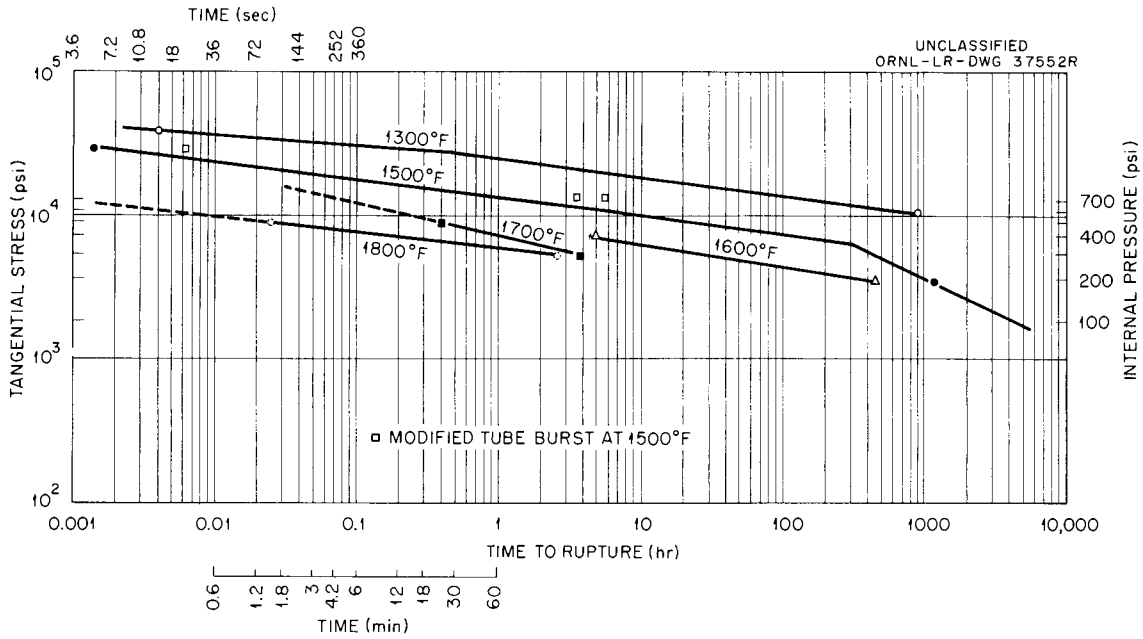


**Fig. 5.1. Results of Burst Tests of 0.020-in.-Wall, 0.75-in.-OD Type 304 Stainless Steel Tubing.**

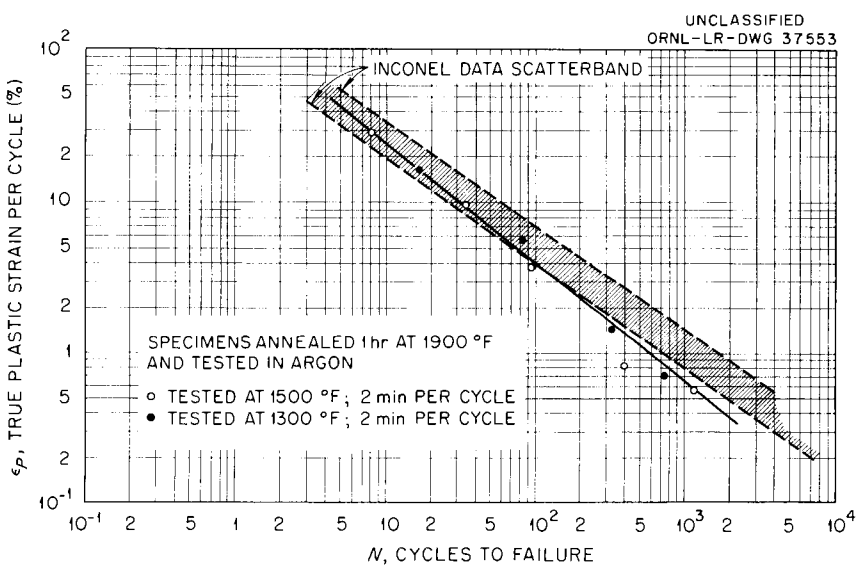


**Fig. 5.2. Strain-Cycling Properties of 0.060-in.-Wall Type 304 Stainless Steel Tubes.**

## Bowing Studies

Bowing of the fuel elements as a result of nonuniform temperature distribution presents a serious problem. Hot streaks will develop because of the fuel element configuration that will cause bowing of the capsules. The bowing will lead to uneven cooling, which will in turn produce more distortion. An investigation has been initiated to determine the magnitude of the deformation under hot-streak conditions. The testing apparatus used to obtain the hot-streak condition is similar to that shown previously,[9] but the length of the specimen and heater has been increased to 30 in.

A test was conducted at 1370°F with a hot streak of 1500°F in which the specimen was rigidly fixed at the top. The bottom of the specimen capsule was restrained from horizontal movement but was free to move in the vertical direction. As the hot streak was applied, the tube bowed toward the strip heater. Movement in the horizontal direction at the midpoint of the tube was 0.006 in., and an increase in length of 0.026 in. was measured. Measurements made after cooling the tube to room temperature indicated that plastic deformation of the tube had occurred. Refinements are being made in the apparatus before additional tests are conducted.

## Effect of Gaseous Environments on Properties of Type 304 Stainless Steel

In order to evaluate the performance of type 304 stainless steel as a capsule for bulk $UO_2$ fuel, it is necessary that its mechanical properties in the service environment be determined. Since the exact service environment is not known in this case, the approach taken to this problem has been that of studying the effect of the various gases on the behavior of the capsule material. Because of steam leakage into the reactor system and the large amount of graphite present, certain amounts of $CO$, $CO_2$, $H_2$, $H_2O$, and $CH_4$ will persist in the system. In

[9] Ibid., p 82.

addition, small amounts of $O_2$ and $N_2$ may be present from residual air.

These various impurity gases have been used in pure form as test environments in much of the work to date. Additional tests using controlled mixtures will be necessary to fulfill the objective of establishing the limiting concentration of contaminants for satisfactory operation.

Effect of Environment on Creep-Rupture Properties

Because of the large number of gases of interest and the subsequent large number of tests which would be required to evaluate the creep properties of this material over a variety of temperatures and stress levels, the investigation of the effect of environment on the creep-rupture properties of type 304 stainless steel was initiated by using a stress which would give a 1000-hr rupture life in air at 1500°F. These conditions are probably more severe than will exist in the reactor, but they are such that any gross environmental effects should be detectable.

Specimens 0.020 in. thick were initially selected for testing, but the scatter of the experimental results was so great that environmental effects could not be separated. Therefore, in order to obtain better reproducibility of results, the specimen thickness was changed. Sheet specimens 0.060 in. thick, with cross-sectional areas of 0.03 in.$^2$, were used to obtain the data presented in Table 5.3 and in Fig. 5.3. From the data of Fig. 5.3 it is evident that the creep rate is decelerated in air and sharply accelerated in CO. The creep behavior in $CO_2$ was similar to that observed for the gaseous environments shown in the scatterband of Fig. 5.3, but the creep rate was consistently slightly greater.

Examination of Creep Specimens After Test

The macroscopic appearances of the 0.060-in.-thick sheet specimens after creep testing are indicated in Table 5.3 and classifled according to magnetic properties. As may be noted, all the specimens, except those tested in argon and in hydrogen, were magnetic.

Table 5.3. Creep Data on 0.060-in.-Thick Type 304 Stainless Steel Sheet Specimens Annealed 1 hr at 1900°F in $H_2$ and Tested at 1500°F and a Stress of 3500 psi

| Test No. | Environment | Time to Rupture (hr) | Strain (%) | Surface Condition |
|---|---|---|---|---|
| 204 | $H_2$ | 319.6 | 11.71 | Very thin, adherent film; surface nonmagnetic |
| 216 | $H_2$ | 478.5 | 14.06 | No visible film; surface nonmagnetic |
| 214 | $H_2$ plus 1.6% $H_2O$ | 362.7 | 14.84 | Very thin, adherent film; surface slightly magnetic |
| 212 | CO | 213.1[a] | 17.2 | Thin, adherent film; surface magnetic |
| 233 | CO | 223.6 | 22.05 | Thin, adherent film; surface magnetic |
| 203 | $CO_2$ | 307.1 | 10.16 | Thick, scaly film; surface magnetic |
| 213 | $CO_2$ | 281.5 | 11.72 | Thick, scaly film; surface magnetic |
| 210 | Air | 901.1 | 21.88 | Thick, scaly film; surface magnetic |
| 202 | $O_2$ | 621.9 | 25.78 | Thick, scaly film; surface magnetic |
| 224 | $O_2$ (dry) | 445.5 | 28.13 | Thin, scaly film; surface magnetic |
| 215 | A | 451.2 | 12.50 | Very thin, adherent film; surface nonmagnetic |
| 223 | A | 345.5 | 14.45 | Very thin, adherent film; surface nonmagnetic |
| 225 | $N_2$ | 516.7 | 16.41 | Very thin, adherent film; surface magnetic |

[a]Test discontinued.

Information is also presented in Table 5.3 with respect to the adherency of the film formed in the various environments. The films formed in air, oxygen, and $CO_2$ at 1500°F showed signs of scaling after 24 hr. The films formed in the other test environments were quite adherent, but they may begin to scale after longer times in the test environment or as a result of thermal cycling. Additional examinations are being carried out on these specimens.

In order to gain a better understanding of the processes by which various environments affect the creep properties of type 304 stainless steel, x-ray and electron-diffraction techniques are being used to identify the surface films formed. The results of examinations of the 0.020-in.-thick creep specimens are summarized in Tables 5.4 and 5.5.

The microstructures of the 0.020-in.-thick specimens creep tested in argon containing 12 ppm oxygen, in CO, and in $CO_2$ are compared in Figs. 5.4, 5.5, and 5.6. As may be seen, the specimens tested in CO and $CO_2$ were heavily carburized.

On the basis of these observations, it is difficult to explain why the creep rate is accelerated in CO and $CO_2$. Both these environments are oxidizing and carburizing, and these factors were previously shown to be strengthening. Although the matrix was heavily depleted in chromium because of carbide formation, it is not felt that this alone could account for the observed creep behavior in CO. The surface reactions that occur may be of importance in explaining this phenomenon.

Environmental Effects on Fatigue

Although intergranular oxidation in specimens tested in air decelerates the creep rate, it may not be beneficial under cyclic stressing. The results of three strain-cycle tests run at 1500°F to compare the fatigue properties of type 304 stainless steel in air and in argon are presented in Table 5.6. It may be seen that the fatigue life is shorter in air than in argon by a factor of 4. Failure is detected in these tests by the propagation of a crack through the specimen wall and, hence, because of the statistical nature of crack propagation, it is necessary to run more than these three tests to

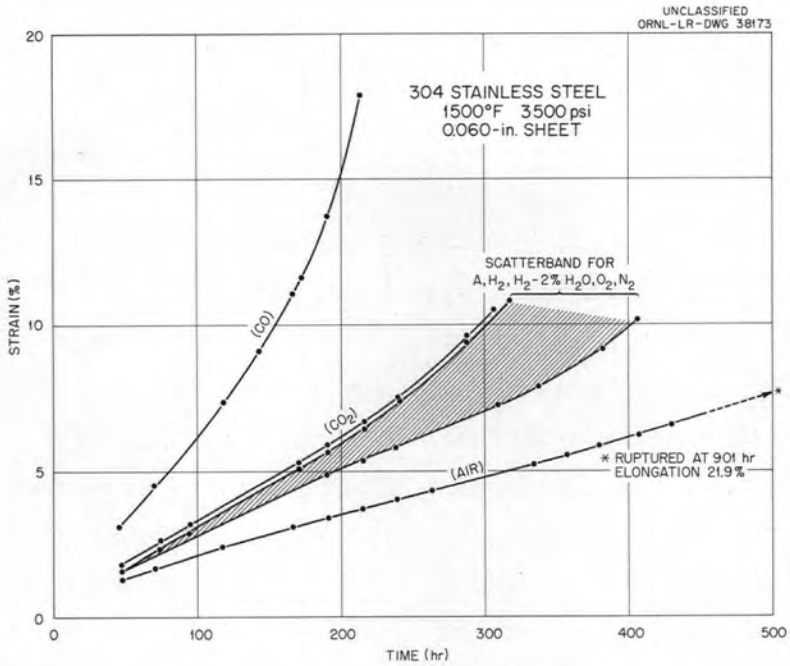


**Fig. 5.3. Creep Curves for Type 304 Stainless Steel in Various Environments at 1500° F.**

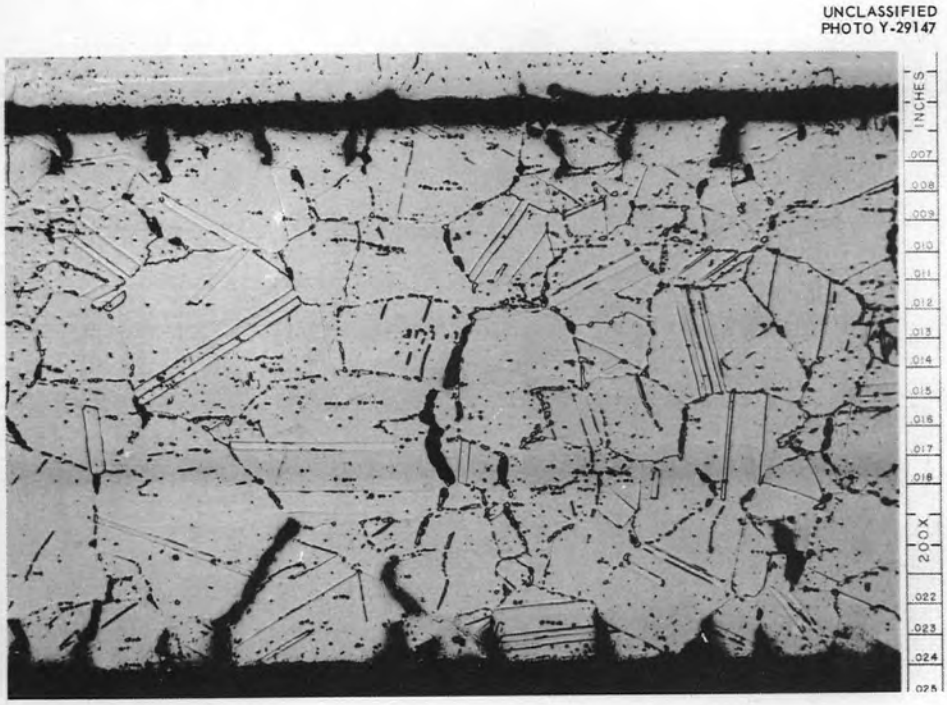


**Fig. 5.4. A Typical Area in the Stressed Portion of Type 304 Stainless Steel Creep Specimen No. 108, Which Was Tested in Argon Containing 12 ppm Oxygen.** Etchant: glyceria regia. Reduced 23%.

Table 5.4. Results of Electron-Diffraction and Electron-Microscope Examinations of 0.020-in.-Thick Type 304 Stainless Steel Creep Specimens Tested in Various Environments at 1500°F

| Specimen No. | Environment | Time in Environment (hr) | Constituents of Film[a] | Appearance of Film |
|---|---|---|---|---|
| | Air | 24[b] | $Fe_3O_4$, $\alpha$-$Fe_2O_3$ (w) | Nodular-type oxide crystals with definite geometrical planes |
| 108 | Argon + 12 ppm $O_2$ | 1146 | $MnCr_2O_4$, $Cr_2O_3$ | Nodular-type oxide crystals with indications of preferential grain-boundary attack |
| 131 | $H_2$ | 236 | $MnCr_2O_4$, $\alpha$-Fe | Advanced nodular-type structure with no indication of formation of well-shaped oxide crystals |
| 132 | Air<br>$H_2$ | 24[b]<br>532 | $MnCr_2O_4$, $\alpha$-Fe | Same as specimen No. 131, with regular oxide crystals at grain boundaries |
| 137 | Argon + 12 ppm $O_2$ | 825 | $Fe_3O_4$, $Cr_2O_3$, $MnCr_2O_4$ (w) | Nodular-type oxide crystals |
| 158 | CO | 201 | $Fe_3O_4$, $Cr_2O_3$ | General nodular growth with numerous almost perfect Crystals showing stepwise growth |
| 165 | CO | 354 | $Fe_3O_4$, $Cr_2O_3$ | Same as specimen No. 158 |

[a]The notation (w) indicates lines of weak intensity.

[b]No stress.

Table 5.5. Results of X-Ray Diffraction Examination of 0.020-in.-Thick Type 304 Stainless Steel Creep Specimens Tested in Various Environments at 1500°F

| Specimen No. | Environment | Time in Environment (hr) | Constituents of Film[a] |
|---|---|---|---|
| | Air | 24[b] | $\alpha$-Fe (w), $NiCr_2O_4$ (w), $Cr_2O_3$ (w), $\alpha$-$Fe_2O_3$ (s) |
| 106 | Air | 1485 | $\alpha$-Fe (w), $NiCr_2O_4$ (w), $\alpha$-$Fe_2O_3$ (s) |
| 108 | Argon + 12 ppm $O_2$ | 1146 | $\alpha$-Fe (s), $Fe_3O_4$ (w), $Cr_2O_3$ (w) |
| 122 | Argon + 54 ppm $O_2$ | 438 | $\alpha$-Fe (w), $NiCr_2O_4$ (w), $\alpha$-$Fe_2O_3$ (s) |
| 130 | Argon + 54 ppm $O_2$ | 434 | $\alpha$-Fe (w), $NiCr_2O_4$ (w), $\alpha$-$Fe_2O_3$ (s) |
| 131 | $H_2$ | 236 | $\alpha$-Fe (s), $Fe_3O_4$ (w), and possibly others |
| 132 | Air<br>$H_2$ | 24[b]<br>532 | $\alpha$-Fe (s), $NiCr_2O_4$ (w), $Fe_3O_4$ |
| 142 | $O_2$ | 620 | $\alpha$-Fe (w), $NiCr_2O_4$ (w), $\alpha$-$Fe_2O_3$, $Cr_2O_3$ (s) |
| 143 | Argon (static) | 434 | $\alpha$-Fe (s), $Fe_3O_4$ (w), $Cr_2O_3$ (w) |
| 158 | CO | 201 | $\alpha$-Fe (s), $Fe_3O_4$ (w) |

[a]The notation (w) indicates lines of weak intensity; (s) indicates lines of strong intensity.

[b]No stress.

UNCLASSIFIED
PHOTO Y-29165

**Fig. 5.5. A Typical Area in the Stressed Portion of Type 304 Stainless Steel Creep Specimen No. 158, Which Was Tested in CO.** Etchant: glyceria regia. Reduced 22%.

UNCLASSIFIED
PHOTO Y-29404

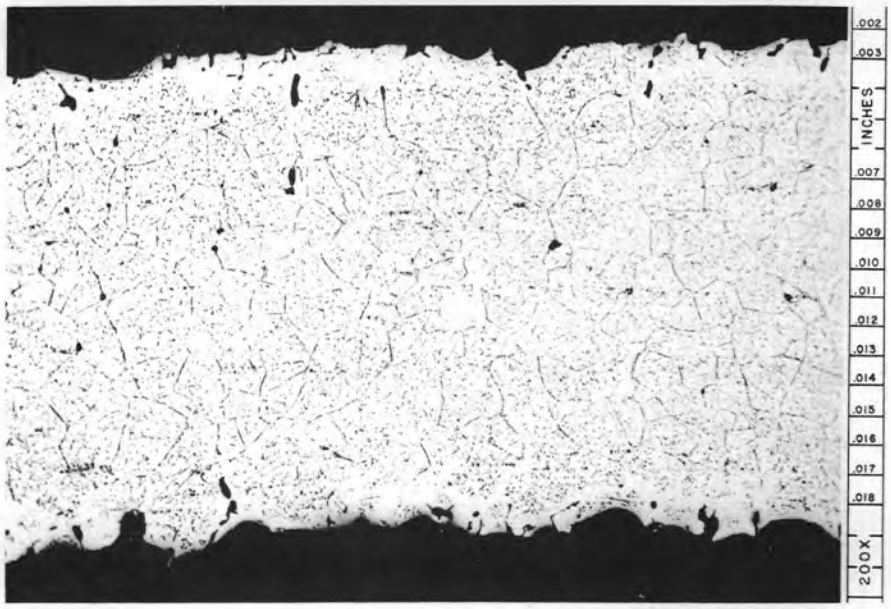


**Fig. 5.6. A Typical Area in the Stressed Portion of Type 304 Stainless Steel Creep Specimen No. 152, Which Was Tested in $CO_2$.** Etchant: glyceria regia. Reduced 22%.

Table 5.6. Strain-Cycle Tests on 1-in.-ID, 0.060-in.-Wall Type 304 Stainless Steel Tube Specimens

| Test No. | Environment | Frequency (min/cycle) | Temperature (°F) | Strain per Cycle (%) | No. of Cycles to Rupture |
|---|---|---|---|---|---|
| 349 | Argon | 2 | 1500 | 0.56 | 1180 |
| 356 | Air | 2 | 1500 | 0.66 | 246 |
| 363 | Air | 2 | 1500 | 0.66 | 342 |

prove or disprove these results. It should also be pointed out that these conditions are much more severe than the expected service conditions.

Reactions of Type 304 Stainless Steel with Gases

In the study of environmental effects, it is evident that the reactions of pure gases with unstressed metal specimens must be studied. A determination of the permissible limits of various gaseous impurities may be made only if the reaction rates and reaction products are known.

Reactions with $CO_2$. The solid products of reaction between type 304 stainless steel and flowing $CO_2$ at 1500°F are a dark magnetic oxide of the composition $3Cr_2O_3 \cdot Fe_2O_3$ at the gas-metal interface and a spinel of the composition $MnO \cdot Cr_2O_3$ as a very thin film next to the metal. Evidences of carburization, decarburization, or soot deposition were not found. The reaction rates do not appear to vary significantly for $CO_2$ concentrations ranging from 0.1% to 100% by volume at this temperature and 1 atm.

In static $CO_2$, carburization, as well as oxidation, occurs, and thus the decomposition product of $CO_2$ is apparently CO. In 300 hr at 1500°F the carbon content of metal specimens increased from 0.010% to 0.37%. It was determined that the carbon was not a constituent of the film (that is, soot) but rather a carbide in the metal. The oxide film, although not identified, is not impervious to further carburization by

CO, since re-exposure of the oxidized sample to pure CO for an additional 170 hr resulted in an increase in the carbon content to 0.72%.

Reactions with CO. In static CO, the reaction products at 1500°F were oxides of various types. The bulk outer oxide was found to be $Fe_3O_4$ and a thin inner oxide was composed of various spinels and $SiO_2$. Carburization of the stainless steel occurs without formation of a gaseous reaction product.

The approximate reactions between stainless steel and $CO_2$ and between stainless steel and CO may be written as follows:

$$2Fe + 6Cr + 12CO_2 \rightarrow 3Cr_2O_3 \cdot Fe_2O_3 + 12CO \qquad (1)$$

$$4Fe + 34Cr + 8CO \rightarrow Fe_3O_4 + FeO \cdot Cr_2O_3 + 8Cr_4C \qquad (2)$$

## Manufacturing Developments

### Manufacturing Variables in End-Closure Fabrication

The study of the design and manufacturing variables associated with the butt-weld, edge-weld, and plug-weld fuel capsule end closures was continued.[10] An apparatus for semiautomatic welding of the three types of closures was assembled, which consists of a d-c welding power supply equipped with a high-frequency pilot circuit and current-decay attachment, a recording ammeter, and a fixture designed to hold and rotate the capsule at variable welding speeds. The rotating fixture and the torch-positioning apparatus are shown in Fig. 5.7. By rotating the torch about its own axis, both horizontal and vertical welds can be made. The variables associated with the manufacture of fuel capsules are being studied during fabrication of the three types of capsules described in the following paragraphs.

Fuel Capsules for ETR-ORR Irradiation Program. The ETR-ORR irradiation-test fuel capsules were manufactured to evaluate assembly and edge-weld joining techniques. The components of a capsule and an assembled unit are shown in Fig. 5.8.

---

[10] GCR Semiann. Prog. Rep. Dec. 31, 1958, ORNL-2676, p 93.

**Fig. 5.7. Rotating Fixture and Torch-Positioning Apparatus for Semiautomatic Welding of Fuel Capsule End Closures.**

**Fig. 5.8. ETR-ORR Irradiation Capsule Components and an Assembled Capsule.**

Difficulties in obtaining satisfactory welds were encountered in the preliminary weld tests, but, after the cap design was modified to give an interference fit between the end cap and the tube, satisfactory welds could be made. The optimum welding conditions were determined to be those shown in Fig. 5.9. More than 50 end-closure welds of the type shown in Fig. 5.10 have been made thus far in the manufacture of the capsules. Each weld has been inspected radiographically and with dye penetrants, and there have been no rejections. A weld-current trace, such as that shown in Fig. 5.11, was made for each weld as a record of the welding variables. It was noted that a smooth current trace was indicative of a good weld and should be useful in establishing the quality of the closure weld.

During manufacture, it was necessary to adjust the head space separately for fuel expansion for each fuel capsule because of the tolerances placed on the tubing length and the individual fuel pellets. The edge weld was found to be adaptable to this variable, since the cap could be recessed or projected 0.025 in. without materially affecting the quality of the weld.

EGCR Fuel Elements. Four EGCR-type fuel elements, such as that shown in Fig. 5.12, have been fabricated for use in loop tests, and fuel capsules containing both dummy fuel (Inconel rod) and $UO_2$ pellets have been made. Considerable difficulty was encountered during welding of the end caps to the tubes because of dimensional differences. All the end caps were remachined, but rejection of welds is still in excess of 30%. Difficulty was also encountered in positioning the element in the graphite sleeve because of inaccessibility for jigging.

Capsules for GETR Irradiation. The fuel capsule stringer assembly for irradiation in the GETR was reviewed, and minor changes in design were recommended. Parts for mockup fuel stringers were assembled, and a furnace-brazing procedure for attachment of thermocouples was recommended. Since suitable facilities for furnace-brazing are not available at the GETR site, an alternate method of attachment by torch brazing was evaluated and approved.

UNCLASSIFIED
ORNL-LR-DWG 35796

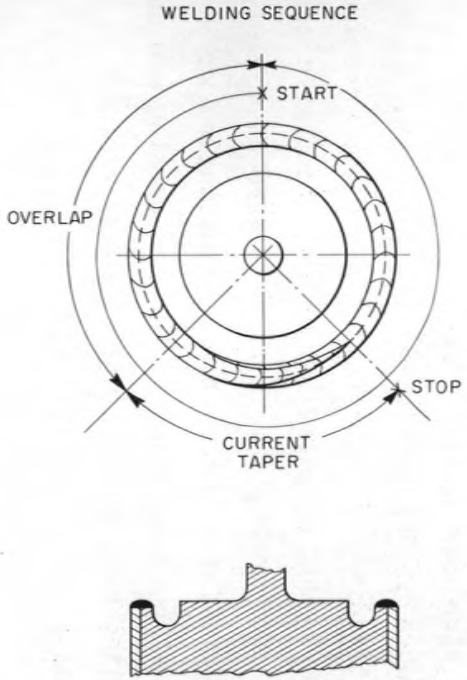


WELDING CONDITIONS
CUP SIZE: 3/8-in. OPENING
ELECTRODE: THORIATED TUNGSTEN 1/16 in. DIA, POINTED.
ELECTRODE PROJECTION FROM CUP: 1 in.
ARC DISTANCE: 0.025 in.
ARGON FLOW: 20 ft³/hr
ARC CURRENT: 18 ± 1/2 amp, DIRECT CURRENT, STRAIGHT POLARITY
WELD SPEED: 6 in./min

**Fig. 5.9. Optimum Welding Conditions for ETR-ORR Irradiation Capsules.**

UNCLASSIFIED
PHOTO Y-28189

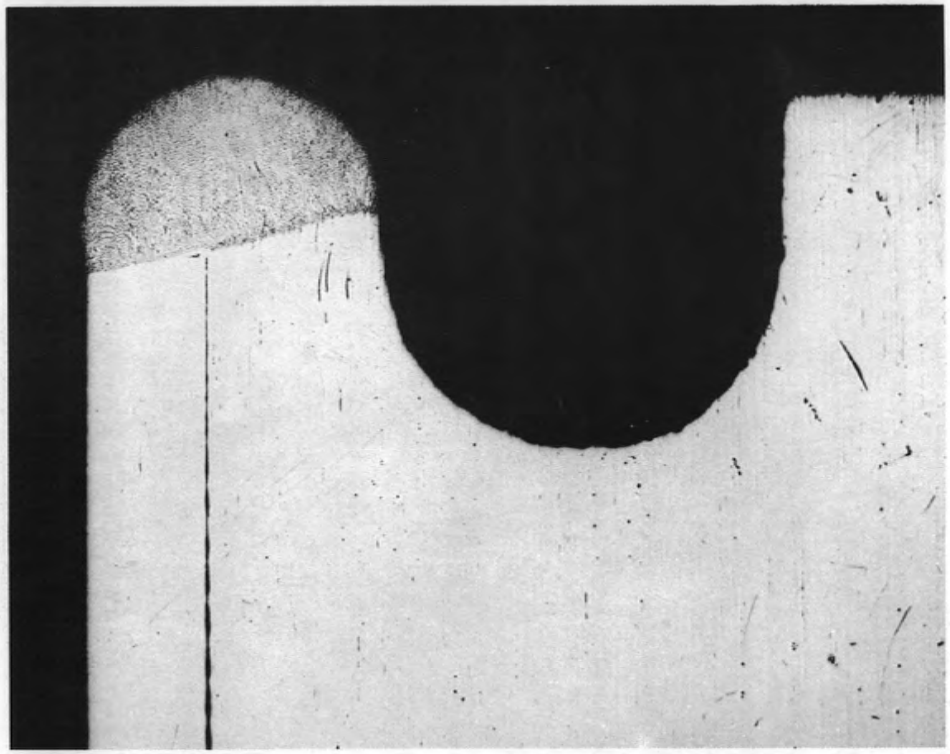

**Fig. 5.10. ETR-ORR Irradiation Capsule Weld. Etchant: oxalic acid. 30X.**

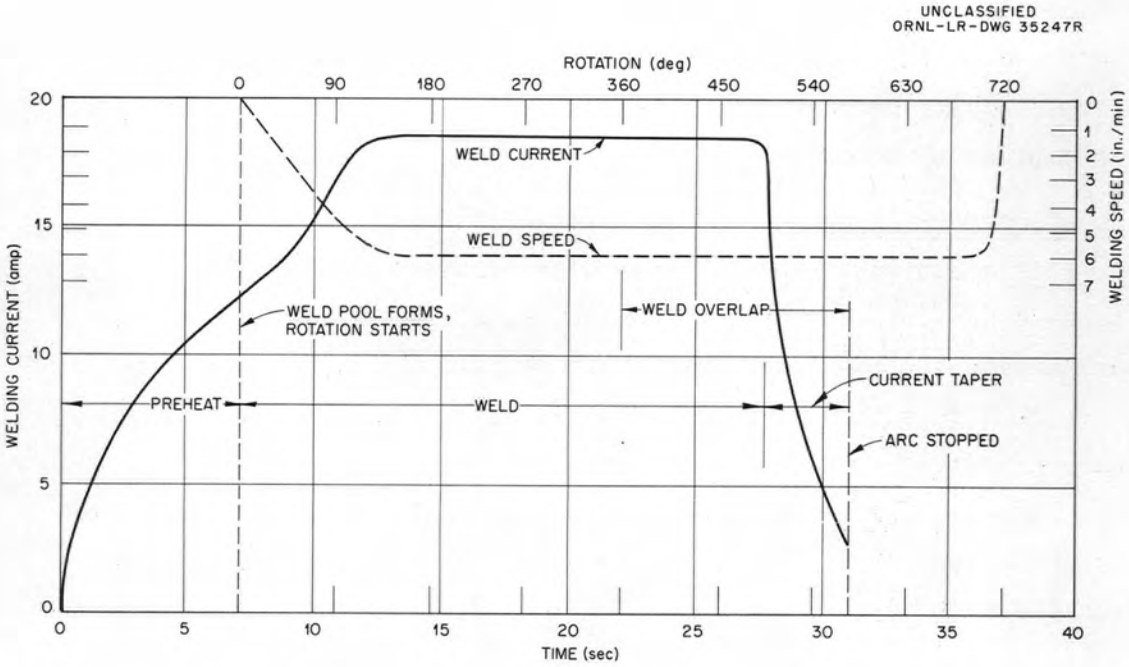


**Fig. 5.11. Welding Sequence for ETR-ORR Capsules.**

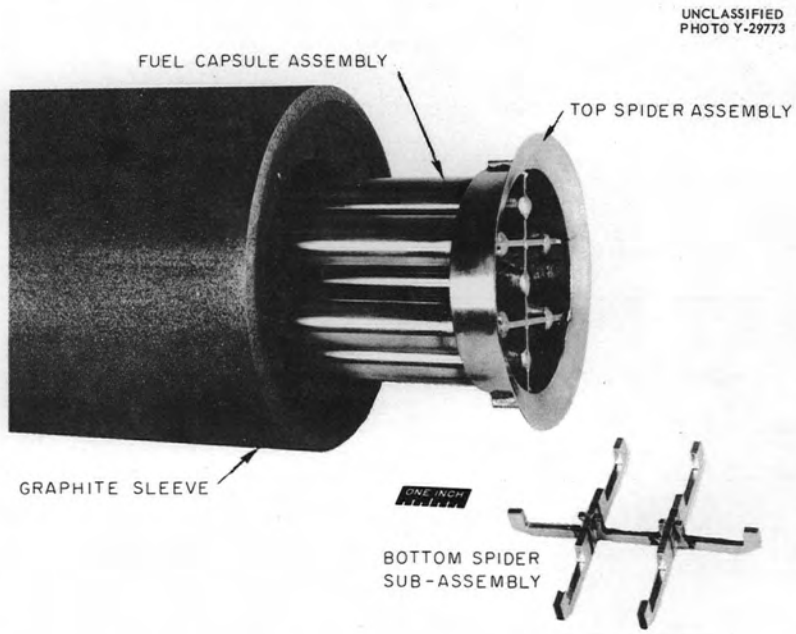


**Fig. 5.12. EGCR Fuel Element Components.**

Difficulties in attaching the internal thermocouples were encountered because the heat input to the thermocouple seal weld caused cracking in the braze and leakage of helium from the thermocouple seal. Relocation of the final seal weld enabled leaktight assemblies to be made.

End-Closure Testing

In addition to the fuel capsules mentioned above, specimens for tube-burst tests and other strength tests have been prepared for evaluation of the three end-closure designs. Tensile tests have been completed on such specimens, and thermal-cycling tests are being carried out.

End-Closure Tensile Tests. Simple tensile tests were used to determine the strengths of the three types of end closures. The tensile test data, presented in Table 5.7, indicate that each of the

Table 5.7. Room-Temperature Tensile Strengths of Three Types of Fuel Capsule End Closures

| Type of Weld Closure | Maximum Load (lb) | Rupture Load (lb) | Elongation (%) | Location of Failure |
|---|---|---|---|---|
| Butt | 4300 | 4100 | 63 | Tube |
| Plug | 4300 | 4000 | 56 | Tube |
| Edge | 3400 | 3300 | 13 | Fusion zone |

three types of end closure has load-carrying ability far in excess of that required. Typical ruptured specimens are shown in Fig. 5.13. The edge weld, which was not as strong as the other welds, failed adjacent to the weld fusion zone as a result of rotation of the joint and tearing of the metal.

Thermal-Cycling Tests. Tubes having the three types of end closures are being thermally cycled between room temperature and 1400°F while pressurized internally with helium to give hoop stresses of

approximately 2600 psi at 1400°F. All specimens are checked weekly for loss in pressure or change in dimensions. Over 200 cycles have been completed with no leakage or change in dimensions. Upon completion of 500 cycles, the specimens will be helium leak tested and examined for effects of the test conditions.

End-Closure Inspection

Work is continuing on the development of adequate techniques for inspection of the three types of closure welds. The inspection techniques will vary considerably with the choice of end closures, but dye-penetrant inspections and helium leak tests can be used equally well on all three of the proposed welds and will be recommended for fuel capsule inspection.

A procedure specification for the use of helium leak detection on fuel element capsules has been completed, and tests are now being conducted to determine the adequacy of the specification. In particular, the possibility of completely outgassing the helium through a large leak during evacuation of the inspection manifold caused some concern. A test was conducted on a 1.5-in.-long fuel capsule containing $UO_2$ pellets with a 0.0135-in. hole drilled in the capsule wall. A positive helium leak rate was detected for over 9 hr. Thus, there seems to be little reason to be concerned about outgassing the helium from a gross defect.

Since neither the dye-penetrant inspection nor the helium leak test are appropriate for the detection of subsurface defects, radiographic and ultrasonic inspection techniques are also being studied. The basic radiographic inspection methods are illustrated in Fig. 5.14. The sensitivity of the inspection will vary inversely with the amount of material which the radiation must penetrate. In addition, the ability to detect weld cracks will depend upon the orientation of the crack relative to the radiation. Weld cracks could not be detected in edge-fusion joints. Work is under way to establish optimum techniques for radiographic inspections of each type of end closure. Very thin metal foil penetrometers are being used for measurement of the contrast

and detail sensitivities. After optimum techniques have been established, attempts will be made to simulate calibrated discontinuities.

Efforts are also being made to develop ultrasonic inspection techniques for each of the weld configurations. At present there is no promising method for ultrasonic inspection of edge-weld closure. The basic method for the inspection of butt and plug welds is shown in Fig. 5.15. The ultrasound beam is aligned in a diametrical plane at an angle $\theta$ that will cause the refracted beam in the metal wall to travel longitudinally toward the weld. A crack or similar discontinuity will reflect the sound so as to return it along the same path to the ultrasonic transducer. The capsule is rotated about its axis to permit inspection of the entire weld. Attempts to use this technique have been rather inconclusive thus far. These techniques appear promising in theory, however, and further efforts are being made to overcome the difficulties which have been encountered.

Selection of Reference End Closure

The edge-fusion type of weld joint has been selected as the reference end closure for the fuel capsules, primarily because of ease of assembly and weldability. Its use will permit a wider range of tolerances for both the tubing and the end caps and will minimize the rejections for weld defects. This type of weld can be inspected adequately for surface defects, such as porosity and weld-zone cracks, by the dye-penetrant technique. Internal porosity and weld inclusions could be detected by radiography; however, radiography would not detect subsurface cracks or poor weld penetration because of poor orientation of the radiation with respect to the weld joint. Subsurface defects of the latter type can be adequately controlled and minimized, however, by use of the automatic welding equipment discussed above.

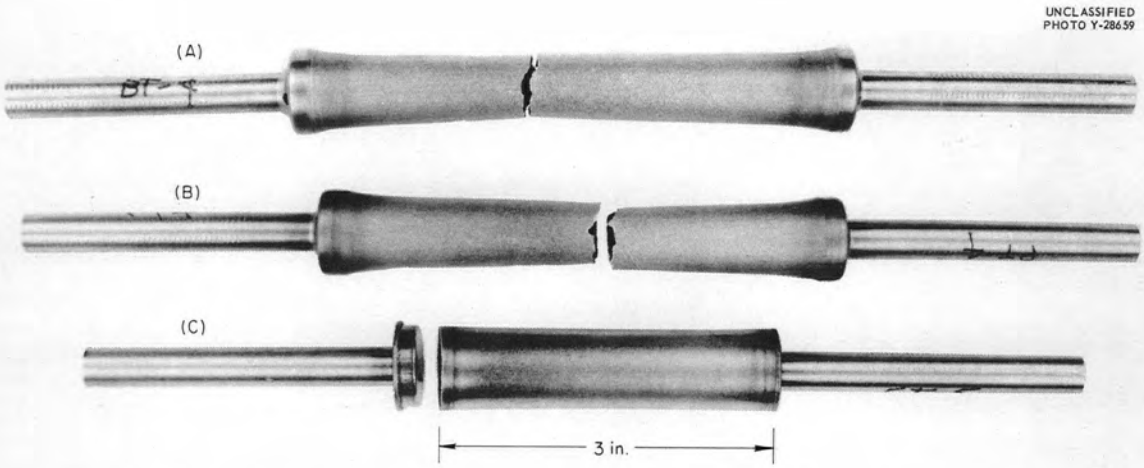


**Fig. 5.13. Typical Failures of Tensile Specimens at Room Temperature. (A) Butt-welded end closure. (B) Plug-welded end closure. (C) Edge-welded end closure.**

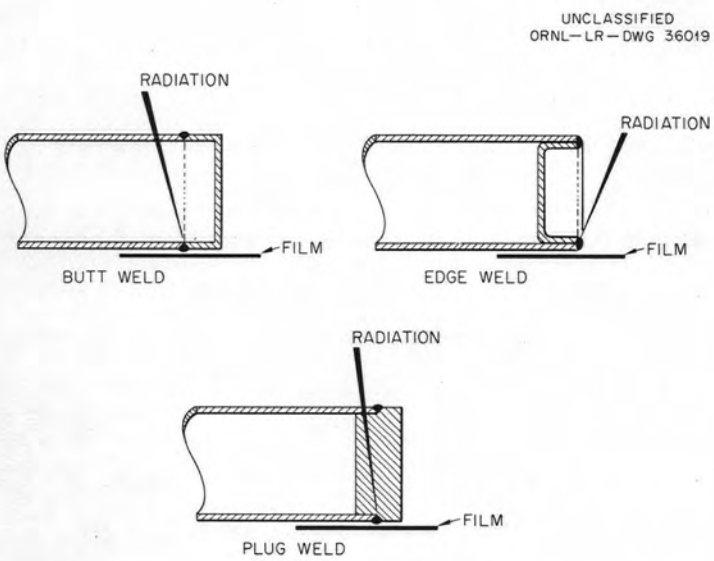


**Fig. 5.14. Basic Radiographic Procedure for Inspection of End-Closure Welds.**

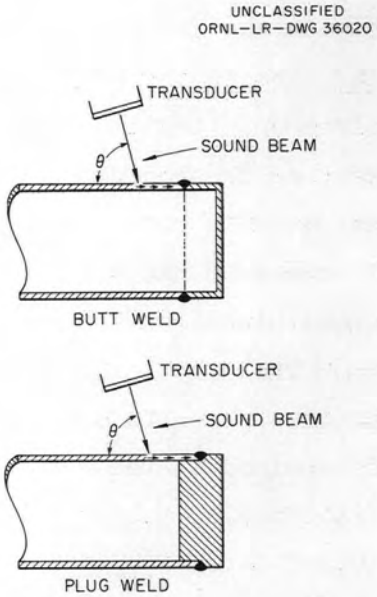


**Fig. 5.15. Basic Ultrasonic Procedure for Inspection of End-Closure Welds.**

## Inspection of Fuel Capsule Tubing

### Evaluations of In-Plant Inspections of Capsule Tubing

As mentioned previously,[11,12] eddy-current, visual, and dye-penetrant methods must be used for adequate nondestructive inspection of the 3/4-in.-OD, 0.020-in.-wall, type 304 stainless steel tubing for fuel capsules. It is hoped that these inspections can be accomplished in the manufacturer's plant. An opportunity to gage the effectiveness of such in-plant inspection was afforded by the purchase of approximately 1300 ft of capsule tubing for use in a critical assembly.[12] This tubing was subsequently inspected at ORNL by pulse-echo-ultrasonic, resonance-ultrasonic, and eddy-current techniques, and random samples were inspected by radiography and fluorescent penetrant techniques. The eddy-current inspection of this tubing rejected about 10% because of the presence of indications which exceeded that produced by a reference standard. The reference standard is a milled longitudinal slot 0.0025 in. deep on the outer surface of a tube. During the pulse-echo-ultrasonic examination, no discontinuities were detected which were as deep as the rejection standard of 0.0025 in. The radiographic examination of a random 100-ft sample disclosed no discontinuities. The fluorescent-penetrant examination of the same sample revealed a few small pinholes which proved to be less than 0.0005 in. in depth.

The only serious discrepancy in this tubing was the failure of much of the tubing to comply with the tolerances on wall thickness, as determined by the resonance-ultrasonic technique. Of the 115 pieces (1150 ft) of tubing purchased to the commercial tolerance of ±10% (0.002 in.), 24 pieces had wall thicknesses which exceeded 0.022 in., 83 pieces were within the ±0.002-in. tolerance, and 8 pieces were within ±0.001 in. Of the 10 pieces (100 ft) of tubing purchased to a wall-thickness tolerance of ±0.001 in., only 1 piece was within the prescribed

---

[11] The ORNL Gas-Cooled Reactor, ORNL-2500, Part 2, Section 4.3.4 (Apr. 1, 1958).

[12] GCR Semiann. Prog. Rep. Dec. 31, 1958, ORNL-2676, p 90.

tolerance, the other 9 being within ±0.002 in.

A second lot of approximately 1500 ft of similar tubing has been procured with no inspection requirements in the purchase specification. This lot of tubing is now being evaluated at ORNL by all available nondestructive testing techniques. The results of these inspections will provide information on the quality of tubing which has not been inspected by the manufacturer and will give an indication of the product improvement which can be expected by inspection during manufacture. Preliminary results indicate about a 30% rejection by the eddy-current technique.

Evaluation of Welded Tubing

A program of nondestructive evaluation of welded and redrawn, 3/4-in.-OD, 0.020-in.-wall, type 304 stainless steel tubing from several manufacturers has been initiated. Measurements of wall thickness have shown less eccentricity of the welded tubing than is normal for seamless tubing. In general, the over-all quality and integrity of the tubing has been quite similar to that of seamless tubing.

Evaluation of Thin-Walled Tubing

Approximately 120 ft of 1/2-in.-OD, 0.003-in.-wall, type 304 stainless steel tubing was evaluated by use of radiography, fluorescent penetrants, and probe-coil eddy-current techniques. Because of the fragile nature of the tubing, the pulse-echo-ultrasonic or encircling-coil eddy-current techniques were not used. The probe-coil eddy-current technique demonstrated that the wall thickness varied from 0.0027 and 0.0031 in., with most of the variation being present as eccentricity. Radiography revealed many narrow longitudinal striations which reduced the wall to thicknesses as low as 0.0025 in. In addition, there were many discrete discontinuities with depths between 0.0005 and 0.001 in. The fluorescent penetrants indicated only a few very shallow surface discontinuities.

Approximately 35 ft of 3/4-in.-OD, 0.004-in.-wall, type 304 stainless steel tubing was evaluated by the use of radiography, fluorescent penetrants, probe-coil eddy-current, and pulse-echo-ultrasonic techniques.

The wall thickness was found to vary from 0.0040 to 0.0054 in. The most serious discontinuities were detected by the radiographic inspection and included surface roughness, pitting, and localized thickness variations. The most severe wall-thickness change reduced the wall to about 0.0033 in. The pits, which attained depths up to about 0.0007 in., are illustrated in Fig. 5.16.

Inspection of Engineering Materials

Inspection was performed on 10,477 ft of stainless steel tubing in accordance with RMIS-2.[13] A defect greater than 5% of the wall thickness was used as the criterion for rejection, and only 198 ft of tubing was rejected. Over 1200 machined parts of stainless steel for use in irradiation capsules were inspected by dye-penetrant, visual, and radiographic methods, with only twelve parts being rejected.

Welds were inspected with the intended application as the criterion for the type of inspection performed and for rejection. The results of these inspections are presented in Table 5.8. In addition, twenty-nine

Table 5.8. Results of Inspection of Welded Components for Engineering Tests

| | Weld Type[a] | | | |
|---|---|---|---|---|
| | C | CN | B | BN |
| No. inspected | 947 | 210 | 8 | 9 |
| No. rejected | 143 | 10 | 1 | 0 |
| % rejected | 14.6 | 4.8 | 12.5 | 0 |

[a]See ref. 13.

welds on ORR-ETR fuel capsules for the irradiation program were inspected by visual, dye-penetrant, and radiographic methods. One capsule was rejected because of a defective closure weld on the extension tube. All

[13]Reactor Material Specifications, TID-7017 (Oct. 29, 1958).

UNCLASSIFIED
PHOTO Y-28884

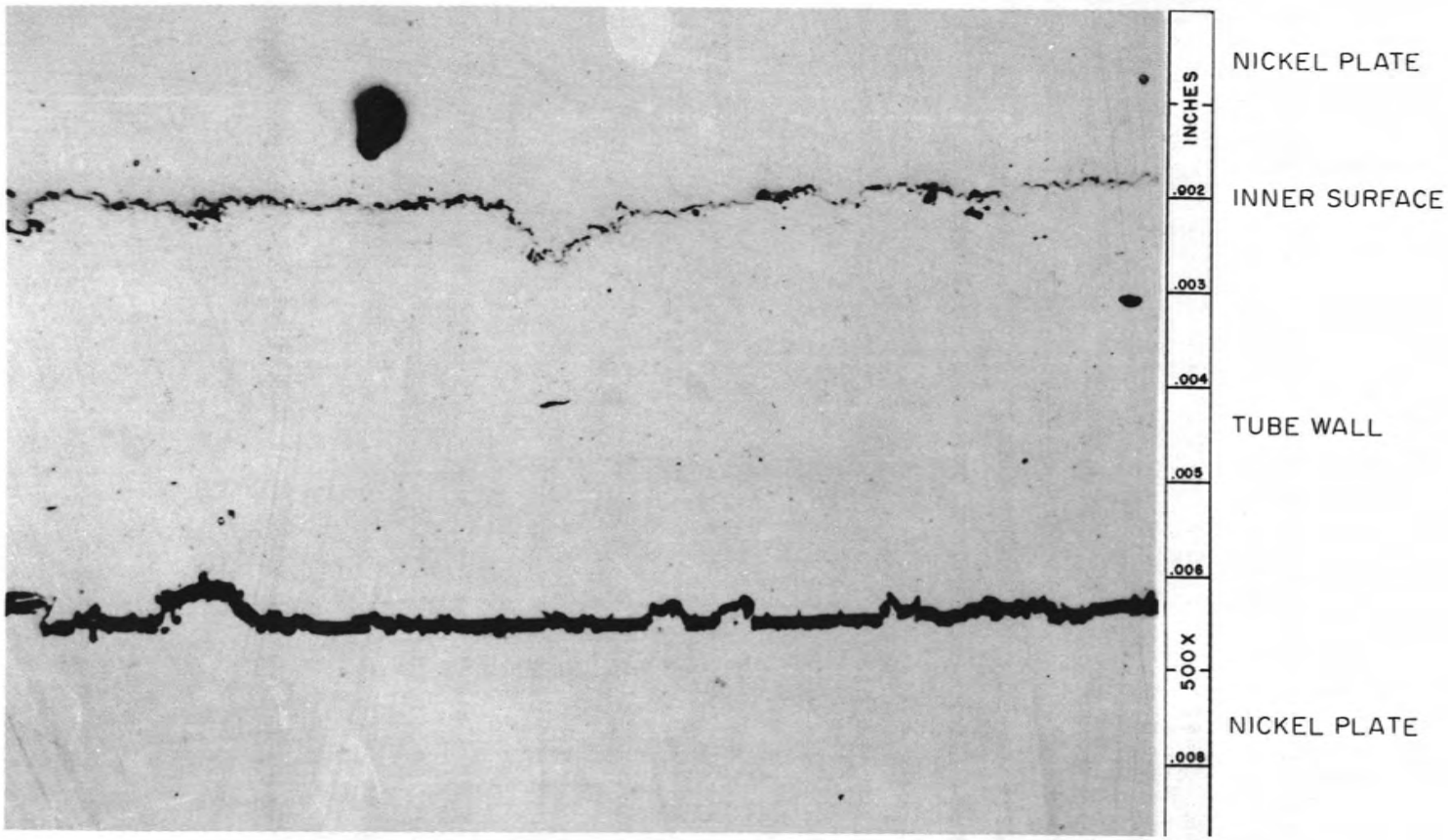


Fig. 5.16. Pits Found by Radiographic Inspection of $\frac{3}{4}$-in.-OD, 0.004-in.-Wall, Type 304 Stainless Steel Tubing. As polished.

fuel capsule end-closure welds were acceptable.

## Beryllium Investigations

### Evaluation of Extruded Tubing

An experimental quantity of 50 ft of 0.8-in.-OD, 0.040-in.-wall, beryllium tubing was obtained in the as-extruded condition. This lot of tubing was ordered to determine the current capabilities of industry in producing capsule tubing and to provide a quantity of material for testing. The tubing was evaluated by fluorescent-penetrant, resonance- and pulse-echo ultrasonic, and radiographic techniques. The penetrant technique revealed the presence of many tiny pinholes, porous areas, and a few cracks. All these indications were quite shallow. A few crack-like indications were detected by the ultrasonic technique. Some of these proved to be heavy scratches and scored areas on the inner surface.

The wall thickness, as measured by the resonance-ultrasonic technique, varied from 0.053 in. to 0.036 in., with one isolated area only 0.024 in. thick. The radiographic technique detected many scored areas and gouges on the inner surface, with depths up to 0.003 in. Other common discontinuities were pits and very small high-density inclusions.

### Welding and Brazing

After inspection, a portion of the tubing was machined into lengths for end-closure fusion-weld specimens; edge-weld and plug-weld types of end caps were machined from extruded rod. Upon welding, it was noted that excessive porosity occurred in the molten metal adjacent to the tube in each case. Since no defects were noted in previous welded specimens which had been machined from QMV beryllium, the porosity was believed to have been caused by a contaminant introduced during the extrusion of the tubing. Samples were heated to approximately 1500°F in vacuum in a quartz tube, after which a scattered white deposit was noted on the internal surface of the beryllium tube. An analysis is presently being run to determine the nature of the contaminants in the extruded metal prior to continuing weld tests.

The fabrication of beryllium tubing into fuel capsules for evaluation of the physical properties and for in-pile testing will require joining beryllium to other metals. Although techniques have been developed[14,15] for making dissimilar metal joints with beryllium, none of the brazing alloys studied thus far have satisfactory properties at the desired operating temperature of a gas-cooled beryllium fuel element (600°C). The behavior of high-temperature brazing alloys on beryllium is being studied with the apparatus shown in Fig. 5.17. The sample in the form of a T-joint is placed in a quartz tube and is heated by induction in vacuum to the melting point of the braze metal. The operator may then visually observe the behavior of the alloy on the joint and determine the optimum brazing conditions. Several brazing alloys that melt in the 1000 to 1100°C range and wet beryllium are presently being evaluated.

---

[14] D. W. White and J. E. Burke (eds.), The Metal Beryllium, Chap. 5, ASM (1955).

[15] Joining of Beryllium, DMIC-Memo-13 (Mar. 30, 1959).

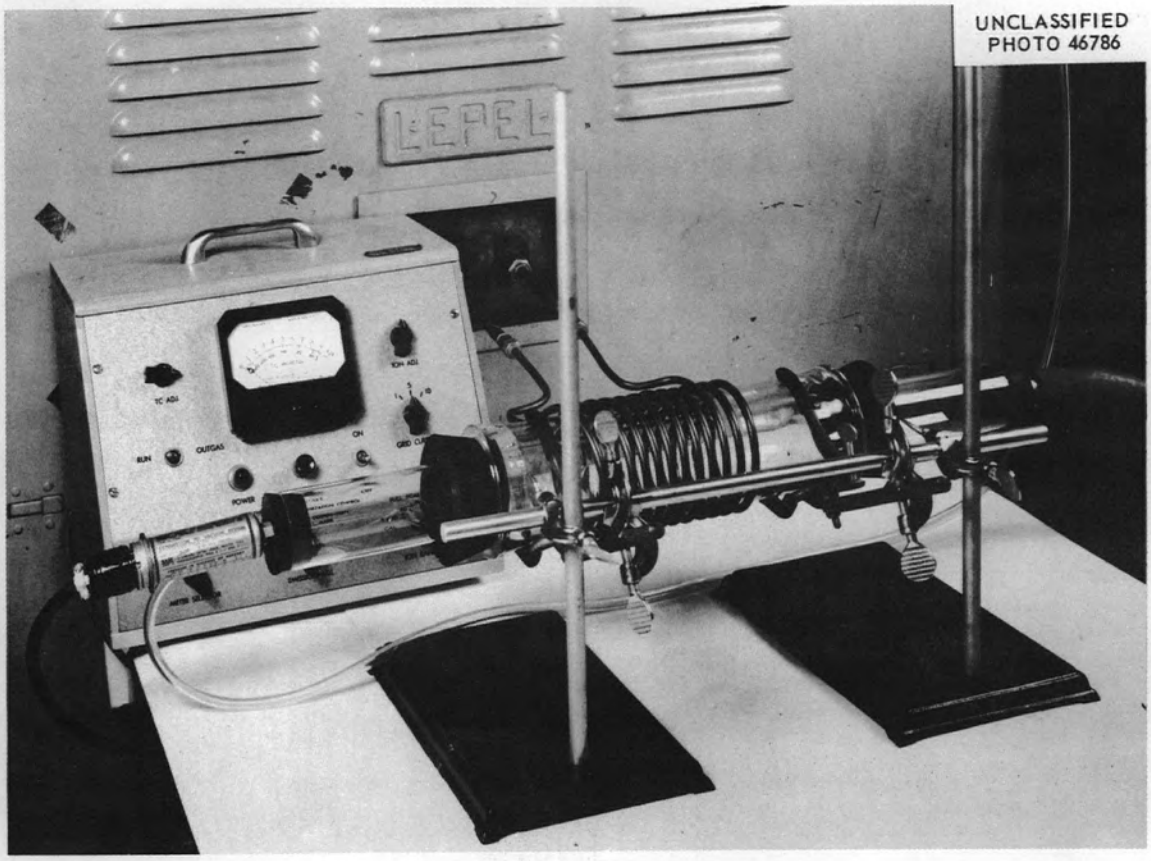


**Fig. 5.17. Apparatus for Induction Brazing of Beryllium.**

# 6. IN-PILE TESTING OF COMPONENTS AND MATERIALS

## Fuel Capsule Irradiation Program

Irradiation of full-size (diameter only) single fuel rod specimens is under way at the ORR, and preparation of a second set of experimental assemblies has been initiated. Five miniature capsules have been irradiated in the LITR, six are being irradiated, and two are ready for insertion. The GETR helium loop has been assembled and some fuel stringers have been installed for shakedown tests. Ten capsules have been assembled for irradiation in the ETR, but delays, largely caused by installation requirements of large loops for other programs, have prevented initiation of irradiation. One capsule, installed for flux measurement, has been irradiated for several weeks.

The irradiation program has been altered by adding a second set of ORR experiments that are to include tests at temperatures up to 1600°F and an increased number of experiments with low-density $UO_2$ under conditions that closely represent the latest predicted operating conditions for the EGCR.

### Full-Diameter Prototype Fuel Capsules

Construction of the experimental facility and installation of eight experimental capsules were completed at the ORR. The locations of the capsules in the reactor pool and of other components in the reactor building are shown in Fig. 6.1. The pool components and the cadmium shutter mechanism for thermal cycling are shown in Fig. 6.2 as installed in a reactor poolside mockup facility for shakedown and dimensional checks.

Irradiation of the eight capsules was initiated April 11, 1959, during ORR operational cycle X. For this and the subsequent reactor cycle, approximately two months, a helium-nitrogen gas mixture was used to maintain all capsule temperatures at 1300°F. Commencing with reactor cycle XII, the temperatures of experimental assemblies 02, 05, 06, and 08 were increased. The control gas mixture has been changed to helium-argon (95% He–5% A) for all capsules, in order to utilize the

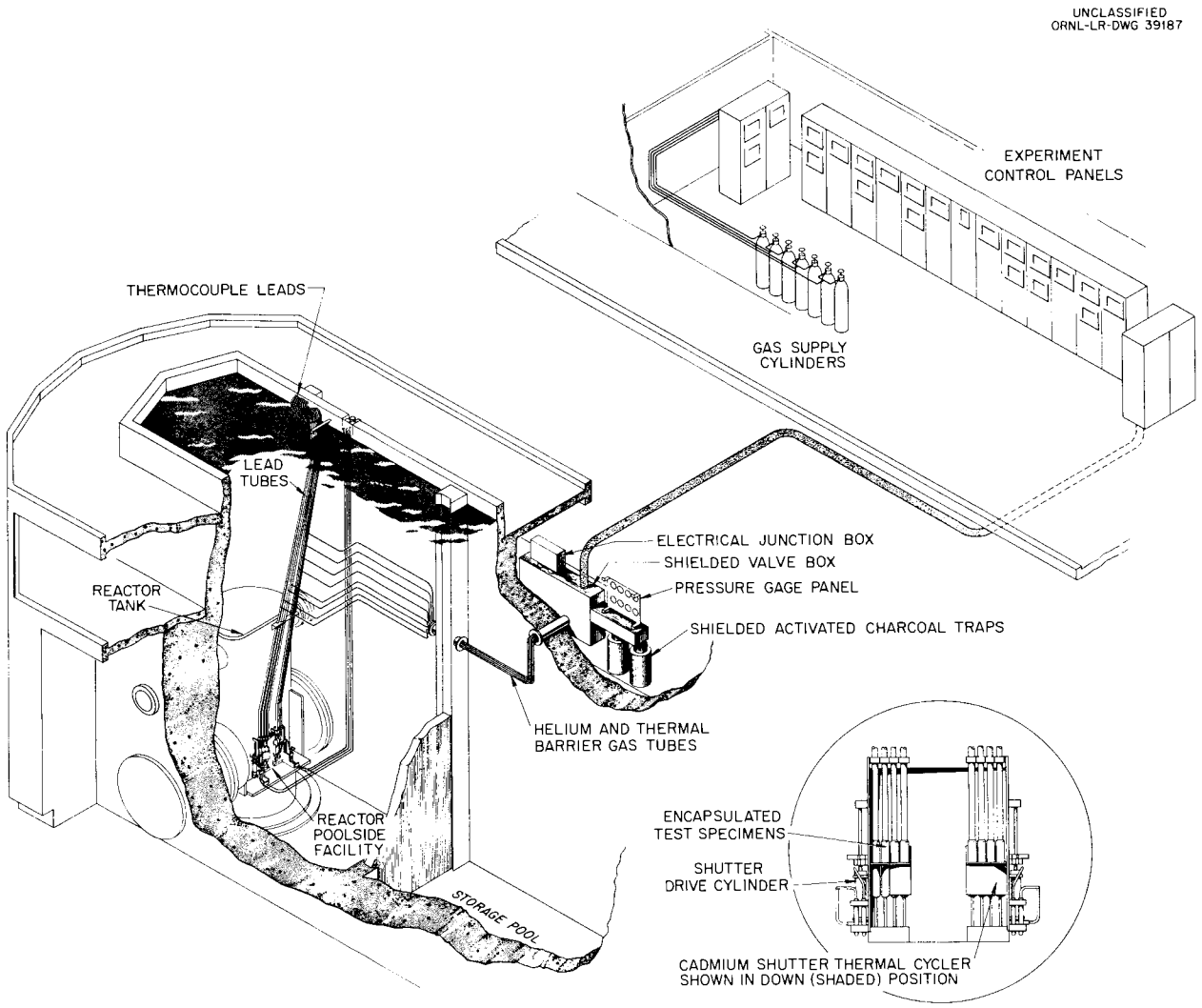


**Fig. 6.1. Experimental Facilities for Irradiation of Full-Diameter Prototype Fuel Capsules in the ORR.**

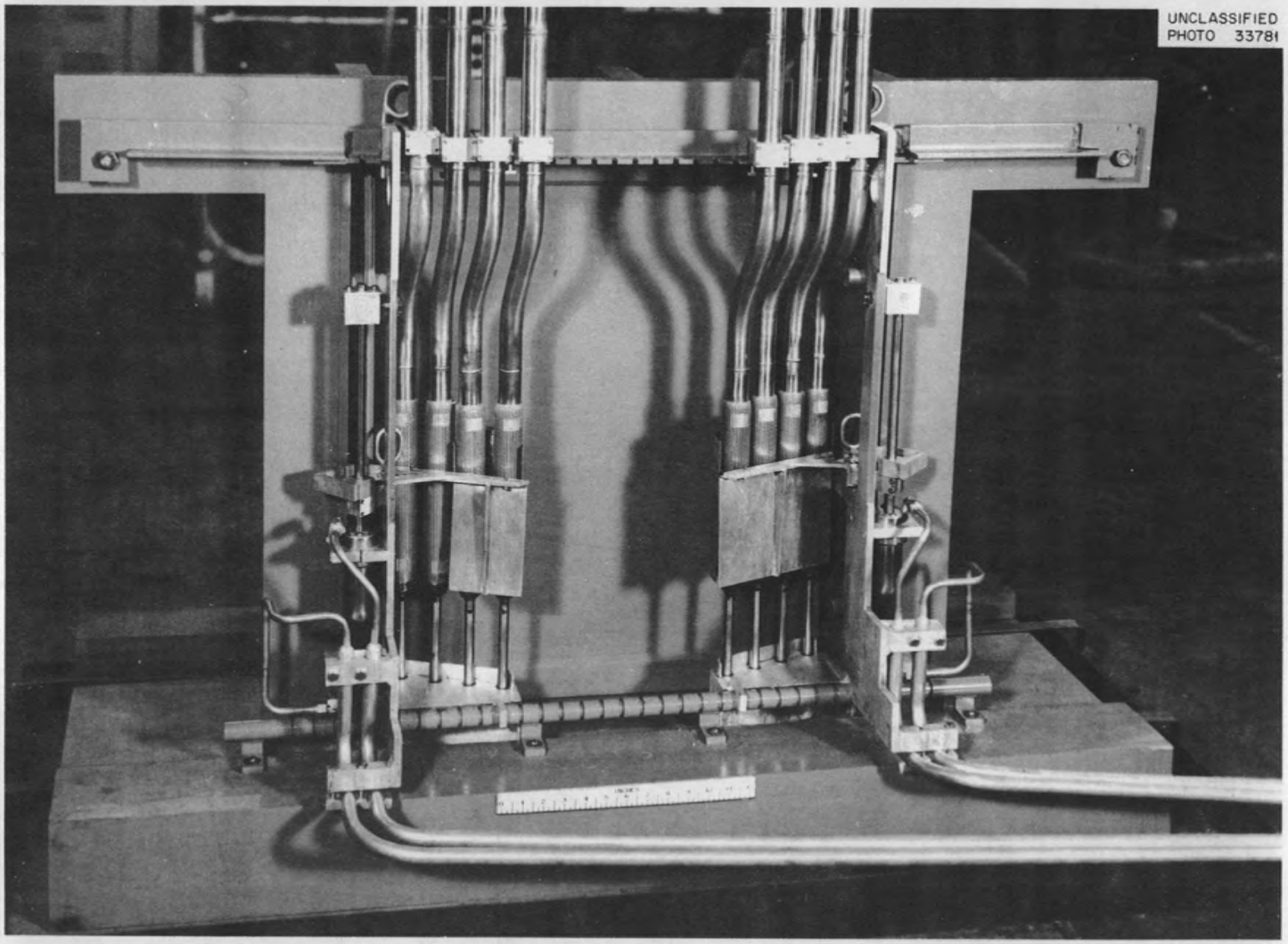


Fig. 6.2. Pool Components and Cadmium Shutter Mechanism for Thermal Cycling of Full-Diameter Prototype Fuel Capsules in the ORR Pool.

lower thermal conductivity of argon to obtain the higher temperatures. A typical set of recent operating conditions is presented in Table 6.1.

Thermal cycling of experiments 03 through 08 by use of the cadmium shutters was conducted during reactor cycle XI. Plots of temperature vs time for capsule 05 for cycling with the use of the shutters and with the use of reactor control are shown, respectively, in Figs. 6.3 and 6.4. Cycling has been discontinued temporarily pending review of the appropriate number of cycles for tests of EGCR fuel.

The first ETR capsule, which was installed to verify flux predictions, has operated for a limited time. The temperature achieved, that is, 1200°F, was below the design value, but the flux is considered to be acceptable for later capsules, since design changes were made to increase the thermal barrier gas gap and to reduce metal spacer conduction.

Control equipment for the 14-unit installation has been completed at the ETR by the Phillips Petroleum Co. Ten capsules fabricated at ORNL have been delivered to the ETR, but installation in the reactor has been delayed repeatedly by interference from several large loop installations.

Reduced-Size Prototype Fuel Capsules

Construction of the helium-cooled loop for operation in the General Electric Test Reactor (GETR) was completed by Ralph M. Rogers Co., Inc. The preliminary check of the loop and instrumentation was completed, and operation of the loop was turned over to the reactor operations group. Shakedown tests with an electrically heated fuel assembly are now in progress to calibrate the cladding thermocouples prior to irradiation of the initial fuel capsule loading.

The loop consists of five irradiation facility tubes mounted in the GETR pool 1 3/4 in. from the reactor vessel and approximately 2 5/8 in. apart. The facility tubes are of concentric-tube design having an inner tube 1.027 in. in diameter into which fuel stringers are inserted for irradiation. A layer of Thermoflex insulation 1/4 in. thick on the interior of the outer tube reduces the heat loss to the

Table 6.1. Operating Conditions for Full-Diameter Prototype Fuel Capsules Being Irradiated in the ORR Pool

| Capsule Number | Argon in Control Gas (%) | Capsule Temperature (°F) | | | | No. of Thermal Cycles | | |
|---|---|---|---|---|---|---|---|---|
| | | Design | Average | Hottest Thermocouple | Coldest Thermocouple | By Use of Experiment Shutter | By Reactor Control | Total |
| 0-1 | 45 | 1300[a] | 1335 | 1412 | 1236 | 0 | 18 | 18 |
| 0-2 | 80 | 1600[b] | 1543 | 1612 | 1461 | 0 | 18 | 18 |
| 0-3 | 61 | 1300[a] | 1299 | 1328 | 1240 | 4 | 18 | 22 |
| 0-4 | 24 | 1300[a] | 1268 | 1300 | 1218 | 4 | 18 | 22 |
| 0-5 | 34 | 1600[b] | 1487 | 1582 | 1365 | 90 | 18 | 108 |
| 0-6 | 100 | 1600[b] | 1484 | 1570 | 1412 | 90 | 18 | 108 |
| 0-7 | 100 | 1300[a] | 1298 | 1409 | 1175 | 90 | 18 | 108 |
| 0-8 | 100 | 1600[b] | 1369 | 1450 | 1240 | 90 | 18 | 108 |

[a]Average temperature indicated by the six thermocouples.

[b]Highest temperature indicated by the thermocouples.

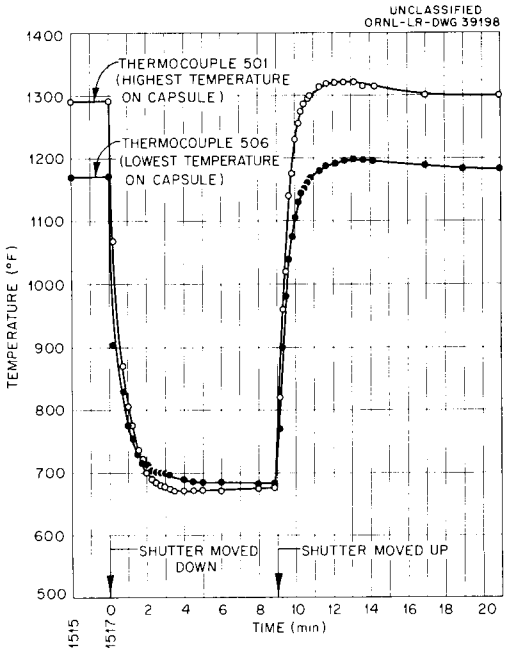


**Fig. 6.3. Temperature vs Time for Thermal Cycling of Experimental Assembly 05 with the Use of Cadmium Shutters.**

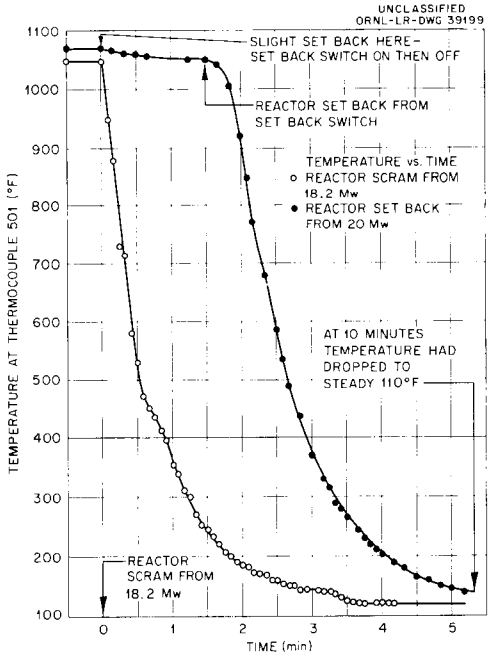


**Fig. 6.4. Temperature vs Time for Thermal Cycling of Experimental Assembly 05 with the Use of Reactor Control.**

reactor pool water. The loop is designed to maintain the helium coolant gas at 780°F and 300 psi at the midpoint of the in-pile section. The upper ends of the facility tubes, which terminate near the top of the reactor vessel, provide the means for inserting and extracting fuel capsules. A view of the loop from the top of the reactor pool is shown in Fig. 6.5. The sheathed thermocouple leads extend through and are sealed in the top can. The helium coolant enters and leaves the facility tube at a point approximately one third of the way down from the top seal by means of 1 1/2-in.-dia stainless steel pipes externally insulated with Thermoflex. The coolant lines penetrate the reactor pool wall at the second floor level of the reactor building, at which point are located the control valves, heaters, and filters shown in Fig. 6.6.

The loop design is predicated on maintenance of a constant capsule surface temperature. This is accomplished by controlling the gas flow and the 15-kw heater output for each facility tube, respectively, by the capsule and exit gas temperatures.

A 32-ft-long, 8-in.-OD, 60-tube economizer provides the gas passage to and from the basement where the compressors, vent tank, dump tanks, precooler and control panel are located. Three 200-$ft^3$ dump tanks provide for storage of the loop gas volume. Four axial-flow-compressors are provided, each in an individual pressure vessel, as shown in Fig. 6.7, to prevent helium leakage to the atmosphere. Two compressors in series provide the required flow of 405 cfm at a pressure drop of 35 psi. A set of two additional compressors is provided for standby protection. The control panel is located adjacent to the pump room area and isolated from it by a heavy concrete shielding wall.

Considerable difficulty has been encountered with the compressors and the shaft seals at the compressor-housing penetrations. Repeated failures have resulted in loss of helium and delays in calibrating the thermocouples. Seals from a different vendor are being installed, and modifications of the compressor housings to enclose the motors are under consideration. The fuel capsule assemblies now installed have

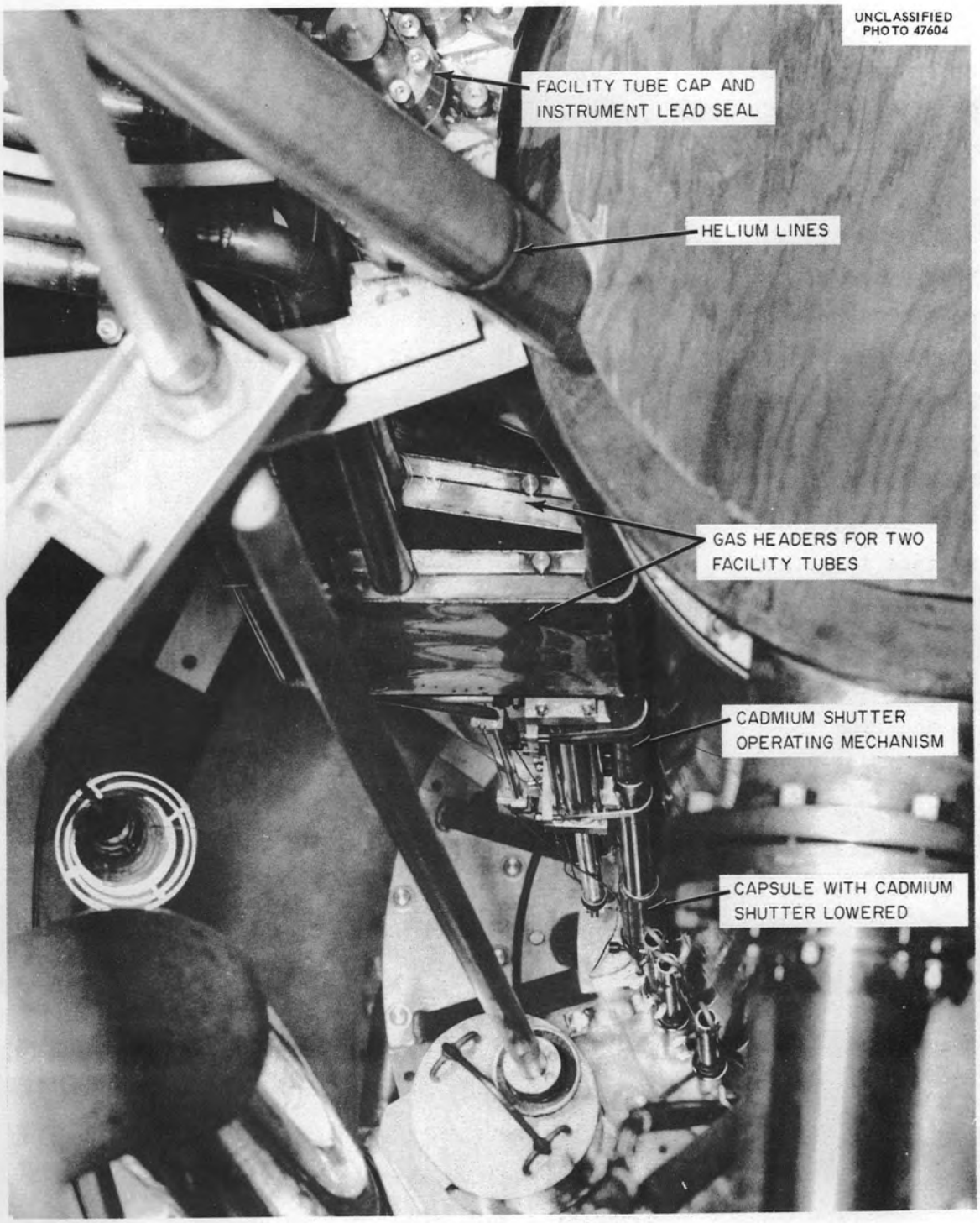


**Fig. 6.5. View of GETR Loop from Top of Reactor Pool.**

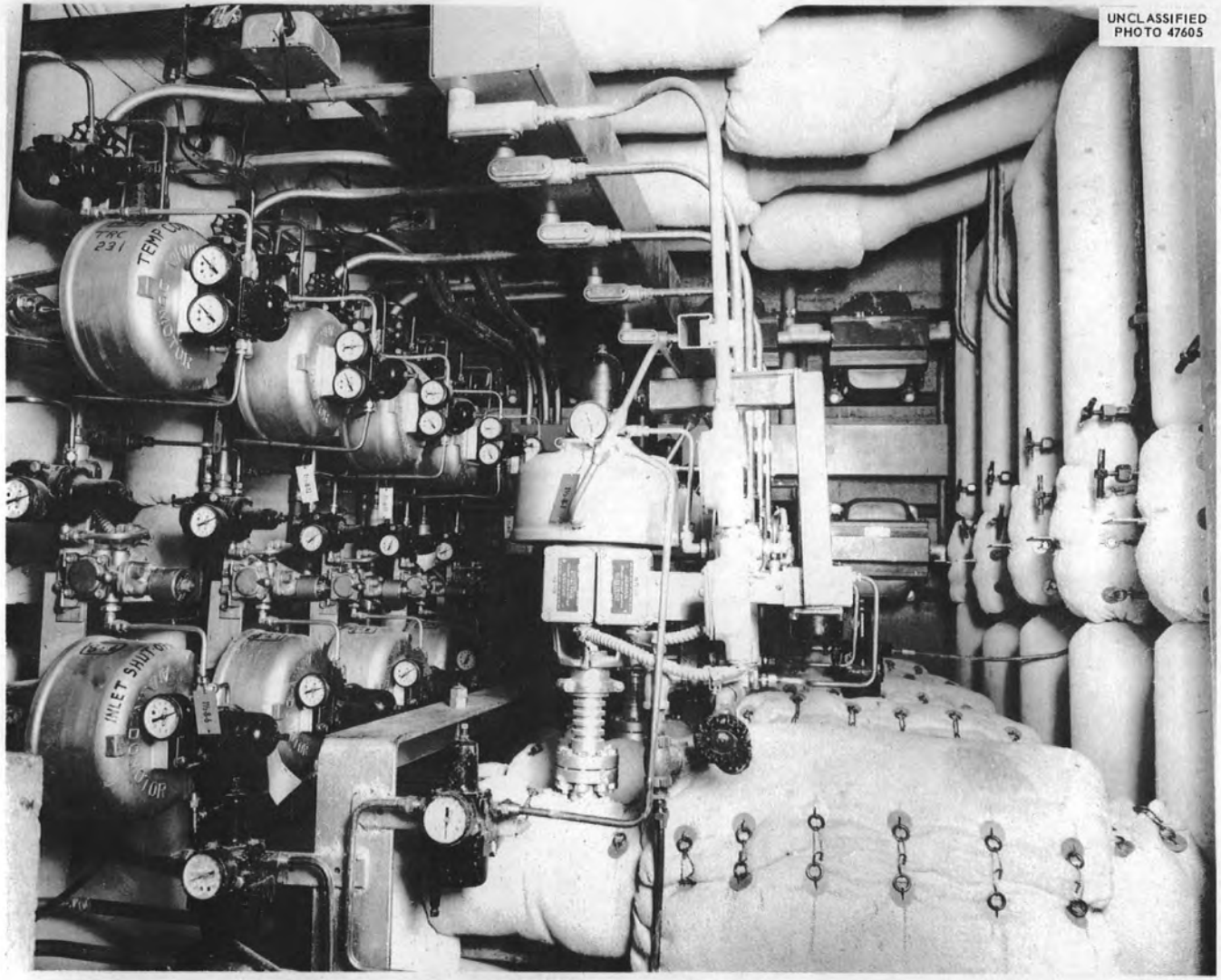


Fig. 6.6. Control Valves, Heaters, and Filters of GETR Loop.

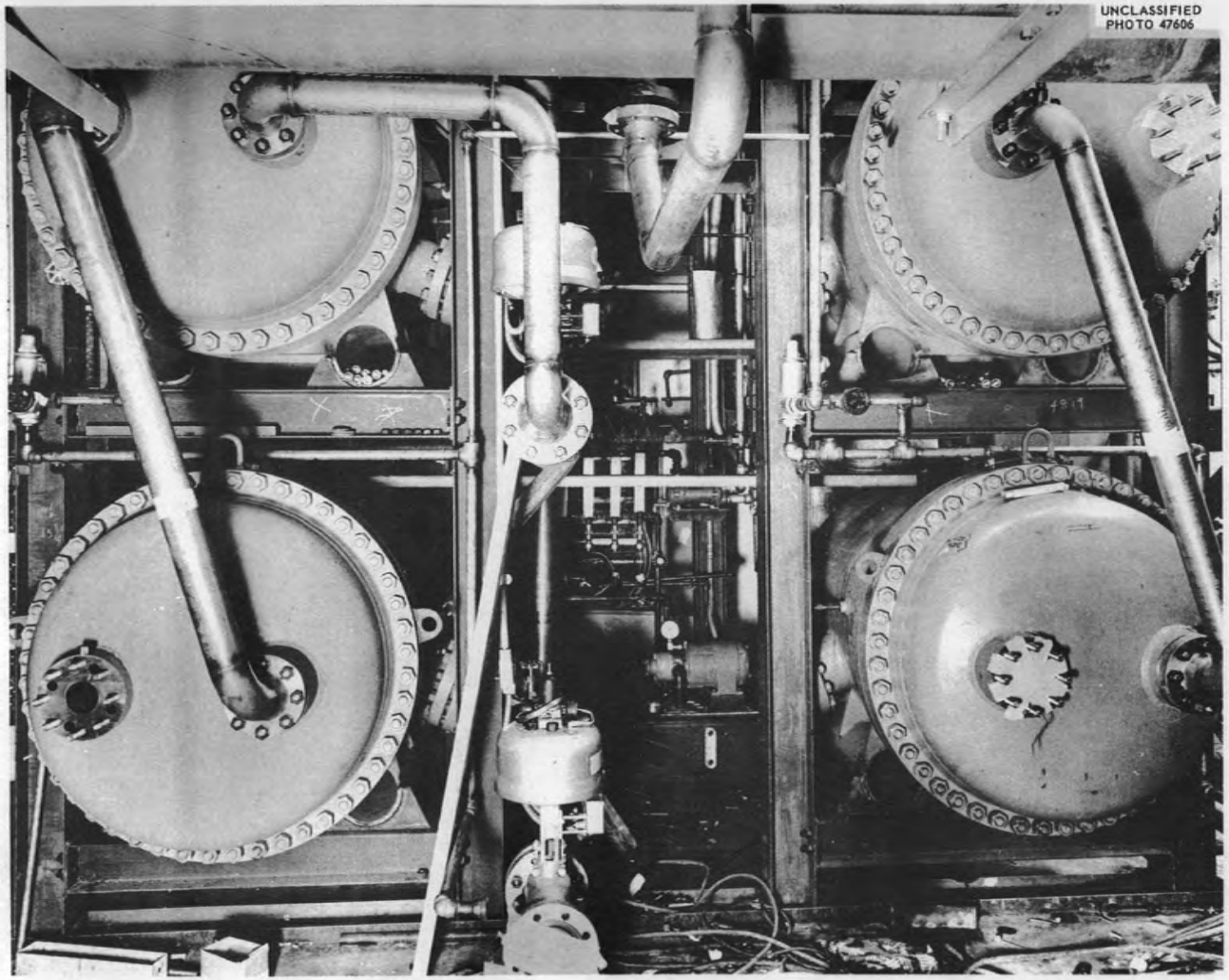


Fig. 6.7. Helium Compressor for GETR Loop.

accumulated little irradiation time.

Four sets of thermal flux measurements were made to determine the unperturbed flux as a function of distance along the facility tube for each of the five irradiation positions and to determine the flux depression of a loaded fuel capsule. The average perturbed thermal flux for each position, as determined from these measurements, is given in Table 6.2. Pellet enrichment values for a design power output of 30,000 Btu/hr·ft that were based on the experimental flux values and estimates of flux variations throughout the reactor cycle are also presented in Table 6.2.

Table 6.2. Average Perturbed Thermal-Neutron Flux for Each Facility and Pellet Enrichment Required for a Design Power Output of 30,000 Btu/hr·ft

| Facility Position | Average Thermal-Neutron Flux (neutrons/cm$^2$·sec) | Pellet Enrichment (wt %) | | |
|---|---|---|---|---|
| | | Lower Capsule | Middle Capsule | Upper Capsule |
| | x $10^{13}$ | | | |
| 1 | 1.82 | 2.6 | 3.5 | 3.8 |
| 2 | 1.73 | 2.6 | 3.5 | 4.1 |
| 3 | 1.73 | 2.6 | 3.5 | 4.1 |
| 4 | 1.61 | 2.9 | 3.8 | 4.1 |
| 5 | 1.80 | 2.9 | 3.5 | 3.8 |

Each of the five parallel facility tubes in the loop is designed to contain a fuel stringer, which consists of three fuel capsules joined together at the ends, as illustrated in Fig. 6.8. Each capsule in the stringer is a separate experimental assembly and contains fuel of the density, enrichment, and configuration desired. The fuel pellets in the capsules are reduced-size prototypes of the GCR-2 pellets and are 0.5 in. OD and 0.5 in. long; some of the pellets are hollow cylinders,

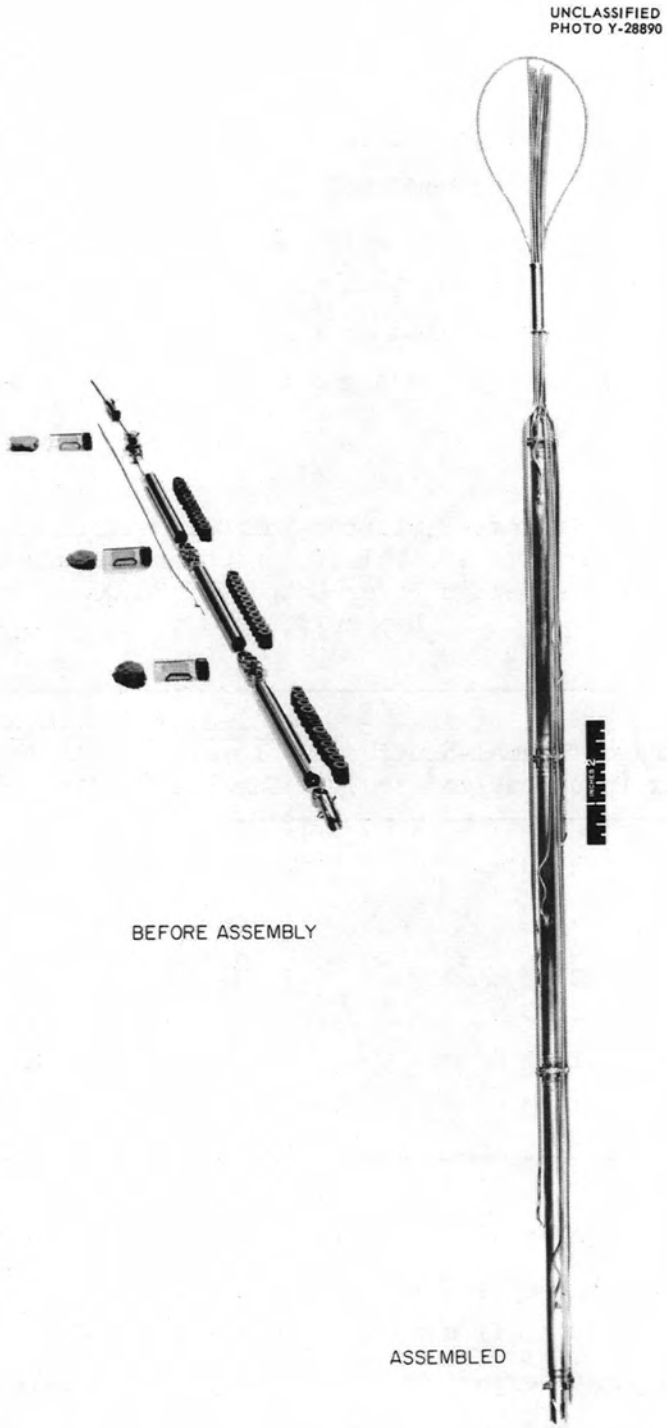


**Fig. 6.8. Fuel Stringer for Irradiation of Reduced-Size Prototype Fuel Capsules in Helium-Cooled Loop in GETR.**

0.23 in. ID. There are 12 pellets in each type 304 stainless steel capsule, which is 6.7 in. long and 0.504 in. ID, with a 14-mil wall. The capsules are fitted with ceramic insulators and spacers at each end and closed with type 304 stainless steel caps.

The surface temperature of each capsule is monitored by three thermocouples. The central temperature of the upper capsule is measured by an internal thermocouple which extends into the fuel. The lower capsule has a thermocouple which extends into the cooling gas in order to measure the temperature of the helium after it passes over the stringer. A stringer of three capsules therefore has eleven thermocouples attached to it. These are Chromel-Alumel stainless-steel-sheathed thermocouples, except the internal thermocouple, which is platinum–platinum-10% rhodium.

The junctions of the thermocouples that monitor the capsule temperatures are formed by the manufacturer and are completely enclosed. The thermocouple is sealed gastight, and the junction is not in contact with the capsule wall. In order to form the junction, the tip of the sheathed thermocouple is bent in a jig to form a 45° angle, and the sheathed end of the thermocouple is spot-welded to the capsule wall. The thermocouple is then torch-brazed to the sheath with a predetermined amount of 85% Ag–15% Mn alloy.

Tests were conducted to determine whether the thermal shock of the brazing would fracture the fuel pellets. Solid pellets were not cracked, but a rejected capsule containing hollow pellets was examined; it was found that the pellets had been fractured beneath every thermocouple junction. The breaks were very clean, and the pellets had not shattered. It was therefore considered that this method of thermocouple attachment would be satisfactory. This method of attachment gives a much stronger joint than can be obtained when a bare wire is attached.

An ORNL representative was present to inspect the welded joints of the capsules and to observe the techniques used in the brazing of the thermocouple attachments. Each of the first five stringers was

thoroughly inspected at each step of construction. Although it is known that the temperature of the thermocouple junction will be less than the true temperature of the capsule, it is hoped that, by the use of careful uniform attachment procedures and uniform manufacturing processes, the differential temperature will be constant for identical conditions.

An experiment was devised by GEVAL (General Electric Company, Vallecitos, California) personnel to measure the difference between the true capsule temperature and that indicated by the sheathed thermocouples. A capsule mockup was fabricated that consists of a section of the capsule tubing with the sheathed thermocouples attached in the usual manner and with bare-wire thermocouples attached both on the outside and on the inside of the tubing. A Globar heater was placed inside the section of tubing to simulate nuclear power. The entire experimental assembly was lowered into a loop facility tube in the GETR, and an attempt was made to measure the difference between the true capsule temperatures (measured by the capsule internal thermocouples) and the temperatures indicated by the external bare-wire and sheathed thermocouples as a function of power, temperature, and coolant mass flow. The results obtained in this test were unsatisfactory because, without the nuclear power of the other stringers, the gas temperatures were too low. The Globar power was only 1/3 of the expected nuclear power, and it was necessary to use low mass flows because of the low temperatures and powers. Further, several of the thermocouples were damaged when the experiment was installed, and thus the desired data could not be obtained.

At the termination of the Globar test, although the results were inconclusive, it was apparent that several hundred degrees difference existed between the true capsule temperature and that measured by the sheathed thermocouple at operating conditions. It was also apparent that the bare-wire thermocouples gave measured temperatures that were much closer to true values.

At the time the Globar test was in operation, the first two stringers, Nos. 1-3 and 1-4, were placed in facility tubes in the

loop. Since the two stringers had been installed and a reactor startup was imminent, a decision was made to allow the stringers to operate at a temperature that allowed a safe margin (400°F) until the Globar mock-up could be rebuilt and retested. In the event that the temperature of the capsule exceeded the temperature limitation (800°F for 50 cfm or above, and 900°F for below 50 cfm) the cadmium shutter of the facility tube was to be lowered.

Two more stringers that were nearly completed were altered by converting one of the thermocouples on each capsule to a bare-wire thermocouple and attaching it at a spot adjacent to a sheathed thermocouple. The open end of the thermocouple was covered with a ceramic cement for insulation. The stringers with bare-wire thermocouples (Nos. 1-1 and 1-2) were then inserted in the reactor. The data obtained from operation of these stringers are, as yet, inconclusive, but apparently there is danger of the bare-wire thermocouples shorting to the thermocouple sheath, despite the presence of the ceramic cement insulation. The fifth stringer (No. 1-5) for the first loading (now under construction) will also have one bare-wire thermocouple on each capsule, but the bare-wire thermocouples will be insulated with ceramic beads to prevent shorting to the sheath.

The Globar mockup has been rebuilt and will be reinserted into the reactor so that the facility will contain four stringers and one Globar heater experiment. The nuclear heat from the four stringers should increase the gas temperatures and provide a more realistic calibration for the sheathed thermocouples. At the time the sheathed thermocouples are calibrated, the operating parameters of the stringers will be reviewed.

Each stringer contains one capsule (the upper one) with a platinum-platinum-10% rhodium central thermocouple. This thermocouple is not influenced by the rate of flow of the coolant. The junction of the thermocouple extends far enough into the hollow pellets for only radial heat losses to be important. The temperature difference across a hollow cylinder, assuming uniform power production, is proportional to

the power and inversely proportional to the thermal conductivity of the cylinder. The central temperatures of the four stringers have not exceeded 1000°F, and the maximum temperature difference from center to capsule has not exceeded 600°F. It is expected that the flux pattern will shift to increase the power at the top of the capsule, but in the short period of operation accumulated thus far there are no indications of a temperature increase. Operation for a full reactor cycle will be necessary to determine the effect of fuel burnup on the flux pattern in the experiment.

The gas temperatures of the experiment (with four stringers contributing fission heat, gas flow reduced to 40 cfm, and preheater power at 100%) have not exceeded 330°F at the inlet header and an estimated 370°F (after passing through the preheater) at the top of the facility tube. The methods of thermocouple attachment, as well as the problems of low gas temperatures, will be reviewed as soon as sufficient operating time has been accumulated to establish the shift of flux with reactor cycle and a thermocouple evaluation test has been completed.

Miniature Capsule Fission-Gas-Release Experiments

Six miniature capsules are installed in LITR facilities for experimental determinations of fission-gas release as a function of temperature, and six capsules have been removed for examination. The capsules are Inconel and they contain hollow, cylindrical, $UO_2$ pellets. Sheathed Chromel-Alumel thermocouples are welded into slots in the capsules to measure the wall temperatures. Pellet central void temperatures have been measured with various high-temperature thermocouples. The apparatus for these irradiations was described previously.[1]

Originally it was planned to investigate the temperature range between 2000 and 3000°F using platinum–platinum-10% rhodium thermocouples, although only limited thermocouple life could be expected at the higher temperatures. Difficulties experienced with internal pellet temperature measurement have, however, caused diversion of considerable

[1] GCR Semiann. Prog. Rep. Dec. 31, 1958, ORNL-2676, p 113.

effort from the main objective to testing of new thermocouples and various methods for their mechanical support. Experience revealed that the platinum thermocouples would fail at about 2200°F if the beads were exposed at the end of the ceramic insulator support. Recessing the beads into the end of the Alundum insulator prolonged their lives, but, at temperatures of 2400 to 2500°F, the emf drifted downward with time, with an indicated decrease of 50°F/day. A magnesium oxide insulated thermocouple sheathed in tantalum, which initially indicated 2360°F, was indicating only 2000°F in about six days.

More recently, rhenium-tungsten thermocouples insulated with beryllium oxide have been used. Two were sheathed in tantalum and a third was supported from the insulator. Two of these failed during the initial heatup; the third (one of the two sheathed in tantalum) is still operating after 850 hr. The initial indicated temperature of 2660°F dropped to 2320°F after numerous reactor shutdowns and remained stable between shutdowns. Tungsten is difficult to use because it is very brittle and easily work-hardened, but the rhenium-tungsten thermocouple appears to show promise for central $UO_2$ pellet temperature measurement. If a successful installation can be developed, these thermocouples should be useful up to temperatures in the range 3000 to 4000°F.

Originally the thermocouples that were tack-welded into grooves cut into the capsule wall were cooled by the high-velocity air stream that cooled the capsule, and they gave erratic temperature measurements. Filling the slot with a high-melting-point silver brazing alloy has reduced variances between measurements at radial locations to the scatter expected from the thermocouple readings.

Thus far, thermocouples for measuring central pellet temperatures have been installed only in the top enclosures of the dual-enclosure capsules. The capsule has now been redesigned to accommodate a thermocouple in each end, and the facility tube has been altered to provide an improved filter arrangement to trap fuel particles in the event of a capsule rupture.

Capsule irradiation experience thus far is described in Table 6.3. The temperatures shown for the "a" capsules are the highest indicated by the thermocouples. The high temperature was usually measured shortly after the initial heatup. Capsule L-2a failed at the pellet central thermocouple insulator seal because of a defective closure weld.

## Examinations of Irradiated Capsules

Eight miniature capsules have been irradiated and removed from the LITR for analysis. Seven of these were double capsules, and thus fifteen samples were available for examination. Included in the eight capsules are those designated $UO_2$-1-1 and $UO_2$-1-2, which were mentioned previously.[2] These capsules were irradiated in the LITR, as stated above, primarily for the purpose of studying fission-product release from $UO_2$. The principal variables in these experiments are operating temperature, $UO_2$ density, power density, and burnup. A summary of the fission-gas-release data obtained thus far is presented in Table 6.4.

### Analysis of Fission-Gas-Release Data

It is premature to try to relate the available fission-gas-release data to existing diffusion equations because of uncertainties in the temperature measurements and the difficulty of interpreting the effect of the temperature gradient between the inside and outside of the fuel pellets. The data show that below central operating temperatures of approximately 2250°F the ratio of radioactive gas existing outside the $UO_2$ pellet (95% theoretical density) to the total existing at the time of sampling is small (~0.04%) and that the variation with temperature is less than 0.005% per 100°F. Only one capsule has been examined that had a central operating temperature of more than 2250°F. This capsule contained pellets of $UO_2$ with a theoretical density of 85% and a central operating temperature of 2550°F. The fission gas release was

[2] GCR Semiann. Prog. Rep. Dec. 31, 1958, ORNL-2676, p 116.

Table 6.3. Operating Conditions for Miniature Capsules Irradiated in the LITR

| Experiment Number | Date Installed | Present Status | Irradiation Time (hr) | $UO_2$ Pellet Theoretical Density (%) | Pellet Enrichment (% $U^{235}$) | Pellet Central Temperature (°F) | LITR Core Location |
|---|---|---|---|---|---|---|---|
| L-1a | 10-23-58 | Removed 2-25-59 | 2479 | 93.2 | 10 | 1850 | C-47 |
| 1b | | | 2479 | 93.2 | 10 | 2100[a] | C-47 |
| L-2a | 2-25-59 | Ruptured and removed 4-7-59 | 726 | 84.8 | 20 | 2480 | C-47 |
| 2b | | | 726 | 84.8 | 20 | 2540[a] | C-47 |
| L-3a | 5-19-59 | In operation | | 75 | 10 | (b) | C-28 |
| 3b | | | | 75 | 10 | | C-28 |
| L-4a | 9-30-58 | Removed 4-28-59 | 4194 | 92.5 | 10 | 2350 | C-42 |
| 4b | | | 4194 | 92.5 | 10 | 2500[a] | C-42 |
| L-6a | 10-23-58 | Removed 5-18-59 | 4208 | 73.6 | 10 | 2250 | C-28 |
| 6b | | | 4208 | 74.2 | 10 | 2500[a] | C-28 |
| L-7a | 3-17-59 | In operation | | 95.3 | 10 | 2160 | C-57 |
| 7b | | | | 95.3 | 20 | 2600[a] | C-57 |
| L-8a | 4-28-59 | In operation | | 84.6 | 20 | 2660 | C-47 |
| 8b | | | | 85.0 | 20 | | C-47 |
| L-13a | 11-11-58 | In operation | | 92.9 | 10 | 2230 | C-46 |
| 13b | | | | 92.9 | 10 | 2560[a] | C-46 |
| L-14a | 12-30-58 | Removed 3-17-59 | 1565 | 94.7 | 20 | 2080 | C-57 |
| 14b | | | 1565 | 94.7 | 20 | 2260[a] | C-57 |
| L-15a | 12-22-58 | Removed 4-7-59 | 2155 | 91.6 | 20 | 1620 | C-58 |
| 15b | | | 2155 | 89.7 | 20 | 2055[a] | C-58 |
| L-18a | 4-28-59 | In operation | | 84.9 | 30 | (c) | C-42 |
| 18b | | | | 85.2 | 30 | | C-42 |
| L-17a | 4-7-59 | In operation | | 93.7 | 30 | 2410 | C-58 |
| 17b | | | | 93.8 | 30 | 2600[a] | C-58 |

[a]Estimated from capsule wall and "a" capsule center temperature measurements.
[b]Calculated temperature 3000°F; rhenium-tungsten thermocouple failed during heatup.
[c]Calculated temperature 2760°F; rhenium-tungsten thermocouple failed during heatup.

**Table 6.4. Fission Gas Release from LITR Capsules**

| Capsule Number | Central $UO_2$ Temperature (°F) | Temperature Difference Across $UO_2$ (°F) | Pellet Enrichment (% $U^{235}$) | Irradiation Flux (neutrons·$cm^{-2}$·$sec^{-1}$) | Bumup (Mwd/MT) | $UO_2$ Density (% of theoretical) | Fission Gas Existing at Time of Reactor Shutdown (disintegrations/min, dpm) | | | | | Percentage of Existing Fission Gas Which Escaped from the $UO_2$ | | | | |
|---|---|---|---|---|---|---|---|---|---|---|---|---|---|---|---|---|
| | | | | | | | $Kr^{85m}$ | $Kr^{88}$ | $I^{131}$ | $Xe^{133}$ | $Xe^{135}$ | $Kr^{85m}$ | $Kr^{88}$ | $I^{131}$ | $Xe^{133}$ | $Xe^{135}$ |
| | | | | $\times 10^{13}$ | | | | | | | | | | | | |
| $UO_2$-1-1 | 1760 | 100 | 15 | 1 | 4,800 | 96 | $3.2 \times 10^{12}$ | | $5.8 \times 10^{12}$ | $1.4 \times 10^{13}$ | $5.6 \times 10^{12}$ | 0.026 | | $1.3 \times 10^{-4}$ | $9.1 \times 10^{-3}$ | $2.4 \times 10^{-3}$ |
| $UO_2$-1-2a | 1770 | 280 | 15 | 3.1 | 16,000 | 96 | | $2.4 \times 10^{13}$ | $1.9 \times 10^{13}$ | $4.2 \times 10^{13}$ | $7.8 \times 10^{12}$ | | 0.01 | $2.7 \times 10^{-6}$ | 0.033 | 0.012 |
| $UO_2$-1-2b | 2000 | | 15 | 3.1 | 16,000 | 97 | | $2.4 \times 10^{13}$ | $1.9 \times 10^{13}$ | $4.2 \times 10^{13}$ | $7.8 \times 10^{12}$ | | 0.02 | $4.9 \times 10^{-6}$ | 0.033 | 0.012 |
| L-1a* | 1600 | 300 | 10 | 2.8 | 7,000 | 95 | | | | | | | | | | |
| L-1b* | 2100 | | 10 | 2.8 | 7,000 | 95 | | | | | | | | | | |
| L-14a | 2100 | 300 | 20 | 1.6 | 7,000 | 95 | $8.5 \times 10^{12}$ | $2.1 \times 10^{13}$ | $1.7 \times 10^{13}$ | $3.8 \times 10^{13}$ | $1.1 \times 10^{13}$ | 0.029 | 0.011 | $1.3 \times 10^{-5}$ | 0.014 | 0.006 |
| L-14b | 2200 | | 20 | 1.6 | 7,000 | 95 | $8.5 \times 10^{12}$ | $2.1 \times 10^{13}$ | $1.7 \times 10^{13}$ | $3.8 \times 10^{13}$ | $1.1 \times 10^{13}$ | 0.057 | 0.019 | $1.7 \times 10^{-5}$ | 0.029 | 0.017 |
| L-15a | 1600 | 200 | 20 | 1.4 | 7,000 | 95 | $7.1 \times 10^{12}$ | $1.8 \times 10^{13}$ | $1.6 \times 10^{13}$ | $3.2 \times 10^{13}$ | $1.0 \times 10^{13}$ | 0.019 | 0.004 | $5.5 \times 10^{-5}$ | 0.010 | 0.004 |
| L-15b* | 1900 | | 20 | 1.4 | 7,000 | 95 | | | | | | | | | | |
| L-2a* | 2400 | 500 | 20 | 2.5 | 5,000 | 85 | | | | | | | | | | |
| L-2b | 2500 | | 20 | 2.5 | 5,000 | 85 | | | | $5.0 \times 10^{13}$ | | | | | 9.0 | |
| L-4a | 1600 | 200 | 10 | 1.5 | 13,000 | 95 | $6.9 \times 10^{12}$ | $1.7 \times 10^{13}$ | | $3.1 \times 10^{13}$ | $6.3 \times 10^{12}$ | 0.011 | 0.021 | | 0.028 | $8.5 \times 10^{-3}$ |
| L-4b | 1900 | | 10 | 1.5 | 13,000 | 95 | $7.0 \times 10^{12}$ | $1.7 \times 10^{13}$ | | $3.1 \times 10^{13}$ | $6.4 \times 10^{12}$ | 0.012 | 0.020 | | 0.04 | $7.5 \times 10^{-3}$ |

*Capsule L-1 was used only for the postirradiation heatup experiment; capsules L-15b and L-2a had lost their gas.

9% of the existing $Xe^{133}$, which is more than 200 times that found for any of the lower temperature experiments. It seems that this increase in fission gas release can be attributed mostly to temperature rather than to the decrease in density, because, as described below, a capsule containing pellets of 95% theoretical density evolved 5.5% of the $Xe^{133}$ existing at the time of heating when subjected to a post-irradiation heat treatment at 2500°F.

Post-irradiation heat treatments, at 2100°F and 2500°F, of two capsules (L-1a and L-14) caused the evolution of considerable amounts of solid fission products, as indicated in Table 6.5. The evolution of $Xe^{133}$ from capsule L-14 was 5.6% compared with 0.02% before heating. The evolution of $Xe^{133}$ from capsule L-1 was not determined because of possible interference with the $I^{131}$ measurement. Methods of collection of the fission products were changed as improvements were suggested to facilitate the operation and to obtain more accuracy in the analyses, and equipment has been developed to measure the gases as well as the solids in future heating experiments.

For the measurements described in Table 6.5, capsule L-1 was placed in an Inconel tube and heated in a tube furnace. Three hours were required to reach a temperature of 2100°F, and this temperature was held for 1 hr. An 0.8-μ Millipore filter and a liquid-nitrogen-cooled charcoal trap were placed in series with the tube, as shown schematically in Fig. 6.9. Purified helium was passed slowly over the sample. A pressure of ~1 to 10 mm Hg was maintained in the furnace tube. When the apparatus was disassembled, the activity measured through the walls of the apparatus was approximately 20 r/hr at 6 in. from the heated portion of the tube, 500 mr/hr at the filter assembly, and 10 r/hr at the charcoal trap. The tube was washed in 6 N NaOH for 45 min and then rinsed. This was followed by a 6 N $HNO_3$ wash. The tubing was still active and was then placed in aqua regia, where most of the exterior oxide was taken off before the activity was brought down. Aliquots of each solution were taken for analysis.

Table 6.5. Evolution of Solid Fission Products by Post-Irradiation Heat Treatment

| | Fission-Product Isotope | | | | | |
|---|---|---|---|---|---|---|
| | $Nb^{95}$ | $Zr^{95}$ | $I^{131}$ | $Cs^{137}$ | $Sr^{89}$ | $Ru^{103}$ |
| Capsule L-1 | | | | | | |
| Total fission-product isotope activity at time of reactor shutdown, dpm | $2.8 \times 10^{13}$ | $4.4 \times 10^{13}$ | $3.0 \times 10^{13}$ | $4.3 \times 10^{11}$ | $2.2 \times 10^{13}$ | $2.4 \times 10^{13}$ |
| Percentage of fission-product isotope evolved by post-irradiation heating to 2100°F | 0.16 | 0.05 | 12.4 | 11.4 | 0.02 | 0.007 |
| Capsule L-14 | | | | | | |
| Total fission-product isotope activity at time of reactor shutdown, dpm | $1.7 \times 10^{13}$ | $3.7 \times 10^{13}$ | $3.3 \times 10^{13}$ | $3.0 \times 10^{11}$ | $3.0 \times 10^{13}$ | $2.3 \times 10^{13}$ |
| Percentage of fission-product isotope evolved by post-irradiation heating to 2500°F | 0.005 | 0.007 | 7.4 | 5.5 | 0.01 | 0.001 |

Capsule L-14 was heated to 2500°F in a mullite tube. A small charcoal trap, heated to 150°C, was placed next to the mullite tube to extract iodine and other solid fission products from the inert gases before the gases were collected in the liquid-nitrogen-cooled charcoal trap, as shown in Fig. 6.10. No helium sweep gas was used in this experiment. The time required for heatup was 3 hr, and the capsule was held at 2500°F for 1 hr. The method of collection was the same as that used for capsule L-1, except that a copper-foil sleeve was placed in the cold end of the mullite tube. The copper foil was dissolved directly in 6 N $HNO_3$, except for a small piece cut from it. This small piece was washed in an alkaline solution and then processed. The analyses showed that most of the iodine was lost in the piece dissolved directly in $HNO_3$. The ratio of cesium fission-product activity in the solution of foil dissolved directly in the $HNO_3$ to that in the sample first processed in caustic was 10 to 1. The iodine yield was calculated by multiplying the amount found in the small piece by ten.

Capsule L-15 was heated to 1500°F in one system and then heated to 2100°F in another. The fission products evolved were collected separately and are being analyzed.

The short half-life fission products had decayed by the time the analytical results presented in Table 6.2 had been obtained. The fission products, $Nb^{95}$, $Zr^{95}$, $Sr^{89}$, and $Ru^{103}$ were evolved in small amounts, but up to 12% of the $I^{131}$ and $Cs^{137}$ existing in the $UO_2$ at that time was evolved during the heat treatment. Since many iodides, including CsI, have boiling points below 2500°F, the effect of pressure buildup due to these isotopes in fuel elements containing $UO_2$ operating above 2250°F needs to be investigated further.

The measurements of fission products have been made thus far with the use of gamma- and beta-ray spectroscopy or ion chambers. The stable fission products have not been measured because their concentrations in samples of gas taken directly from the capsules are too small for measurement on the mass spectrometer when the concentrations of

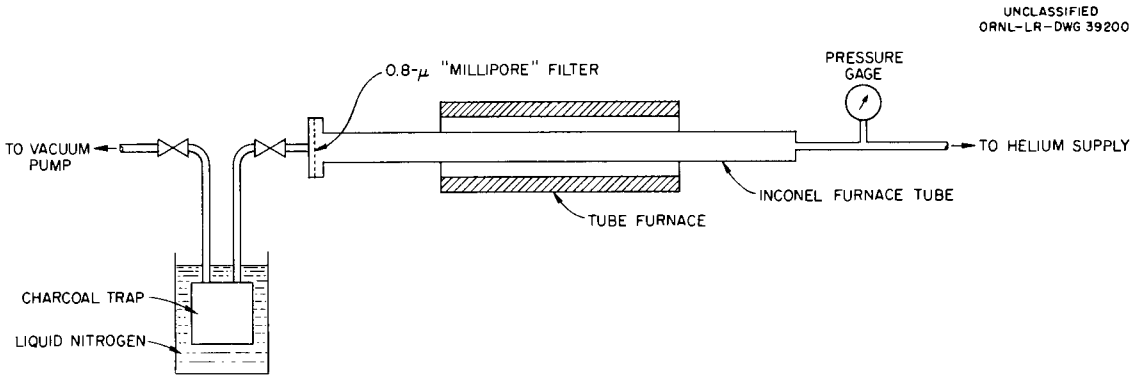


**Fig. 6.9. Apparatus for Post-Irradiation Heat Treatment of Capsule L-1.**

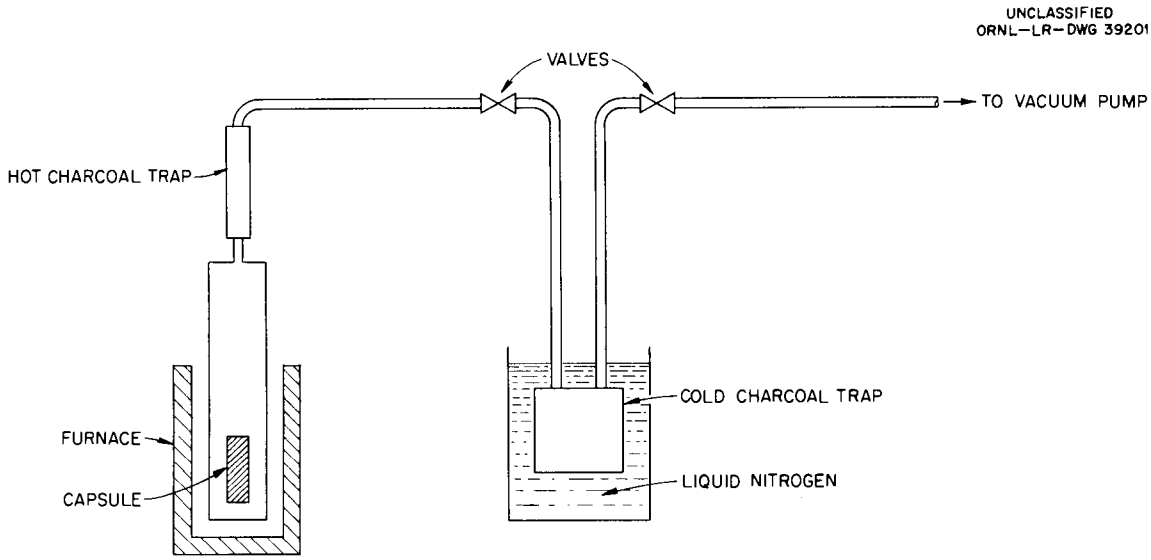


**Fig. 6.10. Apparatus for Post-Irradiation Heat Treatment of Capsule L-14.**

radioactive products is low enough for safe handling. An apparatus is being constructed which will remove non-fission-gas contaminants and concentrate the xenon and krypton by means of a Toepler pump. It will be used in conjunction with post-irradiation heat treatments to obtain suitable mass spectrometer samples.

As discussed in the preceding section, difficulties with the thermocouples have precluded accuracy in the measurements of the temperatures reported for the fission-gas-release experiments. Bench tests are planned for the development of more reliable thermocouples for these experiments as soon as a high-temperature inert-atmosphere furnace can be obtained. In the meantime, the best temperatures obtained from initial readings, calculated values, and comparisons with previous low-temperature irradiations will be used. The difference between calculated temperatures and initial temperatures for all capsules containing platinum—platinum-rhodium thermocouples is reported to be less than 100°F. Temperature measurements available for post-irradiation heat treatments are more accurate than the in-pile measurements and may be used to verify gas release vs temperature data obtained for in-pile experiments.

Method of Calculation of Fission-Product Evolution

The calculations of fission-product evolution are based on the work of Blomeke and Todd,[3] in which $N_t$, the number of fission-product atoms of a particular species present at decay time t, is given by

$$N_t = \left(\frac{N_s}{N_{25}^o}\right) \quad N_{25}^o \left(\frac{N_\tau}{N_s}\right)\left(\frac{N_t}{N_\tau}\right) \quad ,$$

where $N_s/N_{25}^o$ is the saturation value of the fission-product atom per initial atom of $U^{235}$ and is a function of neutron flux; $N_{25}^o$ is the

[3] J. O. Blomeke and Mary F. Todd, Uranium-235 Fission-Product Production as a Function of Thermal Neutron Flux, Irradiation Time, and Decay Time, ORNL-2127 (Aug. 19, 1957).

number of $U^{235}$ atoms initially present in the sample; $N_\tau/N_s$ is the fraction of saturation attained in irradiation time $\tau$, which may be a function of neutron flux as well as of $\tau$; $N_t/N_\tau$ is the ratio of the fission-product atoms existing at decay time t to those existing at the end of the irradiation. The terms $N_s/N_{25}^o$, $N_\tau/N_s$, and $N_t/N_\tau$ are presented in graphical form for the more plentiful fission-product species in the report by Blomeke and Todd.[3]

In using the equation for $N_t$, $N_{25}^o$ is obtained from the weights of the pellets and the nominal enrichment. The neutron flux is obtained from analysis of cobalt-aluminum alloy flux monitors. The irradiation time, $\tau$, is obtained by dividing the kilowatt-hours of power generated by the reactor while the sample is in the reactor by 3000 kw, the nominal operating power of the reactor. The assumption is made that this irradiation time is continuous; that is, the reactor downtime while the sample is in the reactor is disregarded. Since the flux-monitor calibration is based on the same assumptions, the results should not be greatly in error, except possibly for short-lived elements.

For the calculations of evolution of radioactive noble-gas fission products, the volume of the collection bottle is measured, and the fractional volume of the sample is determined from the known volumes of the collection apparatus. A gamma-ray spectrum analysis of the sample is then made. The time elapsed between reactor shutdown and the time the sample is removed from the collection apparatus is considered to be the decay time, $t_d$. The time elapsed between the sampling time and the counting is called the counting time, $t_c$. The decay constants are obtained from the report by Blomeke and Todd.[3]

The data are then indicated as the ratio of measured to calculated activity at reactor shutdown, $(\lambda N_\tau)_{meas}/(\lambda N_\tau)_{calc}$, where $(\lambda N_\tau)_{meas}$ is the disintegrations per sample per second at counting time $t_c$ times $e^{\lambda t_c}$ divided by the fractional volume of the sample times $N_{t_d}/N_\tau$. The value of $N_{t_d}/N_\tau$ is obtained from reference 3. The calculated values are obtained from the expression

$$(\lambda\ N_\tau)_{calc} = \lambda \left(\frac{N_s}{N_{25}^o}\right) \quad N_{25}^o \left(\frac{N_\tau}{N_s}\right) ,$$

where all but $N_{25}^o$ are obtained from reference 3 by using appropriate values of flux and $\tau$.

The volatile radioactive fission products are treated somewhat similarly; that is, fractional volumes of various washings, samplings, etc., are counted and the results are calculated back to reactor shutdown.

Post-Irradiation Pellet and Capsule Examinations

Upon completion of the fission-product sampling, all the capsules removed from the reactor thus far have been shipped to GEVAL to be opened and examined. Of the nine capsules shipped to GEVAL, work is essentially completed on three; the remaining six capsules were shipped only recently. Operating data for the pellets that have been examined are listed below:

| | $UO_2$-1-1 and $UO_2$-1-2 | $UO_2$-2-1 |
|---|---|---|
| Burnup | 4800 Mwd/MT | 92 Mwd/MT (bottom pellets) |
| Density | 96% of theoretical | 95% of theoretical |
| Pellet dimensions | 0.156 in. OD, 0.078 in. ID | 3/4 in. OD, 0.25 in. ID |
| Inner $UO_2$ temperature | 1760°F | 1850°F |
| Outer $UO_2$ temperature | 1670°F | 950°F (cladding) |
| Thermal cycles | 52 | 30 |
| Enrichment of $UO_2$ | 15% $U^{235}$ | 1.9% $U^{235}$ |

Results of Examination of Capsule $UO_2$-1-1. The pellets were all cracked radially, except for the bottom half-pellet, as shown in Fig. 6.11. This exception indicates that the thermal stress barely exceeded the tensile strength of the $UO_2$. The thermal stress has been calculated to be 12,600 psi. An orange- to rust-colored deposit

was noted on the insides of the pellets and on the thermocouple. A gamma-ray scan of this material indicated typical fission products, but there was insufficient material for a detailed analysis. The presence of titanium from the titanium getter in the capsule was suspected, but none was found in a chemical analysis of the deposit. The Chromel-Alumel thermocouple appeared to be undamaged. Dimensional measurements made on the uncracked half-pellet showed the change caused by irradiation to be less than 1%, which was the maximum error in the original measurement.

Results of Examination of Capsule $UO_2$-1-2. The capsule was accidentally torn apart during the opening process, and some of the pellets were broken. The pellet at the center of the capsule, shown in Fig. 6.12, was least damaged by the accident. No more radial cracks were found than in most of the pellets in capsule $UO_2$-1-1, although the thermal stress was calculated to be approximately three times greater. The thermocouple in this capsule was also in good condition.

Results of Examination of Capsule $UO_2$-2-1. The capsule was a full-diameter prototype, which was described previously.[4] During the first two thirds of the irradiation time the capsule was in such a high flux position that it could not be fully inserted into the reactor lattice. Consequently the flux ranged from $\sim 0.036 \times 10^{13}$ neutrons/cm$^2$·sec at the top to $\sim 0.84 \times 10^{13}$ neutrons/cm$^2$·sec at the bottom. The latter third of the operating time was in a fairly uniform flux of approximately $1 \times 10^{13}$ neutrons/cm$^2$·sec. Temperatures of the cladding ranged from ~900°F at the top to ~1650°F at the bottom. The temperature in the center of the $UO_2$ pellets in the middle zone of the capsule was ~1830°F.

A red- to orange-colored scale was noted on the surface of the type 304 stainless steel cladding, and a crack was found at one of the Chromel-Alumel thermocouple attachment positions. The thermocouple

[4] GCR Semiann. Prog. Rep. Dec. 31, 1958, ORNL-2676, p 114.

Fig. 6.11. $UO_2$ Pellets from Capsule $UO_2$-1-1 After Irradiation.

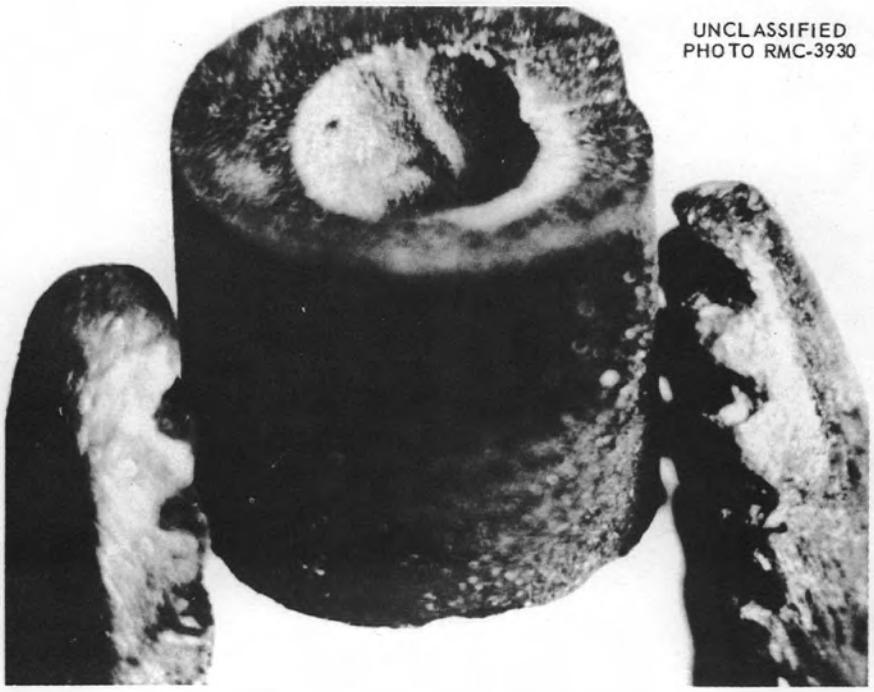


Fig. 6.12. $UO_2$ Pellet from Capsule $UO_2$-1-2 After Irradiation.

was attached by spark-discharge welding, and the joint was reinforced with Coast-Metals alloy No. 52, a brazing alloy containing a small amount of boron and silicon. A cap through which the thermocouple entered the capsule was positioned directly over the point of attachment. This cap altered the flow pattern of the cooling water on the outer surface of the capsule and could have caused some thermal stress of the capsule. An over-all view of the fuel pellets is presented in Fig. 6.13, and an end view of the bottom pellet before removal is presented in Fig. 6.14.

Density Measurements. Measured density changes showed an increase of 1% for the $UO_2$ of capsule $UO_2$-1-1 and decreases of 2% and 1% for the top and bottom sections, respectively, of the $UO_2$ of capsule $UO_2$-1-2. These changes are less than the expected error in measurements of such small fragments. The change in density of the larger pieces of $UO_2$ in capsule $UO_2$-2-1 was less than 1%.

Burnup Measurements. Analyses of cobalt-foil activation measurements and $Cs^{137}$-to-$U^{235}$ ratio measurements have yielded two different sets of burnup data. It is suspected that diffusion of the cesium may cause varying concentrations through the fuel and thus cause the cesium-to-uranium ratio to be useless unless an average can be taken. A check on the measurements will be made by mass spectrometer analysis of the $U^{236}$-to-$U^{235}$ ratio. The as-received burnup data, that is, the percentage of $U^{235}$ which fissioned, are given in Table 6.6.

Fission Products Leached from the Capsule Walls. Each capsule was leached in 8 N $HNO_3$ for 14 to 17 days, and the solutions were analyzed for $Cs^{137}$ and $Sr^{89}$. The first leach was checked at 8 days and at 17 days, and no significant change in activity was found. The cesium was precipitated in duplicate with chloroplatinic acid after removal of other fission products by scavenging. The dry precipitate was compared to a cesium standard on a 256-channel gamma-ray spectrometer. The strontium was precipitated in duplicate with ammonium oxalate after removal of other fission products by scavenging and precipitation. The dry precipitate was beta-ray counted. Samples of these leach

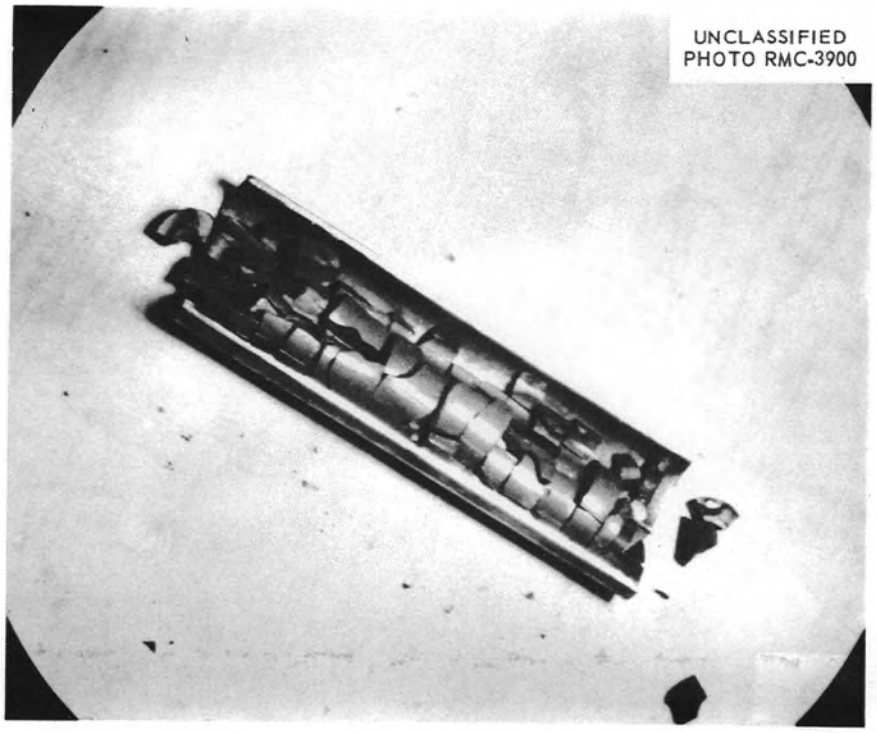


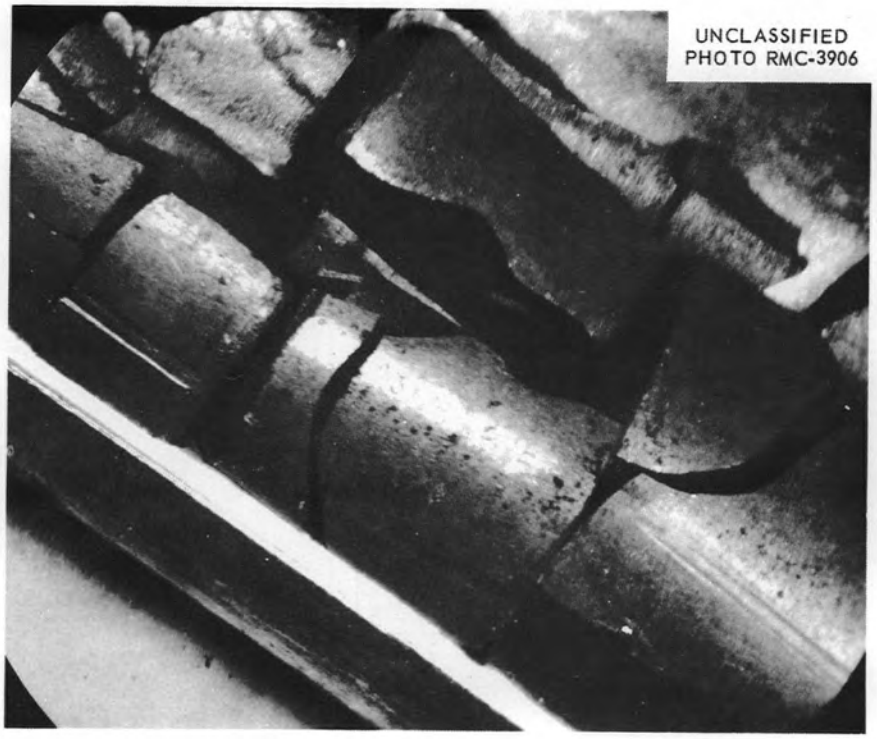


Fig. 6.13. $UO_2$ Pellets in Capsule $UO_2$-2-1 After Irradiation.

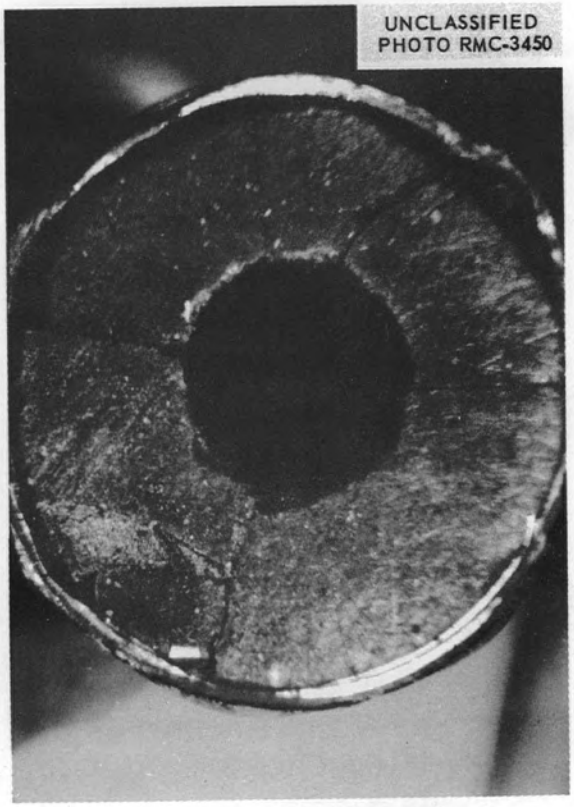


Fig. 6.14. End View of $UO_2$ Pellet in Capsule $UO_2$-2-1 After Irradiation.

Table 6.6. Burnup Data for Capsules $UO_2$-1-1, $UO_2$-1-2, and $UO_2$-2-1

| Capsule | Pellet Enrichment (% $U^{235}$) | Burnup from Cesium-Uranium Ratio (%) | Burnup from Cobalt Activation (%) |
|---|---|---|---|
| $UO_2$-1-1 | 15 | 5.0 | 3.8 |
| $UO_2$-1-2 top | 15 | 6.8 | 12.7 |
| $UO_2$-1-2 bottom | 15 | 6.7 | 12.7 |
| $UO_2$-2-1 bottom | 1.8 | 0.5 | 0.6 |

solutions were analyzed on the 256-channel spectrometer.

The amounts of $Cs^{137}$ and $Sr^{89}$ found on the capsule walls are compared with the total amounts existing, corrected to time of reactor shutdown,[3] in Table 6.7. These values may be affected by the addition of activity from $UO_2$ dust clinging to the capsule walls.

Table 6.7. Fission Products Found on Capsule Walls

| | Fission Product | |
|---|---|---|
| | $Cs^{137}$ | $Sr^{89}$ |
| Capsule $UO_2$-1-1 | | |
| Calculated total fission-product activity at time of reactor shutdown, dpm | $6.5 \times 10^{10}$ | $6.2 \times 10^{12}$ |
| Percentage found on cladding | 7 | 1.8 |
| Capsule $UO_2$-1-2 | | |
| Calculated total fission-product activity at time of reactor shutdown, dpm | $4.4 \times 10^{11}$ | $3.8 \times 10^{13}$ |
| Percentage found on cladding | 0.1 | 0.07 |
| Capsule $UO_2$-2-1 | | |
| Calculated total fission-product activity at time of reactor shutdown, dpm | $6.9 \times 10^{10}$ | $9.8 \times 10^{12}$ |
| Percentage found on cladding | 0.08 | 0.04 |

## Instantaneous Fission-Gas-Release Experiment

The instantaneous fission-gas-release experiment described in the previous report[5] has now been in operation for about three months. The layout of the experimental apparatus is shown in Fig. 6.15, and a flow diagram for the experiment is shown in Fig. 6.16. The desired power in the fuel is obtained by automatically positioning the sample in the reactor. The temperature desired at a given power is obtained by varying the air flow past the fuel capsule. Fission gases evolved from the sample are entrained in a variable-flow helium stream and carried past a high-level Geiger-Mueller counter and a scintillation counter. The output of the scintillation counter is fed to a single-channel, pulse-height analyzer. Since the rate of helium sweep can be varied, the time of decay of the fission products entrained in the helium stream can be varied. The apparatus, as installed initially, contained a sample of $ThO_2$-$UO_2$ that was 4 wt % $U^{235}$. A schematic diagram of the fuel capsule is presented in Fig. 6.17. The apparatus performed satisfactorily in the initial test with only minor changes.

The activity of the fission products in the gas stream was unexpectedly higher than was predicted by capsule tests in which only long-lived isotopes were measured. At a fuel temperature of 1820°F, the activity of the gas stream was observed to reach an apparent equilibrium value in 1 hr of irradiation time, and it is thought that the time was extended somewhat by drift of the measuring equipment. The true equilibrium time was probably somewhat less than 1 hr.

The time to reach equilibrium becomes significant only after decay times of longer than 1 min, as indicated in Fig. 6.18. For times shorter than 6 min the shorter-lived elements dominate the gas activity. The gas activity increases by a factor of 25 between a 12.5-min decay time and a 0.8-min decay time. It is to be emphasized that the gas evolves at a constant rate fixed by the number of fissions per second and the temperature of the sample. The only variable is the length of

[5] GCR Semiann. Prog. Rep. Dec. 31, 1958, ORNL-2676, p 135.

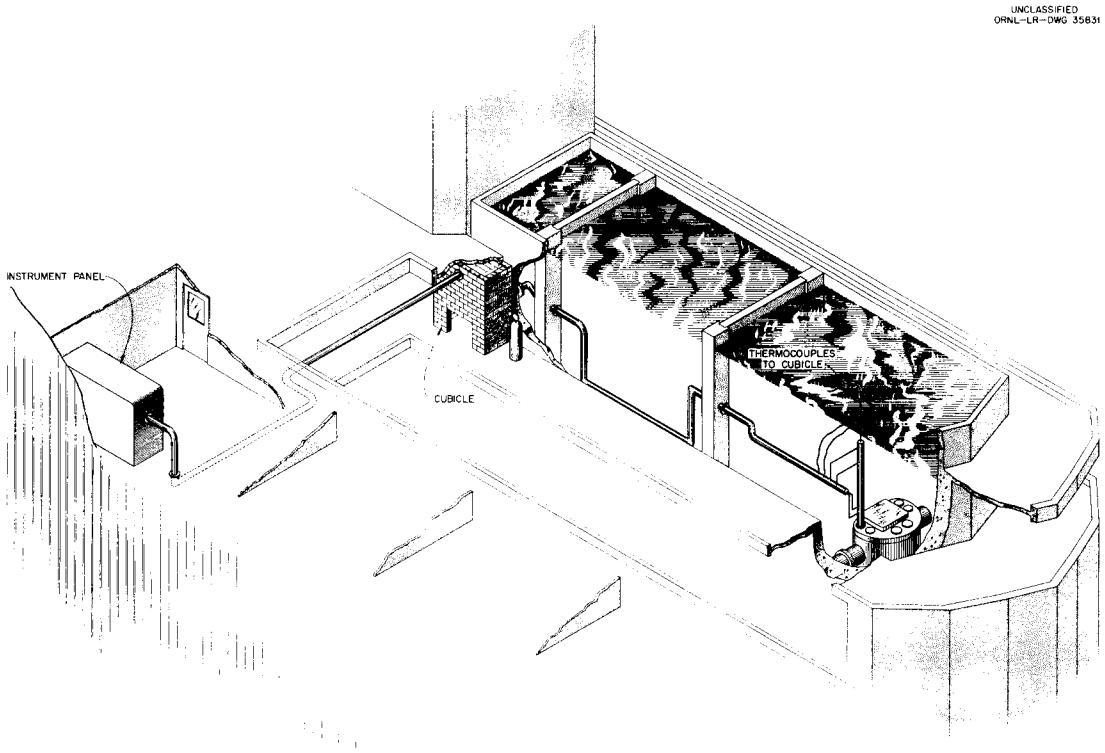


Fig. 6.15. Experimental Apparatus for Instantaneous Fission-Gas-Release Experiment in the ORR.

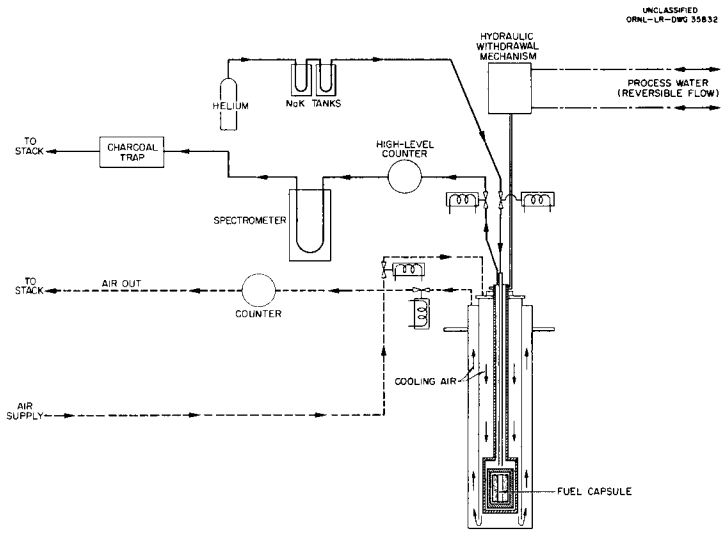


Fig. 6.16. Flow Diagram for Instantaneous Fission-Gas-Release Experiment.

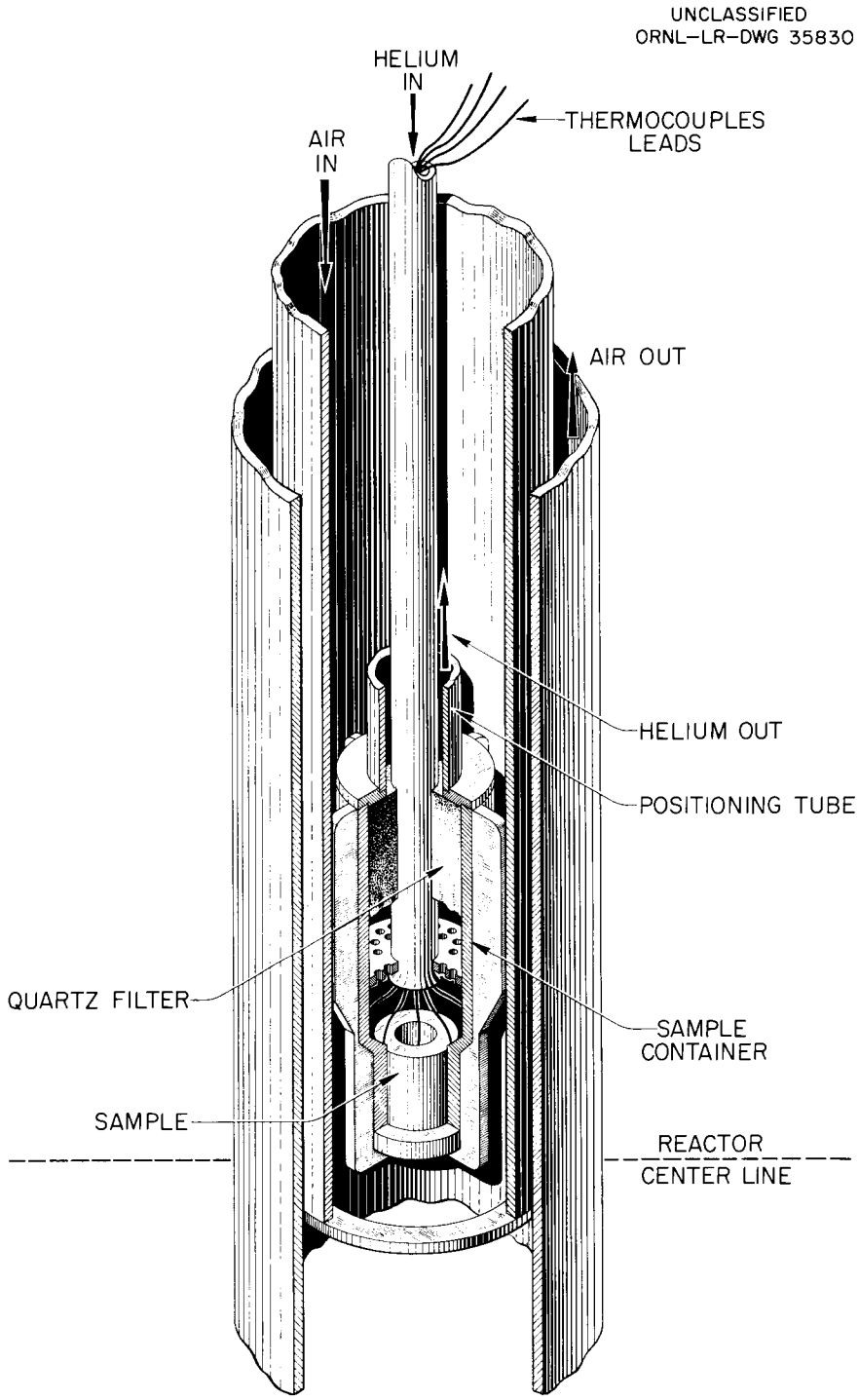


**Fig. 6.17. Fuel Capsule Assembly for Instantaneous Fission-Gas-Release Experiment.**

time the entrained fission products spend between the sample and the counter.

By allowing a trapped sample of the gas to decay and observing the half lives, as well as the energies, the following isotopes were identified: $Kr^{87}$, $Kr^{88}$, $Kr^{85m}$, $Xe^{133}$, $Xe^{135}$, $Xe^{138}$, $Cs^{138}$, $Rb^{88}$, $I^{131}$, $La^{140}$. Other activities may have been present, but they could not be identified. Since the shortest half life of the above products is 17 min, it is obvious that these products are not responsible for the high gas activities indicated in Fig. 6.18. Improved instrumentation is therefore being installed which should make it possible to identify the short-lived products. At a decay time of 1 min from sampling to counting, the half life of the gross activity indicated in Fig. 6.18 is approximately 0.7 min. The calculated activities of the gross fission products at a decay time of 1 min after fission have a half life of approximately 0.7 min.[6] The flux was $1 \times 10^{14}$ neutrons/cm$^2$.sec.

The fact that the activities are what would be expected if there were no delay due to diffusion led to the speculation that the greater part of the fission-product release could have been from surface recoil. Since diffusion is temperature-dependent and recoil release should not be temperature-dependent, a study of activity vs temperature at constant power and constant helium sweep rate was made in which temperature was the only variable. The results are presented in Fig. 6.19.

It was noted that the activity of the gas was an exponential function of temperature. This result would be expected if the gas were being released by a diffusion-dominated process. At around 1050°F the process becomes recoil-dominated. By comparing the activity of the recoil portion of the curve with the total activity at 1820°F, the contribution by diffusion is seen to be a factor of 11 higher than that from recoils. The conclusion appears to be that the majority of fission products in the helium sweep at high temperatures are released

---

[6] R. C. Bolles and N. E. Ballou, Nuclear Science and Engineering 5, Fig. 7-A (March 1959).

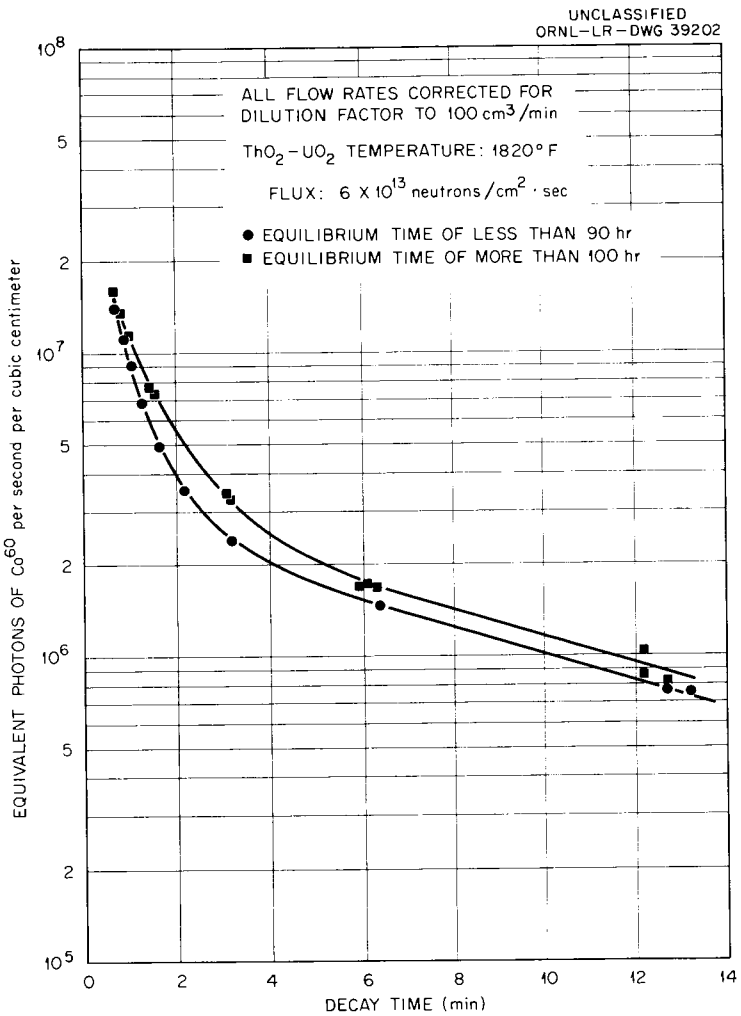


**Fig. 6.18. Activity of Fission Products as a Function of Time Between Sampling and Counting.**

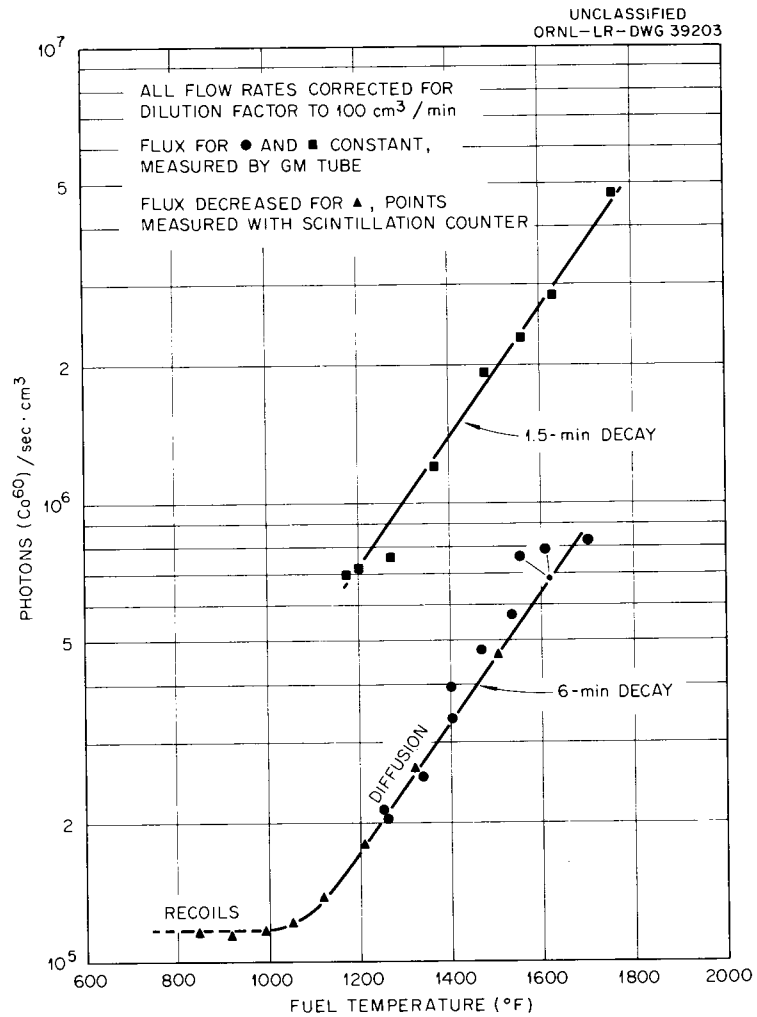


**Fig. 6.19. Activity of Fission Products as a Function of Fuel Temperature.**

by a diffusion process and that the diffusion time from the instant of fission to the moment of release from the fuel must be short. The observed products may diffuse for only a short distance, however, since the observed activity represents only 10% of the total activity expected 40 sec after fission for all fission products from a depth of $9.4 \times 10^{-4}$ cm (the recoil distance in the fuel). The longer lived fission products are obscured by the more active short-time diffusion from near the surface.

The next samples will be in the form of rectangles of $UO_2$ 1 in. long, 0.7 in. wide, and 0.03 in. thick. Two samples will be placed together so that the thermocouples may be sandwiched between them. Thermocouples will also be pressed against the outer surfaces of the samples, and the temperature difference between the outer and inner surfaces may be utilized for a rough estimate of thermal conductivity as a function of irradiation.

## Closed-Cycle-Loop Irradiation Facility in ORR

Construction of the facility described in the previous report[7] has been completed, and, except for some minor repairs, the facility is now operable. Several leaks have been repaired, a new seal has been installed for the thermocouple leads, and a second compressor is being installed in the shielded compressor room.

A flow diagram of the loop is presented in Fig. 6.20 and the capsule assembly is shown in Fig. 6.21. The first capsule to be irradiated will consist of $UO_2$ canned in coated graphite. The coating on the graphite is the Minnesota Mining and Manufacturing Company siliconized silicon carbide. Two specimens which have survived heating tests in air at 2000°F will be used in the first experiment. The cooling gas will be either $CO_2$ or air.

---

[7] GCR Semiann. Prog. Rep. Dec. 31, 1958, ORNL-2676, p 120.

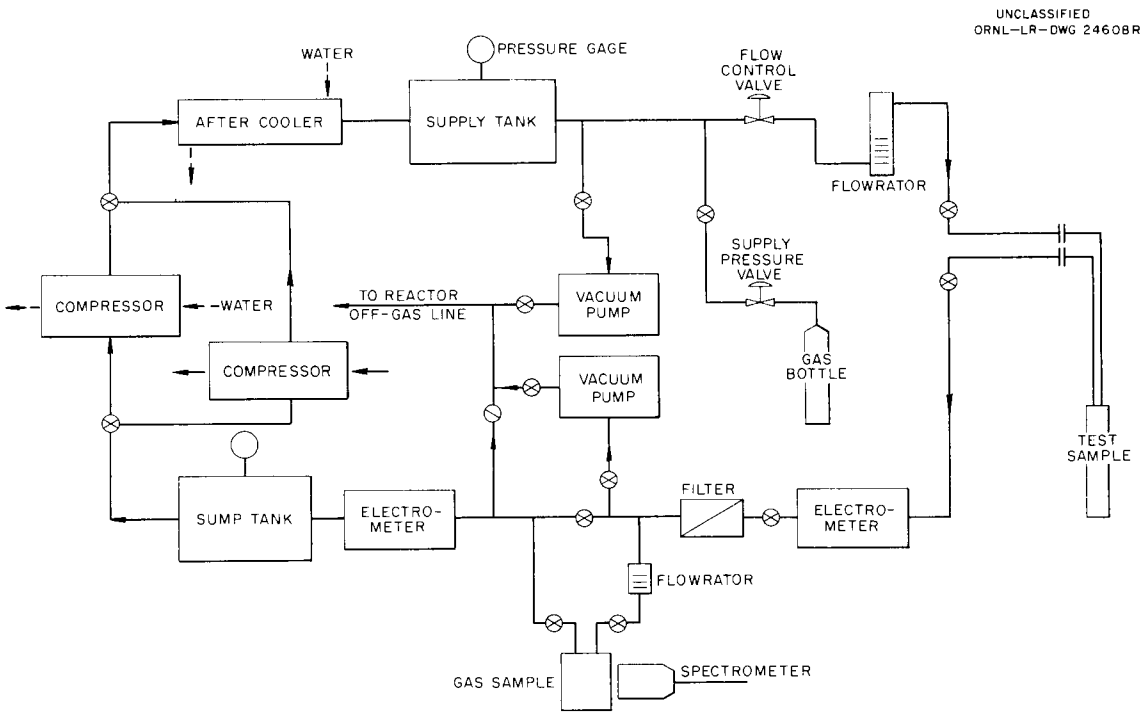


**Fig. 6.20. Flow Diagram of Closed-Cycle-Loop Irradiation Facility in the ORR.**

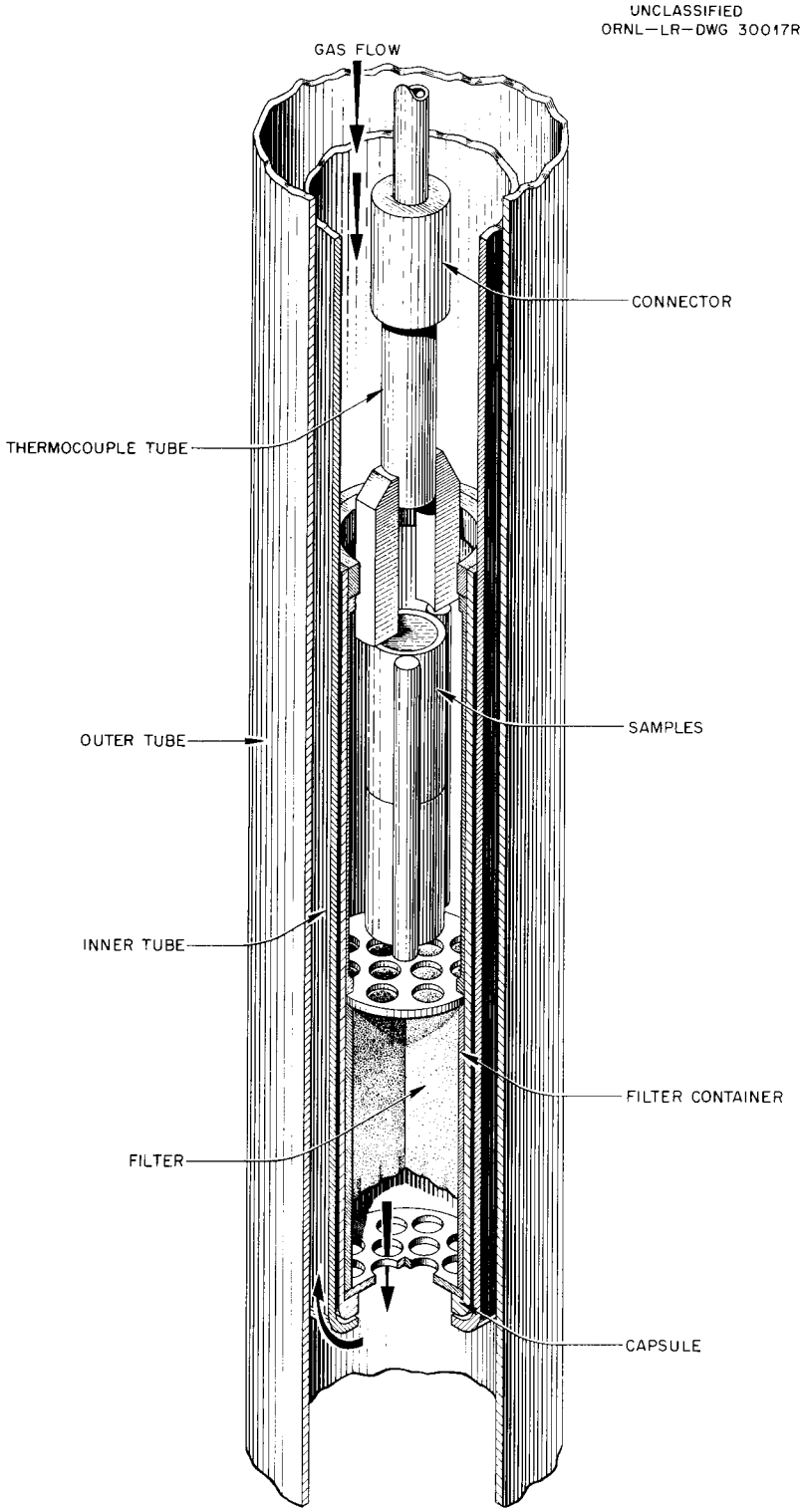


**Fig. 6.21. Fuel Capsule Assembly for Irradiation in Closed-Cycle Loop in ORR.**

## SiC-Si Coating for High-Density Graphite

In the interest of developing a moderator capable of withstanding high temperatures in an oxidizing atmosphere, SiC-Si coated graphite[8] is being examined for oxidation resistance after irradiation. Tests performed previously[9] demonstrated that the coating material was not appreciably affected at a temperature of 2000°F in air for periods of time ranging up to 1000 hr. Near sonic air blasts at 1830°F did not produce erosion damage, and rapid thermal cycles did not crack or damage the coating.

The coating on the graphite was demonstrated to be gastight by the fact that a very small pinhole in the coating would result in oxidation of the graphite. In order to determine the effect of an internal pressure, such as might be produced by buildup of fission gas, a special 6-in.-long coated graphite tube that was 1/2 in. OD, 1/4 in. ID, and closed at one end was procured. The tube was coated on the outside only and was threaded at the open end. The threaded end of the tube was copper-plated and then screwed and silver-soldered onto an Inconel tube. A platinum-wound heater was placed over the lower 3 in. of the graphite tube. The graphite tube was then pressurized to 100 psig with helium, and the temperature was brought up to 2000°F. The system was periodically checked for leaks by closing off the helium supply and observing the pressure. After 1050 hr at 2000°F, the tube was examined and no evidence of damage was found. No detectable leakage of helium had occurred.

Two coated cylinders which had been irradiated in the ORR to a total dose of $6 \times 10^{19}$ neutrons/cm$^2$ were found to be essentially unchanged in density. Oxidation tests indicated the coating to be intact. These cylinders were replaced in the ORR and irradiated to a total dose of $5 \times 10^{20}$ neutrons/cm$^2$ at reactor water temperatures.

---

[8] Developed by J. R. Johnson of Minnesota Mining and Manufacturing Company.

[9] GCR Semiann. Prog. Rep. Dec. 31, 1958, ORNL-2676, p 132.

At discharge the cylinders had decreased in density ~1%. One of the cylinders appeared to be unchanged, but the other had blistered (Fig. 6.22). The blistered sample had a metallic appearance before irradiation (Sample A, Fig. 6.23). When the blistered sample was immersed in $CCl_4$, bubbles were observed, and the weight of the sample increased with time of immersion. Thus it was apparent that the coating had failed. The other sample was oxidation-tested for 207 hr at 2000°F and did not change in weight. The density of this sample returned to its preirradiation value during the high-temperature annealing.

Two more samples, which had been irradiated to a total dose of $6.3 \times 10^{20}$ neutrons/cm$^2$ at reactor water temperature, have now also been taken out of the reactor. The densities of these specimens had decreased by ~2%. Both specimens appeared to be sound and did not exhibit leaks when placed in hot silicone oil. They have been tested for oxidation-resistance at 2000°F in air for 186 hr, and no weight changes have been observed (±0.0007 g). These samples also returned to their original density during the oxidation test at 2000°F.

## Neutron Damage to Chromel-Alumel Thermocouples

The thermal response of Chromel-Alumel thermocouples irradiated up to a total dose of $4 \times 10^{20}$ neutrons/cm$^2$ in the ORR does not differ significantly from that of unirradiated thermocouples. The test wires were assembled in clusters of three similar 20-gage wires approximately 14 in. long that were welded together at one end. These assemblies were inserted in Heliarc-sealed aluminum capsules. Pull wires were attached to the capsules to facilitate removal from an irradiation tube inserted in the B-9 reflector piece in the ORR.

Upon completion of irradiation, the assemblies were removed from the capsules in a hot cell, and a similar (from same spool) unirradiated wire was welded to the cluster of irradiated wires by means of a remotely operated thermocouple welder (see Fig. 6.24). The cluster of 4 wires was inserted in a furnace (see Fig. 6.25), and the difference

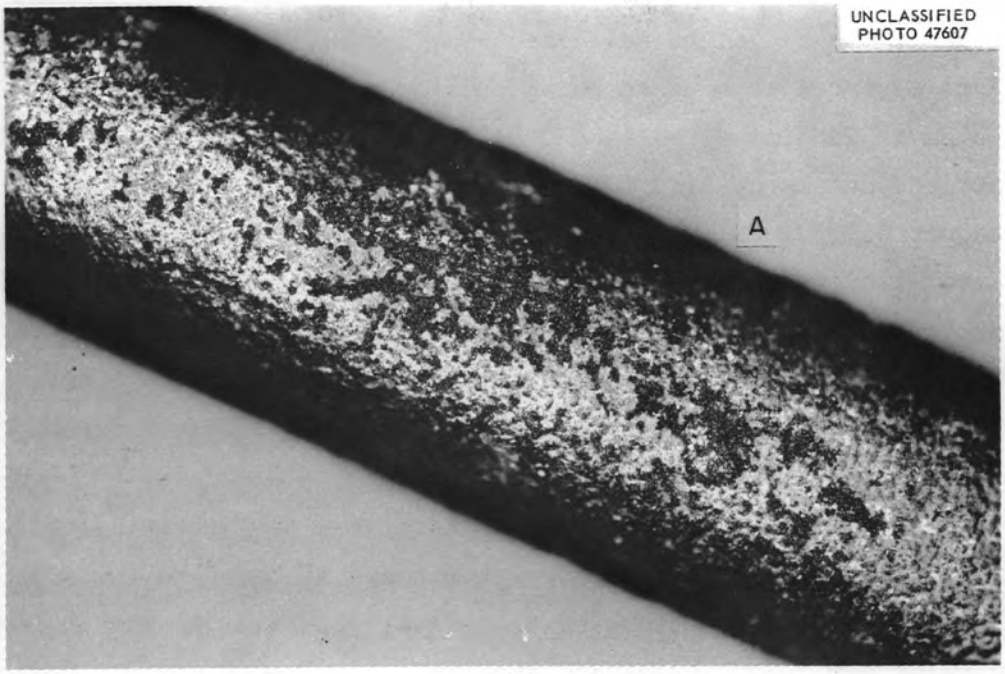


Fig. 6.22. One of Two SiC-Si Coated Graphite Cylinders That Was Irradiated to a Total Dose of $5 \times 10^{20}$ Neutrons/cm$^2$·sec. This sample (A) blistered; the other sample was unchanged.

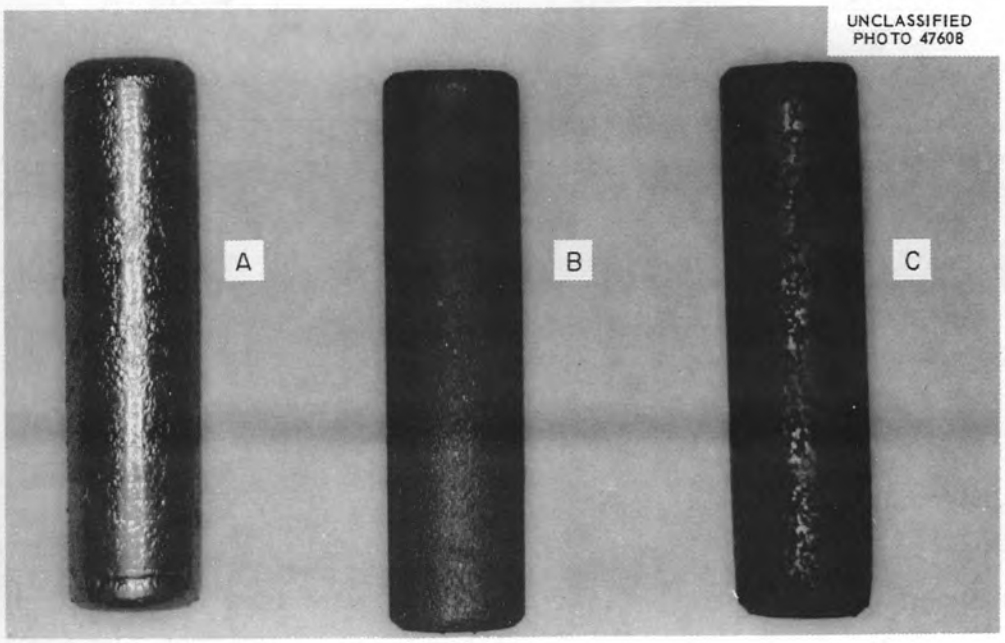


Fig. 6.23. SiC-Si Coated Graphite Rods Before Irradiation.

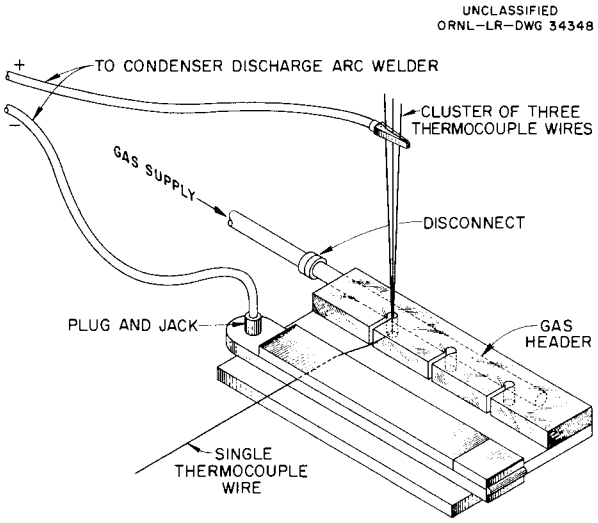


**Fig. 6.24. Remote Thermocouple Welder.**

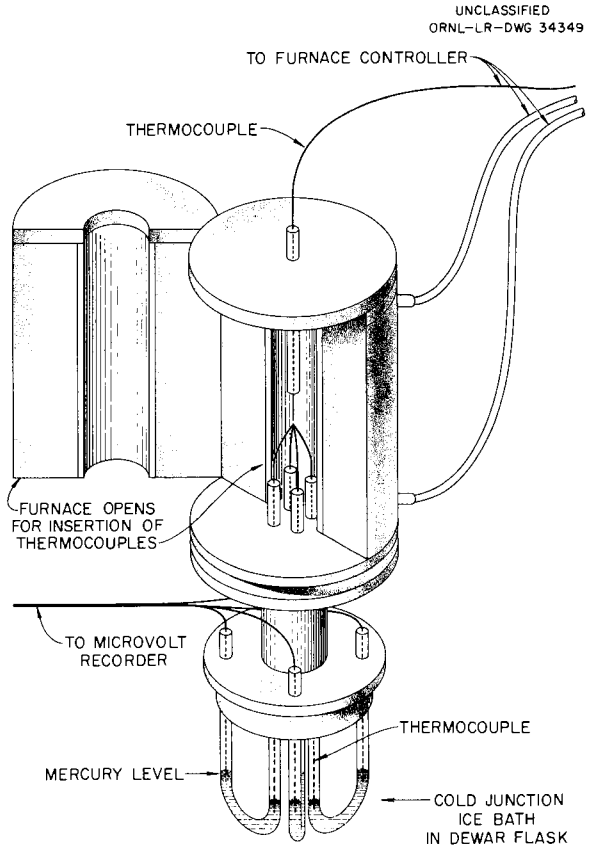


**Fig. 6.25. Apparatus for Remote Calibration of Thermocouples.**

in emf between the unirradiated wire and each of the irradiated wires was obtained as a function of temperature.

At least three complete sets of error emf vs temperature measurements were made from ambient to 1000°C to ambient for each irradiated wire. In general, at a given neutron dose, the error emf for Alumel wire was greater in magnitude (and in per cent deviation) than for Chromel wire. The Chromel error was always less than 0.75%, whereas the Alumel error was greater than 0.75% at low neutron exposures and averaged approximately 0.75% at $4 \times 10^{20}$ neutrons/cm$^2$. These errors tend to be compensating (rather than additive) in the complete thermocouple, and generally are not linear with temperature. Annealing seems to reduce the error, and there appears to be a rather anomalous decrease in error with increasing neutron dosage. The net error in emf output of the irradiated thermocouples is, however, either less than or approximately equal to the 0.75% tolerance for unirradiated wires. It should be noted that there was no preirradiation aging (annealing) of the test wires and that similar aging effects, anomalous shifts in calibration, etc. have been found in carefully controlled tests on unirradiated wires at the University of Tennessee.

## Radiation Effects on Structural Steels

The effects of fast-neutron irradiation on steels and welds used in pressure-vessel construction are being studied. The present investigation is a continuation and extension of the study carried out in the Homogeneous Reactor Program, and it has been possible to base the radiation metallurgy program on the results of the HRP studies.[10] An attempt is being made to determine whether service conditions and the effects of fast-neutron irradiation may cause reactor structural materials to fail in a brittle manner, that is, to rupture without appreciable plastic deformation. The greatest concern is for the steels used in the construction of the pressure vessel. For

[10] HRP Quar. Prog. Rep. Jan. 31, 1959, ORNL-2696, p 162.

practical purposes, the pressure vessel must be made of carbon steel, a material that is capable of failing in a brittle manner under certain conditions of service. Previous tests have shown that irradiation of carbon steels tends to reduce their ductility and to increase their tendency to exhibit brittle behavior. Elevated irradiation temperatures will often, but not always, result in lessening the irradiation effects.[11]

Experimental equipment has been assembled for this study and irradiation experiments were initiated in the ORR. Also, Charpy impact tests were made in a hot cell on specimens irradiated in the LITR and MTR. All the Charpy impact specimens irradiated in the LITR and MTR have been tested, but a large backlog of subsize Izod impact and tensile specimens remains to be tested. The first two irradiation experiments in the ORR will be completed soon.

Both standard-size Charpy V-notch and subsize Izod specimens were irradiated in the MTR and LITR at temperatures between 140 and 175°F to provide a comparison between the behavior of standard-size specimens and the subsize specimens previously used in this study. Although there was some variation in the results, the general trend was that the subsize Izod specimens gave lower ductile-brittle transition temperatures than did the standard-size Charpy V-notch specimens. The difference averaged 50°F for unirradiated specimens and 150°F for specimens exposed to $10^{20}$ neutrons/cm$^2$ (above 1 Mev). Thus the transition temperature shift was greater for the larger specimens.

Charpy V-notch specimens of several carbon and alloy steels, in several heat treatments, were irradiated at temperatures of 120 to 330°F. The data from these tests, Fig. 6.26, show an approximately logarithmic increase of transition temperatures with increasing neutron exposure from $2 \times 10^{18}$ to $1 \times 10^{20}$ neutrons/cm$^2$. Exceptions to these data were for a quenched and tempered low-alloy steel that showed a greater transition temperature shift (point "A," Fig. 6.26), and a high-purity, vacuum-melted, iron-carbon alloy, which showed a much

[11] J. C. Wilson et al., Solid State Division Ann. Prog. Rep. Aug. 31, 1958, ORNL-2614, p 98.

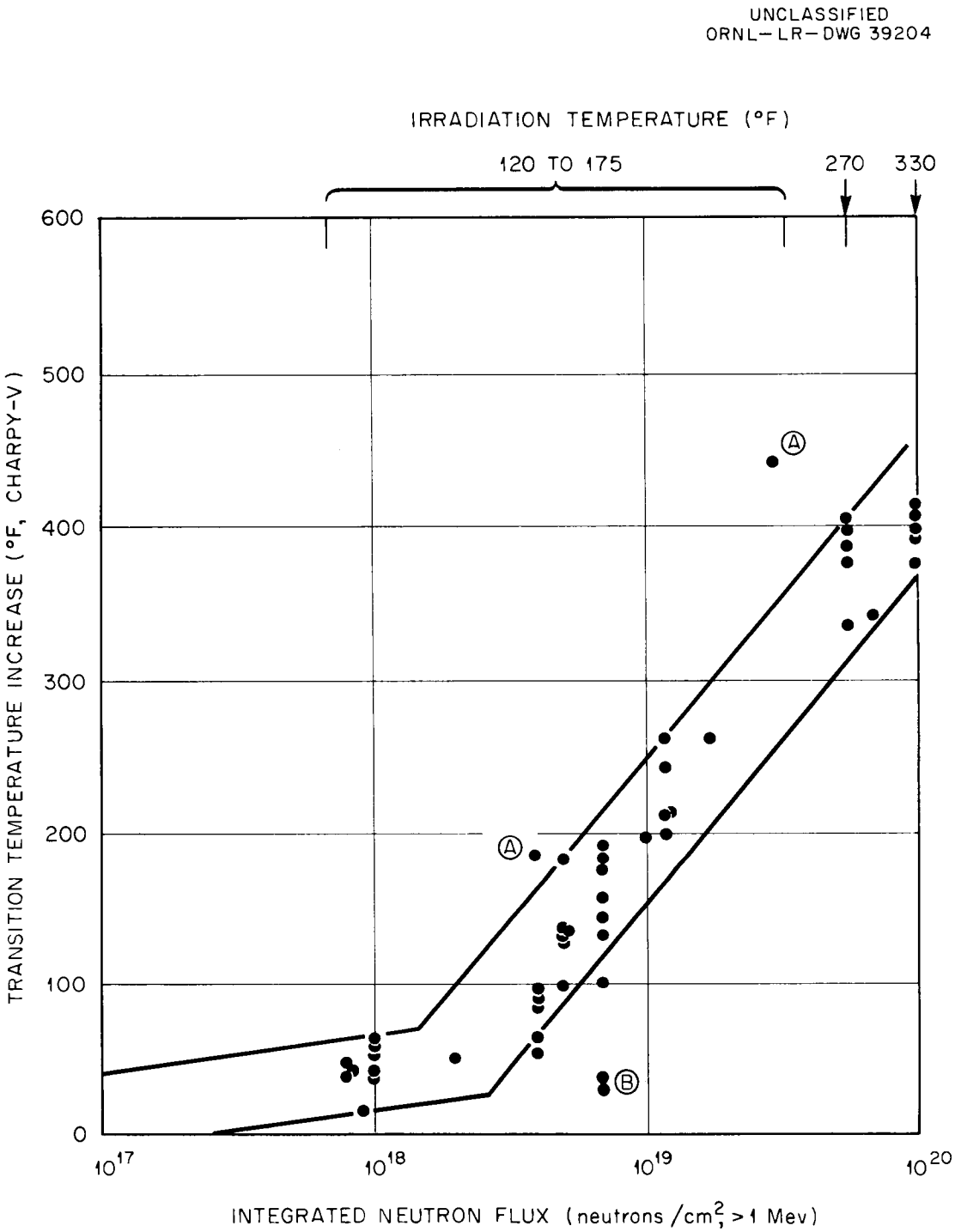


**Fig. 6.26. Effect of Fast-Neutron Irradiation on Charpy-V Impact Transition Temperatures of Several Steels.**

smaller transition temperature shift (point "B," Fig. 6.26).

Data obtained previously at elevated irradiation temperatures[11] and some post-irradiation annealing data obtained during this period indicate that irradiation at temperatures between 200 and 500°F may lead to greater increases in ductile-brittle transition temperatures than does irradiation at lower temperatures. The beneficial effects of elevated irradiation temperatures become significant in a narrow temperature range between about 550 and 600°F. This temperature range varies for different heats of the same class of steel. Thus the effects of irradiation temperature are more complex than has been supposed, and more detailed study of the combined effects of temperature, neutron flux, and neutron dose is required.

## Status of Hot Cell Modifications and Hot Cell Equipment

The modifications to cell 6, building 3025, previously described, continue. The contractor work is scheduled for completion June 19 and the ORNL participation phase is scheduled for completion July 15. The cell should be operational August 15.

Examination of the irradiated prototype capsules requires the use of the ORR hot cell and cell 6. The decanning and NaK removal equipment for the ORR hot cell has been constructed and proof-tested on flux-depression experiment capsules.

Cell 6 equipment will measure pressure and volumes of fission gas released, profile of the capsule, and density of the $UO_2$. Remote slitting and machining apparatus will allow further examination of the fuel pellets, and metallographic equipment will prepare polished samples for photomicrographs. All equipment, with the exception of a cutoff machine, has been fabricated. The cutoff machine is being constructed.

## 7. OUT-OF-PILE TESTING OF MATERIALS AND COMPONENTS

### Materials Compatibility Tests

Engineering-scale out-of-pile tests of reactor materials compatibility and fuel element assembly structural integrity were continued in facilities described previously.[1,2] Three 1000-hr, high-temperature, pot-type, static-helium tests (Nos. 9, 10, and 11) were completed in which various metal specimens were exposed to the impurities evolved from type AGOT graphite. Tests 10 and 11 were conducted in equipment modified to facilitate holding the metal test section at a temperature 400°F or more above the graphite and bulk mean gas temperatures. These tests were conducted with a maximum specimen temperature of 1500°F and a graphite temperature of 1100°F. A test with a metal specimen temperature of 1600°F and a graphite temperature of 1100°F is currently in progress, and specimens designed for testing at temperatures up to 1800°F are being fabricated. These tests with the metal test section at a temperature above the temperature of the graphite and the temperature of the coolant gas more closely simulate actual reactor fuel rod operating conditions than did the previous tests in which the graphite, the gas, and the metal specimens, as well as the test container, were all at the same temperature.

Three low-pressure thermal-convection loop tests (Nos. 6, 7, and 8), in which low-velocity helium circulation was induced by a temperature differential imposed on the loop, were also completed. Test No. 8 which was to be a long-term test (5000 hr) of type AGOT graphite was terminated after 2754 hr because of gas leakage from the loop piping. A second long-term test (No. 9) of type TSF graphite has completed 2280 hr and is continuing.

---

[1] The ORNL Gas-Cooled Reactor. Materials and Hazards, ORNL-2505 (May 22, 1958), p 12.33.

[2] GCR Semiann. Prog. Rep. Dec. 31, 1958, ORNL-2676, p 138.

Construction of a forced-circulation loop designed for studying corrosion and erosion effects on full-scale fuel element assemblies with gas velocities similar to reactor design velocities was completed and placed in operation. The first 1000-hr test in this facility has been completed.

A high-pressure thermal-convection test facility containing two high-pressure loops was also completed. These loops are designed to evaluate the effects of reactor coolant pressures on fuel element assemblies, and the effect of the relatively high gas pressure on graphite out-gassing and corrosion. Both loops are currently in operation with helium at approximately 300 psig; the test section temperature is 1400°F.

Static Tests

A summary of operating conditions and results obtained from static-helium tests during this report period is presented in Table 7.1. Earlier test results were presented previously.[2] Tests 8 and 9 were conducted under isothermal conditions, as were the previous tests.

Following test 9 the test facilities were modified, as mentioned above, to include a type 304 stainless steel test section heated independently of the test container. This test section consists of a 3/4-in.-OD, 0.020-in.-wall tube located along the central axis of the test vessel; the test section is heated by two internal tubular heaters. An internally heated test section is shown in Fig. 7.1 prior to installation in the test facility. Tests 10 and 11 were both run with test section temperatures of 1500°F near the top and 1300°F near the bottom and a graphite temperature of 1100°F. Type AGOT graphite was used in both tests. In test 10 the ratio of metal surface area to available gas volume was similar to that of tests 3 through 9. In test 11 the relative amount of metal surface was decreased by omitting the stainless steel mesh in order to more nearly simulate the surface area-to-volume ratios anticipated for the EGCR. The parameters of tests 10 and 11 are compared in Table 7.2.

Table 7.1. Summary of Conditions and Metallurgical Results of Pot-Type Tests of the Compatibility of Structural Materiols and Graphite in Static Helium at High Temperatures

| Test No. | Maximum Specimen Temperature (°F) | Moximum Graphite Temperature (°F) | Type of Graphite | Total Elapsed Time of Test (hr) | Maximum Observed Impurity Concentration of Gas (vol %) | Specimens Included and Metallurgical Results |
|---|---|---|---|---|---|---|
| 8 | 1100 | 1100 | TSF | 1000 | 3.62 | Stainless and low-alloy steels and Fe-Al base alloys: Stainless steel specimens (types 304, 310, 316, and 410) showed quite consistent weight gains that ranged from 0.02 to 0.04 mg/cm$^2$. Metallographic examinations of type 410 specimens showed a zone of apparent decarburization to a depth of 0.5 mil; other stainless steels showed no surface changes. Croloy 2$\frac{1}{4}$ and T-1 steel specimens showed consistent but small weight losses, althaugh no surface change could be seen metallographically. |
| 9 | 1400 | 1400 | AGOT | 1000 | 6.58 | Stainless and low-alloy steels and Fe-Al base alloys: Specimens of types 304, 310, and 316 stainless steel showed weight gains in the range from 0.14 to 0.18 mg/cm$^2$. Specimens of type 410 stainless steel showed smaller gains (0.08 to 0.10 mg/cm$^2$). Weight losses of 0.11 to 0.15 mg/cm$^2$ were experienced on T-1 and Croloy 2$\frac{1}{4}$ steel specimens, while DB-2 (Fe-Al base alloy) showed no detectable weight change. Metallographic examinations of these specimens are still in pragress. |
| 10 | 1500 | 1100 | AGOT | 1000 | 5.5 | A type 304 stainless steel test section heated independently of the pot: Regions of the test section below 1460°F exhibited a black, tightly adherent oxide layer composed predominantly of $Fe_3O_4$; however, reaction films which formed at regions above this temperature had a silvery appearance and spalled in certain areas, revealing a dark-gray reaction layer underneath. Analyses of these films are being attempted with spectrographic and electran diffraction techniques. Examinations of the test section for weight changes and metallographic appearance are as yet incomplete. |
| 11 | 1500 | 1100 | AGOT | 1000 | 3.5 | Test specimens same as those of test No. 10: Both high- and low-temperature regions of the test section showed similar gray-black reaction layers. Reaction films were extremely smooth and tightly adherent. Metallurgical and chemical analyses of the specimens are currently in progress. |
| 12 | 1600 | 1100 | AGOT | 200 | | Test specimens same as those in test No. 10: Test cantinuing. |

Table 7.2. System Parameters for Static Tests 10 and 11 Which Were Run With Independently Heated Type 304 Stainless Steel Test Sections

| | Test 10 | Test 11 |
|---|---|---|
| Graphite volume, $ft^3$ | 0.74 | 0.95 |
| Graphite surface area, $ft^2$ | 16.35 | 20.90 |
| Metal surface area, $ft^2$ | 87.31 | 18.64 |
| Helium volume, $ft^3$ | 3.64 | 3.44 |

Analyses of gas samples taken from test 10 showed that the amounts of impurities evolved during the test were comparable with those evolved during test 8 in which all components had been maintained at 1100°F. The levels of impurities observed during test 11, however, followed a different pattern, and the maximum level of impurities was only 3.5% by volume compared with 5.5% in test 10. At the conclusion of the 1000-hr test period, the total impurity level in test 11 had only dropped to 2.5% compared with 0.07% in test 10. The behavior of ($N_2$ + CO) impurities was particularly different in the two tests. In test 10 the combined impurities reached a maximum immediately after the vessel reached 1100°F and then decreased; in test 11 a similar peak was observed during initial operation but a second increase was observed after approximately 40 hr at temperature that continued throughout the remainder of the test.

Static test 12 is currently under way with type AGOT graphite at 1100°F and test specimen temperatures of 1600°F near the top and 1560°F near the bottom. A direct-resistance-heated test section designed for a maximum specimen temperature of 1800°F is being fabricated for future static tests.

With one exception, samples of austenitic stainless steels in tests 8 through 11 showed no surface changes other than a thin, tightly adherent, black oxide tarnish, which was accompanied by a very small specimen weight gain. In static pot test 10, a type 304 stainless steel test section held at 1500°F formed a completely different type of

reaction layer, which was silvery in color, nonmagnetic, and poorly adherent. The appearance of this test section is shown in Fig. 7.2. In certain areas, spalling of this outer layer occurred, and a thin gray under-layer was apparent. In contrast, the type 304 stainless steel test section that was held at 1500°F in static test 11 showed a typical black reaction layer which appeared to be tightly adherent and more like the oxide tarnish found in tests prior to static test 10. The portions of the two test sections that were held at 1500°F in tests 10 and 11 are compared in Fig. 7.3. Analyses of the reaction layers on these specimens are under way.

Low-Pressure Thermal-Convection Loop Tests

A summary of operating conditions and results obtained from low-pressure thermal-convection loop tests 5 through 9 is presented in Table 7.3. The austenitic stainless steel specimens exposed in these tests showed slight weight gains and reaction layers that were extremely thin and ranged from gray to black in color. The type 410 stainless steel specimens were similar to the austenitic steel specimens, except that the type 410 stainless steel specimen from test 5 showed surface decarburization.

The low alloy steels exposed in these tests also showed weight gains, but the gains were of greater magnitude than those of the stainless steels. Reaction layers on these materials were correspondingly heavier than on stainless steels. A visual examination of T-1, Croloy 2-1/4, and Croloy 3M specimens from test 7 showed the reaction films on these materials to be silvery in color, in contrast to the smooth black films found on comparable specimens in tests 5 and 6 and in earlier thermal-convection tests. Exfoliation of this outer silvery film occurred during handling, and a second reaction layer was revealed which was black and quite powdery. The T-1 steel specimens are shown at various stages of exfoliation in Fig. 7.4. Electron diffraction patterns of the outer film showed it to consist mainly of $Fe_3O_4$, while analysis of the underfilm revealed patterns characteristic of $Fe_3O_4$

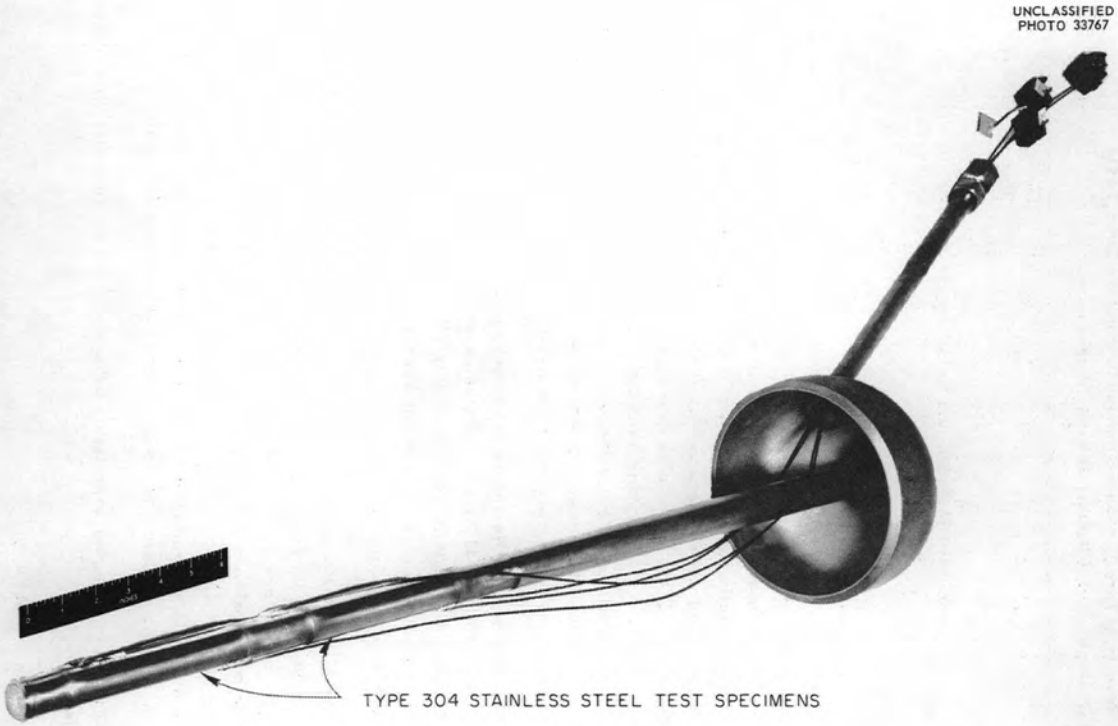


**Fig. 7.1. A Typical Internally Heated Specimen for a Static Gas Test.**

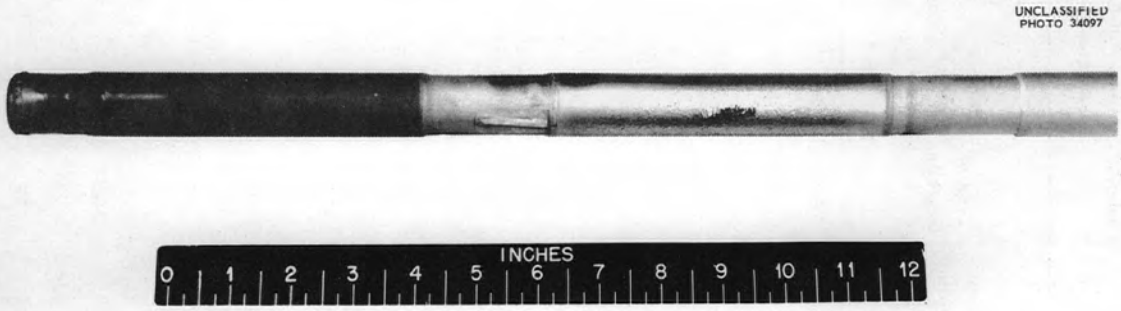


**Fig. 7.2. After-Test Appearance of Heated Type 304 Stainless Steel Specimen Tested in Static Pot Test No. 10.** The blackened area on the left operated between 1300 and 1450° F, while the silver-appearing area on the right operated at 1500° F. The test system contained AGOT graphite at 1100° F.

Table 7.3. Summary of Conditions and Metallurgical Results of Low-Pressure Thermal-Convection Loop Tests of the Compatibility of Structural Materials, Graphite, and Helium at High Temperatures

| Test No. | Maximum Temperature (°F) | Type of Graphite | Total Elapsed Time of Test (hr) | Maximum Observed Impurity Concentration of Gas (vol %) | Specimens Included and Metallurgical Results |
|---|---|---|---|---|---|
| 5 | 1300 | TSF | 1000 | 4.43 | Stainless and low-alloy steels: Austenitic stainless steels (types 304, 316, and 310) showed consistent weight gains that range from 0.1 to 0.3 mg/cm$^2$, while type 410 stainless steel specimens showed various degrees of weight loss. No surface changes were detected metallographically for the austenitic steels; type 410 stainless steel specimens exhibited a decarburized zone approximately 0.75 mil deep. Croloy 3M and Croloy 2$\frac{1}{4}$ steels exhibited weight gains comparable to the gains of austenitic steels, and no surface changes were found by metallographic examination. T-1 steel specimens lost from 0.5 to 0.8 mg/cm$^2$, but metallographically showed no surface changes. DB-2 was unaffected by the test environment; it showed no weight or metallurgical changes. No apparent deposition of carbon resulted in cold-leg regions of the loop. |
| 6 | 1400 | AGOT | 1000 | 12.6 | Stainless and low-alloy steels: Weight gains amounting to 0.2 to 0.4 mg/cm$^2$ were detected on types 304, 316, 310, and 410 stainless steel specimens. Considerably higher weight gains (2.5 to 4.0 mg/cm$^2$) occurred for T-1, Croloy 2$\frac{1}{2}$, and Croloy 3M specimens. Metallographic examinations of specimens have not been completed. No carbon deposits were found in the cold-leg regions of the loop. |
| 7 | 1100 | AGOT | 1000 | 4.9 | Stainless and low-alloy steels: Stainless steel specimens showed weight gains approximately one-half those of comparable specimens in test No. 6. Specimen surfaces were lightly tarnished by a black oxide film. Low-alloy steels (Croloy 2$\frac{1}{4}$, Croloy 3M, and F-1) exhibited a brittle, silvery outer reaction layer which spalled profusely upon handling and revealed a heavy black underlayer. The outer layer was identified as $Fe_3O_4$ and the underlayer as $Fe_xO$. Metallographic examinations of specimens have not been completed. There was no evidence of carbon deposition in cold-leg regions of the loop. |
| 8 | 1400 | AGOT | 2754 | 19.6 | Scheduled 5000-hr test terminated prematurely because of helium leakage; data processing not yet completed. |
| 9 | 1400 | TSF | 2280 | 5.5 | Scheduled 5000-hr test under way. |

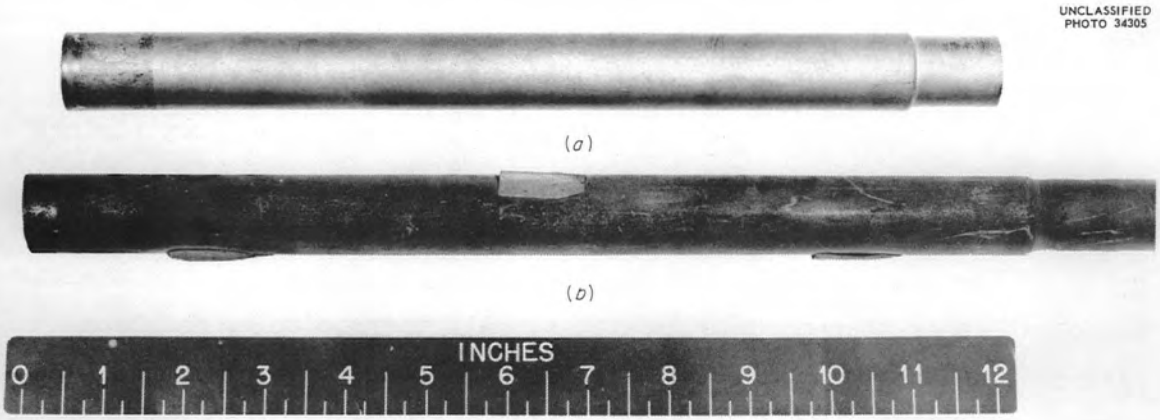


**Fig. 7.3. Comparison of Heated Test Sections from Static Tests 10(a) and 11(b).** The sections shown were both held at 1500°F. Both test systems included AGOT graphite, which was held at 1100°F. The relative area of metal surface was considerably greater in test 10 than test 11.

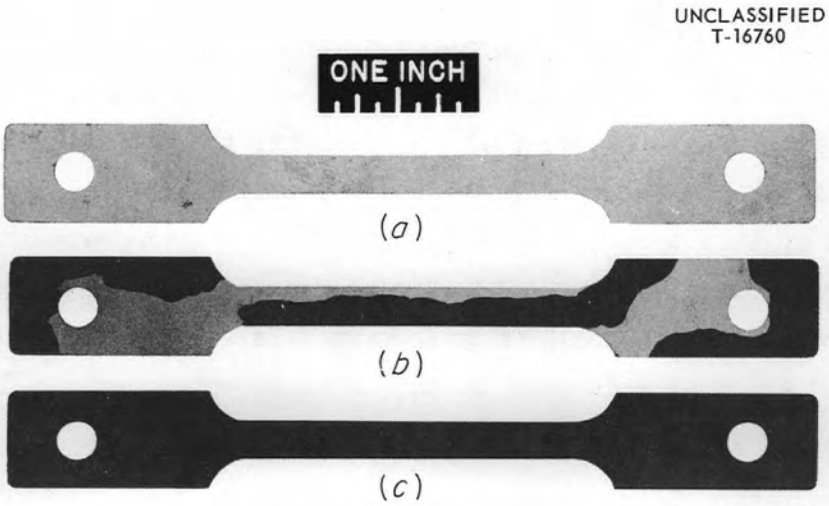


**Fig. 7.4. Appearance of T-1 Steel Specimens Tested with AGOT Graphite in Helium at a Temperature of 1100°F in Low Pressure Thermal Convection Loop No. 7.** (a) Specimen with outer reaction layer intact, as it appeared immediately after the test. (b) and (c) Specimens with outer covering, which spalled upon handling, partially and completely removed.

and α-Fe. It is believed that during the test the underfilm may have been composed of $Fe_xO$, which decomposes upon cooling into iron and magnetite. Test 8, which was scheduled for 5000 hr, was interrupted prematurely after 2754 hr because of gas leakage from the loop piping. Examination of the loop indicated that the leakage was caused by catastrophic oxidation of the type 316 stainless steel pipe at a point of thermocouple attachment; further examination disclosed similar attack at other thermocouple locations. All thermocouples had been insulated at the point of junction with a high-temperature Sauereisen cement.

High-Pressure Thermal-Convection Loops

Two high-pressure thermal-convection loops are currently in operation with helium at a pressure of approximately 300 psig. The test sections of these loops, which operate at 1400°F, each contain type AGOT graphite and simulated full-scale EGCR fuel element assemblies such as that shown in Fig. 5.12 of Chap. 5 of this report. For the first test, which is scheduled for 1000 hr, four of the seven fuel rods in the fuel element assembly contain $UO_2$ pellets; the other three contain Inconel filler bars to approximate the $UO_2$ pellet weight. Upon completion of this test the fuel element will be transferred to the forced-circulation loop and subjected to gas velocities approximating EGCR design velocities for 1000 hr. Test 2 is scheduled for 5000 hr of operation. All fuel rods used in this test assembly contain Inconel in place of the $UO_2$ pellets.

Forced-Circulation Loop Test

The first 1000-hr test was completed in the forced-circulation loop shown in Fig. 7.5. The test section, containing type TSF graphite and a simulated full-scale EGCR fuel element assembly, was operated with argon at 1400°F, 30 psig, and a velocity of 300 ft/sec. Argon is used in this loop so that mass flow rates equivalent to those for helium at design pressure can be achieved in a low-pressure test facility. The problems and cost associated with high-pressure loop construction were

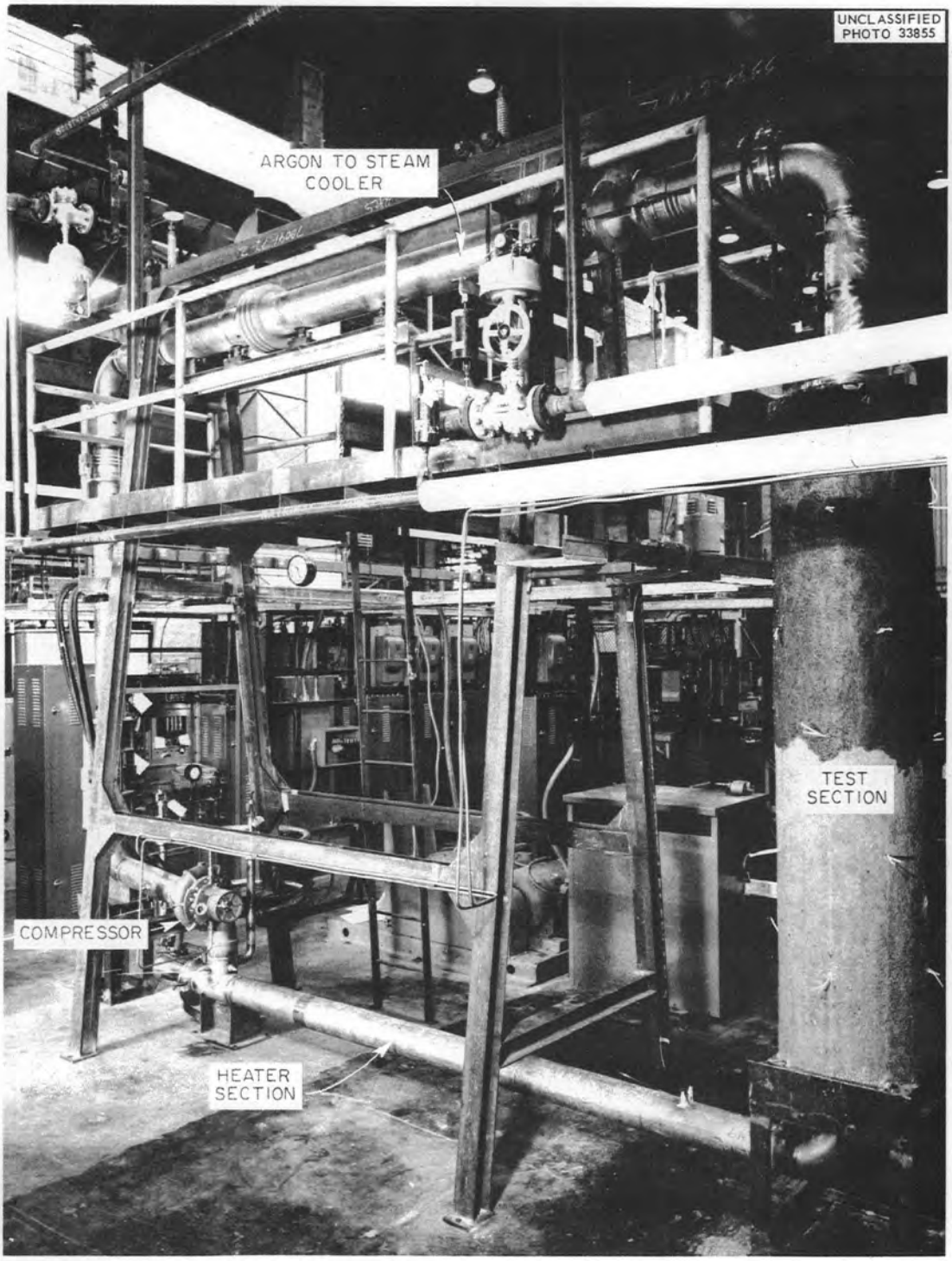


**Fig. 7.5. Forced-Circulation Loop for Out-of-Pile Tests of Full-Scale EGCR Fuel Elements.**

thus avoided. The compressor for this loop operated satisfactorily at approximately 15,000 rpm with a 600°F inlet gas temperature throughout the 1000-hr test. This single-stage centrifugal compressor with a 400-cycle, totally enclosed, water-cooled motor and grease-lubricated ball bearings was supplied by the AiResearch Division of The Garrett Corporation. Examinations of the loop components are under way.

## Evolution of Gases from Graphite

Some experimental data were reported previously[3] on volumes and compositions of gases released at low pressures by 3/4-in.-dia, 2-in.-long cylindrical specimens of various graphite samples over the temperature interval 200 to 1000°C. In the more recent studies described here, the temperature interval has been extended to 2000°C, additional samples of graphite have been included, larger specimens (1 1/2 in. dia, 2 in. long) have been examined, and rates of gas evolution at 300, 600, and 1000°C have been measured.

For studies at 1000°C and below, the desired temperature was obtained by use of an external resistance furnace; the apparatus and techniques were essentially those described previously.[3] Study of the 1 1/2-in.-dia, 2-in.-long cylinders necessitated replacement of the 1-in.-dia quartz specimen tube with a similar tube 2 in. in diameter. The apparatus was modified by inclusion of a McLeod gage between the specimen tube and the Toepler pump to permit measurement of the pressure over the specimen during the degassing operation.

For studies at 1000°C and above, a General Electric Model 4HM-15L3, 450-kc induction heater was used. The work coil (2 3/8 in. ID) consisted of 5 turns of 1/4-in.-dia copper tubing covered with Tygon tubing and was immersed in a water bath which also served to cool the 2-in.-dia quartz specimen tube. The cylindrical graphite specimens (1 1/4 in. dia, 1 in. long) were mounted on a tungsten wire inserted in a No. 55 drill hole 1/4 in. deep in the specimen. The specimen

---

[3] GCR Semiann. Prog. Rep. Dec. 31, 1958, ORNL-2676, p 147.

temperature was measured by observation with an optical pyrometer. The evolved gases were recovered by a Toepler pump and collected and handled in a manner identical to that used for gases obtained by resistance heating. Initial difficulties with a mercury-vapor discharge within the specimen tube were alleviated, but not eliminated, through changes in coil dimensions and tap settings; the occasional discharge which appears is associated with a narrow range of pressures in the specimen tube.

The composition data presented previously were obtained from mass-spectrometer examination of the gas samples; consequently, no breakdown of the mass 28 material into its $N_2$ and CO components has been possible. In recent months the application of gas chromatography to these samples has permitted separate determinations of $N_2$ and CO. Some of the previous studies have, accordingly, been repeated to obtain information on these materials.

Materials received for examination have included AGOT-III, received from National Carbon Co. in December 1958 and designated by them as current production; Speer-Moderator No. 1-F-Process, March 1959; and Speer-Moderator No. 2, March 1959. All materials were received as bars nominally 4 x 4 x 50 in., which were wrapped in heavy paper. Portions removed from these bars and the machined specimens were stored in plastic bags until used.

The volumes and compositions of the gases evolved from AGOT-II and AGOT-III specimens of different sizes at temperatures of 1000°C and below are listed in Tables 7.4 and 7.5. It appears that CO is a major fraction of the mass 28 material obtained upon heating to 1000°C; only below 400°C is $N_2$ appreciable in comparison with CO. No marked differences from the results presented previously for AGOT-II are evident. The recent data obtained for samples of TSF-II (Table 7.6) are also similar to data previously obtained.[3]

The total volume of gas evolved per unit volume of graphite shows no dependence on sample size over the relatively small range studied and with the considerable pumping times used in these studies. Stepwise heating of specimens at several temperatures up to 1000°C yields nearly the

Table 7.4. Volume and Composition of Gases Evolved by $1\frac{1}{2}$-in.-dia, 2-in.-long AGOT-II Graphite Specimens

| Temperature (°C) | Time (hr) | Gas Volume ($cm^3$/100 $cm^3$ of graphite) | Gas Constituents | | | | | | | | | | | | |
|---|---|---|---|---|---|---|---|---|---|---|---|---|---|---|---|
| | | | $H_2$ | | $H_2O$ | | $CO_2$ | | Mass 28 Material | | Hydrocarbons | | $SO_2$ | | $H_2S$ |
| | | | vol % | $cm^3$ | vol % | $cm^3$ | vol % | $cm^3$ | vol % | $cm^3$ | vol % | $cm^3$ | vol % | $cm^3$ | (vol %) |
| 200 | 2.5 | 0.5 | 2.4 | | 81 | 0.4 | 1.1 | | 9.7 | 0.1 | 3.0 | | 0.2 | | 1.4 |
| 300 | 2 | 0.4 | 4.3 | | 50 | 0.2 | 7.0 | | 16.7 | 0.1 | 8.3 | | 1.7 | | 7.9 |
| 400 | 2.5 | 0.8 | 1.1 | | 79 | 0.6 | 6.1 | 0.1 | 12.7 | 0.1 | 1.1 | | | | |
| 500 | 3 | 1.2 | 7.2 | 0.1 | 17.6 | 0.2 | 22 | 0.3 | 18.7 | 0.2 | 24 | 0.4 | | | |
| 600 | 4 | 1.8 | 7.8 | 0.1 | 6.7 | 0.1 | 57 | 1.0 | 15.5 | 0.3 | 12.4 | 0.3 | 0.9 | | |
| 700 | 3 | 2.3 | 13.2 | 0.3 | 7.4 | 0.2 | 46 | 1.1 | 16.0 | 0.4 | 14.7 | 0.3 | 1.9 | | |
| 800 | 3.5 | 3.3 | 15.3 | 0.5 | 3.7 | 0.1 | 40 | 1.3 | 33 | 1.1 | 5.7 | 0.2 | 1.4 | 0.1 | |
| 900 | 4 | 3.7 | 24 | 0.9 | 0.3 | | 0.3 | | 74 | 2.7 | 1.5 | 0.1 | | | |
| 1000 | 4.5 | 4.6 | 29 | 1.3 | 0.7 | | 0.5 | | 69 | 3.3 | 0.4 | | | | |
| 1000 | 6.5 | 1.9 | 42 | 0.8 | 2.0 | | 0.1 | | 55 | 1.1 | 0.3 | | | | |
| 1000 | 4 | 0.7 | 38 | 0.3 | 1.7 | | 0.1 | | 60 | 0.4 | 0.3 | | | | |
| 1000 | 3.5 | 0.4 | 44 | 0.2 | 1.8 | | 0.1 | | 54 | 0.2 | 0.4 | | | | |
| | Total | 21.6 | | 4.5 | | 1.8 | | 3.8 | | 10.0 | | 1.3 | | 0.1 | |

**Table 7.5. Volume and Composition of Gases Evolved by AGOT-III Graphite**

| Specimen Size (in.) | Temperature (°C) | Time (hr) | Gas Volume ($cm^3$/100 $cm^3$ of graphite) | Gas Constituents | | | | | | | | | | | | | | | | |
|---|---|---|---|---|---|---|---|---|---|---|---|---|---|---|---|---|---|---|---|---|
| | | | | $H_2$ | | Hydrocarbons | | $H_2O$ | | $CO_2$ | | Mass 28 Material | | $N_2$ | | CO | | $SO_2$ | | $H_2S$ (vol %) |
| | | | | vol % | $cm^3$ | vol % | $cm^3$ | vol % | $cm^3$ | vol % | $cm^3$ | vol % | $cm^3$ | vol % | $cm^3$ | vol % | $cm^3$ | vol % | $cm^3$ | |
| ¾ × 2 | 300 | 19 | 1.9 | 0.8 | | 0.5 | | 85 | 1.6 | 2.0 | | 11 | 0.2 | | | | | | | 0.9 |
| | 600 | 5.5 | 6.8 | 4.4 | 0.3 | 1.3 | 0.1 | 39 | 2.6 | 47 | 3.2 | 8.5 | 0.6 | | | | | | | |
| | 600 | 16 | 1.5 | 11 | 0.2 | 17 | 0.2 | 31 | 0.5 | 24 | 0.4 | 16 | 0.2 | | | | | | | 1.5 |
| | 1000 | 4 | 13.5 | 12 | 1.6 | 0.6 | 0.1 | 2 | 0.3 | 28 | 3.8 | 52 | 7.1 | | | | | 4.8 | | |
| | 1000 | 17 | 3.7 | 42 | 1.5 | 1.1 | | 0.8 | | 0.1 | | 56 | 2.1 | | | | | | | |
| | | Total | 27.4 | | 3.6 | | 0.4 | | 5.0 | | 7.4 | | 10.2 | | | | | | 0.6 | |
| ¾ × 2 | 1000 | 7 | 27.3 | 18 | 4.8 | 2.3 | 0.6 | 25 | 7.0 | 21 | 5.8 | 32 | 8.7 | | | | | 0.5 | | |
| | 1000 | 11 | 2.8 | 40 | 1.1 | 1.6 | | 4 | 0.1 | 0.5 | | 53 | 1.5 | | | | | | | |
| | | Total | 30.1 | | 5.9 | | 0.6 | | 7.1 | | 5.8 | | 10.2 | | | | | | 0.1 | |
| 1¼ × 1 | 300 | 2 | 1.7 | 1.5 | | 4 | | 68 | 1.3 | 3.5 | | 22 | 0.4 | 21 | 0.4 | 1 | | | | |
| | 600 | 2.5 | 6.5 | 3.5 | 0.2 | 14 | 0.9 | 47 | 3.0 | 23 | 1.5 | 13 | 0.8 | 5 | 0.3 | 8 | 0.5 | | | |
| | 1000 | 0.5 | 15.6 | 14 | 2.1 | 3 | 0.5 | 3 | 0.5 | 32 | 4.9 | 48 | 7.4 | 1 | 0.2 | 47 | 7.2 | | | |
| | 1000 | 10 | 6.0 | 31 | 1.9 | 4 | 0.2 | 10 | 0.6 | | | 55 | 3.3 | 3 | 0.2 | 52 | 3.1 | | | |
| | | Total | 29.8 | | 4.2 | | 1.6 | | 5.4 | | 6.4 | | 11.9 | | 1.1 | | 10.8 | | | |
| 1½ × 2 | 300 | 1.5 | 1.1 | 1.3 | | 3 | | 83 | 0.9 | 1.7 | | 12 | 0.1 | 11 | 0.1 | 1 | | | | |
| | 400 | 3.5 | 0.9 | 1.0 | | 3 | | 90 | 0.8 | 2.0 | | 4 | | 2 | | 2 | | | | |
| | 500 | 3.25 | 1.3 | 2.7 | | 14 | 0.1 | 43 | 0.5 | 26 | 0.3 | 15 | 0.2 | 6 | 0.1 | 9 | 0.1 | | | |
| | 600 | 2.5 | 3.6 | 2.4 | 0.1 | 10 | 0.4 | 15 | 0.5 | 57 | 2.1 | 15 | 0.6 | 2 | 0.1 | 13 | 0.5 | | | |
| | 700 | 4 | 3.2 | 4.0 | 0.1 | 5 | 0.1 | 16 | 0.5 | 58 | 1.9 | 13 | 0.4 | 4 | 0.1 | 9 | 0.3 | | | |
| | 800 | 5 | 7.4 | 1.9 | 0.1 | 2 | 0.1 | 10 | 0.7 | 66 | 4.9 | 15 | 1.1 | 4 | 0.3 | 11 | 0.8 | | | |
| | 900 | 4.25 | 3.9 | 13 | 0.5 | 1 | | 1 | | 8 | 0.3 | 78 | 3.0 | 1 | | 77 | 3.0 | | | |
| | 1000 | 4.5 | 5.1 | 29 | 1.5 | 2 | 0.1 | 1 | | 0.2 | | 68 | 3.5 | 3 | 0.2 | 65 | 3.3 | | | |
| | | Total | 26.5 | | 2.3 | | 0.8 | | 3.9 | | 9.5 | | 8.9 | | 0.9 | | 8.0 | | | |
| 1½ × 2 | 300 | 5.5 | 0.6 | 0.5 | | 2.7 | | 75 | 0.5 | 6.2 | | 13 | 0.1 | | | | | 0.4 | | 1.1 |
| | 300 | 19 | 0.2 | 1.3 | | 6.3 | | 56 | 0.1 | 9.2 | | 26 | 0.1 | | | | | 0.2 | | 0.4 |
| | 600 | 1.5 | 2.1 | 1.8 | | 4.6 | 0.1 | 55 | 1.1 | 32 | 0.7 | 7.3 | 0.2 | | | | | | | |
| | 600 | 8.5 | 3.5 | 1.6 | 0.1 | 2.1 | 0.1 | 11 | 0.4 | 77 | 2.7 | 8.3 | 0.3 | | | | | | | |
| | 600 | 11.5 | 0.4 | 5.2 | | 6.5 | | 11 | | 61 | 0.2 | 15 | 0.1 | | | | | | | |
| | 1000 | 0.75 | 12.8 | 5.9 | 0.8 | | | 1 | 0.1 | 31 | 4.0 | 59 | 7.6 | | | | | 0.9 | | |
| | 1000 | 20 | 4.7 | 24 | 1.1 | 0.2 | | 1 | | 0.2 | | 71 | 3.3 | | | | | 2.2 | | |
| | | Total | 24.3 | | 2.0 | | 0.2 | | 2.2 | | 7.6 | | 11.7 | | | | | | 0.3 | |

Table 7.6. Volume and Composition of Gases Evolved by $1\frac{1}{2}$-in.-dia, 2-in.-long TSF-II Graphite Specimens

| Temperature (°C) | Time (hr) | Gas Volume ($cm^3$/100 $cm^3$ of graphite) | Gas Constituents | | | | | | | | | | | | | |
|---|---|---|---|---|---|---|---|---|---|---|---|---|---|---|---|---|
| | | | $H_2$ | | Hydrocarbons | | $H_2O$ | | $CO_2$ | | Mass 28 Material | | $N_2$ | | CO | |
| | | | vol % | $cm^3$ | vol % | $cm^3$ | vol % | $cm^3$ | vol % | $cm^3$ | vol % | $cm^3$ | vol % | $cm^3$ | vol % | $cm^3$ |
| 300 | 2 | 0.9 | 1.8 | | 34 | 0.3 | 26 | 0.2 | 4.3 | | 30 | 0.3 | 19 | 0.2 | 11 | 0.1 |
| 400 | 6.25 | 1.1 | 9 | 0.1 | 16 | 0.2 | 26 | 0.3 | 6 | 0.1 | 40 | 0.4 | | | | |
| 500 | 3 | 2.2 | 14 | 0.3 | 23 | 0.5 | 12 | 0.3 | 13 | 0.3 | 25 | 0.5 | 3 | 0.1 | 22 | 0.4 |
| 600 | 6.5 | 3.1 | 29 | 0.9 | 39 | 1.2 | 6 | 0.2 | 6 | 0.2 | 22 | 0.7 | | | | |
| 700 | 4.75 | 2.7 | 42 | 1.1 | 34 | 0.9 | 2 | 0.1 | 1.1 | | 21 | 0.6 | 3 | 0.1 | 18 | 0.5 |
| 800 | 4.75 | 2.0 | 83 | 1.7 | 5 | 0.1 | 1 | | 0.4 | | 10 | 0.2 | 1 | | 9 | 0.2 |
| 900 | 5.5 | 2.4 | 75 | 1.8 | 1.3 | | 2 | 0.1 | 0.3 | | 21 | 0.5 | 3 | 0.1 | 18 | 0.4 |
| 1000 | 4.5 | 2.7 | 79 | 2.1 | 0.5 | | 4 | 0.1 | 0.2 | | 17 | 0.5 | 1 | | 16 | 0.5 |
| | Total | 17.1 | | 8.0 | | 3.2 | | 1.3 | | 0.6 | | 3.7 | | | | |
| 300 | 3.5 | 1.1 | 1.0 | | 40 | 0.4 | 44 | 0.5 | 2.4 | | 13 | 0.1 | 9 | 0.1 | 4 | |
| 600 | 5.5 | 3.1 | 5 | 0.1 | 21 | 0.7 | 24 | 0.7 | 16 | 0.5 | 34 | 1.1 | 4 | 0.1 | 30 | 1.0 |
| 600 | 16 | 1.0 | 18 | 0.2 | 15 | 0.1 | 36 | 0.4 | 8 | 0.1 | 24 | 0.2 | 5 | | 19 | 0.2 |
| 1000 | 7 | 11.2 | 42 | 4.7 | 1 | 0.1 | 1 | 0.1 | 1 | 0.1 | 55 | 6.1 | 25 | 2.8 | 30 | 3.3 |
| 1000 | 6 | 0.9 | 64 | 0.6 | 0.5 | | 1 | | | | 35 | 0.3 | | | | |
| | Total | 17.3 | | 5.6 | | 1.3 | | 1.7 | | 0.7 | | 7.8 | | | | |
| 300 | 6.5 | 0.9 | 1.8 | | 36 | 0.3 | 27 | 0.2 | 4 | | 30 | 0.3 | | | | |
| 600 | 10 | 4.1 | 17 | 0.7 | 52 | 2.1 | 5 | 0.2 | 6 | 0.2 | 20 | 0.8 | | | | |
| 600 | 10 | 0.7 | 29 | 0.2 | 48 | 0.3 | 3 | | 0.7 | | 19 | 0.1 | | | | |
| 1000 | 5 | 4.7 | 84 | 4.0 | 1.8 | 0.1 | 0.4 | | 0.6 | | 13 | 0.6 | | | | |
| 1000 | 22 | 2.5 | 88 | 2.2 | 1.2 | | 0.6 | | 0.1 | | 12 | 0.3 | | | | |
| 1000 | 17 | 1.3 | 75 | 1.0 | 0.4 | | 3 | | 0.3 | | 21 | 0.3 | | | | |
| | Total | 14.2 | | 8.1 | | 2.8 | | 0.4 | | 0.2 | | 2.4 | | | | |

same total volume and composition of gases as does a single heating at 1000°C; this result is not unexpected, since the gases are removed from the system as evolved and are not permitted to equilibrate with the graphite specimen.

Although an occasional sample shows quite different results (one specimen of TSF-II yielded more mass 28 material than $H_2$), it appears that the gases evolved at 1000°C can be specified with considerable certainty for AGOT and TSF graphites. The data obtained to date on these and other types of graphite are summarized in Table 7.7. It may be observed that AGOT specimens evolve 22 to 32 $cm^3$ of gas per 100 $cm^3$ of graphite, while TSF specimens evolve somewhat smaller quantities of gas. When graphite specimens are heated to 1000°C in the induction furnace, however, nearly twice these volumes of gas are evolved, as indicated in Table 7.8. In general, the two heating techniques cause the release of similar quantities of $H_2O$, $CO_2$, and hydrocarbons from AGOT specimens, but considerably more $H_2$ and CO are released upon induction heating; a considerably higher rate of gas evolution is also observed when the induction heater is used. Specimens which have been thoroughly outgassed at 1000°C in the tube furnace, cooled under helium and then outgassed at 1000°C with induction heating have yielded considerable quantities of gas. Repeated checks with the optical pyrometer have shown no appreciable differences in specimen temperatures obtained by the two heating techniques.

It has been observed (Table 7.8) that very little gas is released above 1400°C; CO is the primary constituent of this small fraction, and nitrogen accounts for most of the remainder. In general, when induction heating is used the total volume of gas evolved below 1400°C is nearly constant for each of the graphites studied; however, specimens cut from the same section of a graphite bar often show wide variation in the relative proportion of gas evolved at 1000 and at 1400°C.

Two specimens, one of AGOT-III and one of TSF-II were outgassed at 1800°C, cooled under vacuum to room temperature, and then removed and stored in laboratory air. After 10 days of storage for the AGOT and

Table 7.7. Volume of Gases Evolved by Various Graphite Specimens Upon Heating to 1000°C

| Type of Graphite | Specimen Size (in.) | Total Gas Volume ($cm^3$/100 $cm^3$ of graphite) | Gas Evolved ($cm^3$/100 $cm^3$ of graphite) | | | | | Temperature of Gas Collection |
|---|---|---|---|---|---|---|---|---|
| | | | $H_2$ | $H_2O$ | Hydrocarbons | $CO_2$ | Mass 28 Material | |
| AGOT-I | $\frac{3}{4} \times 2$ | 32.4 | 11.0 | 2.7 | 0.6 | 4.8 | 13.1 | 100°C intervals from 200 to 1000°C |
| AGOT-II | $\frac{3}{4} \times 2$ | 23.3 | 4.3 | 3.3 | 0.1 | 5.7 | 8.6 | 100°C intervals from 200 to 1000°C |
| | $1\frac{1}{2} \times 2$ | 21.6 | 4.5 | 1.8 | 1.3 | 3.8 | 10.0 | 100°C intervals from 200 to 1000°C |
| | | 28.9 | 5.1 | 2.2 | 0.2 | 2.2 | 18.9 | 300, 600, 1000°C |
| AGOT-III | $\frac{3}{4} \times 2$ | 30.1 | 5.9 | 7.1 | 0.6 | 5.8 | 10.2 | 1000°C |
| | | 27.4 | 3.6 | 5.0 | 0.4 | 7.4 | 10.2 | 300, 600, 1000°C |
| | $1\frac{1}{2} \times 2$ | 24.3 | 2.0 | 2.2 | 0.2 | 7.6 | 11.9 | 300, 600, 1000°C |
| | | 26.5 | 2.3 | 3.9 | 0.8 | 9.5 | 8.9* | 100°C intervals from 300 to 1000°C |
| | $1\frac{1}{4} \times 1$ | 32.9 | 2.7 | 5.0 | 1.1 | 6.9 | 16.5 | 1000°C |
| | | 29.8 | 4.2 | 5.4 | 1.6 | 6.4 | 11.9 | 300, 600, 1000°C |
| TSF-I | $\frac{3}{4} \times 2$ | 18.3 | 12.3 | 1.6 | 0.4 | 0.8 | 3.3 | 200°C intervals from 200 to 1000°C |
| TSF-II | $\frac{3}{4} \times 2$ | 26.3 | 16.2 | 3.2 | 1.8 | 1.2 | 3.5 | 100°C intervals from 200 to 1000°C |
| | $1\frac{1}{2} \times 2$ | 14.2 | 7.8 | 0.4 | 2.8 | 0.2 | 2.3 | 300, 600, 1000°C |
| | | 17.1 | 8.0 | 1.3 | 3.2 | 0.6 | 3.7 | 100°C intervals from 300 to 1000°C |
| | | 17.3 | 5.6 | 1.7 | 1.3 | 0.7 | 7.7 | 300, 600, 1000°C |
| TSF-III | $\frac{3}{4} \times 2$ | 5.5 | 2.4 | 1.2 | 0.6 | 0.1 | 1.3 | 100°C intervals from 200 to 1000°C |
| Great Lakes | $\frac{3}{4} \times 2$ | 10.4 | 6.7 | 0.6 | 0.6 | 0.5 | 1.9 | 200°C intervals from 200 to 1000°C |

*Volume of Co, 8.0 $cm^3$; $N_2$, 0.9 $cm^3$.

Table 7.8. Volume and Composition of Gases Evolved by Various Graphite Specimens in the Temperature Range 1000 to 2000°C

| Type of Graphite | Temperature (°C) | Time (hr) | Gas Volume ($cm^3$/100 $cm^3$ of graphite) | Gas Constituents | | | | | | | | | | | | | |
|---|---|---|---|---|---|---|---|---|---|---|---|---|---|---|---|---|---|
| | | | | $H_2$ | | Hydro-carbons | | $H_2O$ | | $CO_2$ | | Mass 28 Material | | $N_2$ | | CO | |
| | | | | vol % | $cm^3$ | vol % | $cm^3$ | vol % | $cm^3$ | vol % | $cm^3$ | vol % | $cm^3$ | vol % | $cm^3$ | vol % | $cm^3$ |
| AGOT-II | 1000 | 0.5 | 39.7 | 46 | 18.3 | 3.1 | 1.3 | 2.5 | 1.0 | 8.7 | 3.5 | 39 | 15.6 | | | | |
| | 1000 | 1.5 | 29.0 | 82 | 23.8 | 0.6 | 0.2 | 1.9 | 0.6 | 1.1 | 0.3 | 13.3 | 3.9 | | | | |
| | 1400 | 1 | 0.4 | 4.6 | | 0.8 | | 14.4 | 0.1 | 3.3 | | 77 | 0.3 | | | | |
| | 1800 | 0.3 | <0.1 | | | | | | | | | | | | | | |
| | | Total | 69.1 | | 42.1 | | 1.5 | | 1.7 | | 3.8 | | 19.8 | | | | |
| AGOT-III-19 | 1000 | 2 | 59.9 | 42 | 25.5 | 0.2 | 0.1 | 6.4 | 3.8 | 14 | 8.2 | 37 | 22.4 | 3 | 1.8 | 34 | 20.6 |
| | 1400 | 0.5 | 13.8 | 20 | 2.8 | 0.5 | 0.1 | 0.7 | 0.1 | 1.0 | 0.1 | 78 | 10.8 | 3 | 0.4 | 75 | 10.4 |
| | 1800 | 0.75 | 0.4 | 6.5 | | 0.4 | | | | 0.3 | | 93 | 0.4 | | | | |
| | 2000 | 1.25 | 1.0 | 9.6 | 0.1 | 0.7 | | | | 0.2 | | 90 | 0.9 | 8 | 0.1 | 82 | 0.8 |
| | | Total | 75.1 | | 28.4 | | 0.2 | | 3.9 | | 8.3 | | 34.5 | | 2.3 | | 31.8 |
| AGOT-III | 1000 | 1.5 | 56.6 | 39 | 22.2 | 1.5 | 0.9 | 13 | 7.4 | 17 | 9.4 | 30 | 16.9 | 2 | 1.1 | 28 | 15.8 |
| | 1400 | 0.5 | 15.4 | 21 | 3.3 | 0.2 | | | | 0.8 | 0.1 | 76 | 11.8 | 4 | 0.6 | 72 | 11.2 |
| | 2000 | 2 | 0.5 | 4.1 | | 0.6 | | | | 0.3 | | 72 | 0.4 | 17 | 0.1 | 55 | 0.3 |
| | | Total | 72.5 | | 25.5 | | 0.9 | | 7.4 | | 9.5 | | 29.1 | | 1.8 | | 27.3 |
| AGOT-III-19 after exposure to air for 10 days | 1000 | 1 | 3.9 | 74 | 2.9 | 3 | 0.1 | 2.4 | 0.1 | 0.3 | | 21 | 0.8 | 3 | 0.1 | 18 | 0.7 |
| | 1400 | 2.25 | 2.1 | 69 | 1.5 | 2 | 0.1 | 4 | 0.1 | 0.2 | | 25 | 0.5 | 1 | | 23 | 0.4 |
| | 1700 | 0.75 | 0.4 | Not analyzed | | | | | | | | | | | | | |
| | | Total | 6.4 | | 4.4 | | 0.2 | | 0.2 | | | | 1.3 | | 0.1 | | 1.1 |
| TSF-II | 1000 | 1.25 | 35.8 | 79 | 28.1 | 2.8 | 1.0 | 1.0 | 0.4 | 1.3 | 0.5 | 16.3 | 5.8 | | | | |
| | 1000 | 1.25 | 6.0 | 89 | 5.3 | 0.4 | | 1.1 | 0.1 | 0.5 | | 8.9 | 0.5 | | | | |
| | 1400 | 2 | 5.7 | 91 | 5.2 | 1.5 | 0.1 | 1.8 | 0.1 | 0.3 | | 5.2 | 0.3 | | | | |
| | 1800 | | <0.1 | | | | | | | | | | | | | | |
| | | Total | 47.5 | | 38.6 | | 1.1 | | 0.6 | | 0.5 | | 6.6 | | | | |
| TSF-II-13 | 1000 | 3 | 49.5 | 75 | 37 | 5 | 2.4 | 4 | 1.9 | | | 17 | 8.2 | 7 | 3.5 | 10 | 4.7 |
| | 1400 | 2.5 | 2.3 | 22 | 0.5 | | | | | | | 74 | 1.7 | 24 | 0.5 | 52 | 1.2 |
| | 1800 | 0.75 | 0.5 | Not analyzed | | | | | | | | | | | | | |
| | | Total | 52.3 | | 37.5 | | 2.4 | | 1.9 | | | | 9.9 | | 4.0 | | 5.9 |
| TSF-II | 1000 | 3 | 39.6 | 48 | 19.1 | 5 | 0.2 | 10 | 4.1 | 2 | 0.9 | 35 | 13.7 | 2 | 0.8 | 33 | 12.9 |
| | 1400 | 1.75 | 10.7 | 53 | 5.7 | 2 | 0.2 | | | 2 | 0.2 | 39 | 4.2 | 3 | 0.3 | 36 | 3.9 |
| | 1800 | 0.75 | 2.4 | 1 | | | | | | | | 98 | 2.4 | 7 | 0.2 | 91 | 2.2 |
| | | Total | 52.7 | | 24.8 | | 0.4 | | 4.1 | | 1.1 | | 20.3 | | 1.3 | | 19.0 |

**Table 7.8 (continued)**

| Type of Graphite | Temperature (°C) | Time (hr) | Gas Volume ($cm^3$/100 $cm^3$ of graphite) | Gas Constituents: $H_2$ vol % | $H_2$ $cm^3$ | Hydrocarbons vol % | Hydrocarbons $cm^3$ | $H_2O$ vol % | $H_2O$ $cm^3$ | $CO_2$ vol % | $CO_2$ $cm^3$ | Mass 28 Material vol % | Mass 28 Material $cm^3$ | $N_2$ vol % | $N_2$ $cm^3$ | CO vol % | CO $cm^3$ |
|---|---|---|---|---|---|---|---|---|---|---|---|---|---|---|---|---|---|
| TSF-II-13 after exposure to air for 7 days | 1000 | 4.5 | 4.3 | 45 | 2.0 | 0.8 | | 6.5 | 0.3 | 1.2 | 0.1 | 45 | 1.9 | 8 | 0.3 | 37 | 1.6 |
| | 1400 } 1800 } | 0.75 0.5 | 2.0 | 25 | 0.5 | | | | | | | 75 | 1.5 | 5 | 0.1 | 70 | 1.4 |
| | | Total | 6.3 | | 2.5 | | | | 0.3 | | 0.1 | | 3.4 | | 0.4 | | 3.0 |
| Speer Moderator No. 1 | 1000 | 3.75 | 47.6 | 70 | 33.4 | 0.8 | 0.4 | 4.2 | 2.0 | 1.2 | 0.6 | 24 | 11.2 | 1 | 0.2 | 23 | 11.0 |
| | 1400 | 1.25 | 2.1 | 33 | 0.7 | 1 | | | | | | 62 | 1.3 | 11 | 0.2 | 51 | 1.1 |
| | 1800 | 1 | 0.9 | 3 | | | | | | | | 89 | 0.8 | 17 | 0.2 | 72 | 0.6 |
| | | Total | 50.6 | | 34.1 | | 0.4 | | 2.0 | | 0.6 | | 13.3 | | 0.6 | | 12.7 |
| Speer Moderator No. 1 | 1000 | 1.75 | 22.9 | 53 | 12.1 | 0.9 | 0.2 | 3.0 | 0.7 | 1.1 | 0.3 | 39 | 8.8 | (18)* | 3.9 | (21)* | 4.9 |
| | 1400 | 0.75 | 15.1 | 80 | 12.1 | 1.2 | 0.2 | | | 0.3 | | 15 | 2.3 | 6.1 | 0.9 | 9.0 | 1.4 |
| | 1800 | 0.75 | 1.5 | 1.4 | | 0.2 | | | | 0.2 | | 94 | 1.4 | (12)* | (0.2)* | (82)* | (1.2)* |
| | 1800 | 2 | 1.3 | | | | | | | | | 99.5 | 1.3 | 7 | 0.1 | 92 | 1.2 |
| | | Total | 40.8 | | 24.2 | | 0.4 | | 0.7 | | 0.3 | | 13.8 | | 5.1 | | 8.7 |
| Speer Moderator No. 1 | 1000 | 3 | 21.1 | 51 | 10.8 | 3.3 | 0.2 | 2.3 | 0.1 | 2.4 | 0.1 | 42 | 8.8 | 2 | 0.3 | 40 | 8.5 |
| | 1400 | 1 | 16.7 | 68 | 11.9 | 0.7 | | | | 0.3 | | 19 | 3.4 | 1 | 0.2 | 18 | 3.2 |
| | 1800 | 1 | 3.6 | 2.7 | 0.1 | 0.4 | | | | 0.2 | | 95 | 3.5 | 11 | 0.4 | 84 | 3.1 |
| | 1800 | 3 | 1.5 | 5.1 | 0.1 | 1.2 | | | | 0.2 | | 90 | 1.3 | 9 | 0.1 | 81 | 1.2 |
| | | Total | 42.9 | | 22.9 | | 0.2 | | 0.1 | | 0.1 | | 17.0 | | 1.0 | | 16.0 |
| Speer Moderator No. 2 | 1000 | 2 | 27.1 | 75 | 20.4 | 1 | 0.3 | 2 | 0.5 | 0.8 | 0.2 | 21 | 5.8 | 1 | 0.3 | 20 | 5.5 |
| | 1400 | 2 | 1.5 | 4.9 | 0.1 | | | | | 0.2 | | 94 | 1.4 | 13 | 0.2 | 81 | 1.2 |
| | 1800 | 2.5 | 0.9 | 6.6 | 0.1 | 0.3 | | | | 0.2 | | 92 | 0.8 | | | | |
| | | Total | 29.5 | | 20.6 | | 0.3 | | 0.5 | | 0.2 | | 8.0 | | | | |
| Speer Moderator No. 2 | 1000 | 3.75 | 9.6 | 54 | 5.2 | 0.6 | 0.1 | 3 | 0.3 | 0.7 | 0.1 | 42 | 4.0 | | | | |
| | 1400 | 2 | 26.4 | 77 | 20.4 | 1.8 | 0.5 | 2 | 0.5 | 0.3 | 0.1 | 18 | 4.8 | | | | |
| | 1800 | 3 | 1.9 | 0.7 | | | | | | 0.2 | | 96 | 1.8 | | | | |
| | | Total | 37.9 | | 25.6 | | 0.6 | | 0.8 | | 0.2 | | 10.6 | | | | |
| Speer Moderator No. 2 | 1000 | 4.25 | 29.0 | 74 | 21.4 | 1.1 | 0.3 | 2 | 0.6 | 0.9 | 0.3 | 22 | 6.4 | | | | |
| | 1400 | 2 | 4.0 | 44 | 1.8 | 1.4 | 0.1 | | | 0.3 | | 53 | 2.1 | | | | |
| | 1800 | 2.5 | 2.0 | 6.5 | 0.1 | | | | | 0.4 | | 93 | 1.9 | | | | |
| | | Total | 35.0 | | 23.3 | | 0.4 | | 0.6 | | 0.3 | | 10.4 | | | | |

*Questionable results.

after 7 days for the TSF specimen they were again degassed at 1800°C. The second outgassing yielded about tenfold less gas than the original outgassing; rather small volumes of gas are apparently readsorbed during short exposures.

Some preliminary data for the rate of evolution of gases from TSF and AGOT graphites are given in Tables 7.9 and 7.10. The data for TSF graphite also are presented in Fig. 7.6. The data are incomplete in many instances but nevertheless should provide some insight into the rates at which the gases may be expected to be evolved. As may be noted, the temperature has a marked effect upon the rates. The rate of release of the gases is extremely rapid as the sample is heated, and it is difficult to determine the rates of evolution during the first 1 hr at temperature. The volume of gas measured after 1 hr gives some indication of how rapidly the gases are evolved during the first 1-hr period. Accurate measurements of the rates of evolution at 300 and 600°C after prolonged heating also are difficult to obtain because the rates change very slowly after 20 to 40 hr.

The values reported here were obtained under a defined set of experimental conditions. Aside from the temperature, the single factor having the greatest effect on the rate of evolution is the pressure of the evolved gases in contact with the graphite specimen. The gases were pumped off by means of a Toepler pump so that, except for the initial heating period during which the evolution is very rapid, the partial pressures of the gases over the specimen are relatively low and decrease as the rate of evolution decreases. These conditions yield rates quite different from the case where the evolved gases are not removed but, rather, equilibrium conditions are soon attained that are characterized by constant pressures. The pressures over the specimen have been measured only for run No. 1 with TSF-II. They were found to be affected by the rate of evolution of gases by the specimen and the manifold pressures which the Toepler pump was pumping into. The latter effect does not appear to be important at manifold pressures under 1000 μ. For run No. 1 with TSF-II, the pressure in the quartz tube was

Table 7.9. Rate of Gas Evolution by 1 1/2-in.-dia, 2-in.-long TSF-II Graphite Specimens

| Temperature (°C) | Elapsed Time (hr) | Gas Evolved | | | |
|---|---|---|---|---|---|
| | | Run 1 | | Run 2 | |
| | | Rate[a] | Volume ($cm^3$) | Rate[a] | Volume ($cm^3$) |
| 300 | 1 | | 1.0 | | 0.9 |
| | 3 | 0.09 | | 0.1 | |
| | 8 | 0.04 | | | |
| | 18 | 0.02 | | | |
| | 23 | | 1.5 | | |
| | 27 | | | 0.01 | 1.8 |
| 600 | 1 | 0.6 | 3.1 | | 2.1 |
| | 2 | 0.31 | | | |
| | 3 | 0.22 | | | |
| | 4 | 0.19 | | | |
| | 6 | | | 0.11 | |
| | 10 | 0.08 | | | |
| | 16 | | | 0.05 | 4.1 |
| | 22 | 0.06 | | | |
| | 38 | 0.03 | | | |
| | 48 | 0.03 | 6.2 | | |
| 1000 | 2 | 2.0 | 9.3 | 1.1 | 6.5 |
| | 6 | 0.50 | | | |
| | 22 | | | 0.16 | 12.1 |
| | 25 | 0.25 | | | |
| | 40 | 0.15 | 19.5 | | |

[a]Rate given as $cm^3$ per 100 $cm^3$ of graphite per hour.

Table 7.10. Rate of Gas Evolution by AGOT Graphite Specimens

| Temperature (°C) | Elapsed Time (hr) | AGOT-III Specimens ($\frac{3}{4} \times 2$ in.) | | | | | | AGOT-II Specimen ($1\frac{1}{2} \times 2$ in.) | |
|---|---|---|---|---|---|---|---|---|---|
| | | Run 1 | | Run 2 | | Run 3 | | | |
| | | Rate* | Volume ($cm^3$) | Rate* | Volume ($cm^3$) | Rate* | Volume ($cm^3$) | Rate* | Volume ($cm^3$) |
| 300 | 1 | | 0.9 | | 1.2 | | | | 0.6 |
| | $1\frac{1}{4}$ | 0.15 | | | | | | | |
| | $1\frac{3}{4}$ | | | 0.08 | | | | | |
| | 4 | | | | | | | 0.03 | |
| | 8 | 0.05 | | 0.05 | 1.9 | | | 0.016 | |
| | 11 | | | | | | | 0.013 | |
| | 18 | 0.02 | 1.9 | | | | | 0.006 | |
| | 24 | | | | | | | 0.004 | 1.1 |
| 600 | 1 | | | | 4.0 | | | | |
| | $1\frac{1}{4}$ | 1.5 | | | | | | | |
| | 2 | | 5.1 | 0.7 | | | | | |
| | $3\frac{1}{2}$ | 0.7 | | | | | | | |
| | 4 | | | | | | | 0.22 | |
| | 5 | | | 0.16 | | | | | |
| | $6\frac{1}{2}$ | 0.15 | | | 6.8 | | | | |
| | 11 | 0.10 | | | | | | | |
| | 24 | 0.04 | 8.3 | | | | | | 3.8 |
| 1000 | 1 | | 11.0 | | 11.9 | | | | |
| | $1\frac{1}{2}$ | | | 1.0 | | | 20 | | |
| | $2\frac{1}{2}$ | 0.6 | | | | 2.0 | | | |
| | $5\frac{1}{2}$ | 0.4 | | 0.3 | | | | | |
| | 7 | | | | | 0.5 | | | |
| | 9 | 0.25 | | | | | | | |
| | 19 | | | 0.12 | 18 | 0.2 | 30 | | |
| | 22 | 0.12 | 17.2 | | | | | | |

*Rate given as $cm^3$ per 100 $cm^3$ of graphite per hour.

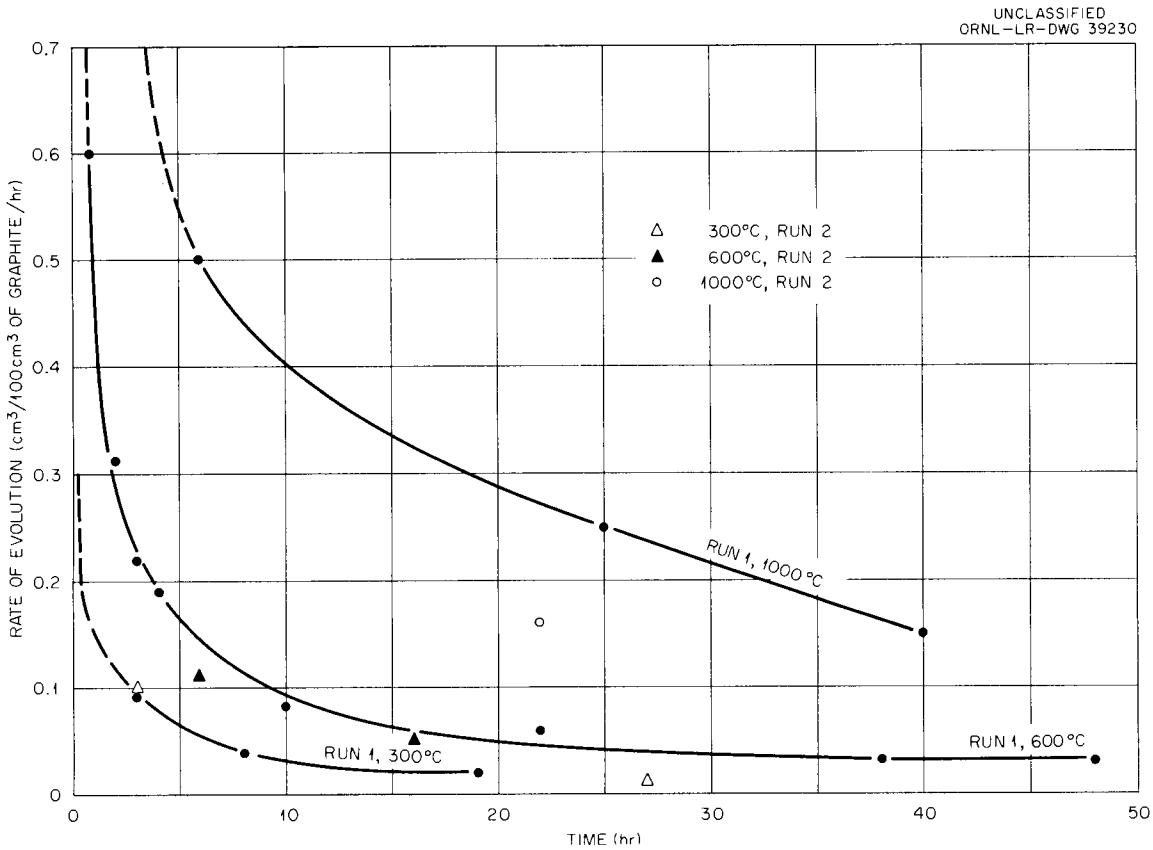


**Fig. 7.6. Rate of Evolution of Gas by 1½-in.-dia, 2-in.-long TSF-II Graphite Specimen at 300, 600, and 1000°C.**

180 μ in 15 min after reaching 300°C, 20 μ after 2 hr, 10 μ after 6 hr, and 3 to 5 μ after 18 hr. At 600°C, a maximum pressure of 320 μ was measured, 35 μ at 2 hr, 12 μ at 10 hr, 5 μ at 22 hr and 3 μ at 48 hr. At 1000°C the pressure was 25 μ after 6 hr, 15 μ after 20 hr, and 10 μ after 40 hr.

Additional studies will be made in the near future. An attempt will be made to define the evolution rates more accurately.

## Analyses of Gases Evolved by Graphite

Gas chromatographic separations were evaluated and adapted to the analysis of the gases evolved from the various types of heated graphite. The evolved gases are $N_2$, $O_2$, $H_2$, CO, $CO_2$, $CH_4$, complex mixtures of higher hydrocarbons, occasional traces of inert gases, and water vapor. The analyses by the gas chromatographic method supplement the results of analyses by mass spectrometric methods, which do not resolve the mass 28 components (CO and $N_2$) in the presence of complex mixtures of hydrocarbons.

The analyses are carried out with a Perkin Elmer Model 154 Vapor Fractometer by passing a sample of the gases, with helium as a carrier gas, through an 8-ft column of 3/8-in. stainless steel tubing packed with Linde 5A molecular sieves. This column absorbs polar compounds, such as $CO_2$ and water, irreversibly, but provides a clean-cut separation of $H_2$, $O_2$, $N_2$, CO, $CH_4$, and some other light hydrocarbons. The concentration of the separated constituents is determined by comparing the thermal conductivity of the eluted gases with that of the carrier gas by means of a conductivity cell equipped with Thermistor elements.

Because of the low pressure of these gas samples, a special technique has been developed for the addition of the samples to the chromatographic column. The samples are received in glass bulbs of 200- or 1000-$cm^3$ capacity at pressures as low as 100 μ. After being dried over anhydrous magnesium perchlorate, the mixture of gases is transferred to an evacuated system of a calibrated volume in which the total pressure of the gas is determined with a McLeod gage. Subsequently, the entire

sample, or a suitable aliquot thereof, is transferred by a two-stage pumping operation over mercury to a 1-$cm^3$ sample loop, which is mounted between two 3-way stopcocks. By appropriate manipulation of these stopcocks, the stream of carrier gas is switched from a bypass loop through the sample loop to inject the sample onto the column, as a small plug, with minimum interruption of the flow of the carrier gas. Sample volumes of 20 to 500 μl have been analyzed by this technique. On the basis of replicate analyses of synthetic samples, the precision of the determination of $N_2$, $O_2$, CO, and $CH_4$ in sample volumes between 100 and 500 μl is about 2%.

Gas samples derived from the materials compatibility program are analyzed by a less involved technique. These samples, which are submitted under a positive pressure of several pounds, are expanded into an evacuated sample loop of a system constructed to minimize the volume of connections. The excess pressure in the sampling system is relieved by momentarily opening the system to atmospheric pressure and the volume of sample in the calibrated loop is transferred to the chromatographic column. At this time concentrations as small as 50 ppm can be measured. Several means for increasing the sensitivity of the method are being evaluated.

## 8. DEVELOPMENT OF TEST LOOPS AND COMPONENTS

### ORR Gas-Cooled In-Pile Loop

The design study[1] of a gas-cooled loop for experimental studies of advanced fuel elements in the ORR was completed. A series of preliminary tests are in progress to check component performance calculations, to provide empirical heat loss data, and to calibrate instrumentation.

A mockup of the seven central cartridges of the 13-cartridge loop heater was tested with air cooling to check heat transfer calculations. A 1000-hr endurance test at a maximum cartridge temperature of 1600°F and 80% of rated power is in progress. The heater design and performance appear to be adequate. An assembly which simulates the riser-regenerator section of the loop is now being constructed that will be used to measure heat losses to the pool water and to evaluate several types of insulation. A compressor test loop now being designed will also incorporate the ORR loop heater and cooler and a test section mockup for thermocouple calibration.

### Special Gas Compressors and Electric Motors

Design studies of the gas-cooled ORR in-pile loop indicated a need for gas compressors capable of producing higher fluid heads at lower volumetric flows than those attainable with centrifugal compressors. Investigation showed that compressors of the regenerative type (sometimes called "turbine" or "peripheral" compressors) might be capable of satisfying the in-pile loop requirements.

It was determined that the motor, the bearings, and the water-cooled housing which had been developed for the grease-lubricated centrifugal compressor described previously[2] could be used for the regenerative compressor. Only minor changes were required in the shaft

---

[1] GCR Semiann. Prog. Rep. Dec. 31, 1958, ORNL-2676, p 160.

[2] Ibid., p 161.

and the flexible member which connects the motor housing to the impeller casing.

The compressor development program was therefore revised to include the following elements: (1) construction and test of one centrifugal compressor, equipped with grease-lubricated bearings, in helium at 600°F and 400 psig, with the temperature in later tests to be increased to 1000°F; (2) room-temperature tests in air of an impeller and casing assembly of the regenerative type of verify its performance in a size applicable to the gas-cooled ORR in-pile loop; (3) tests of gas-lubricated bearings and of two compressors (one purchased) equipped with gas-lubricated bearings; and (4) tests of electric motors for use with gas-lubricated bearing compressors at high temperatures.

Grease-Lubricated Centrifugal Compressors

The fabrication and assembly of an ORNL-designed compressor was completed, and it was found in a cold shakedown test that the electric drive motor could not accelerate the rotary assembly to speeds above 600 to 1000 rpm. The air-gap between the stator and rotor of the drive motor was therefore increased from a radial clearance of 0.014 to 0.025 in. to improve the starting characteristics. In a second cold shakedown test the rotary assembly accelerated rapidly to approximately 5000 rpm, but indications of severe rubbing between the rotating and stationary parts were noted. The compressor was disassembled, and the radial clearances are being increased between the grease shields and the bearing races and between the impeller and its labyrinth.

Regenerative Compressors

Only limited data are available with respect to performance of regenerative compressors under the proposed conditions, and therefore a full-size model was constructed for tests in air at room temperature. The impeller for this machine is shown installed in one-half of the casing in Fig. 8.1. As may be seen, the basic configuration of impeller and casing is relatively simple. Gas enters the compressor from the right-hand (nearly vertical) pipe at the top of the figure. The impeller

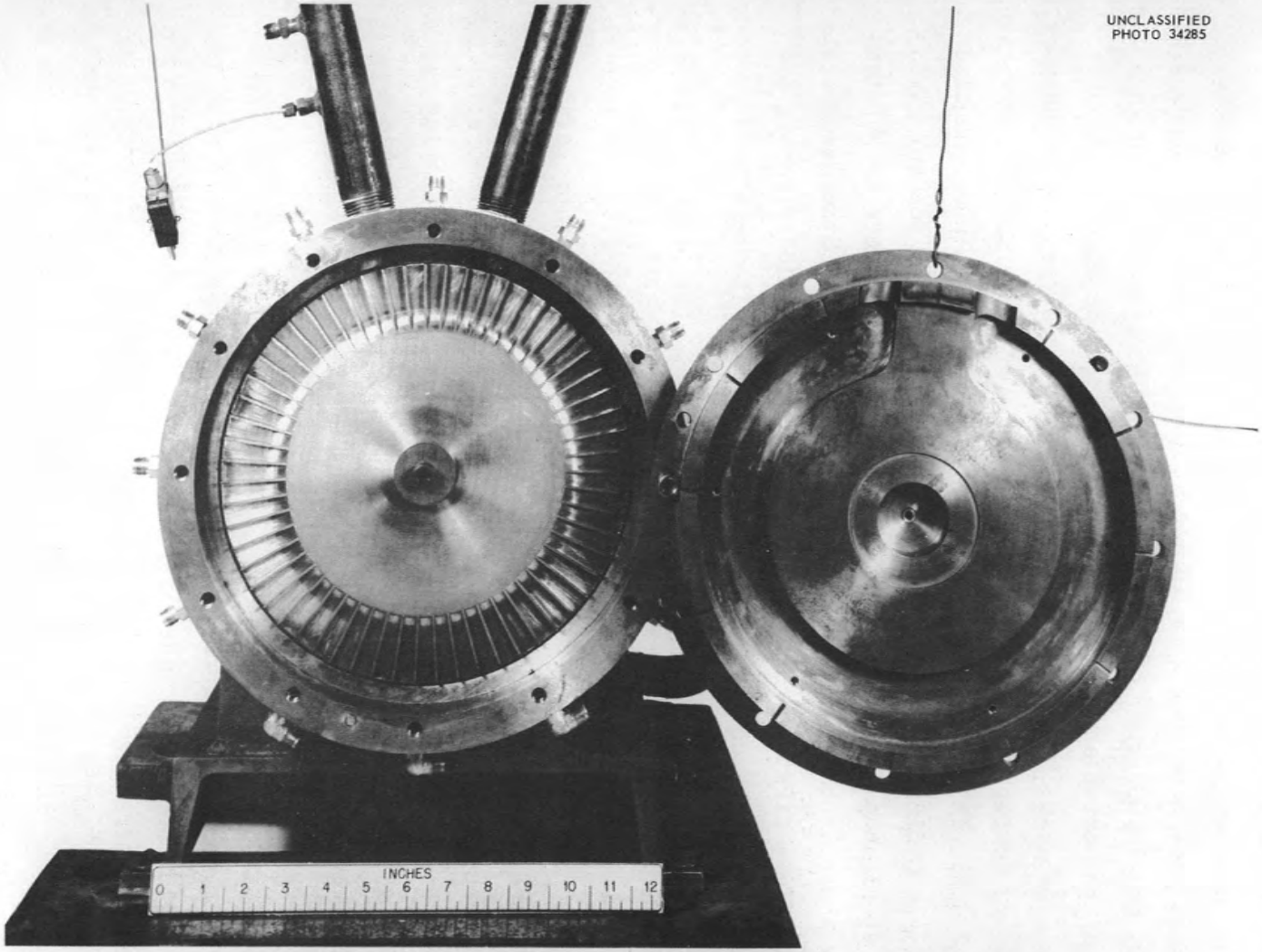


Fig. 8.1. Regenerative Compressor Showing Impeller Installed in the Casing.

turns in a clockwise direction and causes the gas to be carried around the annular passages in the casing and thence out the discharge pipe (at left). An external view of the assembled compressor, complete with bearings and the 20-hp, 12,000-rpm motor, is presented in Fig. 8.2.

Test runs have been made in air at impeller speeds of 6,000, 8,000, 10,000, and 12,000 rpm. A series of filler plates was used to vary the depth of the outer annulus, and test runs were made at annulus depths 0.215, 0.316, and 0.440 in. Curves of head versus flow and of adiabatic efficiency versus flow, for the three depths of outer annulus, are given in Fig. 8.3. It may be noted that the intermediate value of annulus depth ($y = 0.316$ in.) gives the highest values of head for any given speed at all but the greatest values of flow. Efficiency is substantially lower at the maximum annulus depth than at the other two depths tested. To a first approximation, these curves should represent the performance of the compressor over a wide range of temperature, pressure, and gas composition. The design points for four operating conditions of the ORR in-pile loop have been marked on the figure. The characteristic curves for the compressor at each annulus depth could be made to pass through any of these points by a suitable choice of operating speed.

At the lower values of flow, this regenerative compressor can produce a head about four times greater than the maximum theoretically possible at any flow with an ideal centrifugal compressor having radial impeller blades. These high heads are achieved at considerable sacrifice in efficiency, but, fortunately, compressor efficiency is of relatively small importance in the present application in comparison to the advantages gained.

Parts for a compressor of the regenerative type for use with the ORR in-pile loop were completed early in June 1959 and parts for four more compressors have been ordered. Assembly of the first compressor for a test at 600°F is under way.

Gas-Bearing Compressors

All parts of the test equipment for study of a single pneumodynamic bearing have been completed, and assembly is under way. Delivery of the

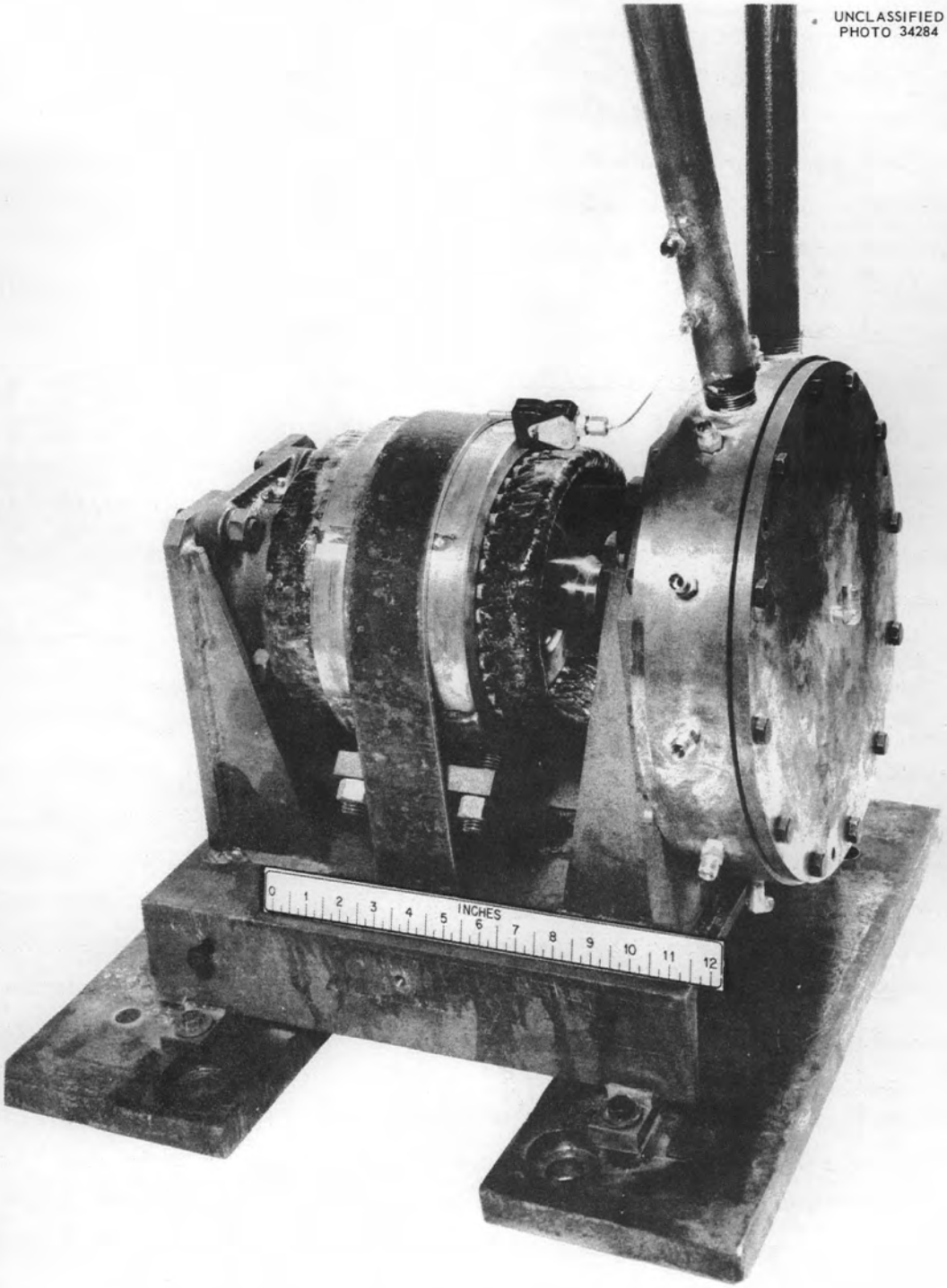


**Fig. 8.2. Assembled Regenerative Compressor and Drive Motor.**

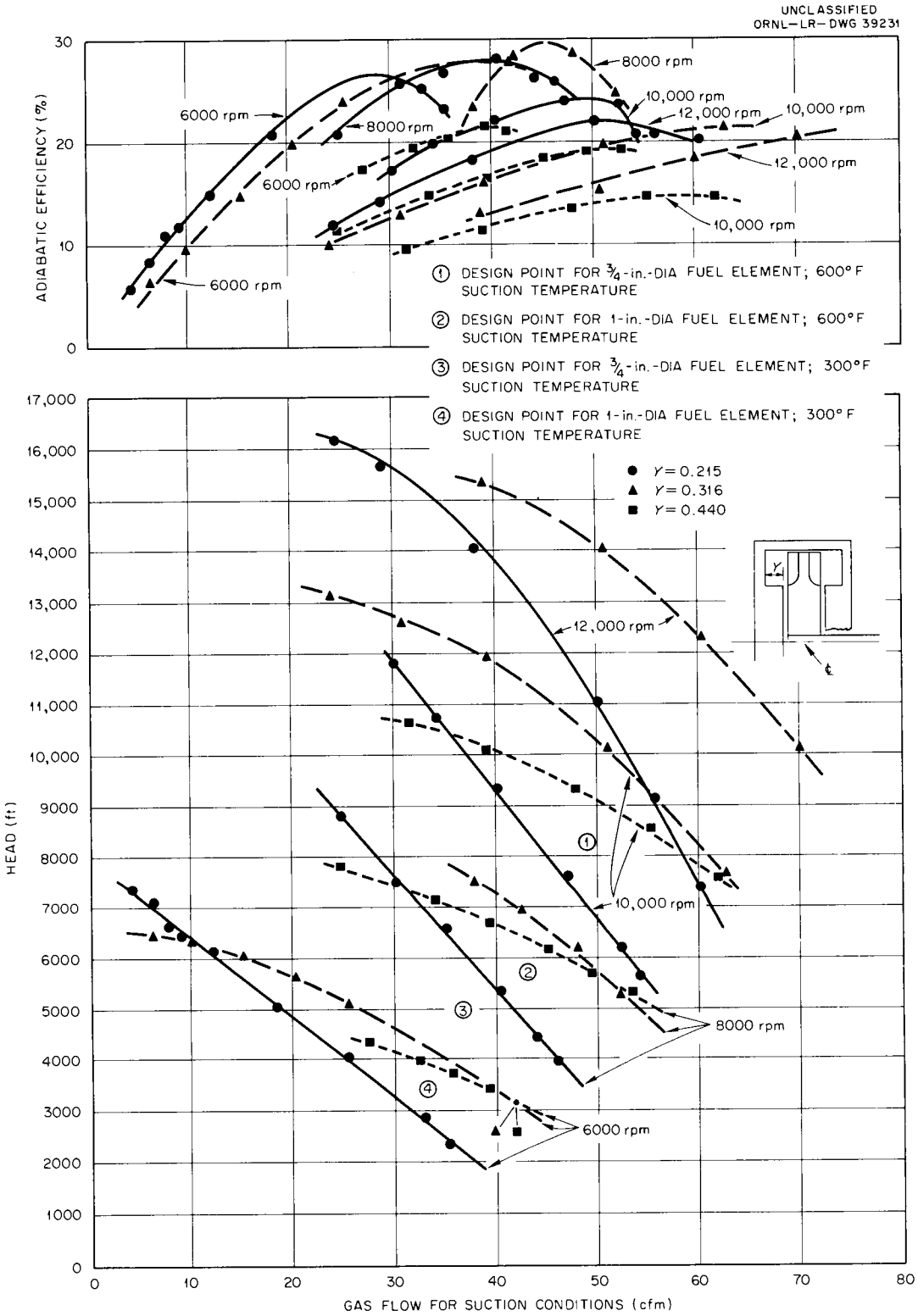


**Fig. 8.3. Performance Curves for Regenerative Compressors.**

gas-bearing centrifugal compressor being built by Bristol-Siddeley Engines, Ltd. (formerly Armstrong-Siddeley Motors, Ltd.), is now expected in August or September 1959. This compressor originally was purchased for operation at 600°F, but the contract was later revised for manufacturer tests at temperatures up to 1000°F. The vendor reports that most of the parts for the compressor have been fabricated, and some subassembly operations are in progress.

Electric Motors for High-Temperature Service

Three motors designed to produce 12 hp at 24,000 rpm and to operate at an ambient temperature of 600°F were received from the Louis-Allis Company. It is planned to test these motors by supporting the rotors on gas-lubricated bearings and using an available centrifugal impeller to provide the necessary load.

Compressors for Forced-Circulation Loop Operating with Argon

A compressor ordered for use with the out-of-pile forced-circulation loop was received from the AiResearch Mfg. Co. and installed in the test loop. This machine has now operated for more than 1000 hr and is being removed from the loop for inspection. Operation has been satisfactory, and the primary purpose of the inspection is to determine whether the bearings can be operated without relubrication for periods longer than the specified 1000 hr.

ORNL-2767
Reactors — Power
TID-4500 (14th ed.)

INTERNAL DISTRIBUTION

1. J. W. Allen
2. S. A. Beall
3. M. Bender
4. D. S. Billington
5. E. P. Blizard
6. A. L. Boch
7. C. J. Borkowski
8. W. F. Boudreau
9. G. E. Boyd
10. E. J. Breeding
11. R. B. Briggs
12. C. E. Center (K-25)
13. R. A. Charpie
14. T. E. Cole
15. J. H. Coobs
16. J. A. Conlin
17. W. B. Cottrell
18. J. A. Cox
19. F. L. Culler
20. H. N. Culver
21. J. H. DeVan
22. L. M. Doney
23. D. A. Douglas
24. L. C. Emerson
25. L. B. Emlet (K-25)
26. E. P. Epler
27. H. L. Falkenberry
28. J. Foster
29. A. P. Fraas
30. J. H. Frye, Jr.
31. G. A. Garrett (K-25)
32. J. M. Googin (Y-12)
33. B. L. Greenstreet
34. W. R. Grimes
35. E. Guth
36. R. F. Hibbs (Y-12)
37. M. R. Hill
38. H. W. Hoffman
39. A. Hollaender
40. A. S. Householder
41. W. H. Jordan
42. P. R. Kasten
43. C. P. Keim
44. M. T. Kelley
45. J. J. Keyes
46. R. B. Korsmeyer
47. J. A. Lane
48. S. A. Levin (K-25)
49. R. S. Livingston
50. H. G. MacPherson
51. W. D. Manly
52. E. R. Mann
53. H. C. McCurdy
54. W. B. McDonald
55. H. F. McDuffie
56. F. R. McQuilkin
57. H. J. Metz
58. A. J. Miller
59. K. Z. Morgan
60. J. P. Murray (Y-12)
61. F. H. Neill
62. M. L. Nelson
63. L. G. Overholser
64. P. Patriarca
65. F. S. Patton (Y-12)
66. A. M. Perry
67. D. Phillips
68. M. E. Ramsey
69. P. M. Reyling
70. A. F. Rupp
71. G. Samuels
72. H. W. Savage
73. A. W. Savolainen
74. O. Sisman
75. E. D. Shipley
76. M. J. Skinner
77. A. H. Snell
78. E. Storto
79. R. D. Stulting
80. C. D. Susano
81. J. A. Swartout
82. E. H. Taylor
83. D. B. Trauger
84. E. Von Halle (K-25)
85. C. S. Walker
86. J. L. Wantland
87. A. M. Weinberg
88. J. C. White
89. E. A. Wick
90. G. C. Williams

91. C. E. Winters
92. J. Zasler
93-96. ORNL - Y-12 Technical Library
Document Reference Section
97-136. Laboratory Records Department
137. Laboratory Records Department,
ORNL R.C.
138-140. Central Research Library

## EXTERNAL DISTRIBUTION

141. Division of Research and Development, AEC, ORO
142-724. Given distribution as shown in TID-4500 (14 ed.) under
Reactors-Power category (75 copies - OTS)

Previous reports in this series are:

| | |
|---|---|
| ORNL-2500 | Parts 1-4, issued April 1, 1958 |
| ORNL-2505 | Issued June 19, 1958 |
| ORNL-2510 | Issued September 18, 1958 |
| ORNL-2676 | Period Ending December 31, 1958 |